

REP

AD-A269 648

Form Approved  
GMB No. 0704 0168

Public reporting burden for this gathering and maintaining the collection of information, include Davis Highway, Suite 1204, Arlington, VA 22204



Including the time for reviewing instructions, searching existing data sources, gathering and maintaining the data needed, and completing and reviewing this collection of information, send comments regarding this burden estimate or any other aspect of this collection of information, including suggestions for reducing this burden, to Washington Headquarters Services, Directorate for Information Operations and Reports, 1215 Jefferson Davis Highway, Suite 1204, Arlington, VA 22204-3022, and to the Office of Management and Budget, Paperwork Reduction Project (0704-0188), Washington, DC 20503

1. AGENCY USE ONLY (Leave blank)

2. REPORT DATE  
15 September 1993

3. REPORT TYPE AND DATES COVERED  
Final Technical Rpt: 10/1/88-9/30/92

4. TITLE AND SUBTITLE  
Metal Slurry Droplet and Spray Combustion

5. FUNDING NUMBERS  
G-N00014-89-J-1135

6. AUTHOR(S)  
W.A. Sirignano, Principal Investigator  
R. Bhatia, Research Assistant

7. PERFORMING ORGANIZATION NAME(S) AND ADDRESS(ES)  
Department of Mechanical and Aerospace Engineering  
University of California, Irvine  
Irvine, CA 92717

DTIC  
SEP 23 1993  
A D

9. SPONSORING / MONITORING AGENCY NAME(S) AND ADDRESS(ES)  
Dr. Gabriel D. Roy  
Office of Naval Research, Code 1132P  
Arlington, VA 22217

10. SPONSORING / MONITORING AGENCY REPORT NUMBER

11. SUPPLEMENTARY NOTES  
This document has been approved for public release and sale; its distribution is unlimited.

12a. DISTRIBUTION / AVAILABILITY STATEMENT  
Available on request. Contact Dr. W.A. Sirignano, University of California, Irvine

93-21894  
21894

13. ABSTRACT (Maximum 200 words)  
Analytical and numerical studies on n-octane and aluminum metal slurry droplet combustion and metal slurry spray combustion are discussed. Two limiting isolated droplet configurations are studied: one with large metal particle enveloped by liquid hydrocarbon and another with many fine metal particles inside a liquid drop. Vaporization models for isolated slurry droplets are formulated which can be used in spray combustion calculations. An analytical model describes the combustion of aluminum particles in air. The particle transient heating, the phase-equilibrium conditions of the vapor and condensed products are analyzed. Mass and energy interactions between the slurry droplets and gas flow are studied in an idealized configuration consisting of parallel droplet streams.  
Without forced convection and preheat of the ambient air to temperatures near the aluminum oxide melting point, the flame does not possess sufficient energy to ignite the metal. Ignition times for the metal particle depend on the solid mass loading and can be several times larger than the liquid fuel burnout time. With many fine metal particles which are initially uniformly distributed in a liquid fuel droplet, depending on the shell characteristics different modes of liquid vaporization from the droplet can occur.  
At different combustor locations, interacting and distinct premixed and diffusion type reaction zones are present. The heating and burning times of the metal agglomerate are much larger than the liquid fuel vaporization times and increase with increasing metal particle size and metal loading of the droplets.

14. SUBJECT TERMS  
Metal slurry vaporization; metal slurry combustion; aluminum particle combustion; aluminum particle burning; slurry droplets and sprays

15. NUMBER OF PAGES  
210

16. PRICE CODE

17. SECURITY CLASSIFICATION OF REPORT  
Unclassified

18. SECURITY CLASSIFICATION OF THIS PAGE  
Unclassified

19. SECURITY CLASSIFICATION OF ABSTRACT  
Unclassified

20. LIMITATION OF ABSTRACT  
SAR

**GENERAL INSTRUCTIONS FOR COMPLETING SF 298**

The Report Documentation Page (RDP) is used in announcing and cataloging reports. It is important that this information be consistent with the rest of the report, particularly the cover and title page. Instructions for filling in each block of the form follow. It is important to *stay within the lines* to meet optical scanning requirements.

**Block 1. Agency Use Only (Leave blank).**

**Block 2. Report Date.** Full publication date including day, month, and year, if available (e.g. 1 Jan 88). Must cite at least the year.

**Block 3. Type of Report and Dates Covered.** State whether report is interim, final, etc. If applicable, enter inclusive report dates (e.g. 10 Jun 87 - 30 Jun 88).

**Block 4. Title and Subtitle.** A title is taken from the part of the report that provides the most meaningful and complete information. When a report is prepared in more than one volume, repeat the primary title, add volume number, and include subtitle for the specific volume. On classified documents enter the title classification in parentheses.

**Block 5. Funding Numbers.** To include contract and grant numbers; may include program element number(s), project number(s), task number(s), and work unit number(s). Use the following labels:

C - Contract	PR - Project
G - Grant	TA - Task
PE - Program Element	WU - Work Unit Accession No.

**Block 6. Author(s).** Name(s) of person(s) responsible for writing the report, performing the research, or credited with the content of the report. If editor or compiler, this should follow the name(s).

**Block 7. Performing Organization Name(s) and Address(es).** Self-explanatory.

**Block 8. Performing Organization Report Number.** Enter the unique alphanumeric report number(s) assigned by the organization performing the report.

**Block 9. Sponsoring/Monitoring Agency Name(s) and Address(es).** Self-explanatory.

**Block 10. Sponsoring/Monitoring Agency Report Number.** (If known)

**Block 11. Supplementary Notes.** Enter information not included elsewhere such as: Prepared in cooperation with...; Trans. of...; To be published in.... When a report is revised, include a statement whether the new report supersedes or supplements the older report.

**Block 12a. Distribution/Availability Statement.** Denotes public availability or limitations. Cite any availability to the public. Enter additional limitations or special markings in all capitals (e.g. NOFORN, REL, ITAR).

DOD - See DoDD 5230.24, "Distribution Statements on Technical Documents."  
DOE - See authorities.  
NASA - See Handbook NHB 2200.2.  
NTIS - Leave blank.

**Block 12b. Distribution Code.**

DOD - Leave blank.  
DOE - Enter DOE distribution categories from the Standard Distribution for Unclassified Scientific and Technical Reports.  
NASA - Leave blank.  
NTIS - Leave blank.

**Block 13. Abstract.** Include a brief (*Maximum 200 words*) factual summary of the most significant information contained in the report.

**Block 14. Subject Terms.** Keywords or phrases identifying major subjects in the report.

**Block 15. Number of Pages.** Enter the total number of pages.

**Block 16. Price Code.** Enter appropriate price code (*NTIS only*).

**Blocks 17 - 19. Security Classifications.** Self-explanatory. Enter U.S. Security Classification in accordance with U.S. Security Regulations (i.e., UNCLASSIFIED). If form contains classified information, stamp classification on the top and bottom of the page.

**Block 20. Limitation of Abstract.** This block must be completed to assign a limitation to the abstract. Enter either UL (unlimited) or SAR (same as report). An entry in this block is necessary if the abstract is to be limited. If blank, the abstract is assumed to be unlimited.

ONR FINAL TECHNICAL REPORT

REPORTING PERIOD: 1 OCTOBER 1988 - 30 SEPTEMBER 1992

METAL SLURRY DROPLET AND SPRAY COMBUSTION

ONR GRANT N00014-89-J-1135

PREPARED BY

W.A. SIRIGNANO, PRINCIPAL INVESTIGATOR  
R. BHATIA, RESEARCH ASSISTANT

DEPARTMENT OF MECHANICAL AND AEROSPACE ENGINEERING  
UNIVERSITY OF CALIFORNIA, IRVINE

SUBMITTED TO DR. GABRIEL D. ROY

15 SEPTEMBER 1993

Accession For	
NTIS Storage <input checked="" type="checkbox"/>	
DACS <input type="checkbox"/>	
Distribution <input type="checkbox"/>	
By	
Distribution/	
Availability Codes	
Date	Availability
A-1	1993

## SUMMARY

Analytical and numerical studies on metal slurry droplet combustion and metal slurry spray combustion are discussed. The slurry droplet consists of liquid hydrocarbon carrier (*n*-octane) and metal fuel (aluminum). Two limiting geometrical configurations for isolated droplets are studied: one with large metal particle enveloped by liquid hydrocarbon and another with many fine metal particles inside a liquid drop. Vaporization models for isolated slurry droplets are formulated which can be used in spray combustion calculations.

By studying transient gas-phase effects on the ignition characteristics of solid particles, it is found that in absence of forced convection unless the ambient air is preheated to large temperatures comparable to the aluminum oxide melting point, the flame does not possess sufficient energy to ignite the metal. Forced convection effects are studied by constructing a film theory based model. Ignition times for the metal particle are found to depend on the solid mass loading and can be several times larger than the liquid fuel burnout time. In the geometrical configuration consisting of many fine metal particles, which are initially uniformly distributed in a liquid fuel droplet, it is found that depending on the shell characteristics different modes of liquid vaporization from the droplet can occur. A general model is formulated to describe the various modes of vaporization. Calculations are made with metal particle size and initial volume fraction as parameters.

An analytical model is constructed to describe the combustion of aluminum particles in air. The particle transient heating is considered, and the phase-equilibrium conditions of the vapor and condensed products are analyzed. Mass and energy interactions between the slurry droplets and gas flow are studied in an idealized configuration consisting of parallel droplet streams. Results show that, at different combustor locations, interacting and distinct premixed and diffusion type reaction zones are present. The heating and burning times of the metal agglomerate are found to be much larger in comparison to the liquid fuel vaporization times and they increase with increasing metal particle size and metal loading of the slurry droplets.

Detailed numerical investigation of the fundamental processes governing the momentum, energy and mass exchanges between the solid, liquid and gas phases of a

vaporizing slurry droplet are presented. A primitive variable based formulation is used to solve the complete set of Navier-Stokes, energy and species equations. The first configuration consists of an isolated slurry droplet with a large spherical solid particle in its core that is suddenly injected in a gaseous high-temperature, laminar, convective environment. The model allows for independent motion of the solid particle core along the axis of symmetry of the slurry droplet, and considers variable gas-phase properties as well as variable liquid-phase viscosities and latent heat of vaporization. Additional features of the model include internal liquid circulation with transient droplet heating, droplet surface regression due to vaporization, and droplet deceleration with respect to the free flow due to drag. The relative motion of the solid particle and the liquid-carrier fluid are very significant during the early stages of the simulation. In that respect, the fluid mechanics dominate the heat and mass transport phenomena involved, thus strongly suggesting a possibility of secondary atomization as a result of the penetration of the solid particle through the gas/liquid interface. A second configuration is used to study the effects of internal circulation and droplet surface regression due to vaporization and agglomeration of the fine solid particles at the interface. The accumulation of the fine particles in a surface shell is predicted.

# Contents

<b>List of Figures</b> . . . . .	<b>iv</b>
<b>List of Tables</b> . . . . .	<b>xi</b>
<b>Table of Symbols</b> . . . . .	<b>xii</b>
<b>Chapter 1 Introduction</b> . . . . .	<b>1</b>
1.1 Background . . . . .	1
1.1.1 Vaporization of Liquid Carrier . . . . .	2
1.1.2 Combustion of Metal . . . . .	4
1.1.3 Spray Combustion of Metal Slurry Droplets . . . . .	6
1.2 Objectives and Organization of the Report . . . . .	7
<b>Chapter 2 Transient Heating and Burning of a Slurry Droplet</b> . .	<b>9</b>
2.1 Introduction . . . . .	9
2.2 Assumptions and Model . . . . .	10
2.2.1 Gas-Phase Analysis . . . . .	11
2.2.2 Liquid-Phase Analysis . . . . .	13
2.2.3 Dry Metal Heating . . . . .	14
2.3 Solution Procedure . . . . .	17
2.4 Results and Discussion . . . . .	19
2.5 Summary . . . . .	27
<b>Chapter 3 Convective Burning of a Droplet Containing a Single Metal Particle</b> . . . . .	<b>30</b>
3.1 Introduction . . . . .	30
3.2 Analysis . . . . .	30
3.2.1 Droplet Dynamics . . . . .	31
3.2.2 Gas-Phase Analysis . . . . .	32
3.2.3 Liquid-Phase Analysis . . . . .	34
3.2.4 Dry Particle Heating . . . . .	38
3.2.5 Metal Melting . . . . .	40
3.3 Solution Procedure . . . . .	41
3.4 Results and Discussion . . . . .	42
3.5 Conclusion . . . . .	51

<b>Chapter 4</b>	<b>Liquid Vaporization from Fine-Metal Slurry Droplets . . . . .</b>	<b>54</b>
4.1	Introduction . . . . .	54
4.2	Analysis . . . . .	55
4.2.1	Droplet Dynamics . . . . .	56
4.2.2	Liquid-Phase Analysis . . . . .	57
4.2.3	Stage I: Surface Regression . . . . .	61
4.2.4	Stage II: Liquid Vaporization through the Shell . . . . .	63
4.2.5	Stage III: Pore Drying . . . . .	69
4.3	Gas-Phase Analysis . . . . .	70
4.4	Results and Discussion . . . . .	73
4.5	Conclusions . . . . .	81
<b>Chapter 5</b>	<b>Metal Particle Combustion With Oxide Condensation . . . . .</b>	<b>83</b>
5.1	Introduction . . . . .	83
5.2	Analysis . . . . .	84
5.3	Solution Procedure . . . . .	94
5.4	Results and Discussion . . . . .	95
5.5	Summary . . . . .	107
<b>Chapter 6</b>	<b>Flame Propagation In Metal Slurry Sprays . . . . .</b>	<b>109</b>
6.1	Introduction . . . . .	109
6.2	Analysis . . . . .	110
6.2.1	Gas-Phase Analysis . . . . .	112
6.2.2	Solution of the Gas-Phase Equations . . . . .	115
6.3	Droplet Analysis . . . . .	116
6.4	Results and Discussion . . . . .	120
6.5	Summary . . . . .	131
<b>Bibliography</b>	<b>. . . . .</b>	<b>132</b>
<b>Appendix A</b>	<b>Ignition of Aluminum and Diffusivity of Oxygen through</b>	
	<b>Al<sub>2</sub>O<sub>3</sub> . . . . .</b>	<b>141</b>
<b>Appendix B</b>	<b>Comments on "Sensitivity of Metal Reactivity to Gaseous</b>	
	<b>Impurities in Oxygen Environments" . . . . .</b>	<b>144</b>
<b>Appendix C</b>	<b>Solution of a Model One-Dimensional Transpiration</b>	
	<b>Problem . . . . .</b>	<b>146</b>
<b>Appendix D</b>	<b>Effect of Thermophoresis on the Oxide Condensation</b>	<b>156</b>

<b>Appendix E Numerical Modeling of a Slurry Droplet Containing a Spherical Particle</b> . . . . .	<b>160</b>
E.1 Introduction . . . . .	160
E.2 Physical Description . . . . .	160
E.3 Assumptions and Governing Equations . . . . .	162
E.4 Gas/Liquid and Solid/Liquid Interface Conditions . . . . .	163
E.5 Solid Particle Drag . . . . .	164
E.6 Treatment of Solid-Particle Motion . . . . .	166
E.7 Numerical Solution Procedure . . . . .	167
E.8 Results and Discussion . . . . .	168
E.9 Conclusions . . . . .	182
<b>Appendix F Analysis Of Shell Formation From A Vaporizing Metal Slurry Droplet</b> . . . . .	<b>184</b>
F.1 Introduction . . . . .	184
F.2 Analysis . . . . .	184
F.3 Solution Procedure . . . . .	191
F.4 Results . . . . .	191
F.5 Conclusions . . . . .	193

# List of Figures

2.1	(a) Schematic of the droplet combustion model. (b) Schematic of the metal surface oxidation and heat transfer. . . . .	10
2.2	Gas-phase temperature, and fuel and oxidizer mass fraction profiles, for $r_{li} = 50 \mu\text{m}$ , $p_\infty = 10 \text{ atm}$ , and $T_\infty = 1000 \text{ K}$ . For all calculations, the liquid fuel is <i>n</i> -octane and the solid fuel is aluminum. . . . .	20
2.3	Droplet surface temperature and fuel mass fraction, for $r_{li} = 50 \mu\text{m}$ and $T_\infty = 1000 \text{ K}$ . . . . .	21
2.4	Droplet radius squared and flame location, for $r_{li} = 50 \mu\text{m}$ and $T_\infty = 1000 \text{ K}$ . . . . .	22
2.5	Heat and mass transfer numbers, for $r_{li} = 50 \mu\text{m}$ and $T_\infty = 1000 \text{ K}$ . . . . .	23
2.6	Vaporization rate and burning constant, for $r_{li} = 50 \mu\text{m}$ and $T_\infty = 1000 \text{ K}$ . . . . .	23
2.7	Gas-phase temperature, and fuel and oxidizer mass fraction profiles for slurry droplet, $r_{li} = 50 \mu\text{m}$ , $r_m = 20 \mu\text{m}$ , $p_\infty = 10 \text{ atm}$ , and $T_\infty = 1000 \text{ K}$ . . . . .	24
2.8	Droplet radius squared and flame location for slurry droplets, $r_{li} = 50 \mu\text{m}$ , $p_\infty = 10 \text{ atm}$ , and $T_\infty = 1000 \text{ K}$ . . . . .	25
2.9	Fuel and oxidizer mass fraction at the oxide-gas interface, and droplet surface temperature, for slurry droplet, $r_{li} = 50 \mu\text{m}$ , $p_\infty = 10 \text{ atm}$ , and $T_\infty = 1000 \text{ K}$ . . . . .	26
2.10	Oxidizer flow rate at the Al-Al <sub>2</sub> O <sub>3</sub> interface, for $r_{li} = 50 \mu\text{m}$ , $r_m = 20 \mu\text{m}$ , $p_\infty = 10 \text{ atm}$ , and $T_\infty = 1000 \text{ K}$ . . . . .	26
2.11	Fuel and oxidizer mass fraction at the oxide-gas interface, and droplet surface temperature, for slurry droplet, $r_{li} = 50 \mu\text{m}$ , $p_\infty = 10 \text{ atm}$ , and $\delta_i = 30 \text{ \AA}$ . . . . .	28
2.12	Relative contribution of the heat fluxes due to the conduction and the aluminum surface oxidation, for $r_{li} = 50 \mu\text{m}$ , $r_m = 20 \mu\text{m}$ , $p_\infty = 10 \text{ atm}$ , and $\delta_i = 30 \text{ \AA}$ . . . . .	28
3.1	(a) Configuration of the slurry droplet. (b) Schematic of the surface oxidation of the dry metal particle. . . . .	31
3.2	(a) Liquid-phase stream function $\Psi_l/r_l^2(U_\infty - U_l)$ for $\beta = 0.5$ . (b) Radial ( $v_r/U_s$ ) and tangential ( $v_\theta/U_s$ ) velocities of the liquid-phase vs. radial distance ( $r/r_l$ ) at various tangential locations, for $\beta = 0$ and $0.25$ . . . . .	36

3.3	Results for vaporization of slurry droplets in air, for $p_\infty=10$ atm, $T_\infty=1500$ K, $U_\infty=50$ m/s, $U_i=10$ m/s, and $r_m/r_i = \beta=0$ (all-liquid droplet), 0.25 and 0.5. (a): droplet radius squared $(r_l/r_i)^2$ ; (b): liquid fuel vaporization rate $\dot{m}_l$ ; (c): droplet surface temperature $T_s$ ; and (d): liquid Peclet number $\log_{10}(Pe_l)$ . Curves 1 are from axi-symmetric calculations and 2 are from effective conductivity calculations. . . . .	44
3.4	Liquid-phase isotherms for vaporization of slurry droplets in air, for $p_\infty=10$ atm, $T_\infty=1500$ K, $U_\infty=50$ m/s, $U_i=10$ m/s, and $r_m/r_i = \beta= 0.5$ . (a): At $t=0.01$ ms, $r_l/r_i=1.000$ , $Re=282.4$ , $T_{min}=300.0$ K, $T_{max}=347.6$ K. (b): At $t=0.05$ ms, $r_l/r_i=1.000$ , $Re=277.2$ , $T_{min}=300.0$ K, $T_{max}=361.7$ K. (c): At $t=4.0$ ms, $r_l/r_i=0.756$ , $Re=73.7$ , $T_{min}=459.5$ K, $T_{max}=471.4$ K. (d): At $t=6.0$ ms, $r_l/r_i=0.553$ , $Re=35.3$ , $T_{min}=474.4$ K, $T_{max}=476.0$ K. . . . .	46
3.5	Results for combustion of slurry droplets in air, for $p_\infty=10$ atm, $T_\infty=1500$ K, $U_\infty=50$ m/s, $U_i=10$ m/s, and $r_m/r_i = \beta=0$ (all-liquid droplet), 0.25 and 0.5. (a): droplet radius squared $(r_l/r_i)^2$ ; (b): liquid fuel burning rate $\dot{m}_l$ ; (c): droplet surface temperature $T_s$ . . . . .	47
3.6	Results for combustion of slurry droplets in air, for $p_\infty=10$ atm, $T_\infty=1500$ K, $U_\infty=50$ m/s, $U_i=10$ m/s, and $r_m/r_i = \beta= 0.25$ and $0.5$ . (a): gas Reynolds number $Re$ ; (b): droplet surface temperature $T_s$ ; (c): oxidizer flow rate $\dot{m}_o$ ; and (d): oxide film thickness $\delta/\delta_i$ . . . . .	50
3.7	Heat fluxes into the particle versus time, for $U_\infty=50$ m/s, $U_i=10$ m/s, and $r_m/r_i = \beta= 0.25$ and $0.5$ . Curve 1: total $\dot{q}_m$ ; curve 2: convective $\dot{q}_c$ ; and curve 3: chemical $\dot{q}_{ch}$ . $\dot{q}_{rad}$ is insignificant. . . . .	51
3.8	Ignition times for slurry droplets burning in air at $p_\infty=10$ atm, $T_\infty=1500$ K, $U_\infty=50$ m/s and $U_i=10$ m/s. (a): Effect of metal radius $\beta = r_m/r_i$ ; (b): Effect of fuel equivalence ratio $\Phi$ , based on the liquid mass in the slurry droplet; (c): Effect of initial Reynolds number, calculated by varying the initial relative gas-droplet velocity. . . . .	52
4.1	Slurry droplet with fine metal particles. . . . .	55
4.2	Thermal conductivity of the solid-liquid mixture vs. solid volume fraction. . . . .	58
4.3	(a) Schematic of the life history of the slurry droplets. (b) Schematic of the wick structure of the shell. . . . .	59
4.4	Total pressure, from static and thermodynamic equilibrium. . . . .	61
4.5	Schematic of vaporization from Stages II and III. (a) shows the bubble attached to the surface, (b) shows the model assumption, and (c) shows pore drying. . . . .	67
4.6	Droplet radius and bubble radius for different metal particle sizes and fixed initial metal volume fraction $\phi_{m_i} = 0.25$ . . . . .	74
4.7	Shell thickness and bubble pressure for different metal particle sizes and fixed initial metal volume fraction $\phi_{m_i} = 0.25$ . . . . .	75

4.8	Droplet surface temperature and bubble temperature for different metal particle sizes and fixed initial metal volume fraction $\phi_{m_i} = 0.25$ . . . . .	76
4.9	Vaporization rate and mass vaporized for different metal particle sizes and fixed initial metal volume fraction $\phi_{m_i} = 0.25$ . . . . .	76
4.10	Bubble inflow rate and bubble vaporization rate for different metal particle sizes and fixed initial metal volume fraction $\phi_{m_i} = 0.25$ . . . . .	77
4.11	Droplet radius and bubble radius for different initial metal loading and fixed metal particle size $r_m = 2\mu\text{m}$ . . . . .	78
4.12	Shell thickness and bubble pressure for different initial metal loading and fixed metal particle size $r_m = 2\mu\text{m}$ . . . . .	78
4.13	Droplet surface temperature and bubble temperature for different initial metal loading and fixed metal particle size $r_m = 2\mu\text{m}$ . . . . .	79
4.14	Vaporization rate and mass vaporized for different initial metal loading and fixed metal particle size $r_m = 2\mu\text{m}$ . . . . .	80
4.15	Bubble inflow rate and bubble vaporization rate for different initial metal loading and fixed metal particle size $r_m = 2\mu\text{m}$ . . . . .	80
5.1	Schematic of the aluminum droplet. . . . .	84
5.2	Droplet combustion model and schematic mass fractions and temperature profiles. . . . .	86
5.3	Gas-phase profiles of the fuel ( $Y_1$ ), oxygen ( $Y_2$ ), oxide ( $Y_3$ ) and inert ( $Y_4$ ) mass fractions, and the temperature ( $T$ ). The flame is at the peak gas temperature. The point of condensation is given by $Y_3 = 0$ . In these calculations: $Y_{2,\infty} = 0.232$ , $p_\infty = 10$ atm, $T_\infty = 2000$ K, $r_{s,i} _{T=300\text{K}} = 25$ $\mu\text{m}$ . . . . .	97
5.4	Time evolution of the fuel vapor ( $M_{1,s}$ ), oxide vapor ( $M_{3,s}$ ), and the net gas fluxes in the inner ( $M_{g,I}$ ) and outer ( $M_{g,II}$ ) zones. Also shown is the fractional mass vaporized, which is the ratio of time integration of the flux of the fuel vaporized to the initial droplet mass. In these calculations: $Y_{2,\infty} = 0.232$ , $p_\infty = 10$ atm, $T_\infty = 2000$ K, $r_{s,i} _{T=300\text{K}} = 25$ $\mu\text{m}$ . . . . .	99
5.5	Time evolution of the droplet surface radius ( $r_s/r_{s,i}$ ) <sup>2</sup> , fuel radius ( $r_{Al}/r_{s,i}$ ), and oxide radius ( $r_{ox}/r_{s,i}$ ). Also shown are the flame ( $r_f/r_s$ ) and condensation ( $r_c/r_s$ ) radii. In these calculations: $Y_{2,\infty} = 0.232$ , $p_\infty = 10$ atm, $T_\infty = 2000$ K, $r_{s,i} _{T=300\text{K}} = 25$ $\mu\text{m}$ . . . . .	100
5.6	Effect of varying ambient pressure and temperature on the droplet surface ( $T_s$ ), condensation ( $T_c$ ), and flame ( $T_f$ ) temperatures. Note the closeness of $T_s$ and $T_c$ . In these calculations: $Y_{2,\infty} = 0.232$ , $r_{s,i} _{T=300\text{K}} = 25$ $\mu\text{m}$ . . . . .	101

5.7	Effect of varying ambient pressure and temperature on the flame ( $r_f/r_{s,i}$ ), condensation ( $r_c/r_{s,i}$ ), and final droplet ( $r_s/r_{s,i} \equiv r_{ox}/r_{s,i}$ ) radii. Since different values of $r_s$ result for different ambient conditions, the radii in this figure are non-dimensionalized by $r_{s,i}$ , to facilitate comparison. Pressure has small effect on the final size, but a large effect on the condensation radius. In these calculations: $Y_{2,\infty} = 0.232$ , $r_{s,i} _{T=300K} = 25 \mu\text{m}$ . . . . .	103
5.8	Effect of varying ambient pressure and temperature on the fuel vapor ( $M_{1,s}$ ), oxide vapor ( $M_{3,s}$ ) and net gas ( $M_{g,I}$ ) fluxes in the gas phase. Effect on the droplet burning time is also shown. To facilitate comparison, the non-dimensional fluxes in this figure are defined as $M_i = \frac{r^2 m_i}{r_{s,i} \rho D}$ , rather than the usual $M_i = \frac{r^2 m_i}{r_s \rho D}$ . In these calculations: $Y_{2,\infty} = 0.232$ , $r_{s,i} _{T=300K} = 25 \mu\text{m}$ . . . . .	105
5.9	Comparison of predicted and experimental values of the droplet burning time. The figure is taken from Turns et al.[74]. Solid lines represent analytical results for three ambient oxygen mole fractions: $X_{2,\infty} = 0.10$ , 0.15 and 0.25. In these calculations $T_\infty = 1660 \text{ K}$ and $p_\infty = 1 \text{ atm}$ . . . . .	106
6.1	Schematic of the parallel slurry droplet stream combustion model and coordinate system. . . . .	111
6.2	Schematic of the life history of the slurry droplets. . . . .	117
6.3	Gas-phase temperature contours for one stream injected at $\chi = 0.5$ , liquid equivalence ratio $\Phi_l = 0.3$ , and $T_\infty = 600 \text{ K}$ . . . . .	122
6.4	Gas-phase temperature contours for one stream injected at $\chi = 0.5$ , liquid equivalence ratio $\Phi_l = 0.5$ , and $T_\infty = 1000 \text{ K}$ . . . . .	122
6.5	Gas-phase oxygen mass fraction versus normalized transverse coordinate ( $\chi$ ) at various streamwise locations ( $\xi$ ), for one stream injected at $\chi = 0.5$ . . . . .	124
6.6	Gas-phase temperature versus normalized transverse coordinate ( $\chi$ ) at various streamwise locations ( $\xi$ ), for one stream injected at $\chi = 0.5$ . . . . .	125
6.7	Droplet radius versus normalized streamwise coordinate ( $\xi$ ), for one stream injected at $\chi = 0.5$ , liquid equivalence ratio $\Phi_l = 0.5$ , and $T_\infty = 1000 \text{ K}$ . . . . .	125
6.8	Droplet and gas-phase temperatures at $\chi = 0.5$ , for one stream injected at $\chi = 0.5$ , liquid equivalence ratio $\Phi_l = 0.5$ , and $T_\infty = 1000 \text{ K}$ . . . . .	126
6.9	Gas-phase temperature contours for injection of three streams at $\chi = 0.25$ , 0.50, and 0.75; and $\Phi_l = 0.5$ , $T_\infty = 1000 \text{ K}$ , $\phi_{m,i} = 10\%$ , and $r_m/r_{l,i} = 0.04$ . . . . .	126
6.10	Gas-phase temperature contours for injection of five streams at $\chi = 0.16$ , 0.32, 0.48, 0.64, and 0.80; and 0.75, $\Phi_l = 0.5$ , $T_\infty = 1000 \text{ K}$ , $\phi_{m,i} = 10\%$ , and $r_m/r_{l,i} = 0.04$ . . . . .	127
6.11	Gas-phase temperature versus normalized transverse coordinate ( $\chi$ ) at various streamwise locations ( $\xi$ ), for three stream injection. . . . .	128

6.12	Gas-phase temperature versus normalized transverse coordinate ( $\chi$ ) at various streamwise locations ( $\xi$ ), for five stream injection. . . . .	129
6.13	Comparison of liquid hydrocarbon vaporization time ( $t_v$ ), dry agglomerate heating time ( $t_a$ ), and the metal burning time ( $t_m$ ), for $\Phi_l = 0.5$ , $T_\infty = 1000$ K, and $r_m/r_{l,i} = 0.02$ . . . . .	129
6.14	Comparison of liquid hydrocarbon vaporization time ( $t_v$ ), dry agglomerate heating time ( $t_a$ ), and the metal burning time ( $t_m$ ), for $\Phi_l = 0.5$ , $T_\infty = 1000$ K, and initial metal loading $\phi_{m,i} = 20\%$ by volume. . . . .	130
C.1	A model transpiration problem. Oxide vapor flows from left to right, and oxygen flows from right to left. . . . .	147
C.2	Oxygen $Y_o$ and vapor oxide $Y_p$ mass fractions and gas temperatures $T$ for $Da = 1.0$ . Also shown is saturation oxide mass fraction $Y_{p,sat}$ . . . . .	150
C.3	Nondimensional mass fluxes of oxygen $M_o$ , oxide vapor $M_p$ and bulk gas $M_g = M_o + M_p$ for $Da = 1.0$ . Also shown is dimensional gas velocity $u$ . . . . .	150
C.4	Oxygen $Y_o$ and vapor oxide $Y_p$ mass fractions and gas temperatures $T$ for $Da = 10.0$ . Also shown is saturation oxide mass fraction $Y_{p,sat}$ . . . . .	151
C.5	Nondimensional mass fluxes of oxygen $M_o$ , oxide vapor $M_p$ and bulk gas $M_g = M_o + M_p$ for $Da = 10.0$ . Also shown is dimensional gas velocity $u$ . . . . .	151
C.6	Oxygen $Y_o$ and vapor oxide $Y_p$ mass fractions and gas temperatures $T$ for $Da = 100.0$ . Also shown is saturation oxide mass fraction $Y_{p,sat}$ . . . . .	152
C.7	Nondimensional mass fluxes of oxygen $M_o$ , oxide vapor $M_p$ and bulk gas $M_g = M_o + M_p$ for $Da = 100.0$ . Also shown is dimensional gas velocity $u$ . . . . .	152
C.8	Oxygen $Y_o$ and vapor oxide $Y_p$ mass fractions and gas temperatures $T$ for $Da = 1000.0$ . Also shown is saturation oxide mass fraction $Y_{p,sat}$ . . . . .	153
C.9	Nondimensional mass fluxes of oxygen $M_o$ , oxide vapor $M_p$ and bulk gas $M_g = M_o + M_p$ for $Da = 1000.0$ . Also shown is dimensional gas velocity $u$ . . . . .	153
C.10	Oxygen $Y_o$ and vapor oxide $Y_p$ mass fractions and gas temperatures $T$ for $Da \rightarrow \infty$ . Also shown is saturation oxide mass fraction $Y_{p,sat}$ . . . . .	155
C.11	Nondimensional mass fluxes of oxygen $M_o$ , oxide vapor $M_p$ and bulk gas $M_g = M_o + M_p$ for $Da \rightarrow \infty$ . Also shown is dimensional gas velocity $u$ . . . . .	155
D.1	Effect of thermophoretic velocity on a condensed oxide particle. . . . .	157
E.1	Schematic of slurry-droplet flow configuration. . . . .	161
E.2	Liquid-phase streamlines (upper half) and velocity vectors (lower half) at $\tau_{Hg} = 1$ of the base case slurry simulation. The outer circle represents the gas/liquid interface, while the inner one represents the solid-particle surface. The gas flow is directed from left to right. . . . .	169

E.3	Time variation of the velocities of the three centers of interest in the base case slurry droplet simulation. These velocities are expressed with respect to a stationary reference frame. . . . .	171
E.4	Liquid-phase isothermal contours at three different times of the base case slurry simulation; (A) $\tau_{Hg} = 0.5$ , (B) $\tau_{Hg} = 1$ and (C) $\tau_{Hg} = 1.5$ . The outer circle represents the gas/liquid interface, while the inner one represents the solid particle surface. The gas flow is directed from left to right. . . . .	172
E.5	Angular variation of pressure differential (in $N/m^2$ ) over the solid-particle surface at three different times of the base case simulation ( $\tau_{Hg} = 0.4, 0.8$ and $1$ ). The pressure at $\theta = 0^\circ$ over the solid surface was used as a reference value. . . . .	173
E.6	Angular variation of tangential velocity on the gas/liquid interface at four different times of the base case simulation ( $\tau_{Hg} = 0.4, 0.8, 1$ and $1.4$ ). . . . .	174
E.7	Angular variation of temperature on the gas/liquid interface of the slurry droplet at four different times of the base case simulation ( $\tau_{Hg} = 0.4, 0.8, 1$ and $1.4$ ). . . . .	175
E.8	Angular variation of vaporization mass flux ( $\rho_g V_{g,n}$ ) on the gas/liquid interface at four different times of the base case simulation ( $\tau_{Hg} = 0.4, 0.8, 1$ and $1.4$ ). . . . .	176
E.9	Time variation of solid particle eccentricities for three slurry droplets with different initial Reynolds numbers ( $Re_g = 100, 50, 20$ ). The eccentricity is defined as the distance of the solid particle center from the geometric center of a slurry droplet. . . . .	177
E.10	Time variation of solid particle eccentricities $ \epsilon $ for the three slurry droplet cases studied. . . . .	180
E.11	Time variation of surface-averaged temperature on the gas/liquid interface and solid-particle temperature for the three slurry droplet cases studied. . . . .	181
F.1	Schematic of the problem. . . . .	194
F.2	Different process in slurry droplet vaporization. . . . .	194
F.3	Liquid-phase velocity vectors of a slurry droplet with particle loading (by volume) = 25%. . . . .	195
F.4	Liquid-phase streamfunctions of a slurry droplet with particle loading (by volume) = 25%. . . . .	195
F.5	Liquid-phase isotherms of a slurry droplet with particle loading (by volume) = 25%. . . . .	195
F.6	Liquid-phase velocity vectors of a slurry droplet with particle loading (by volume) = 25% after the completion of the first layer of the shell. . . . .	195
F.7	Liquid-phase streamfunctions of a slurry droplet with particle loading (by volume) = 25% after the completion of the first layer of the shell. . . . .	196

F.8	Liquid-phase isotherms of a slurry droplet with particle loading (by volume) = 25% after the completion of the first layer of the shell. . .	196
F.9	Liquid-phase velocity vectors of a pure liquid droplet with particle loading (by volume) = 25%. . . . .	196
F.10	Liquid-phase velocity vectors of a pure liquid droplet. . . . .	196
F.11	Liquid-phase isotherms of a pure liquid droplet. . . . .	197
F.12	Liquid-phase isotherms of a slurry droplet with particle loading (by volume) = 25% after the completion of the third layer of the shell. . .	197
F.13	Liquid-phase streamfunction and motion of metal particles. . . . .	197
F.14	Liquid-phase circulation (non-dimensional) vs. time. . . . .	198
F.15	Average surface and volume temperature vs. time. . . . .	198
F.16	Droplet radius squared vs. time. . . . .	199
F.17	Drag coefficient vs. time. . . . .	199
F.18	Drag coefficient vs. time. . . . .	199

# List of Tables

2.1	Physical properties of aluminum and <i>n</i> -octane. . . . .	11
5.1	Properties of aluminum and aluminum oxide. . . . .	88
5.2	Solution summary of equations governing aluminum combustion. . . .	93
E.1	Physical Parameters Used in Base Case Slurry Droplet Simulation . .	165

# Table of Symbols

$A_r$	averaging parameter
$B_M$	mass transfer number
$B_T$	heat transfer number
$C_D$	drag coefficient
$C_p$	specific heat
$\mathcal{D}$	mass diffusivity
$d$	droplet diameter
$f$	stoichiometric liquid fuel/oxygen ratio
$h$	convective heat transfer coefficient
$\Delta H$	heat of combustion of liquid fuel
$k$	thermal conductivity
$L$	latent heat of evaporation
$Le$	Lewis number
$\dot{m}_l$	mass vaporization rate of liquid fuel
$\bar{M}$	average molecular weight of the gas-phase
$N$	number of droplet streams
$N_l$	droplet-sheet density
$Nu$	Nusselt number
$P_1$	vaporization/diffusion length ratio, $P_1 = (R_l^2 \rho_l (1 - \phi_{m,i}) u_{l,i}) / (3L^2 \rho_g u_{g,i})$
$P_2$	fuel/air mass ratio, $P_2 = (N_{l,i} \dot{m}_{l,i} u_{l,i}) / (L \rho_g u_{g,i})$

$P_5$	vaporization/reaction length ratio, $P_5 = R_i^2 \rho_l (1 - \phi_{m,i}) u_{l,i} \rho_i^{a+b-1} M_F^{1-a} / (3 \bar{\rho} \bar{D} M_O^b u_{g,i})$
$P_6$	transfer number, $P_6 = C_p (T_{\text{ref}} - T_{l,i}) / \Delta H$
$P_7$	oxygen/fuel stoichiometric mass ratio, $P_7 = \nu M_O / M_F$
$P_8$	wall heat flux parameter, $P_8 = z_{\text{ref}} \dot{q}_w / L \rho_i u_{g,i} C_p (T_{\text{ref}} - T_{l,i})$
Pe	Peclet number
Pr	Prandtl number
$\dot{Q}_l$	heat penetrating into droplet interior
$S_o$	dimensionless oxidizer flux, $S_o = \dot{m}_o / (4 \pi \bar{\rho} \bar{D} R_i)$
$S_v$	dimensionless liquid fuel vaporization rate, $S_v = \dot{m}_l / (4 \pi \bar{\rho} \bar{D} R_i)$
$S_{o,1}$	oxidation source in fuel conservation eq., $S_{o,1} = -N'_i Y_F S_o$
$S_{o,2}$	oxidation source in oxygen conservation eq., $S_{o,2} = N'_i (1 - Y_O) S_o / P_7$
$S_{o,3}$	oxidation source in energy conservation eq., $S_{o,3} = P_6 (T' - T'_s) N'_i S_o (1 - A_F Nu R' / 2 S_o)$
$S_{v,1}$	vaporization source in fuel conservation eq., $S_{v,1} = N'_i (1 - Y_F) S_v$
$S_{v,2}$	vaporization source in oxygen conservation eq., $S_{v,2} = N'_i (-Y_O) S_v / P_7$
$S_{v,3}$	vaporization source in energy conservation eq., $S_{v,3} = -P_6 (T' - T'_s) N'_i S_v (1 + 1/B_{e\pi})$
$r$	droplet radius
Re	Reynolds number
Sh	Sherwood number
$t$	time
$T$	temperature
$U_s$	maximum surface velocity
$v$	velocity
$\dot{W}$	reaction rate
$X$	mole fraction in the gas-phase
$Y$	mass fraction

$Z$  non-dimensional temperature

### Greek symbols

$\alpha$  thermal diffusivity

$\Gamma$  circulation of liquid vortex

$\eta$  non-dimensional radial coordinate

$\theta$  tangential coordinate

$\mu$  dynamic viscosity

$\rho$  density

$\tau$  non-dimensional time

$\phi_m$  volume fraction of solid in slurry droplet

$\Phi$  overall equivalence ratio based on the mass of liquid fuel

$\Psi$  stream function for liquid motion

### Subscripts

$Al$  aluminum

$F$  fuel

$i$  initial condition

$m$  metal (solid)

$o$  oxidant

$g$  gas-phase

$l$  liquid-phase

$r$  radial direction

$s$  droplet surface

- $\theta$     tangential direction
- $\infty$     condition far away from droplet surface

Symbols not defined in the above nomenclature are defined when first used in the text.

# Chapter 1

## Introduction

### 1.1 Background

There is a growing interest within the combustion community in developing slurry fuels with high volumetric energy release rates for potential application in combustion and propulsion systems. The slurry fuels combine the advantages of spray injectibility and pumpability of liquid fuels, and high energy release rates of solid fuels. Combustion of metal-based slurries has been studied [5, 6, 7, 68, 95, 98, 111, 112] for potential development of high energy density fuels for air breathing propulsion systems as ramjets. Additionally, coal-based slurries have been studied [32, 84, 93, 94] for burning coal in liquid fueled combustors, and calcium-based slurries for reducing SO<sub>2</sub> emissions [63] from coal fueled power plants. A variety of solid constituents such as coal, boron, aluminum, beryllium, etc., in the slurries have been studied, and their potential advantages and disadvantages reported. The advantages of metal (boron, aluminum, or magnesium) based fuels dispersed in a liquid hydrocarbon carrier are reported by [68, 105].

In the combustion of metal slurry droplets, the liquid carrier vaporizes and burns first, exposing the dry metal to a hot oxidizing environment, and a film of metal oxide forms on the metal surface. This oxide skin acts as a barrier to further surface oxidation of the metal and must be retracted before the metal can ignite. The boiling points of the metal and its oxide play a major role in determining the mode of solid particle combustion. When the boiling point of the oxide is larger than the boiling point of the metal itself (e.g., aluminum and magnesium), then the solid fuel

burns in the vapor phase like hydrocarbons. This condition of boiling point of oxide being larger than metal boiling point is known as the Glassman criterion [34, 35] for the vapor-phase combustion of the metals and is based upon the conjecture that the flame temperature (which must be larger than the metal boiling point) is limited by the oxide boiling point. Boron and titanium do not have this property and burn somewhat similar to carbon.

### 1.1.1 Vaporization of Liquid Carrier

Large number of experimental and analytical studies on the subject of vaporization of the liquid carrier are available. Antaki [5, 6] presents theoretical studies using singular perturbation expansions. In the first study, the initial solid composition of the slurry is taken high enough so that the solid particles can support each other, and the overall diameter is assumed to remain constant. Vaporization occurs at the surface of a regressing inner sphere ('rigid porous shell' model). The inner regressing sphere is shown to follow a  $d^3 - law$ , meaning that the cube of the diameter of the regressing liquid surface is constant with time. In the second study [6], the earlier work is extended to include smaller solid mass fractions. Peleg and Timnat [68] give results of an experimental study on combustion of aluminum and boron slurries with kerosene, in a dump combustor. They report aluminum and boron slurries with up to 80% solids burn with reasonable efficiency in the combustor. Petela [69] constructs a simple mathematical model for combustion of coal-oil droplets. Turns and coworkers [98, 111], experimentally and analytically studied the ignition of aluminum slurry droplets and the vapor phase combustion of aluminum. Individual droplets were supported on silicon carbide filaments, and exposed to oxygen mole fractions ranging from 0.10 to 0.25 and gas temperatures from 1250 to 1800 K, at one atmospheric pressure. Their results show that for initial diameters of 500 to 1100  $\mu\text{m}$ , the ignition times of Al slurry droplets range from 0.2 to 1.2 s, roughly equal to the burning times of JP-10 under corresponding conditions. The addition of carbon particles (0.35  $\mu\text{m}$  diameter) produced hollow agglomerates which fragmented. Lee et al. [54, 55], in an analytical and experimental study on the combustion characteristics of carbon/JP-10 slurries with alkyl azides and dihalides, proposed the formation of an interior void as the liquid is depleted from the inner core of the slurry droplet. However, the dynamic

equilibrium conditions within the droplet interior and the gas phase have not been considered, and these are essential to the physics of the problem of the liquid fuel vaporization from a slurry droplet. Also, the effects of the gas-phase convection on the vaporization rates and the subsequent burning process have yet to be addressed.

Under certain conditions microexplosions of slurry droplets have been observed. Cho et al. [19] present a theoretical study to elucidate a mechanism for the disruptive burning of boron slurry droplets. Takahashi et al. [95, 96] present the results of an experimental study on the combustion behavior of boron slurry droplets. They report quiescent burning of boron slurry droplets for short periods of time with an envelope flame of vaporized JP-10, which is followed by a disruption of the droplet. As the environment oxygen content is increased, the disruption is seen to occur earlier, largely because of the increased diffusion-flame temperature. The disruptive combustion of A/C/JP-10 slurry droplets is studied experimentally by Wong and Turns [112]. Further discussion of previous theories on the vaporization of liquid carrier from the slurry droplets and the disruption phenomenon can be found in Chapter 4.

Another important effect in the modeling of slurry droplets yet to be addressed is the effect of unsteady gas phase heat and mass transfer on the liquid fuel burning. In burning of an isolated droplet, upon completion of the liquid burnout the hydrocarbon flame will collapse inwards onto the metal surface, thus affecting the temperature rise of the solid agglomerate. Also, earlier studies have employed a lumped capacity formulation which assumes that the slurry droplet has a spatially uniform temperature, thus implying infinite thermal conductivity of the liquid and metal. Although this may be a reasonable limit for the metal, it is certainly inappropriate for the liquid fuel [88]. These effects cannot be properly described by a quasi-steady gas phase heat and mass diffusion theory.

Several researchers in the past have considered the unsteady nature of all-liquid droplet combustion. Earlier workers [89], in an effort to obtain analytic solutions, neglected the convective term in the conservation equations. In such an approach, the variable density appearing in the equation of state is assumed constant, thus abandoning the equation of state. Crespo and Liñan [23] made an asymptotic analysis by taking the density ratio of the ambient gas and liquid phase to be a small parameter. Chervinsky [18] transformed the problem into the mass coordinate plane, in which

the droplet is shown to become a stationary point source. To obtain closed form analytic solutions, certain mathematical approximations were employed. A particular difficulty in this approach is obtaining useful results in the physical plane. Also in analytic approaches, the liquid phase transient heating has not been properly taken into account. Law et al. [52], assuming quasi-steady gas phase transport, examine the initial fuel vaporization accumulation effects. With this approach, the flame radius for droplets burning in air is found to increase beyond bounds and approaches infinity at the end of vaporization. This unrealistic result is due to the neglect of the unsteady terms in the conservation equations.

In summary, it is now established that in combustion of slurry droplets, the liquid carrier vaporizes and burns in the first stage, leaving behind an agglomerate of dry solid particles which then heats, ignites and burns. After an initial decrease dependent on solid loading, the droplet radius becomes fixed. A rigid porous shell is established on the droplet surface and the agglomerates formed are hollow. Removal of the oxide film results in ignition and subsequent burning of the metal agglomerate.

### 1.1.2 Combustion of Metal

Aluminum particle combustion has been extensively studied in the past, both experimentally and analytically, from a view point of determining combustion efficiencies of metalized solid propellants. The burning mechanism of aluminum is complicated by product condensation because of the nature of the volatility differences between the fuel and its combustion products. An early study to model the vapor-phase diffusion flame of aluminum combustion was performed by Brzustowski and Glassman [13, 14]. Price [74] presents a literature review on combustion of aluminum in metalized propellants. Experimental results on aluminum particles combustion (Friedman and Maček [30, 31]; Maček [57]) have shown that minimum ambient temperature necessary for ignition is well defined as a function of partial pressure of oxygen in the atmosphere. The ignition temperatures are observed to be close to the melting temperature of the oxide (2325 K), due to the presence of the relatively impermeable thin metal oxide coating that forms on the surface. After melting of

the oxide, aluminum burns mostly in the gas phase. The burning mechanism of aluminum is complicated by product condensation because of the nature of the volatility differences between the fuel and its combustion products. It is well known [74] that in environments containing water vapor, nitrogen, carbon dioxide, etc., the aluminum oxide resulting from vapor phase reaction of aluminum and oxygen will condense. Law [50, 51] presents a simplified approach (quasi-steady gas-phase) for combustion modeling in these cases. The condensation of vaporized oxides on the droplet surface and the motion of the condensed oxides have been included in Law's models.

In a recent review article, Brewster [12] describes the general features of aluminum condensation. The gas phase is divided into two zones, an inner zone devoid of condensed particles and an outer zone which includes the condensed particles. In the inner zone, the direction of the gas velocity (inwards or outwards from the droplet surface) has to be determined by the net gaseous mass flux. If the net gaseous mass flux in the inner zone is positive and the flux in the outer zone is negative, then it results in trapping the condensed oxide at the radius of condensation. This phenomenon is speculated in the experimental work of Wilson and Williams [110]. Thermophoresis can cause the condensed particles to move outwards, from the radius of condensation. However, convection would drive the particles back.

A critical aspect in these studies has been the neglect of the thermodynamic phase equilibrium between condensed and the vapor phases. As a result of this neglect, the condensation is assumed to occur only at fixed radial positions: at the flame and at the droplet surface. In addition, these models require arbitrary specification of the droplet surface temperature and the flame temperature, rather than being determined in the model. Thus, even though it is assumed that the flame temperature is limited by the boiling point of the aluminum oxide, the partial pressure of oxide and the total gas pressure have no role in determining the flame temperature, which is always fixed at 3850 K. In reality, the calculated gas temperatures and oxide vapor-liquid thermodynamic equilibrium must determine whether there exists condensed oxide at the flame. As the combustion products move away from the flame, where the temperature is highest, they will undergo condensation at some location beyond the flame. Additionally, implicit in Law's models is the assumption that the product  $r^2 v_r$ , where  $v_r$  is the gas radial velocity, is independent of the radial position  $r$ . Due to oxide condensation, the velocity far from the particle surface will be negative, i.e., directed

inwards. This flux has to be determined in the model. This need was recognized by King [48] who proposed a model for single particle aluminum combustion in  $\text{CO}_2\text{-N}_2$  atmospheres. In this model, aluminum gas reacts with  $\text{CO}_2$  producing  $\text{AlO}$ .  $\text{AlO}$  then reacts with liquid surface aluminum to form  $\text{Al}_2\text{O}$  gas, causing droplet radius reduction. Aluminum oxide condensation is assumed to occur in a thin zone whose location is arbitrarily determined by specifying a condensation temperature. It is also noted that an effect of the oxide condensation on the particle surface is that, even as the aluminum is continuously depleted from the droplet, liquid oxide accumulates on the particle, and the particle radius does not go to zero upon the completion of aluminum vaporization. Turns et al. [98] have experimentally observed final particle sizes of 60% to 80% of the initial aluminum particle size. At present, an empirical correlation (Hermesen [43]) continues to be widely employed to predict aluminum particle burning rate in solid rocket motors (Sabnis et al. [82]). Another correlation is used by Vilyunov et al. [103].

### 1.1.3 Spray Combustion of Metal Slurry Droplets

To examine the ignition and combustion characteristics of the slurry droplets, a spray calculation is necessary. As a first step in understanding of complex phenomenon of spray combustion of metal slurry droplets, we seek to understand the heat and mass transfer interactions between the slurry droplets and the gas flow. This calculation has to be made in order investigate the manner in which one or more reaction zones spread from one group of droplets to another, and it is a logical first before fully randomized parcels of droplets are explored. No previous analytical studies could be found on the topic of spray combustion of the metal slurry droplets. However, spray combustion of hydrocarbon droplets has been extensively studied. Extensive reviews on spray combustion are available (e.g., Sirignano [88], Faeth [28]).

## 1.2 Objectives and Organization of the Report

Even though slurry fuels are widely employed today, their vaporization, ignition and combustion characteristics are not fully understood. The main goal of this work focuses on understanding the details of the above characteristics, and providing some important information on the practical implications involved in both isolated-droplet and spray configurations.

The specific goals are to gain insights and mathematical descriptions of the processes of liquid heating and vaporization, hydrocarbon-fuel vapor combustion, metal particle heating, oxidation and burning, and spray burning as they relate to metal slurry fuels. Two geometrical configurations are studied: one consisting of an isolated slurry droplet which contains a single solid particle in its core, and, another consisting of many fine metal particles which are initially uniformly distributed. While the first configuration is not the dominant type formed by an atomization process, it does represent a limit that may be expected with a small droplet or a droplet with a large particle in the distribution of droplet and particle sizes found in a practical spray. However, many unique and interesting features of the vaporization of the liquid carrier from slurry droplets can only be studied by analyzing the second configuration.

A two-part analysis is presented in the following chapters. In the first part, we present studies on isolated-droplet vaporization and combustion. First, we construct models for a slurry droplet containing a single metal particle in its core. In Chapter 2, the usual quasi-steady gas-phase assumption is relaxed, The objective here is to explore the effect of transient gas-phase, i.e., the effect of collapse of the hydrocarbon flame towards the end of liquid fuel burnout, on the ignition characteristics of the metal part. In Chapter 3, a film-theory-based model is constructed to describe the vaporization in a convective environment. The goal is to formulate a simplified vaporization model which can be used in spray combustion calculations. Further, the model is extended to include the combustion of the liquid fuel, so that ignition characteristics of the metal particle can be studied. The gas phase includes the effects of variable thermophysical properties and nonunitary Lewis number. The liquid-phase includes the effects of transient heating and circulation. Next, in Chapter 4, liquid vaporization from a slurry droplet consisting of many fine-metal particles is analyzed. The gas phase includes the effects of variable thermophysical properties

and nonunitary Lewis number. The liquid-solid phase includes the effects of transient heating and variable number density of the solid particles. A model for the combustion of aluminum particles is presented in Chapter 5. The model does not require any *a priori* knowledge of the droplet surface and flame temperatures, in an effort to determine the mass fraction of condensed products at the flame. These temperatures are determined using phase equilibrium and thermochemical data. The particle transient heating is considered, and the phase-equilibrium conditions of the fuel and vapor and condensed products are analyzed. Thereby, no assumptions about limiting temperatures are made.

In all of the above studies, the emphasis is on the modeling effort and correct physical representation of the various phenomena involved. Each chapter is self-contained and thus can be read independently. Analytical and computational techniques are employed to solve the governing conservation equations. The specific objective is to construct simplified models which result in useful insights on liquid vaporization and metal combustion and which can be used for spray combustion calculations.

In Chapter 6, we make an analytical and computational study of vaporizing and burning liquid hydrocarbon-metal slurry droplet streams injected into a hot gas. The objective is to investigate the mass and energy interactions between the slurry droplets and the gas flow. An idealized configuration consisting of parallel droplet streams is used. The droplet models described in the previous sections are assimilated into a spray formulation. The governing gas-phase equations are analytically integrated by using the Green's function approach, and a resulting set of first order nonlinear ordinary differential equations is numerically solved. Effects of varying metal particle size and solid loading are studied.

## Chapter 2

# Transient Heating and Burning of a Slurry Droplet

### 2.1 Introduction

An important effect in the modeling of slurry droplets that has yet to be addressed is the effect of unsteady gas phase heat and mass transfer on the liquid fuel burning. On the completion of the liquid burnout, the flame will collapse inwards onto the metal surface, thus affecting the temperature rise of the solid agglomerate. Also, previous studies (see section 1.1.1) have employed a lumped capacity formulation which assumes that the slurry droplet has a spatially uniform temperature, thus implying infinite thermal conductivity of the liquid and metal. While this may be a reasonable limit for the metal, it is certainly inappropriate for the liquid fuel [88]. These effects cannot be properly described by a quasi-steady gas phase heat and mass diffusion theory.

In this chapter, we consider an idealized configuration of a slurry droplet in which a hydrocarbon film surrounds a single metal particle. While such a slurry droplet is unlikely to be formed by an atomization process, it does represent a limit that may be expected with a small droplet or a droplet with a large particle. We solve the unsteady gas phase conservation equations, coupled with a transient solution for the liquid-metal slurry heating. Calculations are made to show the importance of such an approach in case of metal slurry droplets.

## 2.2 Assumptions and Model

An idealized configuration of the slurry droplet, in which a hydrocarbon film (*n*-octane) surrounds a single metal particle (aluminum), is shown in Figure 2.1. Physical

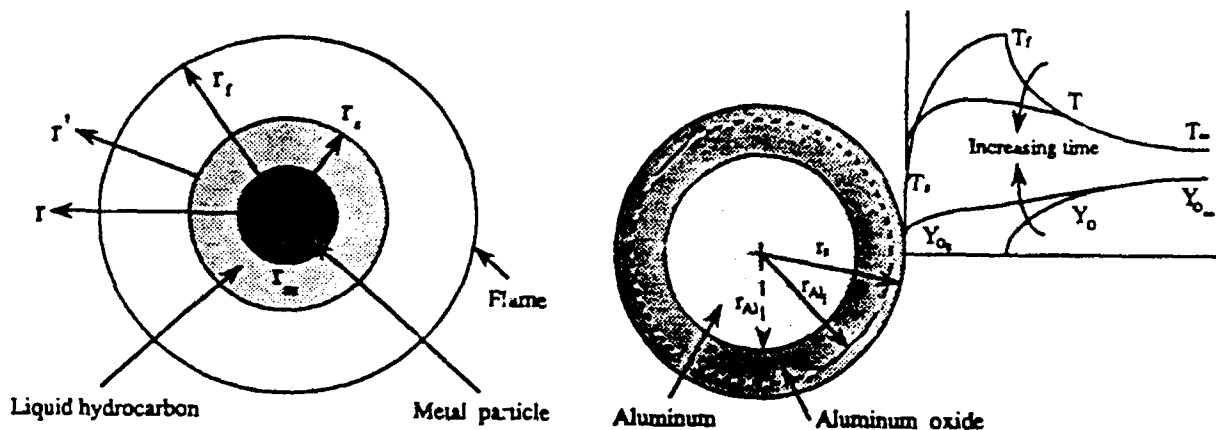


Figure 2.1: (a) Schematic of the droplet combustion model. (b) Schematic of the metal surface oxidation and heat transfer.

properties of *n*-octane and aluminum employed in this study are listed in Table 2.1. The droplet burns in a stagnant ambient gas (air). The following assumptions are made: 1) the flow field around the droplet is spherically symmetric; 2) the gas-phase Lewis number is unity; 3) the mixture specific heat is a constant; 4) Fick's law of diffusion holds; 5) a single step infinitely fast chemical reaction occurs in the gas phase. After the slurry droplets are exposed to a hot oxidizing environment, the liquid fuel vaporizes and burns, leaving behind a dry metal particle. The dry metal heats to the melting point of the aluminum (933.1 K), then the phase change occurs. Continued heating causes further temperature rise and slow oxidation of the metal until the oxide coating melts ( $\sim 2300$  K), at which point ignition is presumed to occur.

Property	Al	n-C <sub>8</sub> H <sub>18</sub>
Atomic Weight $M$	26.98	114.22
Density $\rho$ (g/cm <sup>3</sup> )	2.7	0.703
Specific Heat $C_p$ (cal/g-K)	0.206	0.578
Thermal Diffusivity $\alpha$ (cm <sup>2</sup> /s)	0.86	$6.84 \times 10^{-4}$
Saturated Vapor Pressure $p_F$ (atm)	-	$\exp(10.7288-4278.76/T_s)$
Melting Point (K)	933.1	-
Heat of Vaporization $L$ (cal/g)	94.885	$10.087(569.35-T_s)^{0.38}$
Heat of Combustion $\Delta H$ (cal/g)	-	10600

Table 2.1: Physical properties of aluminum and *n*-octane.

### 2.2.1 Gas-Phase Analysis

The total pressure in the gas phase is assumed constant; thus the general form of the momentum equation is not considered. The conservation equations are given by:

$$\frac{\partial \rho}{\partial t} + \frac{1}{r^2} \frac{\partial}{\partial r} (\rho r^2 v_r) = 0 \quad (2.1)$$

$$\rho \left\{ \frac{\partial h}{\partial t} + v_r \frac{\partial h}{\partial r} \right\} = \frac{1}{r^2} \frac{\partial}{\partial r} \left\{ r^2 \rho \alpha \frac{\partial h}{\partial r} \right\} + \dot{q}''' \quad (2.2)$$

$$\rho \left\{ \frac{\partial Y_F}{\partial t} + v_r \frac{\partial Y_F}{\partial r} \right\} = \frac{1}{r^2} \frac{\partial}{\partial r} \left\{ r^2 \rho D \frac{\partial Y_F}{\partial r} \right\} + \dot{m}_F''' \quad (2.3)$$

$$\rho \left\{ \frac{\partial Y_o}{\partial t} + v_r \frac{\partial Y_o}{\partial r} \right\} = \frac{1}{r^2} \frac{\partial}{\partial r} \left\{ r^2 \rho D \frac{\partial Y_o}{\partial r} \right\} + \dot{m}_o''' \quad (2.4)$$

where  $\dot{q}'''$ ,  $\dot{m}_F'''$  and  $\dot{m}_o'''$  represent the source terms arising from combustion. The equation of state is given by:

$$\rho = pM/R_u T \quad (2.5)$$

Invoking the above mentioned assumptions 2, 3 and 5, we make the Schvab-Zel'dovich transformation, which gives:

$$\rho \left\{ \frac{\partial \beta_i}{\partial t} + v_r \frac{\partial \beta_i}{\partial r} \right\} = \frac{1}{r^2} \frac{\partial}{\partial r} \left\{ r^2 \rho \alpha \frac{\partial \beta_i}{\partial r} \right\} \quad (2.6)$$

where the three Schvab-Zel'dovich variables are given by:

$$\beta_1 = C_p(T - T_\infty) + \Delta H Y_F \quad (2.7)$$

$$\beta_2 = Y_r - f(Y_o - Y_{o\infty}) \quad (2.8)$$

$$\beta_3 = C_p(T - T_\infty) + f \Delta H (Y_o - Y_{o\infty}) \quad (2.9)$$

Note that of these variables, only two are linearly independent. Making a change of radial coordinate from the droplet center to the droplet surface, such that

$$r' = r - r_s(t) \quad (2.10)$$

the conservation Eqs. (2.1) and (2.6) become:

$$\frac{\partial}{\partial t}(\rho r^2) + \frac{\partial}{\partial r'} \left\{ \rho r^2 (v_r - \dot{r}_s) \right\} = 0 \quad (2.11)$$

$$\rho \left\{ \frac{\partial \beta_i}{\partial t} + v_r \frac{\partial \beta_i}{\partial r'} - \dot{r}_s \frac{\partial \beta_i}{\partial r'} \right\} = \frac{1}{r^2} \frac{\partial}{\partial r'} \left\{ r^2 \rho \alpha \frac{\partial \beta_i}{\partial r'} \right\} \quad (2.12)$$

Next, we define a streamfunction  $\psi$  to eliminate the continuity equation (2.11), as:

$$\frac{\partial \psi}{\partial t} = -\rho r^2 (v_r - \dot{r}_s) \quad (2.13)$$

and

$$\frac{\partial \psi}{\partial r'} = +\rho r^2 \quad (2.14)$$

Changing coordinates from  $(t, r')$  to  $(\tau, \psi)$ , ( $\tau = t$ ), which is the von Mises transformation (Schlichting [87]), Eq. (2.12) becomes:

$$\frac{\partial \beta_i}{\partial \tau} = \frac{\partial}{\partial \psi} \left\{ \alpha \rho^2 r^4 \frac{\partial \beta_i}{\partial \psi} \right\} \quad (2.15)$$

To obtain the solution in the physical plane, we use the relation

$$r^3 = r_s^3(t) + 3 \int_0^\psi \frac{d\psi}{\rho} \quad (2.16)$$

The initial conditions on the Schvab-Zel'dovich variables are:

$$\beta_1(t = 0, \psi) = 0 = \beta_2(t = 0, \psi) = \beta_3(t = 0, \psi)$$

Making energy and species balances at the droplet-gas interface in the usual way (Kanury [47]), the boundary conditions in the von Mises plane can be obtained as:

$$\left. \frac{\partial \beta_1}{\partial \psi} \right|_{\psi=0} = \frac{\dot{q}_d + \dot{m}_F \{L + \Delta H(Y_{F_s} - 1)\}}{4\pi(\rho r_s)^2 \alpha} \quad (2.17)$$

$$\left. \frac{\partial \beta_2}{\partial \psi} \right|_{\psi=0} = \frac{\dot{m}_F(Y_{F_s} - 1)}{4\pi(\rho r_s)^2 \alpha} \quad (2.18)$$

$$\left. \frac{\partial \beta_3}{\partial \psi} \right|_{\psi=0} = \frac{\dot{q}_d + \dot{m}_F L}{4\pi(\rho r_s)^2 \alpha} \quad (2.19)$$

where  $\dot{m}_F$  and  $\dot{q}_d$  represent the vaporization rate and the heat penetrating into the droplet interior, respectively.  $Y_{F_s}$  is determined from a phase equilibrium (Clausius-Clapeyron) relation. On the completion of liquid vaporization,  $\dot{m}_F$  goes to zero. In the relations (2.17-2.19), it is implicit that the gradient of the oxidizer mass fraction at the liquid-gas interface is zero. This gradient becomes non-zero upon the collapse of the flame, and the process is modeled in the section 2.3. The boundary conditions at a surface far away from the droplet-gas interface are given by:

$$\beta_1|_{\psi \rightarrow \infty} \rightarrow 0, \quad \beta_2|_{\psi \rightarrow \infty} \rightarrow 0, \quad \beta_3|_{\psi \rightarrow \infty} \rightarrow 0 \quad (2.20)$$

The flame is located at the surface where the fuel and the oxidant concentrations are in stoichiometric proportions. This implies that, at the flame,

$$\beta_2 = f Y_{O_\infty} \quad (2.21)$$

## 2.2.2 Liquid-Phase Analysis

In the idealistic configuration of Figure 2.1, the metal and liquid components of the slurry are separated and the local thermophysical properties are readily determined. The energy equation for transient, spherically symmetric droplet heating is:

$$r_s'^2 \frac{\partial Z}{\partial \tau} - \frac{1}{2} \eta \frac{dr_s'^2}{d\tau} \frac{\partial Z}{\partial \eta} = \frac{1}{\eta^2} \frac{\partial}{\partial \eta} \left\{ \chi \eta^2 \frac{\partial Z}{\partial \eta} \right\} \quad (2.22)$$

where the following definitions are used:

$$r_s' = r_s/r_{li} \quad Z = T/T_i \quad \tau = \alpha_l t/r_{li}^2 \quad \eta = r/r_s$$

and  $\chi$  is given by:

- (a)  $\chi = 1$ , for all-liquid droplet, or the liquid region ( $\eta > r_m/r_s$ ) of the slurry droplet;  
 (b)  $\chi = \alpha_m/\alpha_l$ , for the metal region ( $\eta < r_m/r_s$ ) of the slurry droplet.

The initial and boundary conditions are:

$$\text{at } \tau = 0, \quad Z = 1 \quad (2.23)$$

$$\text{at } \eta = 0, \quad \left. \frac{\partial Z}{\partial \eta} \right|_{\eta=0} = 0 \quad (2.24)$$

$$\text{at } \eta = 1, \quad \left. \frac{\partial Z}{\partial \eta} \right|_{\eta=1} = \frac{q_d r_s' r_{li}}{4\pi k_l T_i r_s^2} \quad (2.25)$$

At the liquid-metal interface the heat flux is continuous, and this condition is incorporated by using a harmonic averaging of the liquid and metal thermal conductivities (Patankar [66]). Also, liquid mass conservation implies:

$$\dot{m}_F = -4\pi \rho_l r_s^2 \dot{r}_s \quad (2.26)$$

### 2.2.3 Dry Metal Heating

The quasi-steady theory of droplet vaporization and combustion results in a constant ratio of flame radius to droplet radius. Thus, the theory will be extremely limited in describing the physical process near the liquid vaporization times. Further, with the quasi-steady assumption it is not possible to model the collapse of the flame and the subsequent conductive heating of the dry metal. In this stage of burning of slurry droplets, the dry metal heats rapidly until the phase change of metal occurs. As the metal thermal diffusivity is large (about three orders of magnitude larger than the liquid diffusivity, and Biot number  $\approx 7 \times 10^{-4} \ll 1$ ), in this section we assume that the metal is isothermal. Note that the fuel vapor is still burning in the gas phase. The metal heat rise may be given by:

$$\frac{4}{3}\pi r_m^3 \rho_m C_{p,m} \frac{dT_m}{dt} = \dot{q}_m \quad (2.27)$$

The heat flux,  $\dot{q}_m$ , consists of  $\dot{q}_d$ , and additionally, the fluxes due to radiation and chemical reaction, i.e.,

$$\dot{q}_m = \dot{q}_d + \dot{q}_{rad} + \dot{q}_{ch} \quad (2.28)$$

In the Wong and Turns [111] study, a model for the rate of oxidation of an aluminum agglomerate, based on the work of Aylmore et al. [8], is given as:

$$\dot{q}_{ch} = A_{sp} C X_O^{0.45} \exp(-E/RT) \quad (2.29)$$

where  $A_{ch} \propto A_{sp}(d/d_p)(1 - \theta)$ , and  $C \propto Q_{Al} K_o(1 - \theta)/d_p$ .  $\dot{q}_{ch}$  represents the heat generated by the chemical reaction,  $A_{sp} = \pi d^2/4$ , and  $A_{ch}$  is the reactive surface area,  $X_O$  is the ambient oxygen mole fraction, the activation energy  $E = 51.9$  kcal/mole (from Aylmore et al.),  $d$  and  $d_p$  are the agglomerate and particle diameters,  $\theta$  is the porosity,  $K_o$  is the frequency factor, and  $Q_{Al}$  is the heat of reaction of aluminum per unit mass. The above relation is critical in explaining the agglomerate ignition times, and the factor  $C$  is determined from their own experimental results. The main conclusion from the Aylmore study is that they were unable to propose a quantitative analysis of aluminum oxidation. Also, the Aylmore study is for single aluminum strips, rather than an agglomerate. Further, the cited study is limited to aluminum oxidation in the temperature range 400-650 C, while the above equation (2.29) gives significant fluxes for temperatures above 1000 C. Thus, the model proposed by Wong and Turns may not yield to the generalizations. Therefore, we propose another approach.

To model the heating process of the dry particle, consider a spherical particle of initial radius  $r_{Al}$ , oxidizing in an environment consisting of the remnant flame of the vaporized liquid fuel, shown schematically in Figure 2.1 (this approach is a modification of the suggestion by Mills [62]). The particle radius may increase due to surface oxidation of metal, even though the density of the oxide is larger than that of the metal ( $\rho_{Al} = 2.7$  gm/cc,  $\rho_{ox} = 3.97$  gm/cc). Balancing heat at the particle surface, we have:

$$\frac{d}{dt} \left\{ \frac{4}{3} \pi r_{Al}^3 (\rho C_p)_{Al} T + \frac{4}{3} \pi (r_s^3 - r_{Al}^3) (\rho C_p)_{ox} T \right\} = \dot{m}_o \Delta H_c + 4 \pi r_s^2 k_g \left. \frac{\partial T}{\partial r} \right|_{r=r_s} - \sigma \epsilon 4 \pi r_s^2 (T^4 - T_\infty^4) \quad (2.30)$$

where the particle temperature is taken uniform. We are making the assumption of fast aluminum oxidation and slow oxidizer diffusion, and neglecting any equilibrium laws at the oxide-gas interface which may determine the rate of oxidizer flow.

Conduction from the flame is, initially, the prime heating mechanism of the dry particle. The radiation heat transfer effects are not significant during the pre-ignition process (Friedman and Maček [30, 31]; also refer to the Appendix A). An estimate of the relative importance of radiation to convection can be made as:

$$\dot{q}_r/\dot{q}_c = \frac{\epsilon\sigma(T^4 - T_\infty^4)}{h(T - T_\infty)} \quad (2.31)$$

where  $h$  is convection heat transfer coefficient and  $\epsilon \approx 0.3$ , say. Further, for  $Nu \approx 2$ ,  $h = k_g/r_m$ . Then

$$\dot{q}_r/\dot{q}_c = \frac{\epsilon\sigma r_m(T^4 - T_\infty^4)}{k_g(T - T_\infty)} \approx \begin{cases} \frac{4\epsilon\sigma r_m T^3}{k_g} & \text{for } T \approx T_\infty \\ \frac{\epsilon\sigma r_m T^3}{k_g} & \text{for } T \gg T_\infty \end{cases} \quad (2.32)$$

For  $r_m = 10 \mu\text{m}$ ,  $k_g = 0.15 \text{ W/m-K}$ ,  $T = 2300 \text{ K}$ , we get  $\dot{q}_r/\dot{q}_c = 0.055$ . This represents the maximum relative value of the radiant flux. Thus, the contribution of radiant flux would be small. The calculations neglect radiation heat transfer. We need an additional relation for the oxygen transfer rate to the particle surface. Balancing mass at the particle surface, we have:

$$\dot{m}_{o_s} = 4\pi r_s^2(\rho\mathcal{D})_g \left. \frac{\partial Y_o}{\partial r} \right|_{r=r_s} = 4\pi r_s^2(\rho\mathcal{D})_{ox} \left. \frac{\partial Y_{ox}}{\partial r} \right|_{r=r_s} \quad (2.33)$$

where  $\dot{m}_{o_s}$  is the oxidizer mass flux at the oxide-gas interface, and for simplicity, we have assumed Fickian diffusion of the oxygen through the aluminum oxide, governed by a transient, spherically symmetric equation as:

$$\rho_{ox} \frac{\partial Y_{ox}}{\partial t} = \frac{1}{r^2} \frac{\partial}{\partial r} \left\{ (\rho\mathcal{D})_{ox} r^2 \frac{\partial Y_{ox}}{\partial r} \right\}; \quad r_{Al}(t) \leq r \leq r_s(t) \quad (2.34)$$

with the initial and boundary conditions:

$$\text{at } t = 0, Y_{ox} = 0 \quad (2.35)$$

$$\text{at } r = r_{Al}(t), Y_{ox} = 0 \quad (2.36)$$

$$\text{at } r = r_s(t), Y_{ox} = Y_{o_s} \quad (2.37)$$

A model for the diffusion coefficient of the oxygen through the solid aluminum oxide is given in the Appendix A. Using the transformation

$$\eta = \frac{r - r_{Al}(t)}{r_s(t) - r_{Al}(t)}; \quad 0 \leq \eta \leq 1$$

the Eq. (2.34) becomes

$$\frac{\partial Y_{ox}}{\partial t} = \frac{1}{r_s - r_{Al}} \left\{ (1 - \eta)\dot{r}_{Al} + \eta\dot{r}_s + \frac{2D_{ox}}{r} \right\} \frac{\partial Y_{ox}}{\partial \eta} + \frac{D_{ox}}{(r_s - r_{Al})^2} \frac{\partial^2 Y_{ox}}{\partial \eta^2} \quad (2.38)$$

The rate of growth of the oxide film can be obtained by stoichiometry of the reaction  $2 \text{Al} + 3 \text{O} \rightarrow \text{Al}_2\text{O}_3$ , requiring that 9 kg of aluminum are consumed for each 8 kg of oxygen, such that:

$$\frac{d}{dt} \left\{ \frac{4}{3} \pi \rho_{Al} r_{Al}^3 \right\} = -\frac{9}{8} \dot{m}_o \quad (2.39)$$

Similarly, as 17 kg of oxide shell are formed for each 8 kg of oxygen consumed, the outer radius of the particle is given by:

$$\frac{d}{dt} \left\{ \frac{4}{3} \pi \rho_{ox} (r_s^3 - r_{Al}^3) \right\} = \frac{17}{8} \dot{m}_o \quad (2.40)$$

It is well known that a continuous film of oxide grows over nascent aluminum surface that is exposed to an oxidizing atmosphere (see e.g., Hatch [42], and Merzhanov et al. [59]). At room temperature, the limiting thickness ( $\delta_i$ ) is about 25 to 30 Å. In our work, we shall vary  $\delta_i$  between 10 and 30 Å.

The oxygen flow rate at the Al-Al<sub>2</sub>O<sub>3</sub> interface is given by:

$$\dot{m}_o = 4\pi r_{Al}^2 (\rho D)_{ox} \left. \frac{\partial Y_{ox}}{\partial r} \right|_{r=r_{Al}} \quad (2.41)$$

The last four equations, along with the unsteady gas-phase conservation equations (5.10) and the heat balance Eq. (2.30), complete the problem definition. Continuous heating of aluminum particles causes the phase change, which occurs at 933.1 K, and, during this change the metal temperature remains constant. After the phase change, the metal heating continues to be described by Eq. (2.30). The droplet keeps heating until the melting point of the oxide is reached, at 2300 K. At this point, the ignition is assumed to occur.

## 2.3 Solution Procedure

The gas-phase boundary conditions, for different time periods, are summarized below:

(a) For the liquid vaporization period ( $t < t_v$ ), use Eqs. (2.17, 2.18 and 2.19) as

$$\dot{m}_F(t) = \frac{4\pi(\rho r_s^2)^2 \alpha}{(Y_{F_s} - 1)} \left. \frac{\partial \beta_2}{\partial \psi} \right|_{\psi=0} \quad (2.42)$$

$$\dot{q}_d(t) = 4\pi(\rho r_s^2)^2 \alpha \left. \frac{\partial \beta_3}{\partial \psi} \right|_{\psi=0} - \dot{m}_F(t)L \quad (2.43)$$

(b) After the liquid vaporization, and until the vapor burnout time ( $t_v < t < t_b$ ), use

$$\dot{m}_F(t) = 0 \quad (2.44)$$

$$\dot{q}_d(t) = 4\pi(\rho r_s^2)^2 \alpha \left. \frac{\partial \beta_3}{\partial \psi} \right|_{\psi=0} \quad (2.45)$$

(c) After the vapor burnout time ( $t > t_b$ ), in the case of a slurry droplet, the oxidizer mass fraction at the oxide-gas interface becomes non-zero. From Eq. (2.33), it follows that

$$\left. \frac{\partial \beta_2}{\partial \psi} \right|_{\psi=0} = \frac{-f(\rho D)_{ox}}{(4\pi\rho_g r_s^2)(\rho\alpha)_g r_s - r_{Al}} \frac{1}{\partial \eta} \left. \frac{\partial Y_{ox}}{\partial \eta} \right|_{\eta=1} \quad (2.46)$$

Eq. (2.45) continues to hold.

The coupled gas and liquid or solid phase equations are solved numerically using a second-order, implicit, finite-difference scheme. Briefly, the solution procedure followed is:

1. Guess a droplet surface temperature  $T_s$ , or use the previous time step value.
2. Calculate the fuel mass fraction at the droplet surface, using the Clausius-Clapeyron relation. Upon completion of liquid vaporization, this step is omitted.
3. In the case of a slurry droplet, and upon completion of vapor burnout, calculate  $\dot{m}_o$  from Eq. (2.41), using the gradient at previous iteration. Update  $r_s$  and  $r_{Al}$ , and solve Eq. (2.38) using  $Y_{o_s}$  at previous iteration.
4. Using relations (7-9), update the Schvab-Zel'dovich variables at the droplet surface.
5. Solve the conservation Eqs. (5.10), subject to the appropriate boundary conditions in step (4) (or as explained above), and relations (2.20). Calculate the gas-phase gradients  $\partial \beta_i / \partial \psi$  at the droplet surface (or  $Y_{o_s}$ ).
6. Find  $\dot{m}_F$  and  $\dot{q}_d$ , as explained above.

7. Solve the liquid phase equations (2.22 and 5.24) to obtain updated  $T_s$  and  $r_s$ . This step is valid until the liquid vaporization time.
8. Find the flame location from the relation (2.21), and then determine the gas-phase temperatures, and fuel and oxidizer mass fractions.
9. Update the density from the equation of state (2.5), and determine  $r(t, \psi)$  from (2.16).
10. Check for convergence on  $T_s$  (and  $Y_{o,s}$ , in case step 3 is in use), otherwise iterate between steps (2) to (10).

To resolve large gradients near the droplet surface, and due to the non-linear relation between the von Mises coordinate  $\psi$  and the radial coordinate, Eq. (2.16), it is necessary to use a non-uniform grid in the von Mises plane. A cubically increasing mesh

$$\psi_n = n^3 \Delta\psi$$

where  $n$  is the grid point number, has been employed. The gradients at the droplet surface, in Eqs. (17-19), have been evaluated using second-order-accurate approximations. The solution converges rapidly, within a few iterations, even for large time steps.

## 2.4 Results and Discussion

First, the results for burning of an all-liquid droplet are presented. Figure 2.2 shows the successive distributions of temperature, and fuel and oxidizer mass fractions around a burning droplet of 50  $\mu\text{m}$  initial radius, at various times. The droplets are initially at a temperature of 300 K. The oxidizer (air) is at a pressure of 10 atm and a temperature of 1000 K. The droplet lifetime here is about 4 ms. As expected, there exist large thermal and fuel vapor concentration gradients near the droplet surface. The fuel mass fraction drops rapidly with the radial coordinate, and with the thin flame assumption employed, there exists no fuel outside the flame and no oxidizer within the flame. The gas-phase temperature rises and peaks at the flame location. A regressing droplet surface is seen here by the shift of the fuel mass fraction and temperature profiles towards the ordinate. Observing the temperature peaks for

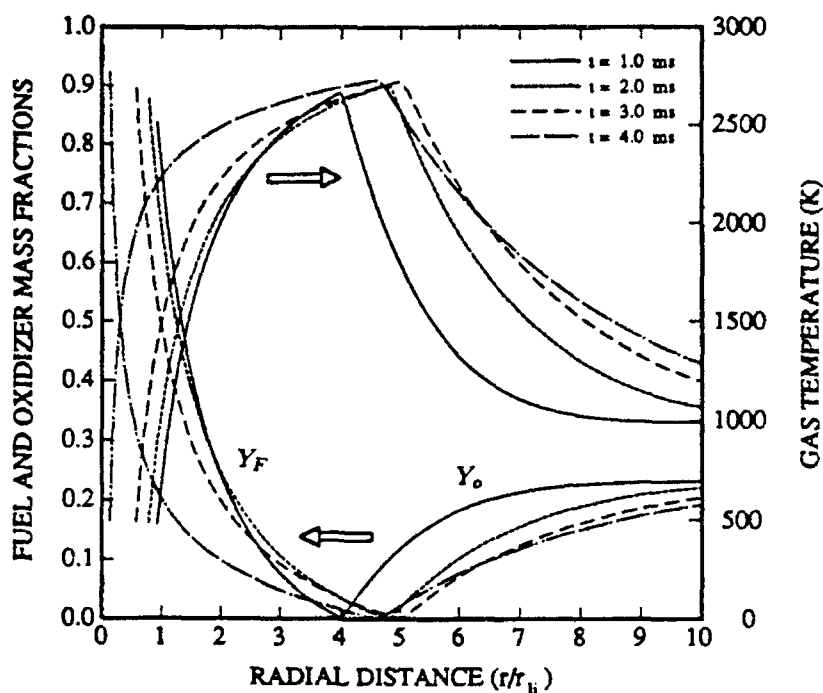


Figure 2.2: Gas-phase temperature, and fuel and oxidizer mass fraction profiles, for  $r_{Li} = 50 \mu\text{m}$ ,  $p_{\infty} = 10 \text{ atm}$ , and  $T_{\infty} = 1000 \text{ K}$ . For all calculations, the liquid fuel is *n*-octane and the solid fuel is aluminum.

various times, it may be seen that at later times, as explained below, the flame has started to move back towards the droplet center.

Figure 2.3 shows the droplet surface temperature and fuel mass fraction as a function of time. The gas-phase pressure is a parameter here. The droplet surface temperature rises and then becomes somewhat steady, as the droplet heats to its boiling point at the prevalent pressure. After completion of liquid vaporization, the plot shows the center temperature, rather than the surface temperature, which quickly rises to values near the flame temperature. This is due to two reasons: firstly, there is now an absence of the liquid to be vaporized, which acts as an energy sink; and secondly, there is the decrease of the flame radius. Like the surface temperature, the fuel mass fraction rises rapidly and then reaches approximately steady values. On the completion of vaporization, the fuel mass fraction drops rapidly, and after a short period goes to zero, which indicates the extinguishment of the flame. During this short period, the droplet has completely vaporized but the fuel vapor in the gas phase is still burning. Note that at a pressures near 1 atm, the difference in liquid vaporization and the vapor burnout times is not large; however with increased pressure, this difference

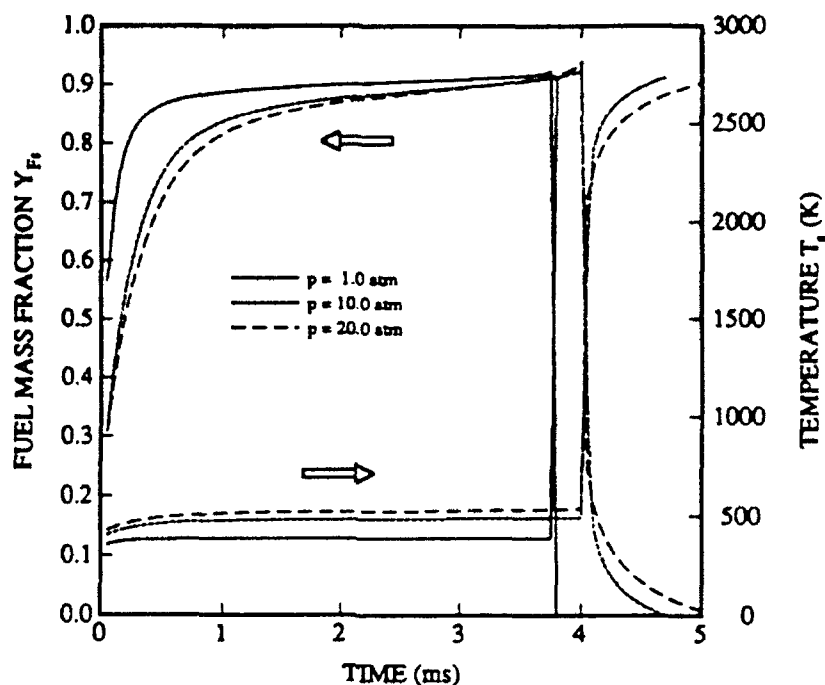


Figure 2.3: Droplet surface temperature and fuel mass fraction, for  $r_{l_i} = 50 \mu\text{m}$  and  $T_\infty = 1000 \text{ K}$ .

becomes significant. This situation is made clearer in Figure 2.4, which shows the droplet radius squared and the flame location with time. Here, the radii are non-dimensionalized by initial droplet radius. The droplet radius curve shows an initial period where the liquid fuel gets heated close to the thermodynamic equilibrium temperature. Then, the radius decrease is apparently in accordance with the  $d^2$ -law. The flame, with the flame sheet approximation employed in this study, begins at the droplet surface, and for a period of time becomes somewhat stationary, and then rapidly collapses upon the completion of liquid vaporization. These results are in good agreement with experimental observations of free fuel droplets in a freely falling chamber (Kumagai et al. [49]), and low pressure droplet combustion observations (Law et al. [52]). With higher pressures, the flame radii obtained are significantly smaller than those at lower pressures, a trend confirmed many times in the past (e.g Crespo and Liñan [23]; Kanury [47]).

The heat and mass transfer numbers, defined as:

$$B_M = \frac{Y_{F_s}(t) + fY_{O_\infty}}{1 - Y_{F_s}(t)}, \quad B_T = \frac{C_p\{T_\infty - T_s(t)\} + f\Delta HY_{O_\infty}}{L(T_s) + \dot{q}_l(t)}$$

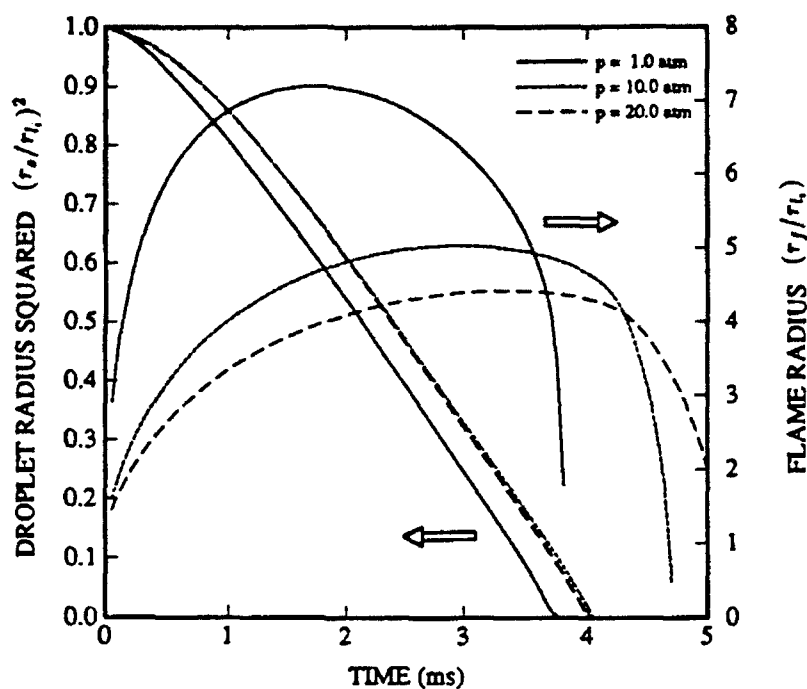


Figure 2.4: Droplet radius squared and flame location, for  $r_{i1} = 50 \mu\text{m}$  and  $T_{\infty} = 1000 \text{ K}$ .

are shown in Figure 2.5. The mass transfer number decreases with pressure increase, and the heat transfer number rises. The reduction in the mass transfer number is due to the slight decrease in the surface fuel mass fraction with the pressure increase, and the lowering of the latent heat of vaporization dominates in the increase of the heat transfer number. Note, this is in stark contrast to the quasi-steady theory, which would predict an increase of  $B_T$ , and so also  $B_M$ , as  $B_M = B_T$  there. The vaporization rate is related to a droplet regression parameter defined by:

$$k = -4 \frac{dr_s^2}{dt}$$

The droplet regression parameter and the mass vaporization rate are plotted in Figure 2.6, as functions of time. The vaporization rate is slower in the beginning, then peaks at times about 1/4 of the droplet lifetime. The droplet regression parameter increases faster initially, and then slows down. The time averaged value of the parameter is in agreement with the values of the burning constant of the quasi-steady theory (Kanury [47]).

Next, we present the results for the metal slurry droplet. In these results, the air is at a temperature of 1000 K, pressure of 10 atm, and the initial droplet

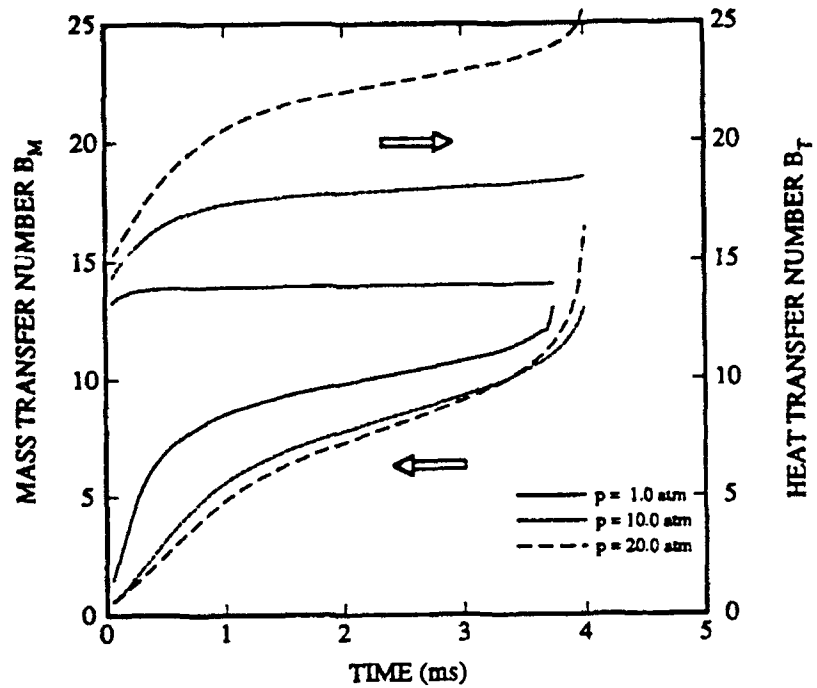


Figure 2.5: Heat and mass transfer numbers, for  $r_{li} = 50 \mu\text{m}$  and  $T_\infty = 1000 \text{ K}$ .

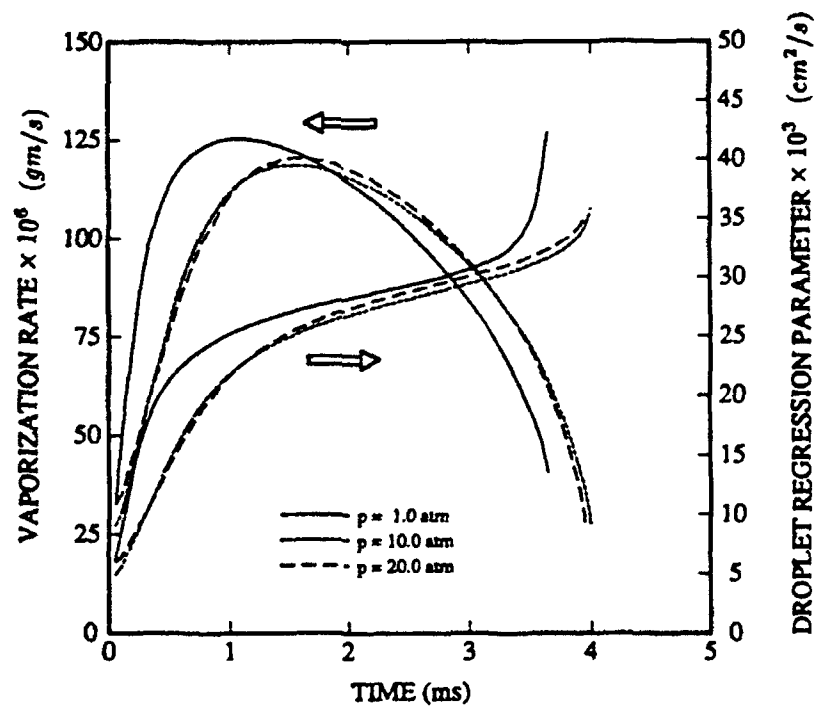


Figure 2.6: Vaporization rate and burning constant, for  $r_{li} = 50 \mu\text{m}$  and  $T_\infty = 1000 \text{ K}$ .

radius is  $50 \mu\text{m}$  and temperature  $300 \text{ K}$ . The distribution of the gas-phase fuel and oxidizer fractions, and the temperature profiles, for a  $20 \mu\text{m}$  metal particle are shown in Figure 2.7. These profiles are similar to those observed for the corresponding

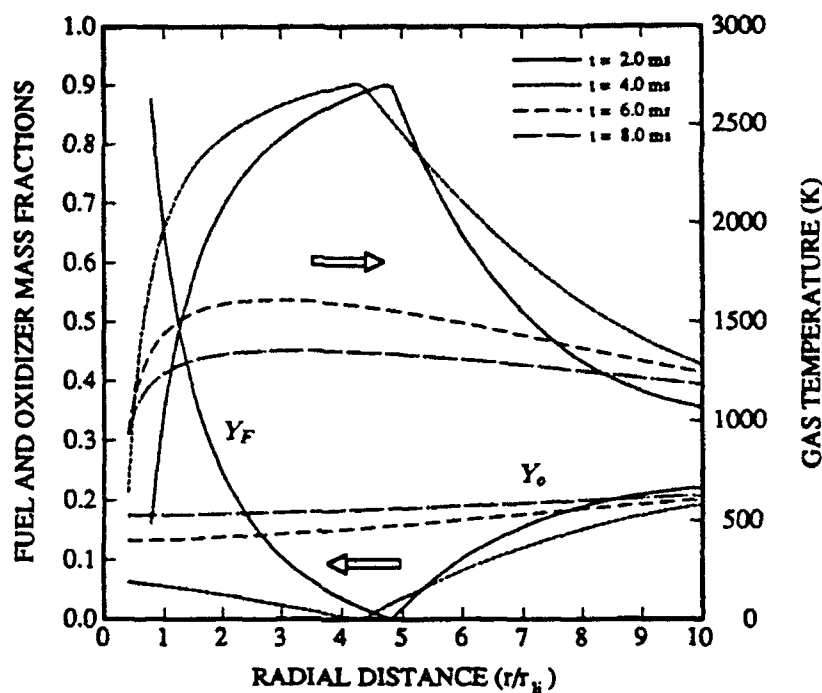


Figure 2.7: Gas-phase temperature, and fuel and oxidizer mass fraction profiles for slurry droplet,  $r_{li} = 50 \mu\text{m}$ ,  $r_m = 20 \mu\text{m}$ ,  $p_\infty = 10 \text{ atm}$ , and  $T_\infty = 1000 \text{ K}$ .

all-liquid droplet, until the liquid vaporization time. After this time, the oxidizer continues to diffuse towards the metal surface, as noted by the non-zero gradient in its profile. The flame progressively collapses onto the metal surface, and the droplet surface temperature rises rapidly. Figure 2.8 shows squared droplet radius and the flame radius as a function of time, for the case of  $10$  and  $20 \mu\text{m}$  metal radii. For comparison purposes, we have also shown the results for an all-liquid droplet. From the plots, it is clear that the vaporization of the slurry droplet, with the assumed geometry, is identical to that of an all-liquid droplet. The only difference is that due to less initial liquid mass the vaporization time is lower, and the flame is located closer to the droplet center. In Figure 2.9, the temperature, and the fuel and oxygen mass fractions at the droplet surface are plotted. The solid line represents the corresponding all-liquid droplet. Again, identical behavior for the fuel mass fraction at the droplet surface is seen. The metal temperature history and the oxygen mass fraction at the oxide-gas interface is now different. The oxygen mass fraction grows with time, and

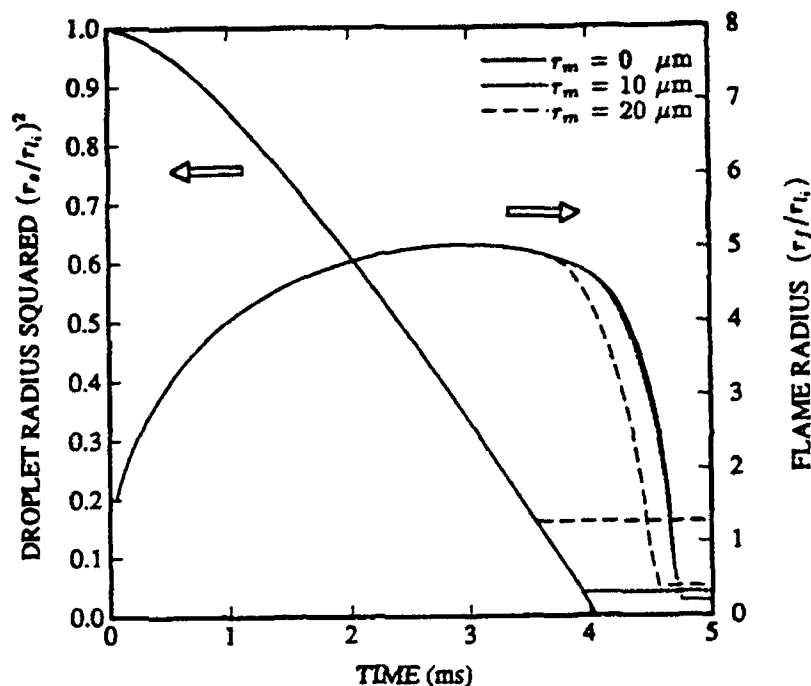


Figure 2.8: Droplet radius squared and flame location for slurry droplets,  $r_{i1} = 50 \mu\text{m}$ ,  $p_{\infty} = 10 \text{ atm}$ , and  $T_{\infty} = 1000 \text{ K}$ .

approaches the ambient value. The flat portion in the temperature plots, at 933.1 K, corresponds to the phase change of solid to liquid aluminum. As expected, the smaller dry metal particles heat faster than the larger ones. For both the 10 and 20  $\mu\text{m}$  particle sizes, the metal temperature is never seen to reach the presumed ignition temperature of 2300 K. The reason for this is that the conduction from the flame is by far the dominating mechanism of heat transfer.

The flux due to the surface oxidation of the aluminum is zero until the oxidizer mass fraction at the metal surface becomes non-zero. As the diffusivity of the oxygen in the oxide is extremely low, there exists a considerable time between the collapse of the liquid vapor flame and the oxygen reaching the Al-Al<sub>2</sub>O<sub>3</sub> interface. Figure 2.10 shows the oxidizer flow rate at the Al-Al<sub>2</sub>O<sub>3</sub> interface, assuming initial film thicknesses of 10 and 30 Å. With an initial film thickness of 30 Å, considerably smaller oxidizer mass flow rates are obtained. The important thing here is the extremely low flow rates in both the cases. This results in a practically insignificant contribution of the surface oxidation flux to the heat flux [refer to Eq. (2.30)].

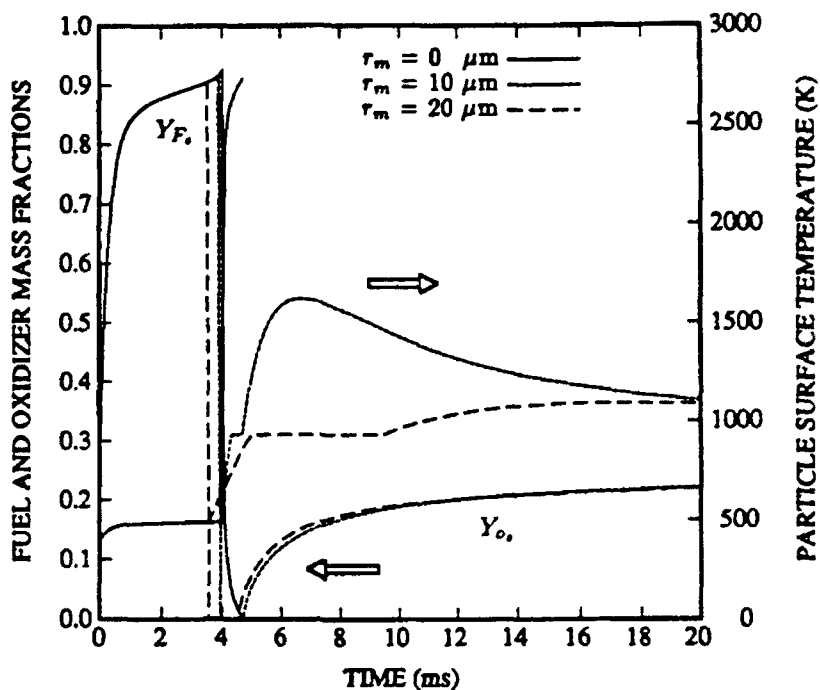


Figure 2.9: Fuel and oxidizer mass fraction at the oxide-gas interface, and droplet surface temperature, for slurry droplet,  $r_{li} = 50 \mu m$ ,  $p_{\infty} = 10 \text{ atm}$ , and  $T_{\infty} = 1000 \text{ K}$ .

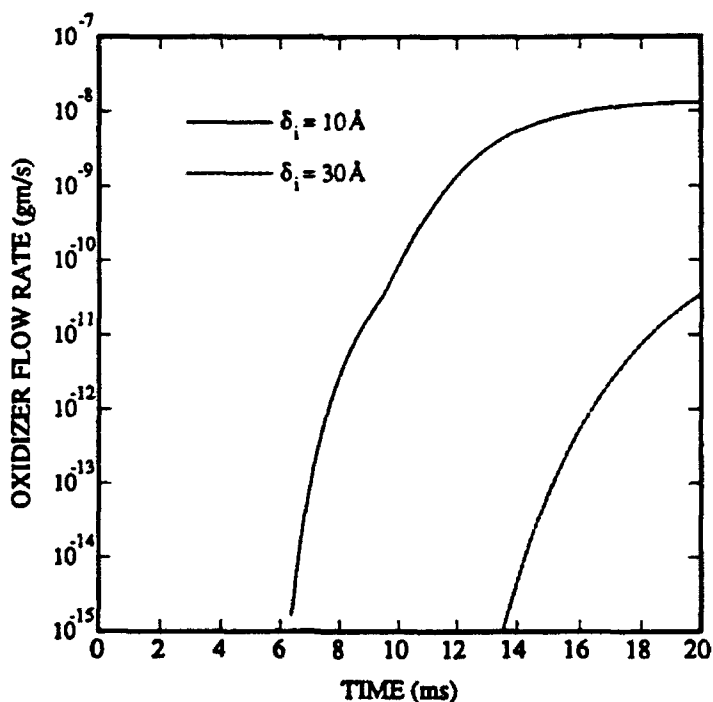


Figure 2.10: Oxidizer flow rate at the Al- $\text{Al}_2\text{O}_3$  interface, for  $r_{li} = 50 \mu m$ ,  $r_m = 20 \mu m$ ,  $p_{\infty} = 10 \text{ atm}$ , and  $T_{\infty} = 1000 \text{ K}$ .

Figures 2.11 and 2.12 show the slurry droplet history for higher preheated air temperatures, of 1500-2500 K. In these cases the initial droplet size is  $r_{l_i} = 50 \mu\text{m}$ ,  $r_m = 20 \mu\text{m}$ ,  $\delta_i = 30 \text{ \AA}$ ; and the ambient pressure is 10 atm. Figure 2.11 shows that the metal particle attains ignition temperature for  $T_\infty > 2000 \text{ K}$ . The contribution of the surface oxidation flux is only somewhat significant for metal temperatures larger than 2000 K. The relative importance of the fluxes due to surface oxidation and conduction is also shown in Figure 2.12. The conductive flux, at first, decreases from its high initial value, and later, decreases slowly. The jump in this case (at a time of about 2 ms) signifies the completion of the liquid vaporization. At about 1 ms later, the aluminum melts. The phase change gets completed by about 10 ms (refer to metal temperature curve for the  $20 \mu\text{m}$  particle radius in Figure 2.9). When the metal temperature exceeds the nearby gas-phase temperature (at some value larger than the ambient gas temperature), the temperature gradient changes sign, and the metal droplet starts to cool. However, the flame due to the combustion of fuel vapor does not seem to possess enough energy to ignite the metal particle. This is as expected, since the film growth data used to model the oxygen diffusivity through the oxide (refer to the Appendix A), predicts insignificant film growth, and hence very small oxidizer fluxes, below these temperatures.

In conclusion, we may state that the oxide film which forms over the aluminum surface, acts as a strong barrier to further surface oxidation. The heat flux due to the surface oxidation of the aluminum is found to be practically insignificant, during the pre-ignition process, compared to the conductive flux from the flame. This is consistent with the observations of Friedman and Maček (see Appendix A). Once the droplet ignites, i.e., the protective aluminum oxide skin retracts, a self sustaining vapor phase combustion of aluminum may result.

## 2.5 Summary

A simple methodology is presented to study droplet combustion with unsteady gas and liquid-phases. Although droplet regression proceeds in a manner not far from the  $d^2$ -law, the quasi-steady formulation is inadequate for describing the flame location. Depending on the ambient pressure and temperature, the vapor burnout

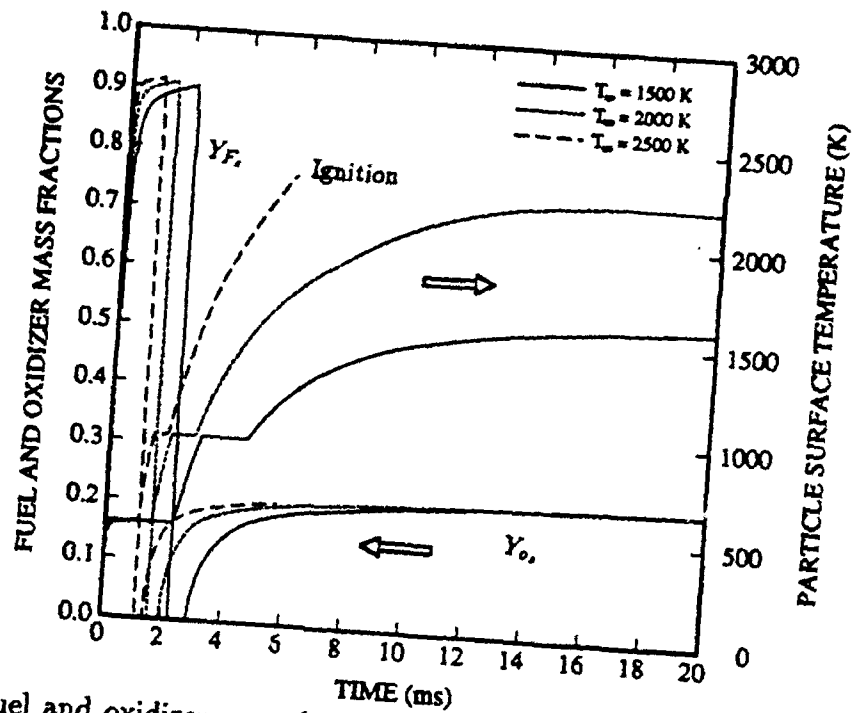


Figure 2.11: Fuel and oxidizer mass fraction at the oxide-gas interface, and droplet surface temperature, for slurry droplet,  $r_{li} = 50 \mu\text{m}$ ,  $p_{\infty} = 10 \text{ atm}$ , and  $\delta_i = 30 \text{ \AA}$ .

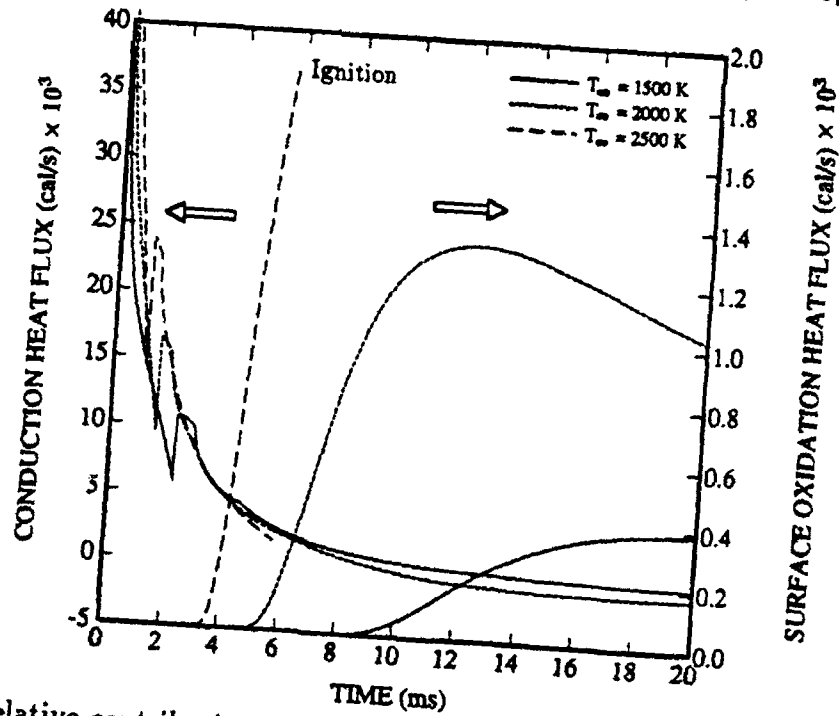


Figure 2.12: Relative contribution of the heat fluxes due to the conduction and the aluminum surface oxidation, for  $r_{li} = 50 \mu\text{m}$ ,  $r_m = 20 \mu\text{m}$ ,  $p_{\infty} = 10 \text{ atm}$ , and  $\delta_i = 30 \text{ \AA}$ .

time can be significantly larger than the liquid vaporization time. With increasing gas-phase pressure, we have found decreasing mass transfer number, increasing heat transfer number, decreasing liquid vaporization rate, and a decreasing flame radius. The difference between the liquid vaporization time and the vapor burnout time is found to be significant at pressures higher than one atmosphere. The model is extended to study the pre-ignition characteristics of an idealized metal slurry droplet. In the absence of convection, it is seen that the flame does not have sufficient energy to ignite the aluminum particles. In order to ignite a slurry droplet with a significant metal mass loading, the ambient air has to be preheated to sufficiently large temperature values. In a practical sense, this means that the metal particle cannot be ignited by the heat released from the liquid fuel burning of the same droplet. Heat release from the burning of other liquid fuel droplets and metal combustion in the spray is necessary to cause ignition. The heat flux due to the surface oxidation of the aluminum is found to be practically insignificant. In a realistic situation, an agglomerate of many fine particles results from the vaporization of a slurry droplet, and it is known that ignition limits decrease considerably with an increase in the reactive area within the agglomerate to the apparent surface area of the agglomerate.

## Chapter 3

# Convective Burning of a Droplet Containing a Single Metal Particle

### 3.1 Introduction

In this chapter, the effect of gas-phase convection on the vaporization rates and its subsequent burning process is addressed. Also, earlier studies have employed a lumped capacity formulation which assumes that the slurry droplet has a spatially uniform temperature, thus implying infinite thermal conductivity of the liquid and metal. While this may be a reasonable limit for the metal, it is certainly inappropriate for the liquid fuel (Sirignano [88]). This chapter includes the effects associated with gas-phase convection, internal circulation, and finite conductivity of the liquid as a first step in developing a comprehensive model that can be used for spray combustion calculations.

### 3.2 Analysis

Here, we consider an idealized configuration of the slurry droplet, in which a hydrocarbon film surrounds a single metal particle, as shown in Figure 3.1. This situation can be expected with a small droplet or with a large particle. An alternative model would involve many particles in a droplet. The slurry droplet of initially known

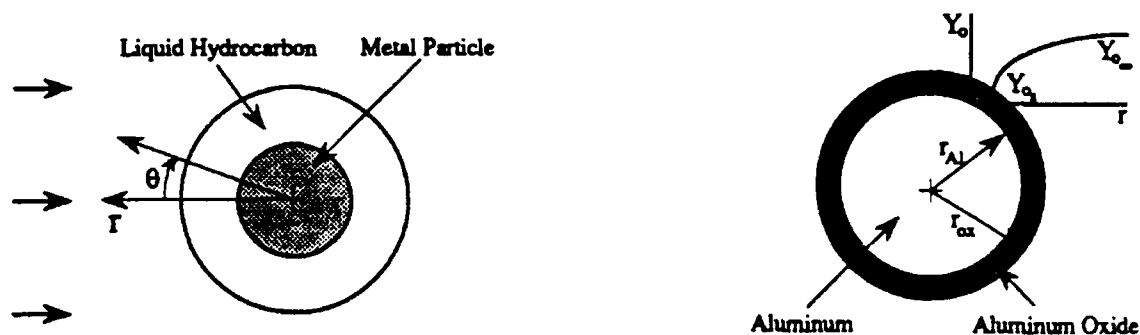


Figure 3.1: (a) Configuration of the slurry droplet. (b) Schematic of the surface oxidation of the dry metal particle.

metal and liquid mass fractions is treated as a spherical droplet of spatially- and time-varying average properties. When the slurry droplets are exposed to a hot oxidizing environment, the liquid fuel vaporizes and burns, leaving behind a dry metal particle. The metal then heats to the melting point of the metal oxide ( $\sim 2300$  K), at which point ignition is normally presumed to occur.

### 3.2.1 Droplet Dynamics

First, we define the metal volume ( $\phi_m$ ) and mass ( $Y_m$ ) fractions in the slurry droplet as

$$\phi_m = r_m^3 / r_l^3 \quad (3.1)$$

$$Y_m = \frac{1}{1 + \left(\frac{1}{\phi} - 1\right) \frac{\rho_l}{\rho_m}} \quad (3.2)$$

Following Abramzon and Sirignano [2], we consider the gas flow to be one-dimensional and the initial droplet velocity parallel to the gas flow direction. For the liquid vaporization stage, the drop location and the velocity are governed by the following equations:

$$\frac{dX}{dt} = U_l \quad (3.3)$$

$$\frac{dU_l}{dt} = \frac{3 \bar{\mu}_\infty (U_\infty - U_l)}{16 \rho_l r_l^2} Re C_D \frac{1 - Y_m}{1 - \phi_m} \quad (3.4)$$

The Reynolds number and the drag coefficient are given by:

$$Re = \frac{2\rho_\infty |U_\infty - U_l| r_l}{\bar{\mu}_\infty} \quad (3.5)$$

$$C_D = \frac{24}{Re} \left[ 1 + \frac{Re^{2/3}}{6} \right] \quad (3.6)$$

The droplet radius reduction is governed by

$$\frac{dr_l}{dt} = -\dot{m}_l / (4\pi\rho_l r_l^2) \quad (3.7)$$

It has been shown by Yuen and Chen [106], that the drag coefficient for evaporating droplets may be approximated by the standard drag curve if the gas viscosity is evaluated at some reference temperature and fuel concentration:

$$T_{ref} = T_s + A_r(T_\infty - T_s) \quad (3.8)$$

$$Y_{ref} = Y_{F_s} + A_r(Y_{F_\infty} - Y_{F_s}) \quad (3.9)$$

where  $A_r = 1/3$  for the 'one-third' averaging rule.

### 3.2.2 Gas-Phase Analysis

The film model developed by Abramzon and Sirignano [2], is extended to include liquid fuel combustion here. The model assumes quasi-steady gas-phase heat and mass transfer, no pressure drop, and the thermal properties (evaluated at reference conditions) are treated as constant. To include the effect of the convective transport "film theory" is used. The formulation is briefly explained below.

The molar and mass fuel vapor fractions at the droplet surface are given by

$$x_{F_s} = P_{F_s} / P \quad (3.10)$$

$$Y_{F_s} = x_{F_s} M_F / \sum_i x_i M_i \quad (3.11)$$

where  $P_{F_s}$  is the fuel vapor saturated pressure, obtained from the Clausius-Clapeyron relation. The Nusselt and Sherwood numbers for a non-vaporizing sphere are taken from Clift et al. [21]:

$$Nu_0 = 1 + (1 + RePr)^{1/3} f(Re) \quad (3.12)$$

$$Sh_0 = 1 + (1 + ReSc)^{1/3} f(Re) \quad (3.13)$$

where  $f(Re) = 1$  for  $Re \leq 1$  and  $f(Re) = Re^{0.077}$  for  $1 < Re \leq 400$

To account for Stefan flow due to droplet regression, the modified Nusselt and Sherwood numbers are calculated as

$$Nu^* = 2 + (Nu_0 - 2)/F_T \quad (3.14)$$

$$Sh^* = 2 + (Sh_0 - 2)/F_M \quad (3.15)$$

where the correction factors are given by:

$$F_T = (1 + B_T)^{0.7} \frac{\ln(1 + B_T)}{B_T} \quad (3.16)$$

$F_M$  is given by an equation of equivalent structure with  $B_T$  replaced by  $B_M$ . The mass and heat transfer numbers are calculated as

$$B_M = \frac{Y_{F_s} + jY_{O_\infty}}{1 - Y_{F_s}} \quad (3.17)$$

$$B_T = \frac{\bar{C}_{pF}(T_\infty - T_s) + f\Delta HY_{O_\infty}}{L(T_s) + \dot{q}_l/\dot{m}_l} \quad (3.18)$$

The instantaneous droplet vaporization rate is given by

$$\dot{m}_l = 2\pi\bar{\rho}_g\bar{D}_g r_l Sh^* \ln(1 + B_M) \quad (3.19)$$

The procedure is iterative, until convergence is reached on  $B_T$  from above, and

$$B_T = (1 + B_M)^\varphi - 1 \quad (3.20)$$

where the parameter  $\varphi$  is given by

$$\varphi = \frac{\bar{C}_{pF} Sh^*}{\bar{C}_{pg} Nu^* Le} \quad (3.21)$$

and the Lewis number is

$$Le = \bar{k}_g / (\bar{\rho}_g \bar{D}_g \bar{C}_{pg}) \quad (3.22)$$

Finally, the heat penetrating into the liquid droplet is given by

$$\dot{q}_l = \dot{m}_l \left\{ \frac{\bar{C}_{pF}(T_\infty - T_s) + f\Delta HY_{O_\infty}}{B_T} - L(T_s) \right\} \quad (3.23)$$

In the above set of equations,  $f$  is the stoichiometric coefficient and the ambient fuel vapor concentration is zero.  $f = 0$  implies vaporization only.

### 3.2.3 Liquid-Phase Analysis

In our model, the metal slurry is conceptualized as a relatively large spherical metal particle (Fig. 1a) surrounded by a liquid film of hydrocarbon fuel. The metal and liquid components of the slurry are separated and the local thermophysical properties (function of temperature) are readily determined.

For all-liquid droplets, the instantaneous liquid vaporization rate is very sensitive to the selection of the transient liquid heating model (Sirignano [88]; Law [53]). It has been demonstrated (Prakash and Sirignano [71]) that heat transfer within the moving droplets is of the pronounced convective type due to intensive liquid circulation caused by the surface friction. The liquid Reynolds number,  $Re_l = U_\infty 2r_l \rho_l / \mu_l$ , and Peclet number,  $Pe_l = Re_l Pr_l$  are found to be very large compared with unity. And, in these cases, there is evidence that the instantaneous velocity field inside droplets may be approximated by the Hill's spherical vortex (Abramzon and Sirignano [2]). We assume that a spherical vortex exists for liquid slurry droplets also. However, the liquid motion changes in the presence of the metal particle. From potential flow theory in a manner similar to the derivation for the classical Hill's spherical vortex (e.g. Batchelor [9]), one can obtain an expression for the modified spherical vortex by taking the radial velocity at the metal sphere to be zero, as

$$\Psi_l = \frac{3(U_\infty - U_l)r_l^2}{2(2 - 5\beta^3 + 3\beta^5)} \left\{ (1 - \beta^2)\beta^3/\delta - (1 - \beta^5)\delta^2 + (1 - \beta^3)\delta^4 \right\} \sin^2 \theta \quad (3.24)$$

where

$$\beta = r_m/r_l \text{ and } \delta = r/r_l \quad (3.25)$$

The radial and tangential velocities in the liquid phase are given by

$$v_r = \frac{3(U_\infty - U_l)}{\delta^2(2 - 5\beta^3 + 3\beta^5)} \left\{ -(1 - \beta^2)\beta^3/\delta + (1 - \beta^5)\delta^2 - (1 - \beta^3)\delta^4 \right\} \cos \theta \quad (3.26)$$

$$v_\theta = \frac{3(U_\infty - U_l)}{2(2 - 5\beta^3 + 3\beta^5)} \left\{ -(1 - \beta^2)\beta^3/\delta^3 - (1 - \beta^5) + 4(1 - \beta^3)\delta^2 \right\} \sin \theta \quad (3.27)$$

The classical Hill's spherical vortex solution is recovered for  $\beta = 0$ . A sample plot of the stream function from Eq. 3.24 is given in Figure 3.2(a), and the velocities are given in Figure 3.2(b). This formulation cannot account for the boundary layer on

the metal surface. Also, the ratio of circulation of the modified spherical vortex to the circulation of Hill's spherical vortex is given by

$$\frac{\Gamma}{\Gamma_{Hill}} = \frac{10r_l(1 - \beta^3)^2(U_\infty - U_l)/(2 - 5\beta^3 + 3\beta^5)}{5r_l(U_\infty - U_l)} = \frac{2(1 - \beta^3)^2}{(2 - 5\beta^3 + 3\beta^5)} \quad (3.28)$$

which shows that  $1 \leq \Gamma/\Gamma_{Hill} \leq 1.2$  as  $0 \leq \beta \leq 1$ . Hence, the two vortices have almost equal strength, and we would expect the metal slurry droplet heating to be convection dominated during the initial stages.

Here, we note that the liquid circulation is likely to result in considerable motion of the solid particle towards the droplet forward stagnation point. In this case, the liquid motion will no longer be given by Eq. 3.24, which neglects both the interface velocity compared to the liquid velocity and the eccentricity of the of the solid particle. The recent detailed calculations of Megaridis and Sirignano [58], seem to indicate that the eccentricity of the aluminum particle along the axis of symmetry becomes significant over the liquid lifetime. In this study, for simplicity, we assume that the solid particle stays in the center of the liquid droplet, which implies that the vaporization rate is not significantly affected by the solid motion. This could be a very poor assumption in extreme cases where the liquid is stripped from the solid particle.

To obtain the maximum liquid surface velocity, the shear stresses at the gas-liquid interface are taken to be equal (Abramzon and Sirignano [2]), obtaining

$$U_s = \frac{1}{32}(U_\infty - U_l) \frac{\mu_g}{\mu_L} Re_\infty C_F = \frac{3(U_\infty - U_l)(1 - \beta^5)}{2 - 5\beta^3 + 3\beta^5} \quad (3.29)$$

where the skin friction coefficient is approximated as

$$C_F = \frac{12.69}{Re^{2/3}(1 + B_M)} \quad (3.30)$$

and this yields the nondimensional velocities as

$$v_r' = \frac{v_r}{U_s} = (1 - \beta^5) \left\{ -\beta^3(1 - \beta^2)/\delta^3 + (1 - \beta^5) - (1 - \beta^3)\delta^2 \right\} \cos \theta \quad (3.31)$$

$$v_\theta' = \frac{v_\theta}{U_s} = (1 - \beta^5) \left\{ -\beta^3(1 - \beta^2)/2\delta^3 - (1 - \beta^5) + 2(1 - \beta^3)\delta^2 \right\} \sin \theta \quad (3.32)$$

The metal (aluminum) diffusivity is three orders of magnitude larger than the liquid (hydrocarbon) diffusivity. Hence, the metal may be treated as essentially isothermal.

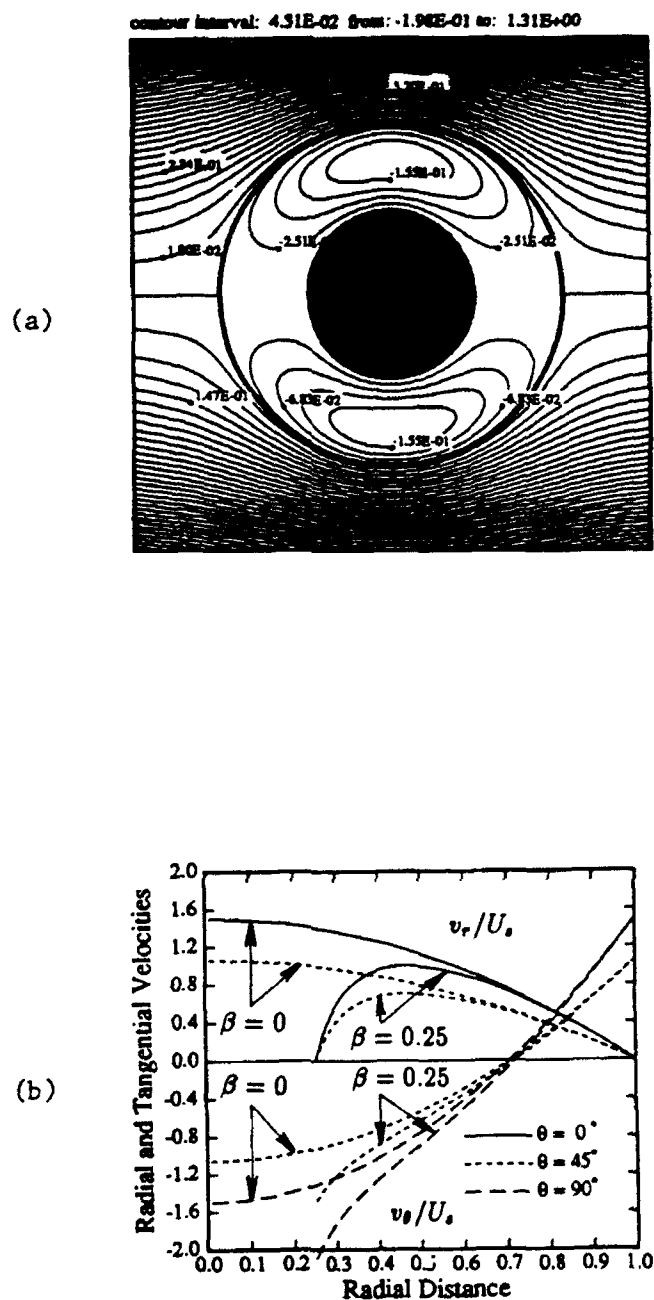


Figure 3.2: (a) Liquid-phase stream function  $\Psi_l/r_l^2(U_\infty - U_l)$  for  $\beta = 0.5$ . (b) Radial ( $v_r/U_s$ ) and tangential ( $v_\theta/U_s$ ) velocities of the liquid-phase vs. radial distance ( $r/r_l$ ) at various tangential locations, for  $\beta = 0$  and 0.25.

thus saving computational time. To analyze the transient droplet heating within the liquid film, we write the energy conservation equation:

$$\rho C_p \left\{ \frac{\partial T}{\partial t} + v_r \frac{\partial T}{\partial r} + \frac{v_\theta}{r} \frac{\partial T}{\partial \theta} \right\} = k \left\{ \frac{1}{r^2} \frac{\partial}{\partial r} (r^2 \frac{\partial T}{\partial r}) + \frac{1}{r^2 \sin \theta} \frac{\partial}{\partial \theta} (\sin \theta \frac{\partial T}{\partial \theta}) \right\} \quad (3.33)$$

This form of the energy equation has a moving boundary condition due to liquid vaporization. By introduction of the transformations

$$\tau = \alpha_l t / r_{li}^2; \quad \tau \geq 0 \quad (3.34)$$

$$\eta = \frac{r - r_m}{r_l(t) - r_m}; \quad 0 \leq \eta \leq 1 \quad (3.35)$$

$$Z = \frac{T - T_i}{T_i} \quad (3.36)$$

where the subscript 'i' refers to the initial conditions, and after some manipulation, we obtain the nondimensional form with a fixed boundary condition:

$$r_l'^2 \frac{\partial Z}{\partial \tau} + \left( \frac{Pe_l v_r' r_l'}{2} - \frac{1}{2} \eta \frac{dr_l'^2}{d\tau} \right) \frac{\partial Z}{\partial \eta} + \frac{Pe_l v_\theta' r_l'}{2(\eta + \xi)} \frac{\partial Z}{\partial \theta} = \frac{1}{(\eta + \xi)^2} \left[ \frac{\partial}{\partial \eta} \left\{ (\eta + \xi)^2 \frac{\partial Z}{\partial \eta} \right\} + \frac{1}{\sin \theta} \frac{\partial}{\partial \theta} (\sin \theta \frac{\partial Z}{\partial \theta}) \right] \quad (3.37)$$

where we have used the following expressions:

$$r_l' = \frac{r_l(\tau) - r_m}{r_{li}}; \quad Pe_l = \frac{2r_{li} U_s}{\alpha_l}; \quad \xi = \frac{r_m}{r_l(\tau) - r_m} = \frac{r_m}{r_{li} r_l'} \quad (3.38)$$

The transformed initial and boundary conditions for the energy equation are given by:

$$\text{at } \tau = 0, \quad Z = 0 \quad (3.39)$$

$$\text{at } \eta = 0, \quad \int_0^\pi \frac{\partial Z}{\partial \eta} \Big|_l \sin \theta d\theta = \frac{2(\rho C_p)_m}{3(\rho C_p)_l} \frac{r_m r_l'}{r_{li}} \frac{dZ}{d\tau} \Big|_m \quad (3.40)$$

$$\text{at } \eta = 1, \quad \int_0^\pi \frac{\partial Z}{\partial \eta} \Big|_l \sin \theta d\theta = \frac{\dot{q}_l r_l' r_{li}}{2\pi k_l T_i r_l'^2} \quad (3.41)$$

$$\text{at } \theta = 0 \text{ and } \pi, \quad \frac{\partial Z}{\partial \theta} = 0 \quad (3.42)$$

The slurry droplet heating model, at  $Pe_l \rightarrow 0$  reduces to the "conduction limit" model implying heat transfer by conduction only. For high  $Pe_l$  numbers, the

convective transport would dominate the thermal diffusion ("vortex model"). Also,  $k_l \rightarrow \infty$  represents the infinite conductivity model.

For the purpose of spray combustion calculations, an alternative approach is to employ the "effective conductivity" model. For all-liquid droplets, it has been proposed (Abramzon and Sirignano [2]) that to simplify the calculations for the internally circulating droplets, a one-dimensional energy conservation equation be solved after empirically enhancing the liquid conductivity. In such a case, the energy equation is

$$r_l'^2 \frac{\partial Z}{\partial \tau} - \frac{1}{2} \eta \frac{dr_l'^2}{d\tau} \frac{\partial Z}{\partial \eta} = \frac{1}{(\eta + \xi)^2} \frac{\partial}{\partial \eta} \left\{ (\eta + \xi)^2 \frac{\partial Z}{\partial \eta} \right\} \quad (3.43)$$

with the initial and boundary conditions

$$\text{at } \tau = 0, \quad Z = 0; \quad (3.44)$$

$$\text{at } \eta = 0, \quad \left. \frac{\partial Z}{\partial \eta} \right|_l = \frac{1}{3} \frac{(\rho C_p)_m}{(\rho C_p)_l} \frac{r_m r_l'}{r_{li}} \left. \frac{dZ}{d\tau} \right|_m \quad (3.45)$$

$$\text{at } \eta = 1, \quad \left. \frac{\partial Z}{\partial \eta} \right|_l = \frac{Q_l r_l' r_{li}}{4\pi k_l T_l r_l^2} \quad (3.46)$$

Also,

$$k_{eff}/k_l = 1.86 + 0.86 \tanh \{2.245 \log_{10}(Pe_l/30)\} \quad (3.47)$$

The Eq. 3.47 is developed for an all-liquid droplet. We assume the correlation holds here, too. This hypothesis will be examined later, in the results section.

### 3.2.4 Dry Particle Heating

In this stage, the dry particle heats rapidly until the phase change of metal occurs. We shall make an approximate calculation, to predict the ignition times of the slurry droplets. As the metal diffusivity is large, we can assume the particle to be isothermal (Biot number  $\approx 2.5 \times 10^{-3} \ll 1$ ), with the heat rise given by:

$$\frac{d}{dt} \left\{ \frac{4}{3} \pi r_{Al}^3 (\rho C_p)_{Al} T + \frac{4}{3} \pi (r_s^3 - r_{Al}^3) (\rho C_p)_{ox} T \right\} = \dot{q}_m \quad (3.48)$$

The heat flux  $\dot{q}_m$  into the metal is composed of heat transfer due to convection, radiation and chemical reaction, i.e.,

$$\dot{q}_m = \dot{q}_c + \dot{q}_{rad} + \dot{q}_{ch} \quad (3.49)$$

There exists evidence in the literature (see e.g. Dwyer and Sanders [25]) that, in a convective, burning liquid fuel droplet case, the flame in the gas phase is situated in the wake of the droplet, and the ability to hold the flame is minimal. The characteristic gas-phase residence time is very short, of the order of  $10^{-5}$  s, and the unsteady effects associated with the collapse of the individual droplet flame may be neglected. In this simplified scenario, the convection heat transfer may be given by:

$$\dot{q}_c = 4\pi r_{ox}^2 h(T_{gas} - T_s) \quad (3.50)$$

The convective heat transfer coefficient  $h$  is given by the Nusselt number correlation in Eq. 3.12. The temperature  $T_{gas}$  in the above equation refers to the temperature of the hot gases in the combustor resulting from the combustion of the liquid fuel. The temperatures in the combustor will depend upon several parameters. To construct a simple model, we assume that  $T_{gas}$  is given by specifying a fuel equivalence ratio ( $\Phi$ ) for the liquid fuel. Then the appropriate flame temperature can be determined (Pratt and Pratt [72]), and this temperature is used as  $T_{gas}$ . Such an approach implies complete combustion of the fuel vapor in the gas phase occurs before dry metal heating commences. Thus,  $T_{gas}$  will continuously increase as the liquid fuel vaporizes. For *n*-octane as the liquid fuel burning in air at an initial temperature of 1500 K and a pressure of 10 atm, highest  $T_{gas}$  values are obtained as 1710, 2093, 2262, 2414, and 2845 K, corresponding to  $\Phi$  values of 0.1, 0.3, 0.4, 0.5, and 1.0.

The radiation heat transfer is given by

$$\dot{q}_{rad} = 4\pi r_{ox}^2 \epsilon_m \epsilon_g \sigma (T_{gas}^4 - T_s^4) \quad (3.51)$$

where  $\epsilon_m = 0.25$  and  $\epsilon_g = 0.10$  are the metal and gas emissivities. The radiation heat transfer is not expected to be significant, for the burning of isolated slurry droplets, as is the case with burning pure liquid droplets. However, when the metal starts to burn, the radiation heat transfer becomes important especially with the formation of condensed oxides.

The heat release due to the surface oxidation of the aluminum is given by

$$\dot{q}_{ch} = 4\pi r_{ox}^2 \dot{m}_o \Delta H_{Al} \quad (3.52)$$

where  $\dot{m}_o$  is the oxygen flow rate at the aluminum oxide-aluminum interface, and  $\Delta H_{Al}$  is the heat of oxidation of aluminum per kilogram of oxygen consumed. To

model the oxidizer flow rate, we employ the strategy proposed in Appendix A. The oxide layer covering the particle (Figure 3.1(b)) has an outer radius  $r_{ox}$ , the thickness of which is given by

$$\delta(t) = r_{ox}(t) - r_{Al}(t) \quad (3.53)$$

where  $r_{Al}$  denotes the radius of aluminum metal. From stoichiometry and known molecular weights, we obtain (Appendix A):

$$\frac{d}{dt} \left\{ \frac{4}{3} \pi \rho_{Al} r_{Al}^3 \right\} = -\frac{9}{8} \dot{m}_o \quad (3.54)$$

$$\frac{d}{dt} \left\{ \frac{4}{3} \pi \rho_{ox} (r_s^3 - r_{Al}^3) \right\} = \frac{17}{8} \dot{m}_o \quad (3.55)$$

The diffusivity of the oxygen through the oxide is given by

$$D_{ox} = \frac{8}{17} 1.9 \times 10^{-5} \exp \left( -\frac{17000}{R_g T_s} \right) \text{ cm}^2/\text{s} \quad (3.56)$$

where  $R_g = 1.987 \text{ cal/mole-K}$ .

On combining the two oxygen mass transfer resistance in series (through the gas and the oxide layer, Figure 3.1(b)), we get (this would imply quasi-steady diffusion of oxygen through the oxide layer):

$$\dot{m}_o = \frac{4\pi r_{ox} (\rho D)_g Y_{o\infty}}{\frac{2}{Sh} + \frac{(\rho D)_g \delta}{(\rho D)_{ox} r_{Al}}} \quad (3.57)$$

The Sherwood number is obtained from Eq. 3.13. The metal temperature rises until the phase change occurs at the melting point of the aluminum. Initial value of  $\delta$  is taken as  $30 \text{ \AA}$ . A discussion on the aluminum ignition criterion and the diffusivity of the oxygen through the aluminum oxide is given in Appendix A.

### 3.2.5 Metal Melting

Melting of aluminum particle occurs at  $933.1 \text{ K}$ , and during the phase change the particle temperature remains at  $933.1 \text{ K}$ . The heat rise after the aluminum phase change continues to be given by Eq. 3.48. At the melting point of the oxide,  $\sim 2300 \text{ K}$ , the ignition is assumed to occur.

### 3.3 Solution Procedure

The ordinary differential equations (3), (4), and (7) are solved using an implicit iterative method. The iterations are terminated when the following conditions are met:

$$|T_s^{k+1} - T_s^k| < 0.01 \text{ K}, \quad (3.58)$$

$$|(\dot{m}_i^{k+1} - \dot{m}_i^k)/\dot{m}_i^k| < 0.01 \quad (3.59)$$

The energy equation (3.37) is solved using an implicit scheme, employing central differences and uniform grid spacings. To handle the integral boundary conditions (3.40, 3.41), knowing that the partial differential equation and the boundary conditions are linear if the velocities and droplet radii are uncoupled from the temperature, we can write the nondimensional temperature as a combination of three independent solutions over an infinitesimal increment of time:

$$Z(\eta, \theta, \tau) = Z_1(\eta, \theta, \tau) + A(\tau)Z_2(\eta, \theta, \tau) + B(\tau)Z_3(\eta, \theta, \tau) \quad (3.60)$$

At time  $\tau$ , we make:

$$Z_1(\eta, \theta, \tau) = Z(\eta, \theta, \tau) \quad (3.61)$$

$$Z_2(\eta, \theta, \tau) = 0 \quad (3.62)$$

$$Z_3(\eta, \theta, \tau) = 0 \quad (3.63)$$

To find the new values of the functions  $Z_1$ ,  $Z_2$ , and  $Z_3$ , we impose the boundary conditions (at the gas-liquid interface):

$$Z_1(\eta = 1, \theta, \tau + \Delta\tau) = Z(\eta = 1, \theta, \tau) \quad (3.64)$$

$$Z_2(\eta = 1, \theta, \tau + \Delta\tau) = 1 \quad (3.65)$$

$$Z_3(\eta = 1, \theta, \tau + \Delta\tau) = 0 \quad (3.66)$$

and at the liquid-metal surface:

$$Z_1(\eta = 0, \theta, \tau + \Delta\tau) = Z(\eta = 0, \theta, \tau) \quad (3.67)$$

$$Z_2(\eta = 0, \theta, \tau + \Delta\tau) = 0 \quad (3.68)$$

$$Z_3(\eta = 0, \theta, \tau + \Delta\tau) = 1 \quad (3.69)$$

To evaluate  $A(\tau)$  and  $B(\tau)$ , we use the physical boundary conditions (3.40, 3.41) as:

$$\int_0^\pi \frac{\partial Z_1}{\partial \eta} \Big|_{\eta=1} \sin \theta d\theta + A(\tau) \int_0^\pi \frac{\partial Z_2}{\partial \eta} \Big|_{\eta=1} \sin \theta d\theta + B(\tau) \int_0^\pi \frac{\partial Z_3}{\partial \eta} \Big|_{\eta=1} \sin \theta d\theta = \frac{Q_l r_l' r_{li}}{2\pi k_l T_l r_l^2} \quad (3.70)$$

$$\int_0^\pi \frac{\partial Z_1}{\partial \eta} \Big|_{\eta=0} \sin \theta d\theta + A(\tau) \int_0^\pi \frac{\partial Z_2}{\partial \eta} \Big|_{\eta=0} \sin \theta d\theta + B(\tau) \int_0^\pi \frac{\partial Z_3}{\partial \eta} \Big|_{\eta=0} \sin \theta d\theta = \frac{2(\rho C_p)_m r_m r_l'}{3(\rho C_p)_l r_{li}} \frac{dZ}{d\tau} \Big|_m \quad (3.71)$$

$A(\tau)$  and  $B(\tau)$  are determined from simultaneous solution of the above two equations. Note that the functions  $Z_1$ ,  $Z_2$ , and  $Z_3$  are re-defined at each time step. As a result, errors associated with the non-linearity due to the couplings amongst temperature, regression rate, and velocities remains of higher order. Briefly, the solution procedure followed is as follows

1. Guess a droplet surface temperature  $T_s$ , or use the previous time-step value.
2. Calculate the fuel mass fraction at the droplet surface ( $Y_{F_s}$ ), using the Clausius-Clapeyron relation.
3. Calculate the averaged physical properties.
4. Find the mass transfer number  $B_M$  (Eq. 3.17), diffusional film correction factor  $F_M$  (Eq. 3.16), modified Sherwood number  $Sh^*$  (Eq. 3.15), and the mass vaporization rate  $\dot{m}_l$  (Eq. 3.19).
5. Calculate the correction factor for the thermal film thickness,  $F_T$  (Eq. 3.16), using the previous iteration value of  $B_T$ . Obtain  $\varphi$  (Eq. 3.21),  $Nu^*$  (Eq. 3.14), and the corrected value of the heat transfer number  $B_T$  (Eq. 3.20). Iterate in this loop, until convergence is reached on  $B_T$ .
6. Find the heat penetrating into the droplet interior  $Q_l$  (Eq. 3.23).
7. Solve the liquid-phase equations, (in one or two dimensions), and obtain new  $r_s$  and  $T_s$ .
8. Check for convergence on  $T_s$ , otherwise iterate between steps (2) and (8).

### 3.4 Results and Discussion

In the following results, the air is at a pressure of 10 atm, temperature 1500 K, and velocity 50 m/s. The droplet has an initial radius of 50  $\mu\text{m}$ , temperature 300

K, and velocity 10 m/s. Vaporization-only is considered first, and these results are obtained with the gas temperature fixed. Figures 3.3 and 3.4 present the dynamic and vaporization history of the slurry droplets from the axi-symmetric calculations, for initial  $\beta = r_m/r_{li}$  values of 0.25 and 0.5. For comparison purposes, results for an all-liquid droplet ( $\beta = 0$ ) under identical conditions, are also presented. Figure 3.3(a) shows the nondimensional droplet radius (squared) of the slurry droplets for different metal particle radii. The radius reduction for the slurry droplets is roughly similar to that for an all-liquid droplet. Curves for the higher metal particle radii tend to end earlier, as the liquid vaporization is complete earlier due to less initial mass. Figure 3.3(b) shows the vaporization rate of liquid fuel for different metal particle radii. When compared with the vaporization rates of an all-liquid droplet, initially the rate for the smaller metal particles is seen to be rising slower. At a later stage, when a considerable fraction of initial liquid mass has vaporized, the rate becomes slightly faster. Figure 3.3(c) shows the surface temperature of the slurry droplets for different metal particle radii. The liquid surface temperature rises somewhat slower for the slurry droplets, in comparison with the all-liquid case. The  $\rho C_p$  product for aluminum is about  $0.54 \text{ cal/cm}^3\text{-K}$ , and that for *n*-octane is about  $0.40 \text{ cal/cm}^3\text{-K}$ . In addition to the  $\rho C_p$  effect, the presence of the solid core causes increased circulation of the liquid fuel (refer to Eq. 3.28). Furthermore, the higher density of the solid ( $\rho_{Al}/\rho_l \approx 4$ ) effectively increases the mass of the droplet to be accelerated to the gas-phase velocity. The droplets with larger initial solid mass fraction are found to accelerate slower. Hence, the relative gas-liquid velocity remains greater in these cases. These effects appear in the Reynolds and Peclet numbers. Figure 3.3(d) shows liquid Peclet number versus time for different metal particle radii. The increased effective heat distribution has an effect similar to that of increasing the effective liquid conductivity.

Figure 3.4 shows the liquid phase isotherms at different times, for the case of  $r_m/r_{li} = 0.5$ . Here, the gas is flowing from the right to left, relative to the droplet center. Very early into the calculations, the heat is transferred into the core from the surface primarily by conduction, as shown by Figure 3.4(a), corresponding to a time of 0.01 ms. After a short time, 0.04 ms in this case, the convection effects start to dominate. From this time to about 3.0 ms, the isotherms closely resemble the streamlines (Figure 3.2(a)), as indicated by Figure 3.4(b). After 3.0 ms, the cold

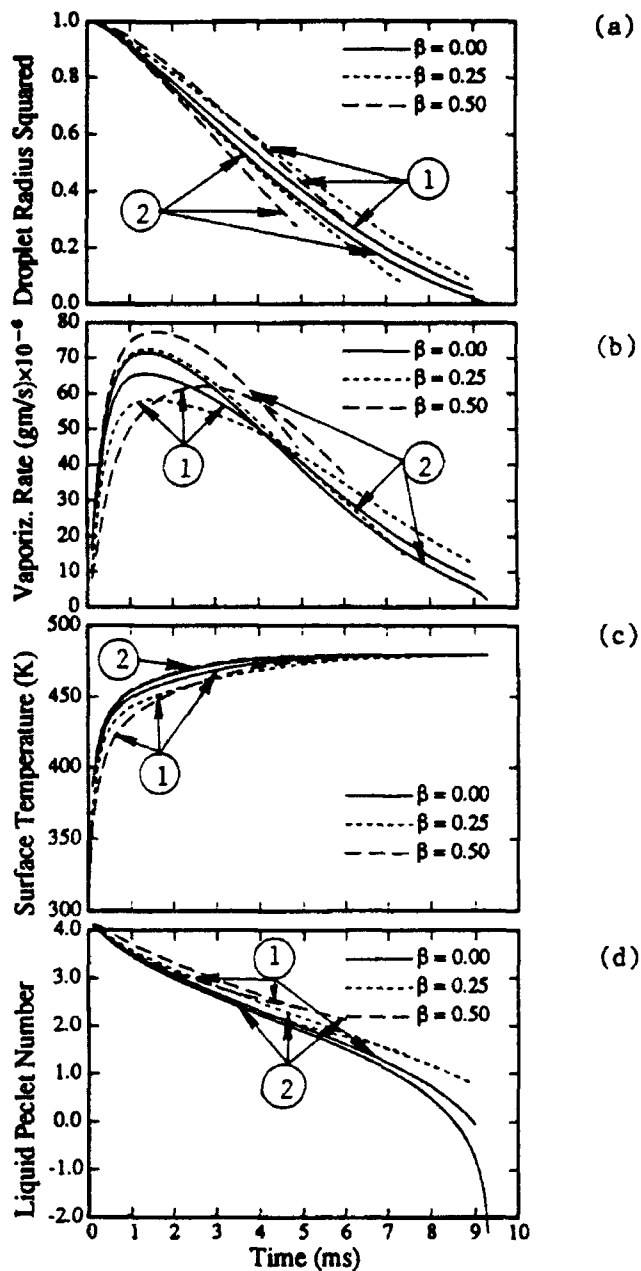


Figure 3.3: Results for vaporization of slurry droplets in air, for  $p_{\infty}=10$  atm,  $T_{\infty}=1500$  K,  $U_{\infty}=50$  m/s,  $U_{i,i}=10$  m/s, and  $r_m/r_{i,i} = \beta=0$  (all-liquid droplet), 0.25 and 0.5. (a): droplet radius squared  $(r_l/r_{i,i})^2$ ; (b): liquid fuel vaporization rate  $\dot{m}_l$ ; (c): droplet surface temperature  $T_s$ ; and (d): liquid Peclet number  $\log_{10}(Pe_l)$ . Curves 1 are from axis-symmetric calculations and 2 are from effective conductivity calculations.

region moves to the droplet front, and the isotherms no longer resemble streamlines; see Figure 3.4(c). As the Peclet number starts to fall, the conduction effects become dominant again. Figure 3.4(d) shows that, at the very end of calculations (6 ms), the isotherms are again spherically symmetric. By this time, most of the liquid fuel has evaporated.

In addition to results for axi-symmetric calculations, Figure 3.3 also presents the dynamic and vaporization history of the slurry droplets from the spherically-symmetric calculations. The results obtained are similar to those obtained for the more complex axi-symmetric calculations. Figure 3.3(a) shows the nondimensional droplet radius (squared) of the slurry droplets for different metal particle radii. Figure 3.3(b) shows the vaporization rate of liquid fuel and Fig. 3c shows the surface temperature of the slurry droplets for different metal particle radii. The vaporization rate is seen to increase with increasing metal radius, and the reason is the increased Peclet number. Figure 3.3(d) shows the liquid Peclet number for different metal particle radii. Larger Peclet number increases the value of the effective thermal conductivity (refer to Eq. 3.47), which in turn results in faster vaporization. This causes some difference in the vaporization rate calculation, when compared with the results from the axi-symmetric model. At higher metal radii case of  $\beta = 0.75$  (not shown here), the correct trend is again obtained. Overall, we see that the effective conductivity correlation produces results which are consistent with those from the extended axi-symmetric calculations. Errors associated with the effective diffusivity are generally larger for slurry droplets than for all-liquid droplets; sometimes they may not be tolerable.

The results for a burning slurry droplet, from spherically symmetric droplet heating model, are presented in Figures 3.5 to Figures 3.7. In all the following results, the ambient gas temperature is a variable (see section on Dry Particle Heating). This axially increasing gas temperature results in faster burning times, compared to a fixed gas temperature. In Figures 3.5 and 3.6, the overall equivalence ratio based on the amount of liquid fuel contained in the slurry droplet is fixed at 0.4. Figure 3.5 shows the results, for burning of slurry droplet under other conditions similar to those employed for the vaporization only case. Figure 3.5(a) shows the nondimensional droplet radius (squared) of the slurry droplets for different metal particle radii. Compared with the vaporization only case, the transfer numbers obtained are quite

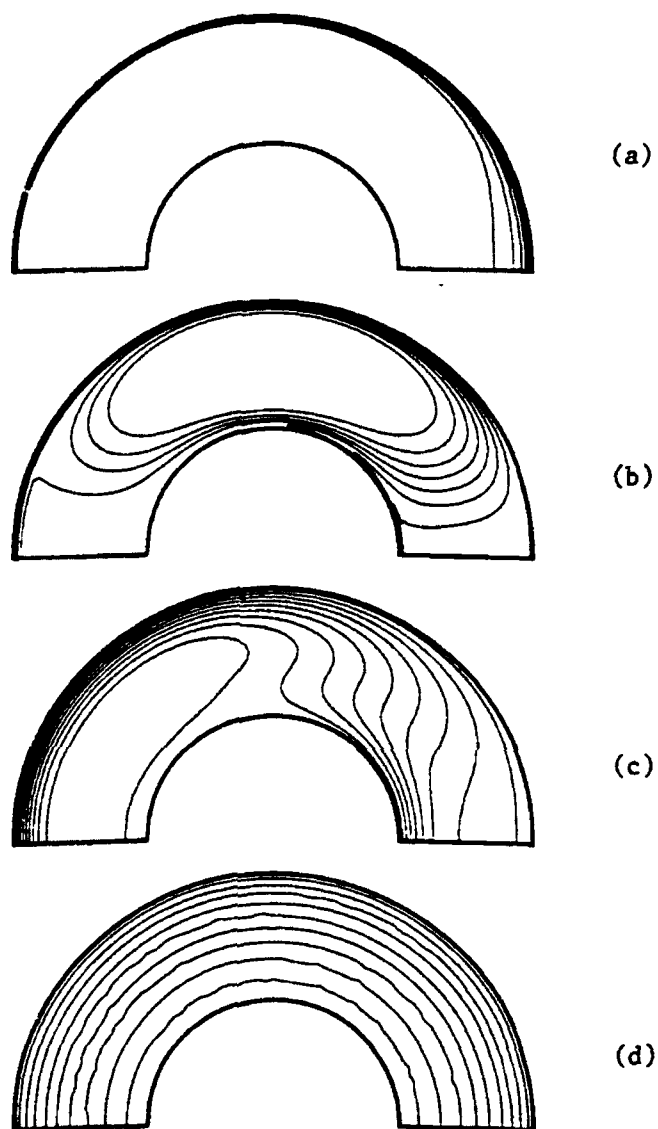


Figure 3.4: Liquid-phase isotherms for vaporization of slurry droplets in air, for  $p_{\infty}=10$  atm,  $T_{\infty}=1500$  K,  $U_{\infty}=50$  m/s,  $U_i=10$  m/s, and  $r_m/r_l = \beta = 0.5$ . (a): At  $t=0.01$  ms,  $r_l/r_l=1.000$ ,  $Re=282.4$ ,  $T_{min}=300.0$  K,  $T_{max}=347.6$  K. (b): At  $t=0.05$  ms,  $r_l/r_l=1.000$ ,  $Re=277.2$ ,  $T_{min}=300.0$  K,  $T_{max}=361.7$  K. (c): At  $t=4.0$  ms,  $r_l/r_l=0.756$ ,  $Re=73.7$ ,  $T_{min}=459.5$  K,  $T_{max}=471.4$  K. (d): At  $t=6.0$  ms,  $r_l/r_l=0.553$ ,  $Re=35.3$ ,  $T_{min}=474.4$  K,  $T_{max}=476.0$  K.

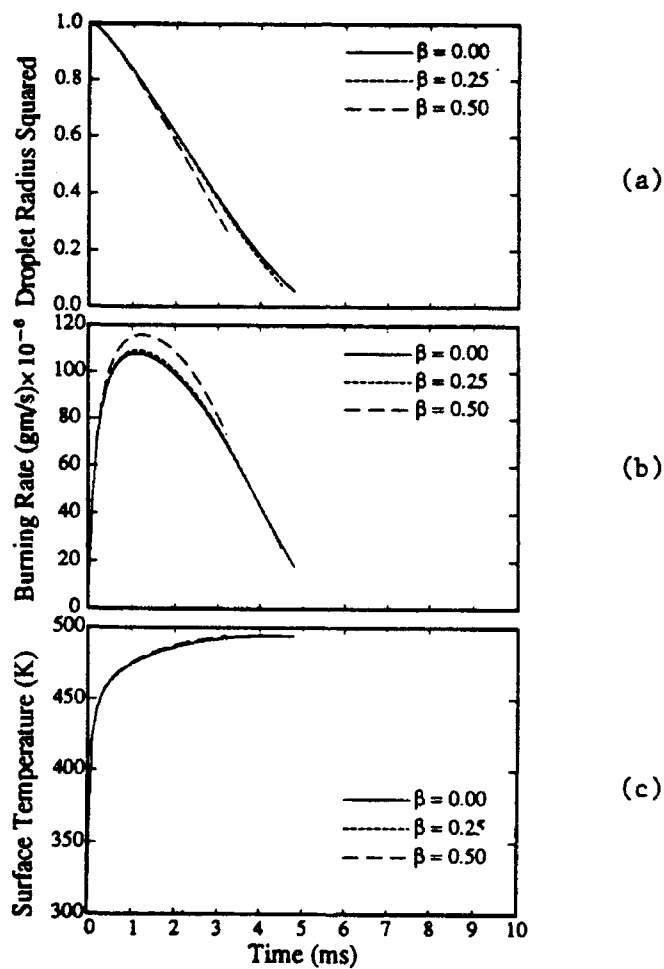


Figure 3.5: Results for combustion of slurry droplets in air, for  $p_\infty=10$  atm,  $T_\infty=1500$  K,  $U_\infty=50$  m/s,  $U_i=10$  m/s, and  $r_m/r_i = \beta=0$  (all-liquid droplet), 0.25 and 0.5. (a): droplet radius squared  $(r_l/r_i)^2$ ; (b): liquid fuel burning rate  $\dot{m}_l$ ; (c): droplet surface temperature  $T_s$ .

large. Hence, the burning rate is larger, and the droplet surface regression is faster. Figure 3.5(b) shows the burning rate of the liquid fuel for different metal particle radii. Figure 3.5(c) shows the droplet surface temperature with time. When compared with the vaporization only case, the droplet life-times here are shorter. Hence, for larger metal particles, even at the end of the droplet lifetime, still a substantial relative gas-particle velocity is left.

Figure 3.6 shows the slurry droplet history for initial  $\beta$  values of 0.25 and 0.5. The gas-phase Reynolds number is shown in Figure 3.6(a). Note that the droplet life-time, from Figure 3.5(a), is about 4.70 and 3.32 ms, for  $\beta = 0.25$  and 0.5, respectively. Figure 3.6(a) shows Reynolds numbers of order 10 for these cases. At these times, it is evident that the dry particle has not accelerated to the gas velocity. The convective heating is stronger for larger particle case. Figure 3.6(b) shows the droplet surface temperature for the two slurry droplets. In addition to the convective effect, the mass of the aluminum particle controls the rate at which the particle heats up. Initially, the surface temperature is limited by the boiling point of the liquid fuel (for our ambient conditions, it is about 490 K). After vaporization of all the liquid fuel from the droplet, the convective flux causes the dry particle temperature (assumed isothermal) to rise rapidly. The flat portion at 933.1 K corresponds to the phase change of solid to liquid aluminum. The curves end at 2300 K, at which point ignition of the metal particle shall occur. Figure 3.6(c) shows the rate at which oxygen is consumed at the oxide-metal interface. The rate becomes nonzero upon the completion of the liquid fuel vaporization. As the metal temperature rises, the diffusivity of oxygen through the oxide shell increases, and the oxidizer flux at the oxide-metal interface increases. However, as the metal gets progressively oxidized, the film thickness increases, and this will slow the rate of oxidation. The growth of the oxide film is shown in the Figure 3.6(d). The larger metal particle results in somewhat slower film growth rate, though the oxidizer flux is greater. This is in accordance with the fact that the oxidizer flow rate through the oxide layer is directly proportional to the particle radius and inversely proportional to the oxide film thickness, *cf.* Eq. 3.57. The outer radius of the particle ( $r_{ox}$ ) grows due to the deposition of mass during oxidation, and the inner radius of the aluminum particle ( $r_{Al}$ ) shrinks due to the consumption of the metal, in accordance with Eqs. 3.55 and 5.23. As expected (see Chapter 2), the chemical heat release is much smaller than the convective heat flux, until the particle

temperature reaches temperatures of about 2000 K, which occurs at about 7 ms for the particle radius of 12.5  $\mu\text{m}$  and at about 9 ms for 25  $\mu\text{m}$  particle. The relative contributions are shown in the Figure 3.7, which shows the total, and the convective and chemical heat fluxes, as used in Eq. 3.48. In cases where the ignition occurs, the metal temperature will rise rapidly to the aluminum boiling point, primarily due to the chemical heat release, where the metal is known to burn in the vapor phase. The reason for the initial low contribution of the chemical term is the low diffusivity of oxygen through the aluminum oxide, which results in the low values of the oxidizer mass flux into the particle, Eq. 3.48 and  $\dot{q}_{ch}$ , Eq. 3.52.

Figure 3.8 shows the ignition times for the slurry droplet burning in air. The ignition times include the time associated with the vaporization of the liquid fuel from the slurry droplet. Figure 3.8(a) shows the effect of increasing the solid radius (or mass loading) in the slurry droplet, and Figure 3.8(b) shows the effect of the gas temperature. For  $\beta$  values of 0.25, 0.5 and 0.75, the corresponding initial solid mass fractions are 5.7%, 35.4%, and 73.7 %. Equivalence ratios  $\leq 0.3$  (corresponding to a highest gas temperature of 2179 K) did not result in ignition of the metal particles considered in this study. In our model, increasing the amount of the liquid fuel results in higher gas temperatures. This implies faster heating of the dry particle, and hence shorter ignition times. It is evident that depending upon, among other parameters, the gas temperatures and the solid loading in the slurry, the metal ignition times can be several times larger than the liquid burnout times. The increase in ignition time is almost linear with the solid particle size, especially for lower equivalence ratios. Increasing the gas temperature results in faster heating of the dry particle, and so shorter ignition times, as shown in Figure 3.7(b) While no direct comparison of results is possible with available experimental data, the Wong and Turns [111, 112] studies, show similar trends for the ignition times. Figure 3.8(c) shows the effect of changing the initial Reynolds number, for a fixed  $\Phi = 0.4$ . This is achieved by decreasing the relative inlet gas-droplet velocity from the usual value of 40 m/s, which corresponds to an initial Reynolds number of about 300. Expectedly, an increase of the initial Reynolds number results in a small decrease in the ignition times (since the metal heating is initially convection dominated). This study does not consider the post-ignition burning of the metal particle, and its effect on the ambient gas temperature.

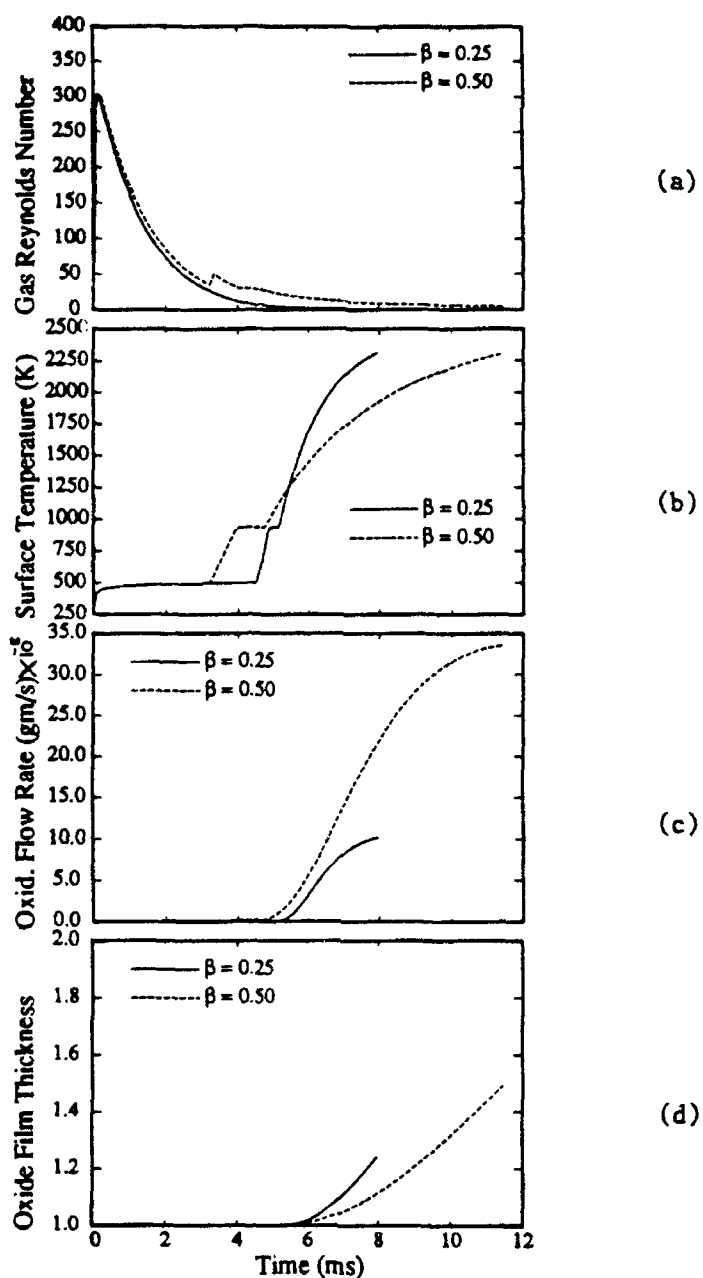


Figure 3.6: Results for combustion of slurry droplets in air, for  $p_\infty=10$  atm,  $T_\infty=1500$  K,  $U_\infty=50$  m/s,  $U_i=10$  m/s, and  $r_m/r_l = \beta = 0.25$  and 0.5. (a): gas Reynolds number  $Re$ ; (b): droplet surface temperature  $T_s$ ; (c): oxidizer flow rate  $\dot{m}_o$ ; and (d): oxide film thickness  $\delta/\delta_i$ .

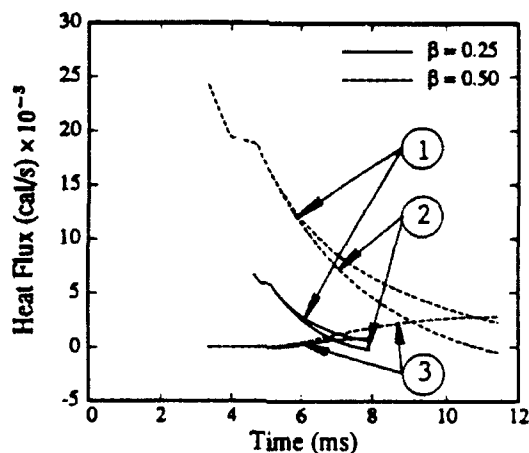


Figure 3.7: Heat fluxes into the particle versus time, for  $U_\infty=50$  m/s,  $U_l=10$  m/s, and  $r_m/r_l = \beta= 0.25$  and  $0.5$ . Curve 1: total  $\dot{q}_m$ ; curve 2: convective  $\dot{q}_c$ ; and curve 3: chemical  $\dot{q}_{ch}$ .  $\dot{q}_{rad}$  is insignificant.

However, this consideration will result in higher gas temperatures, and thus, shorter ignition times.

### 3.5 Conclusion

An idealized configuration of the slurry droplet, in which a metal particle is surrounded by a liquid hydrocarbon carrier, has been studied analytically and numerically. Two scenarios, vaporization only and vaporization followed by combustion of the liquid fuel, have been considered. The model used is an extension of the classical droplet vaporization model. The gas-phase formulation includes the important effects of variable thermophysical properties, nonunitary Lewis number and influence of Stefan flow. Transient heating of the liquid-metal slurry has been studied, using an extended axisymmetric heating model that includes an analytical solution for the liquid motion, and a simplified spherically symmetric model using an effective liquid thermal conductivity. Acceptable agreement is found in the calculations from the two models. The vaporization rates are found to be close to those for all-liquid droplets.

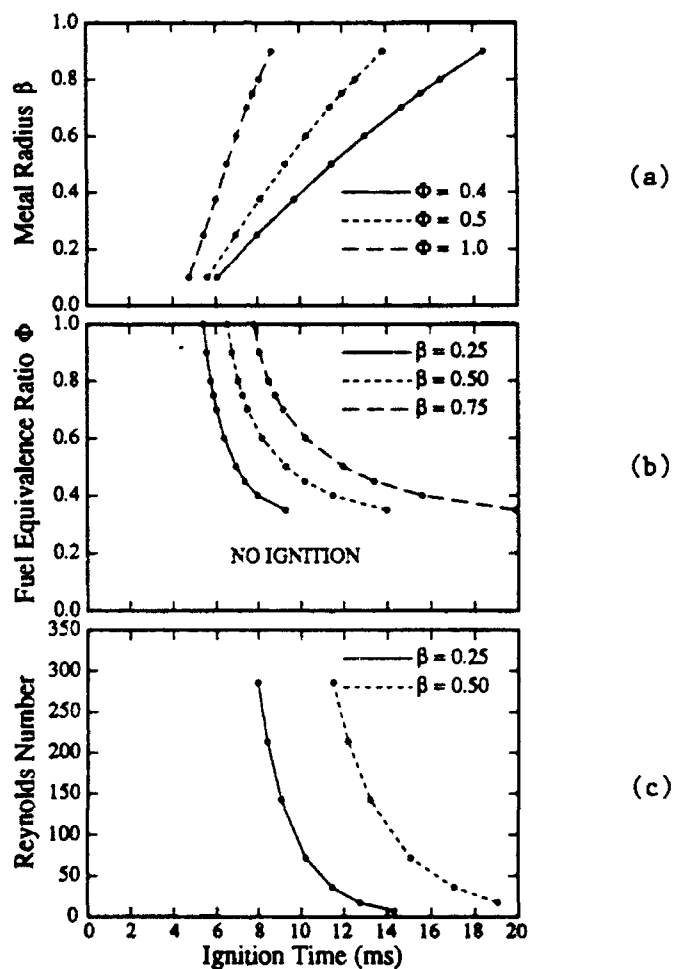


Figure 3.8: Ignition times for slurry droplets burning in air at  $p_\infty=10$  atm,  $T_\infty=1500$  K,  $U_\infty=50$  m/s and  $U_{l,i}=10$  m/s. (a): Effect of metal radius  $\beta = r_m/r_{l,i}$ ; (b): Effect of fuel equivalence ratio  $\Phi$ , based on the liquid mass in the slurry droplet; (c): Effect of initial Reynolds number, calculated by varying the initial relative gas-droplet velocity.

As the metal particle size is increased, the droplets are seen to accelerate slower, due to the added mass. The liquid Peclet number is shown to rise, resulting in greater heat flux into the droplet interior. When combustion of the isolated slurry droplet is considered, it is shown that the heat diffusion from the hot gases is the primary heating mechanism for the dry metal, for temperatures up to 2000 K, above which the heat flux from surface oxidation of the aluminum also becomes important. The metal ignition times increase rapidly with rising metal particle size, and can be several times larger than the liquid fuel burnout time. The spherically-symmetric calculation requires a much shorter computational time, and hence is suitable for the spray combustion computations. Furthermore, the model is applicable to a wide range of droplet sizes and Reynolds numbers.

# Chapter 4

## Liquid Vaporization from Fine-Metal Slurry Droplets

### 4.1 Introduction

The chapter focuses on vaporization of a liquid fuel from a slurry droplet composed of a large number of solid particles (aluminum) dispersed in a liquid hydrocarbon (*n*-octane), as a first step in developing a simple comprehensive model that can be employed in metal slurry spray calculations. Previous studies have established that, after an initial decrease depending on solid loading, the droplet radius becomes fixed (see section 1.1.1). A rigid porous shell is established on the droplet surface, and the agglomerates formed are hollow. Under certain conditions, microexplosions of slurry droplets have been observed.

As recently discussed by Lee and Law [55], the earlier work of Antaki [5, 6] implies a uniform distribution of solid particles inside the slurry droplet, thus resulting in solid agglomerates. It is known that, in general, the agglomerates produced are hollow, especially for initial solid loadings lower than the maximum allowable. This modeling aspect has been addressed in the Lee and Law study by postulating the formation of a bubble inside the slurry droplet. However, the dynamic equilibrium conditions within the droplet interior and the gas phase have not been considered. The present work incorporates these equilibrium conditions, essential to the physics of the problem of the liquid fuel vaporization. Another important aspect in the modeling of slurry droplets that has yet to be addressed is the effect of gas-phase convection

on the vaporization rates and its subsequent burning process. Also, earlier studies have employed a lumped capacity formulation which assumes that the slurry droplet has a spatially uniform temperature, thus implying infinite thermal conductivity of the liquid and metal. Although, this may be a reasonable limit for the metal, it is certainly inappropriate for the liquid fuel [88]. This chapter includes the effects associated with gas-phase convection, finite conductivity of the liquid, and the liquid surface tension.

## 4.2 Analysis

The configuration studied is a slurry droplet in which many fine metal particles are initially uniformly dispersed in a liquid hydrocarbon carrier, as shown in Figure 4.1. The droplet of initially known metal and liquid mass fractions is treated

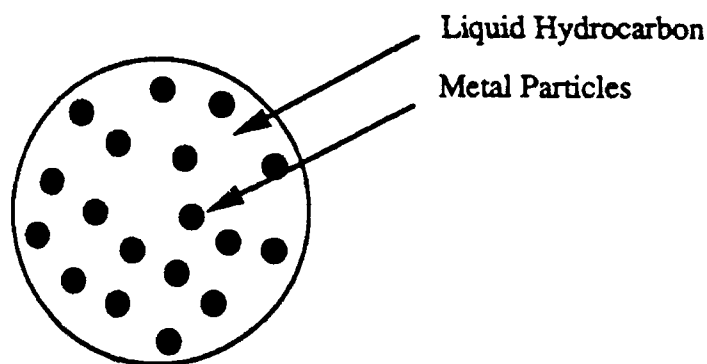


Figure 4.1: Slurry droplet with fine metal particles.

as a spherical droplet of space- and time-varying average properties. When the slurry droplets are exposed to a hot oxidizing environment, the liquid fuel vaporizes and burns, leaving behind a dry metal agglomerate. The metal then heats to the melting point of the aluminum (933.1 K). During the phase change, because of the formation of a thin oxide coating, the particle shape remains spherical, and continued heating causes further temperature rise of the metal until the oxide melts (2315 K), at which point ignition is presumed to occur (see Chapter 2).

### 4.2.1 Droplet Dynamics

Consider a slurry droplet of radius  $r_l$  consisting of  $N$  metal spheres of radius  $r_m$  and density  $\rho_m$  (Figure 4.1). Then, the metal volume and mass fractions are given by

$$\phi_m = \frac{\frac{4}{3}\pi r_m^3 N}{\frac{4}{3}\pi r_l^3} = \frac{N}{(r_l/r_m)^3} \quad (4.1)$$

$$Y_m = \frac{1}{1 + \left(\frac{1}{\phi_m} - 1\right) \frac{\rho_l}{\rho_m}} \quad (4.2)$$

Following Abramzon and Sirignano [2], we consider the gas flow to be one-dimensional and the initial droplet velocity parallel to the gas flow direction. For the surface regression stage, the drop motion and radius reduction are governed by the following equations:

$$\frac{dX}{dt} = U_l \quad (4.3)$$

$$\frac{dU_l}{dt} = \frac{3 \bar{\mu}_\infty (U_\infty - U_l)}{16 \rho_l r_l^2} Re C_D \frac{1 - Y_m}{1 - \phi_m} \quad (4.4)$$

$$Re = \frac{2\rho_\infty |U_\infty - U_l| r_l}{\bar{\mu}_\infty} \quad (4.5)$$

$$C_D = \frac{24}{Re} \left\{ 1 + \frac{Re^{2/3}}{6} \right\} \quad (4.6)$$

It has been shown [106] that the drag coefficient for evaporating droplets may be approximated by the standard drag curve provided the gas viscosity is evaluated at some reference temperature and fuel concentration:

$$T_{ref} = T_s + A_r(T_\infty - T_s) \quad (4.7)$$

$$Y_{ref} = Y_{F_s} + A_r(Y_{F_\infty} - Y_{F_s}) \quad (4.8)$$

where  $A_r = 1/3$  for the "one-third" averaging rule.

### 4.2.2 Liquid-Phase Analysis

Here, the metal slurry is conceptualized as consisting of a suspension of small metal particles in a spherical liquid droplet (Figure 4.1). In this case, the property variations (in space and time) results from varying temperature and composition of the slurry droplet as it heats and liquid fuel vaporizes. Several studies are available to predict thermal conductivity of a solid-liquid mixture. We use the general mixture rule from Nielsen [64]:

$$\frac{k_{mix}}{k_l} = \frac{1 + AB\phi_m}{1 - B\psi\phi_m} \quad (4.9)$$

where  $A$  is a constant which depends upon shape of the solid particles, state of agglomeration, nature of the interface, etc. It is related to the generalized Einstein coefficient  $k_E$  by

$$A = k_E - 1 \quad (4.10)$$

In our case, we take  $k_E = 3$  ( $A = 2$ ) [64]. The constant  $B$  is given by

$$B = \frac{k_m/k_l - 1}{k_m/k_l + A} \quad (4.11)$$

The reduced concentration term  $\psi$  is approximated by

$$\psi \approx 1 + \frac{1 - \phi_{max}}{\phi_{max}^2} \phi_m \quad (4.12)$$

where  $\phi_m$  is the metal volume fraction and  $\phi_{max}$  the maximum metal volume fraction. Geometrical considerations show that, for spherical particles,  $0.5236 \leq \phi_{max} \leq 0.7405$ , depending upon type of the packing. There is some experimental evidence that  $\phi_{max} \approx 0.54$  (Lee and Law [55] and Cho et al. [19]), which corresponds to most open packing. The theoretical value of  $\pi/6$  is used here. A plot of  $k_{mix}/k_l$  vs  $\phi_m$  is given in Figure 4.2.

Figure 4.3(a) shows the vaporization sequence of the slurry droplet. Stage I is characterized by surface regression; here, the vaporization proceeds in a manner similar to that for pure liquid droplets (with modified droplet properties). The onset of shell formation (Stage II) is given by the appearance of a thin shell of solid particles forming on the droplet surface. The manner of further vaporization depends upon the permeability and the strength of the shell. This is discussed in some detail under Stage II. Further vaporization causes an increase in the shell thickness and formation

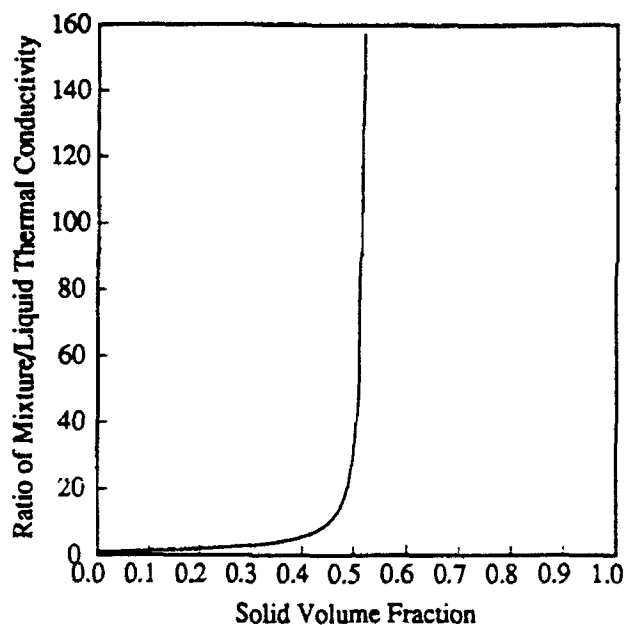


Figure 4.2: Thermal conductivity of the solid-liquid mixture vs. solid volume fraction.

of a bubble in the interior of droplet, whose diameter increases with time. When the shell thickness is at the maximum value, the drying of the pores starts (Stage III). Stage IV involves the dry agglomerate heating, which begins when all the liquid has evaporated. Stage V, is the metal coalescence stage, and is characterized by the coalescence of the individual particles into a single molten droplet.

Mass conservation of liquid implies that an interior bubble of saturated vapor (or vapor plus gas) must form for constant-radius liquid depletion to occur from the interior core through the porous shell. Earlier studies, e.g., Antaki and Williams [6, 7] and Antaki [5], did not take the bubble formation into account, thus implicitly assuming a uniform metal particle density inside the slurry droplet. This implies that the initial solid loading be same as maximum allowable. Cho's [19] model would violate liquid mass conservation. The shell-bubble formulation is proposed in the work of Lee and Law [55]. However, the static and thermodynamic equilibrium at the liquid-bubble interface requires some further thought. The temperature in the liquid core is lower than at the gas-liquid interface. Hence, the saturated vapor pressure in the bubble must be lower than the environmental pressure. Thus, the *static equilibrium cannot be maintained*, and the vapor in the bubble will have to condense back into the liquid phase.

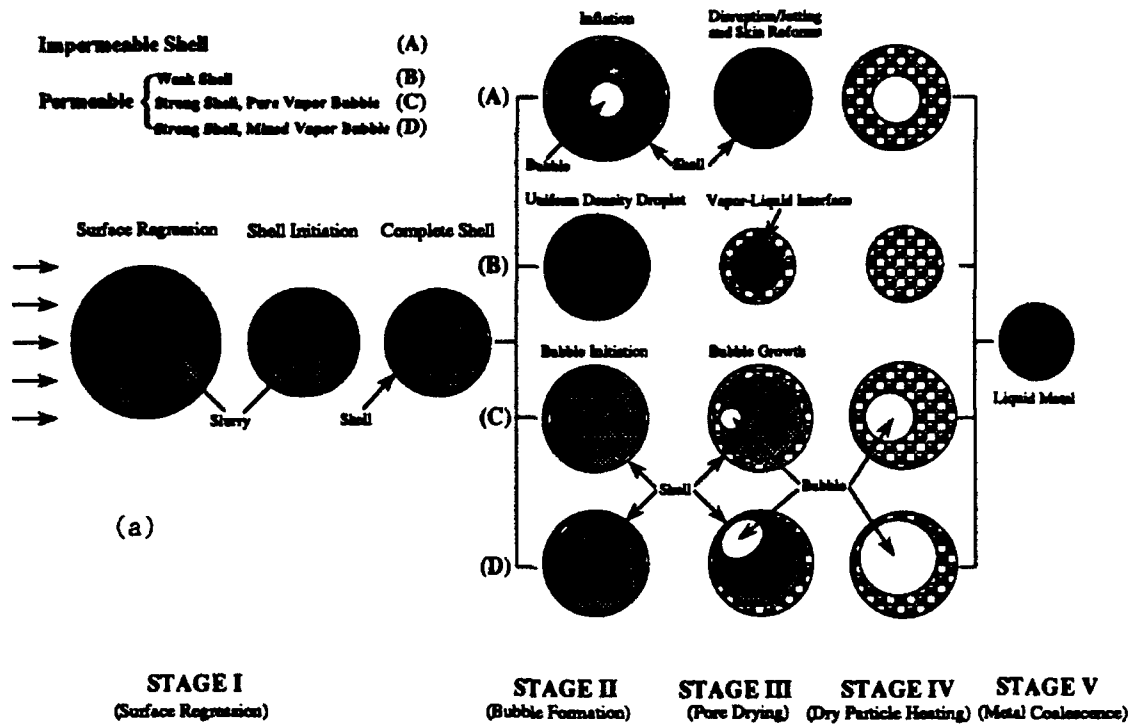


Figure 4.3: (a) Schematic of the life history of the slurry droplets. (b) Schematic of the wick structure of the shell.

Investigating the conditions under which a vapor bubble might exist in the core, we have to examine the structure of the shell. The hydrocarbon is a wetting liquid. As noted earlier, the shell contains a known ( $\phi_{max} = \pi/6$ ) fraction of the metal. Hence, about 48% of the volume is void. The characteristic radius associated with these micropores is about the same order as the radius of the solid particles forming the shell (Marcus [56] suggests that the radius of curvature  $r_c \approx 0.41 r_m$  for randomly packed sphere beds). Consider a wick structure in the shell, as shown in Figure 4.3(b). To make a rough argument, assume that the radius of curvature of the meniscus at the gas-liquid interface is about the same as the pore radius. In the case of quasi-static equilibrium,

$$p_l = p_\infty - \frac{2\sigma_o}{r_c} \quad (4.13)$$

$$p_b = p_l + \frac{2\sigma_i}{r_b} = p_\infty - \left\{ \frac{2\sigma_o}{r_c} - \frac{2\sigma_i}{r_b} \right\} \quad (4.14)$$

where  $\sigma_o$  and  $\sigma_i$  denote the surface tension coefficient at the outer and inner gas-liquid interfaces respectively, and  $p_l$ ,  $p_b$ , and  $p_\infty$  are the pressures in the liquid, bubble, and ambient, respectively.

The bubble radius  $r_b$  is at least an order of magnitude larger than the pore radius, and, hence, the second term in the brackets may be neglected in comparison to the first. Hence, if the "stress" (defined as  $2\sigma_o/r_c$ ) is large, the capillarity might cause the pressure in the vapor bubble to be maintained at a higher value than the saturation pressure. The situation is depicted in the Figure 4.4, for *n*-octane fuel. The figure shows the total pressure in the vapor bubble, consisting of vapor pressure from the Clausius-Clapeyron equation and the stress, as a function of the temperature at the outer gas-liquid interface, for different radii of curvature. It is clear that the surface tension has a large role in the quasi-static equilibrium of the vapor bubble. Hence, in the case of a wick shell, it is possible to maintain a saturation temperature at the bubble-liquid interface at a value lower than the saturation temperature at the liquid-outer gas interface. In general, the pressure difference may not satisfy Eq. (4.14) causing, therefore, an instability of the bubble in the center of the droplet. The situation is further clarified, later [see Eq. (4.23)].

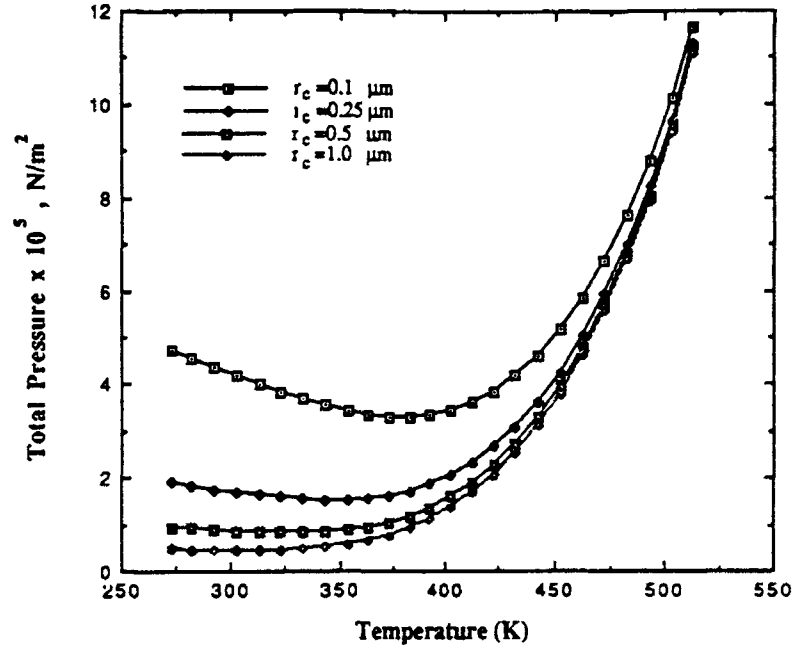


Figure 4.4: Total pressure, from static and thermodynamic equilibrium.

### 4.2.3 Stage I: Surface Regression

The regression history of the slurry diameter due to vaporization is dependent on the initial solid loading. For higher initial solid loadings (with solid volume fractions close to  $\phi_{max}$ ), the slurry diameter may not regress at all. We consider the more general case of low initial solid loading.

For simplicity, we assume (Lee and Law [55]) that the porous shell near the vaporizing surface contains the solid particles that are increasingly concentrated by the regressing liquid surface that results from vaporization. The shell thickness  $\delta$  may be found by using solid mass conservation

$$\frac{4}{3}\pi r_i^3 \phi_{m_i} = \frac{4}{3}\pi \{r_i^3 - (r_i - \delta)^3\} \phi_{max} + \frac{4}{3}\pi (r_i - \delta)^3 \phi_m, \quad (4.15)$$

where  $\phi_{m_i}$  and  $\phi_{max}$  denote the initial and maximum solid volume fractions.

To model the heat transfer in the liquid phase, we take the configuration to be spherically symmetric. In this case, the non-dimensional form of the energy equation is [with  $\eta = r/r_i(t)$ ,  $\tau = \alpha_{mix,i}t/r_{l,i}^2$ ,  $r_l' = r_l(t)/r_{l,i}$ ]

$$r_l'^2 \frac{\partial Z}{\partial \tau} - \left\{ \frac{1}{2} \eta \frac{dr_l'^2}{d\tau} - \frac{C_{p,m} v_m r_l Y_m}{C_{p,mix} \alpha_{mix,i}} \right\} \frac{\partial Z}{\partial \eta} = \frac{(\rho C_p)_{mix,i}}{(\rho C_p)_{mix}} \frac{1}{\eta^2} \frac{\partial}{\partial \eta} \left\{ \frac{k_{mix}}{k_{mix,i}} \eta^2 \frac{\partial Z}{\partial \eta} \right\} \quad (4.16)$$

where the average density and specific heat at any radial location of the slurry droplet can be obtained by mass averaging:

$$\rho_{mix} = \left\{ \frac{Y_m}{\rho_m} + \frac{1 - Y_m}{\rho_l} \right\}^{-1}, \quad C_{p_{mix}} = Y_m C_{p_m} + (1 - Y_m) C_{p_l} \quad (4.17)$$

The velocity of the metal particles  $v_m$  is zero in the droplet core and, in the shell, is given by  $-d\delta/dt$ . The initial and boundary conditions are

$$\text{at } \tau = 0, \quad Z = 0 \quad (4.18)$$

$$\text{at } \eta = 0, \quad \frac{\partial Z}{\partial \eta} = 0 \quad (4.19)$$

$$\text{at } \eta = 1, \quad \frac{\partial Z}{\partial \eta} = \frac{\dot{q}_l}{4\pi k_{mix} r_l T_i} \quad (4.20)$$

The droplet radius reduction is governed by

$$\frac{dr_l}{dt} = -\dot{m}_l / (4\pi \rho_l r_l^2) \quad (4.21)$$

The vaporization progresses according to Eq. (4.16) and equations under the heading Gas-Phase Analysis, until a solid shell forms on the droplet surface. There is experimental evidence (Charlesworth and Marshall [17]) that the shell formation begins from the front stagnation point, and proceeds rapidly towards the rear stagnation point [see Figure 4.3(a)]. A critical stage is reached when the solids in the outermost layer cannot be compacted anymore. On physical grounds, the shell formation should begin as soon as the shell porosity reaches a critical value. Lee and Law [55] characterize the onset of this stage by a critical packing and a critical shell thickness  $\delta_c$ , which is taken to be three times the solid particle diameter. The effect of the internal circulation on the shell formation of a vaporizing slurry droplet is not well understood. The study of Chung [20] concludes that for high Reynolds number ( $Re_r$  or  $Re_\theta \sim 100$ ) cases, the Basset plus curvature forces are stronger than pressure force, and the particle moves towards the droplet surface. Some similar observations are reported in the experimental work of Charlesworth and Marshall [17]. The characteristic time for stabilization of the internal vortex,  $t_{hydr}$ , depends upon the liquid Reynolds number. At  $Re \leq 1$  (viscous regime), this may be estimated at  $t_{hydr} \sim r_s^2/\nu_l$ . At high liquid Reynolds number,  $Re \gg 1$ , the vorticity disturbance transfer from the surface to the interior is convection dominated and  $t_{hydr} \sim r_s/U_s \approx r_s^2/\nu_l Re_l$ . This is about one to two orders of magnitude less than the droplet lifetime. The time taken for shell

formation is comparable to the lifetime. Hence, the internal circulation may play a dominant role in the onset of the shell. Such a behavior may be especially important for smaller droplets. However, this effect is neglected in the present study. We assume that the shell is formed by the radially inward swept solids as the liquid vaporizes. Following Lee and Law, we assume that the critical solid volume fraction corresponds to that for the most open packing (i.e.,  $\phi_{max} = \pi/6$ ) and the corresponding shell thickness is three times the solid particle diameter.

#### 4.2.4 Stage II: Liquid Vaporization through the Shell

The phenomenon during this stage are dependent on the ambient pressure and temperature, the type of the liquid fuel, and the particle size. The manner of liquid vaporization depends upon the permeability, the effective pore radius, the strength of the shell and, depending upon these, several models exist [refer to Figure 4.3(a)]:

##### (A) Impervious Shell, Any Ambient Pressure:

High-molecular-weight organic dispersing agents are often added to liquid fuel to stabilize the slurries. These additives may pyrolyze as the dry outer surface of the shell gets heated to temperatures larger than the liquid fuel boiling point, thus making the shell impervious [19, 112]. Also, the pore spaces between the metal particles could be physically filled by addition of submicron particles, e.g.,  $\sim 0.35 \mu\text{m}$  carbon particles in a slurry droplet consisting of  $4 \mu\text{m}$  aluminum particles, as in the work of Wong and Turns[112]. If the shell is impervious to the gases and liquid flow, then the droplet heating shall result in nucleation inside the shell. Further heating shall cause additional internal vaporization, raising the pressure inside the droplet. This situation is likely to result in:

##### (i) Swelling and Jetting:

If the shell is plastic, it is going to inflate due to internal vaporization and pressure buildup. This stretching of the shell may increase the permeability such that jetting of the liquid fuel (and solid particles) occurs to relieve the internal pressure. The phenomena of swelling and jetting

have been experimentally observed in several situations [7, 55]. Further, Wong and Turns [112] report formation of secondary spheres attached to the primary slurry droplet.

**(ii) Disruption/Fracture:**

If the shell remains impervious, then disruption is going to occur. This case has been observed by many researchers [19, 55, 95, 96, 111, 112].

**(B) Permeable Shell, Low Buckling Resistance:**

The shell formed on the droplet surface has a certain buckling resistance, which depends on its mechanical properties. If the buckling resistance is lower than the "stress", the shell will collapse, and the result will be uniform density vaporization without any bubble. In such a case, the surface regression occurs until the metal packing inside the droplet reaches the critical value. The remaining liquid will get vaporized by the vapor-liquid interface retreating into the porous sphere interior. This scenario is employed by Antaki and Williams [6]. Of the numerous experimental studies available, this case does not seem to be generally observed. It is remarked here that Lee and Law [55] and Takahashi et al. [96] present evidence of a recessed pit on the outer surface of the shell. Lee and Law speculate this phenomenon to be coupled to the flow field since the flat portion of the droplet is always situated in the rearward stagnation region. However, this is probably a result of stress, as explained above, and the shell wall caves in near the rear stagnation region where the shell is weakest as it rigidizes last there. Usually, the shell buckling resistance is larger than the stress, and this situation is considered in the next two cases.

**(C) Permeable Shell, Low Ambient Pressure:**

In this model, the ambient pressure and the stress due to the surface tension on the gas-liquid interface are of the same order of magnitude. So, a liquid fuel vapor bubble can be supported inside the slurry droplet, and this enables conservation of mass in the event of vaporization from a sphere of constant radius. This case is termed the shell-bubble case. This nucleation will start on the inside of the shell from the front stagnation point, where the heat-transfer rate is maximum. Marangoni convection, i.e., thermocapillary force can cause the vapor bubble to be attracted to the warmer temperature [104]. Thus, the bubble may remain attached to the forward stagnation point. Subsequent

vaporization will cause the bubble to grow. Note that, in such a situation, the stress value could be constantly adjusting with the growth in the bubble radius. As noted earlier, this situation is generally unstable and unlikely to exist.

**(D) Permeable Shell, High Ambient Pressure:**

The largest value of the stress is limited by the largest available statistical pore size and the liquid surface tension. If the stress exceeds "bubble point", then blow through occurs and stress gets fixed at the bubble point value. In such a case, the surrounding gas (mostly fuel vapor and nitrogen) enters the shell from the largest pore, and the resulting bubble shall consist of fuel vapor and the gas. The bubble will be located asymmetrically to the droplet center, as shown in the Figure 4.3(a). Scanning electron microscope pictures by Lee and Law [55] and Cho et al. [19] support this observation. This situation is likely to occur when the ambient pressure is relatively higher than the bubble point, as would be expected in realistic combustors.

Depending on the slurry contents, at various times, it is quite possible that a combination of above situations exists. In this study, we use the shell-bubble model to describe the slurry droplet history. Researchers do not agree about whether the porous shell formed can be dry or wet with the liquid carrier, and that is a topic of active research. Lee and Law [55] consider both limiting cases, and based on their analytical procedure and experimental results, reach the conclusion that wet shell gasification is more realistic. The dry shell scenario is shown to cause the maximum porosity of the shell to be 0.68, implying a  $\phi_{max} = 0.32$ , which is well outside the range  $0.5236 \leq \phi_{max} \leq 0.7405$ , and thus leading to physically unrealistic (very loose) packing of the solid particles. It is noted here that their formulation has three potential sources of error:

- (1) The internal vaporization rate, i.e., the mass of liquid going into the vaporized bubble, is neglected.
- (2) The burning rate is given by the classical expression [47]

$$\dot{m}_l = \frac{\pi}{2} \rho_l r_{lc} K \quad (4.22)$$

where  $K$  is the burning constant. The use of  $r_{lc}$  in Eq. 4.22 is justified in the wet shell scenario. However, in the dry shell scenario, vaporization occurs at the liquid radius,  $r_l < r_{lc}$ , which should be employed to determine the burning rate. This is also true in the model of Cho et al. [19].

(3) The effect of capillary force and the pressure balance has not been satisfied.

In this study, we will consider the more general permeable shell case [(D) in Figure 4.3(a)] with high ambient pressure, with the gas bubble consisting of fuel vapor and ambient gas attached to the droplet surface. In such a case, to maintain quasi-static equilibrium, it follows from Eq. (4.14)

$$p_b = p_v + p_g = p_\infty - \left\{ \frac{2\sigma_o}{r_c} - \frac{2\sigma_i}{r_b} \right\} \quad (4.23)$$

where  $p_v$  and  $p_g$  denote the partial pressures of the fuel vapor and the ambient gas (inert) in the bubble. If the bubble is not attached to the surface, that implies  $p_g = 0$ , which is the case [C] in Figure 4.3(a).

In view of our objective of developing a simplified model, we assume that, only for the purpose of heat transport calculations, the bubble is placed spherically symmetric with respect to the droplet center (see Figure 4.5). Thus, we can make a one-dimensional calculation inside the droplet to determine the temperature profile.

To obtain the shell thickness  $\delta$ , usage of the solid mass conservation yields

$$\frac{4}{3}\pi r_i^3 \phi_{m_i} = \frac{4}{3}\pi \{r_i^3 - (r_{lc} - \delta)^3\} \phi_{max} + \frac{4}{3}\pi \{(r_{lc} - \delta)^3 - r_b^3\} \phi_m, \quad (4.24)$$

where  $r_{lc}$  is the outer radius of the slurry droplet.

In the one-dimensional heat diffusion equation, by making the following transformations:

$$\tau = \frac{\alpha_{mix} t}{r_i^2} ; \quad \tau \geq 0 \quad (4.25)$$

$$\eta = \frac{r - r_b(t)}{r_i(t) - r_b(t)} ; \quad 0 \leq \eta \leq 1 \quad (4.26)$$

$$Z = \frac{T - T_i}{T_i}; \quad r_i'(t) = r_i(t)/r_i; \quad r_b'(t) = r_b(t)/r_i; \quad \xi(t) = \frac{r_b(t)}{r_i(t) - r_b(t)} \quad (4.27)$$

we obtain the transformed energy equation with fixed boundaries:

$$\begin{aligned} (r_i' - r_b')^2 \frac{\partial Z}{\partial \tau} + \left\{ \frac{a(r)(r_i - r_b)}{\alpha_{mix}} - \eta(r_i' - r_b') \frac{dr_i'}{d\tau} - (1 - \eta)(r_i' - r_b') \frac{dr_b'}{d\tau} \right\} \frac{\partial Z}{\partial \eta} \\ = \frac{(\rho C_p)_{mix}}{(\rho C_p)_{mix}} \frac{1}{(\eta + \xi)^2} \frac{\partial}{\partial \eta} \left\{ \frac{k_{mix}}{k_{mix}} (\eta + \xi)^2 \frac{\partial Z}{\partial \eta} \right\} \end{aligned} \quad (4.28)$$

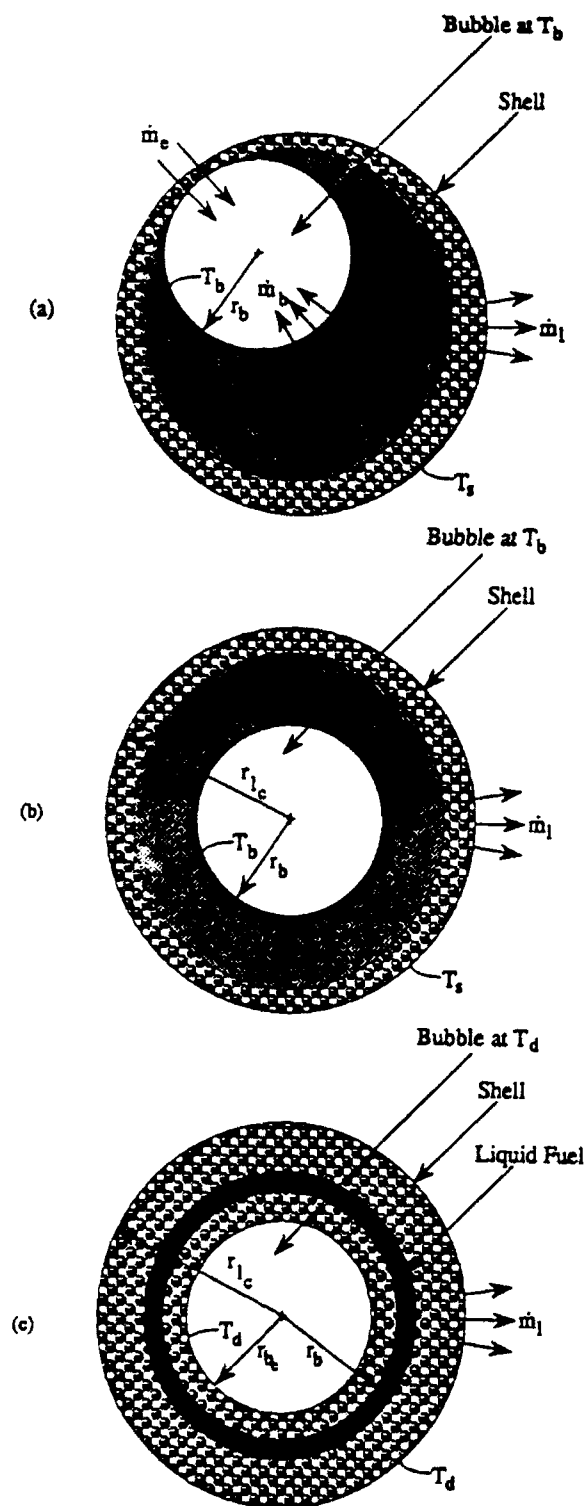


Figure 4.5: Schematic of vaporization from Stages II and III. (a) shows the bubble attached to the surface, (b) shows the model assumption, and (c) shows pore drying.

In the preceding equation, the thermal diffusion resulting from unequal species velocities  $v_m$  and  $v_l$  (i.e., interdiffusion and Dufour effects) is neglected. The function  $a(r)$  is given by

$$a(r) = \begin{cases} \left(\frac{r_b}{r}\right)^2 \frac{dr_b}{dt} & \text{for } r_b < r < (r_l - \delta) \\ \left(\frac{r_b}{r}\right)^2 \frac{(\rho C_p)_l}{(\rho C_p)_{mix}} \frac{1 - Y_m}{1 - \phi_{max}} \frac{dr_b}{dt} & \text{for } (r_l - \delta) < r < r_{lc} \end{cases} \quad (4.29)$$

The preceding equation with  $r'_b(t) = 0$  and  $dr'_b/d\tau = 0$  recovers the energy equation for the surface regression, Stage I, Eq. (4.16). During Stage II, the droplet outer radius remains constant  $r'_l(t) = r_{lc}/r_{li}$  and  $dr'_l/d\tau = 0$ . The initial and boundary conditions for Eq. (4.28) are given by

$$\text{at } \tau = 0, \quad Z = 0 \quad (4.30)$$

$$\text{at } \eta = 0, \quad Z = T_b(t)/T_i \quad (4.31)$$

$$\text{at } \eta = 1, \quad \frac{\partial Z}{\partial \eta} = \frac{\{r_{lc} - r_b(t)\} \dot{q}_l}{4\pi k_{mix} r_{lc}^2 T_i} \quad (4.32)$$

We assume a perfectly mixed bubble, i.e., the incoming mixture mixes perfectly to a uniform fuel mass fraction  $Y_{F_b}$ , and temperature  $T_b$ . The gas thermal diffusivity is about two orders of magnitude smaller than the liquid thermal diffusivity. The incoming mass flow rate into the bubble ( $\dot{m}_e$ ), the bubble vaporization/condensation rate ( $\dot{m}_b$ ), and the bubble volume ( $V_b$ ) are determined by expressing the bubble conservation equations as

$$\dot{m}_b + Y_{F_b} \dot{m}_e = \frac{d}{dt} (\rho_b Y_{F_b} V_b) \quad (4.33)$$

$$\dot{m}_b + \dot{m}_e = \frac{d}{dt} (\rho_b V_b) \quad (4.34)$$

$$\dot{m}_l + \dot{m}_b = \rho_l \frac{dV_b}{dt} \quad (4.35)$$

The above three equations, along with the net mass flux Eq. (4.57), are solved for the four unknowns:  $\dot{m}_l$ ,  $\dot{m}_e$ ,  $\dot{m}_b$  and  $V_b$ . The bubble density  $\rho_b$  is determined from an equation of state:

$$\rho_b = p_b \bar{M} / \mathcal{R}_u T_b \quad (4.36)$$

and the fuel mass fraction is determined as a function of bubble temperature  $T_b$  from the Clausius-Clapeyron relation.

The bubble temperature is found by making an energy balance:

$$(mC_v)_b \frac{dT_b}{dt} = \dot{m}_e C_{p_e} (T_s - T_b) + 4\pi r_b^2 k_{mix} \left. \frac{dT}{dr} \right|_{r=r_b} - \dot{m}_b L(T_b) \quad (4.37)$$

In the Lee and Law [55] model,  $\dot{m}_b$  and  $\dot{m}_e$  are not considered. In the earlier studies (e.g., Antaki [5, 6]) the bubble formation is not considered, which is contrary to experimental evidence since hollow shells have been found after vaporization for slurry droplets without heavy loading. To model the impervious case (A) and the collapsed shell case (B), we can put the external and incoming flux rates to zero, respectively.

#### 4.2.5 Stage III: Pore Drying

This stage begins when the shell thickness reaches a maximum value and all the solid particles in the drop are at maximum compactness. Depending on the thickness of the shell, in general, there is still a substantial mass of liquid trapped in the pores of the agglomerate. The liquid vaporization continues to be described by the equations under Stage III. When the bubble radius reaches its maximum value, called  $r_{b_c}$  in Figure 4.5(c), the surface tension effect on the liquid-gas interface on the droplet surface and the liquid-bubble interface cancel. Hence, the bubble pressure is assumed to be the ambient pressure and the external gas inflow rate  $\dot{m}_e$  is assumed equal to zero. In this section, we employ an expanding bubble-regressing liquid model. The bubble is allowed to expand due to the effects of temperature increase, which changes gas density and the fuel mass fraction equilibrium inside the bubble. The conservation equations are given by

$$\dot{m}_b = \frac{d}{dt}(\rho_b Y_{F_b} V_b) = \frac{d}{dt}(\rho_b V_b) \quad (4.38)$$

where the bubble volume is given by

$$V_b = \frac{4}{3}\pi r_{b_c}^3 + \frac{4}{3}\pi(r_b^3 - r_{b_c}^3)(1 - \phi_{max}) \quad (4.39)$$

The second part of the equation implies that the mass of the non-fuel species remains constant during the pore-drying stage. Since the liquid surface is regressing, the

external vaporization rate and the liquid radius are given by

$$\dot{m}_l = 2\pi\bar{\rho}_g\bar{D}_g r_l Sh^* \ln(1 + B_M) \quad \{\text{see Eq. (4.57)}\} \quad (4.40)$$

$$\dot{m}_l + \dot{m}_b = -\rho_l \frac{dV_l}{dt} = -\rho_l \frac{d}{dt} \left\{ \frac{4}{3}\pi(r_l^3 - r_b^3)(1 - \phi_{max}) \right\} \quad (4.41)$$

and the volume of the dry pores on the outside of the wet pores is assumed to be equal to the volume of the dry pores on the inside of the wet pores. The thermal conductivity of the agglomerate is high; hence, the energy conservation inside the droplet is given by (taking bubble temperature  $T_b =$  surface temperature  $T_s = T_d$ ):

$$\dot{Q}_l - \dot{m}_b L(T_d) = (mC_v)_d \frac{dT_d}{dt} \quad (4.42)$$

The five equations in this section are solved for the five unknowns:  $\dot{m}_l$ ,  $\dot{m}_b$ ,  $V_b$ ,  $V_l$ , and  $T_d$ . The above formulation neglects any resistance to the flow of fuel vapor through the pores. The mean free path of n-octane vapors at 10 atm pressure is estimated to be about 0.04  $\mu\text{m}$ , which is much less than the mean pore size of about 1  $\mu\text{m}$ , thus justifying the neglect of pore resistance.

We have made calculations with an expanding bubble-constant outer liquid radius model, where the bubble is allowed to grow into the inside pores and the outer surface of the droplet is kept wetted with liquid. This results in about 10% reduction in the liquid fuel vaporization time. However, the expanding bubble-regressing liquid formulation is preferred over the expanding bubble-constant liquid model.

### 4.3 Gas-Phase Analysis

The gas-phase conservation equations determine the fuel vaporization and the bubble inflow rates and the heat penetrating into the droplet interior. In this study, we will modify the droplet vaporization model of Abramzon and Sirignano [2] to account for the gas inflow in the bubble corresponding to the vaporization of liquid fuel during Stages II and III. The model assumes quasi-steady gas-phase heat and mass transfer, no pressure drop, and the thermal properties (evaluated at reference conditions) are treated as constant. To include the effect of the convective transport 'film theory' is used. The formulation is briefly explained as follows.

The molar and mass fuel vapor fractions at the droplet surface are given by

$$x_{F_s} = P_{F_s}/P \quad (4.43)$$

$$Y_{F_s} = x_{F_s} M_F / \sum_i x_i M_i \quad (4.44)$$

where  $P_{F_s}$  is the fuel vapor saturated pressure, obtained from Clausius-Clapeyron relation.

The Nusselt and Sherwood numbers for a non-vaporizing sphere are [21]

$$Nu_0 = 1 + (1 + RePr)^{1/3} f(Re) \quad (4.45)$$

$$Sh_0 = 1 + (1 + ReSc)^{1/3} f(Re) \quad (4.46)$$

where  $f(Re) = 1$  at  $Re \leq 1$  and  $f(Re) = Re^{0.077}$  at  $1 < Re \leq 400$ . The convection-augmented external radii of the "film" around the droplet of radius  $r_l$  are given by

$$r_{f,T} = r_l Nu^* / (Nu^* - 2) \quad (4.47)$$

$$r_{f,M} = r_l Sh^* / (Sh^* - 2) \quad (4.48)$$

To account for Stefan flow due to droplet regression, the modified Nusselt and Sherwood numbers are calculated as

$$Nu^* = 2 + (Nu_0 - 2)/F_T \quad (4.49)$$

$$Sh^* = 2 + (Sh_0 - 2)/F_M \quad (4.50)$$

where the correction factors are given by [2]

$$F_T = (1 + B_T)^{0.7} \frac{\ln(1 + B_T)}{B_T} \quad (4.51)$$

and  $F_M$  is given by an equation of equivalent structure with  $B_T$  replaced by  $B_M$ .

Consider a spherical control volume of radius  $r$  ( $r_l < r < r_f$ ). Let  $n_1$  and  $n_2$  denote the mass fluxes [g/cm<sup>2</sup>-s] of fuel and air flowing radially outwards. The fuel vaporization rate  $\dot{m}_l$  and the bubble inflow rate  $\dot{m}_i$  are related to  $n_1$  and  $n_2$  by

$$n_{1_s} = \frac{\dot{m}_l - Y_{F_s} \dot{m}_e}{4\pi r_l^2}, \quad n_{2_s} = \frac{-(1 - Y_{F_s}) \dot{m}_e}{4\pi r_l^2} \quad (4.52)$$

Considering quasi-steady mass transfer, we have

$$r^2 n_1 = r_1^2 n_{1s}, \quad r^2 n_2 = r_1^2 n_{2s} \quad (4.53)$$

Note that for an all-liquid droplet, and also during Stage I vaporization from a slurry droplet,  $n_{2s} = 0$ . Using Fick's law, we get

$$-r^2 \rho_g \mathcal{D}_g \frac{dY_F}{dr} + Y_F r_1^2 (n_{1s} + n_{2s}) = r_1^2 n_{2s} \quad (4.54)$$

Making the substitutions:  $\eta = r_1/r$ ,  $\omega = (b_M Y_F - 1)/(b_M Y_{F_s} - 1)$ , and defining a mass and a heat correction factor to the transfer numbers as

$$b_M = 1 + \frac{n_{2s}}{n_{1s}}, \quad b_T = 1 + \frac{n_{2s} C_{p_g}}{n_{1s} C_{p_F}} \quad (4.55)$$

we obtain

$$\frac{\rho \mathcal{D}}{n_{1s} r_1 b_M} \frac{d\omega}{d\eta} + \omega = 0 \quad (4.56)$$

Integrating the above from  $r = r_1$ ,  $\omega = 1$ ; to  $r = r_f$ ,  $\omega = (b_M Y_{F_\infty} - 1)/(b_M Y_{F_s} - 1)$ , and using Eqs. (4.53), we have:

$$\dot{m}_l - \dot{m}_e = 2\pi \bar{\rho}_g \bar{\mathcal{D}}_g r_1 Sh^* \ln(1 + B_M) \quad (4.57)$$

The mass and heat transfer numbers are calculated as

$$B_M = \frac{Y_{F_s} - Y_{F_\infty}}{1/b_M - Y_{F_s}} \quad (4.58)$$

$$B_T = \frac{\bar{C}_{p_F} b_T (T_\infty - T_s)}{L(T_s) + \dot{Q}_l/\dot{m}_l} \quad (4.59)$$

The heat transfer number is obtained from considerations of energy conservation, and it can be shown that

$$B_T = (1 + B_M)^\varphi - 1 \quad (4.60)$$

The solution procedure is iterative until convergence is reached on  $B_T$  [2]. The parameter  $\varphi$  is given by

$$\varphi = \frac{\bar{C}_{p_F} Sh^*}{\bar{C}_{p_g} Nu^* Le} \frac{1}{b_M} \quad (4.61)$$

$$Le = \bar{k}_g / (\bar{\rho}_g \bar{\mathcal{D}}_g \bar{C}_{p_g}) \quad (4.62)$$

Finally, the heat penetrating into the liquid droplet is given by

$$\dot{Q}_l = 4\pi r_1^2 n_{1s} \left\{ \frac{\bar{C}_{p_F} b_T (T_\infty - T_s)}{B_T} - L(T_s) \right\} \quad (4.63)$$

## 4.4 Results and Discussion

Calculations are performed for a slurry droplet composed of *n*-octane and aluminum particles. The initial droplet size is 50  $\mu\text{m}$  and the temperature is 300 K. The ambient pressure is 10 atm and the temperature is 1000 K. The initial droplet velocity is taken as 10 m/s and the gas velocity is 50 m/s, which gives an initial Reynolds number of about 300. Two sets of results are presented. In the first set, we have kept the initial solid volume fixed at 25%, while varying the radius of the metal particles (thus the total number of metal particles in each drop would be different). In the second set, we have kept the metal radius fixed and varied the initial metal volume fraction. Calculations are terminated when all of the liquid mass is evaporated from the droplet.

Figures 4.6 to 4.10 show the results for liquid vaporization from the slurry droplets initially containing 25% by volume (about 51% by weight) of aluminum particles. The ratios of particle radius to the initial droplet radius shown are 0.02, 0.04, and 0.10, which correspond to particle sizes of 1, 2, and 5  $\mu\text{m}$ , respectively. Figure 4.6 shows the droplet radius and the bubble radius, both normalized by the initial droplet radius. The two kinks in the curves signify transitions from the surface regression regime (Stage I) to the constant-radius vaporization (Stage II), and from Stage II to the pore-drying regime (Stage III). At first the droplet outer radius decreases, and this period is dominated by the initial transient heating of the droplet. The shell begins to form on the droplet surface. After maximum shell compactness is attained, the liquid surface regresses into the pores of the agglomerate, and droplet radius then represents the radius of the liquid surface. Figure 4.7 shows the shell thickness, normalized by the initial droplet radius, and the pressure inside the bubble. As the initial droplet radii and external conditions are same for all the droplets, the initial portions of the droplet sizes and shell thickness overlap. Depending on the metal particle radius (employing  $\delta_c = 6r_m$ ), the shell rigidizes later for the larger metal particles. The duration of the constant-radius vaporization is also dependent on the metal particle size. For the larger metal particle radius of 5  $\mu\text{m}$ , the critical bubble radius is small, and the time for constant-radius vaporization is very short. The bubble starts to grow as soon as the critical shell thickness is attained, with an initial fast rise turning into a slower growth rate later. The point at which the two curves

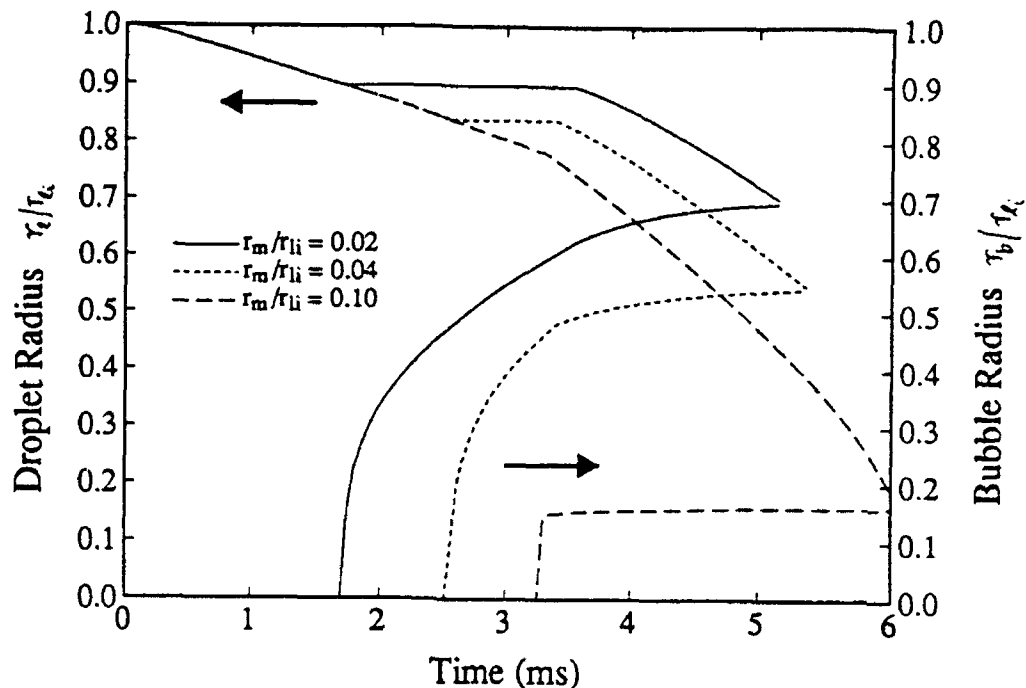


Figure 4.6: Droplet radius and bubble radius for different metal particle sizes and fixed initial metal volume fraction  $\phi_{m_i} = 0.25$ .

for the same metal particle radius meet is the calculation termination point, i.e., all the liquid mass has evaporated (see Figure 4.9). The shell thickness (in Figure 4.7) becomes constant, signifying the packing of all the solid particles in the shell. Figure 7 also shows the pressure inside the bubble. In time prior to the formation of the bubble, we show the pressure inside the liquid droplet. At the onset of the bubble, there is a singularity, for  $r_b \rightarrow 0$  in Eq. (4.23). This is the reason for a peak in the pressure curves at the bubble onset. When the shell reaches its maximum thickness, pore drying commences and, during this stage we have assumed the bubble pressure to be equal to ambient pressure. Figure 4.8 gives the droplet surface temperature and the bubble temperature for the three cases. Prior to the bubble formation, for bubble temperature we show the droplet center temperature. All the droplets are initially at 300 K, and transient heating occurs. The surface temperature quickly rises and asymptotically approaches the liquid boiling temperature at the prevalent pressure. Liquid and metal thermal inertia causes a delay in the rise of the center/bubble temperature. At the onset of the bubble, all the solids are in contact with each other, causing a rise in the mixture thermal conductivity, which results in faster heat diffusion across the droplet interior. This explains the small dip in the surface

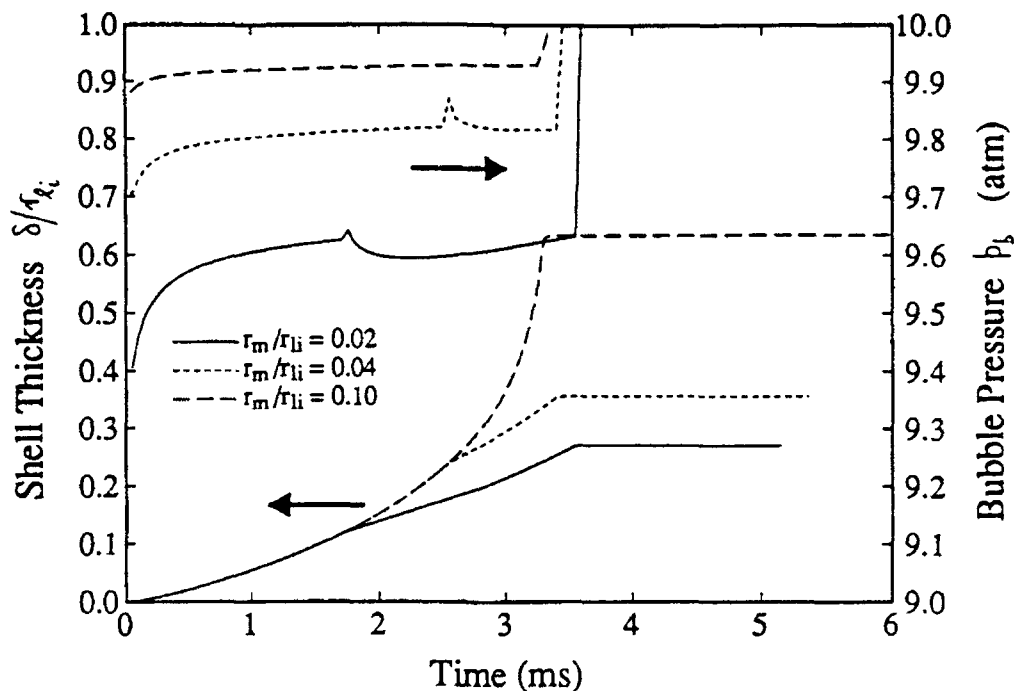


Figure 4.7: Shell thickness and bubble pressure for different metal particle sizes and fixed initial metal volume fraction  $\phi_{m_i} = 0.25$ .

temperature. The peak in the bubble temperature, at this time, is probably related to the peak in the bubble pressure through the equation of the state. During the pore-drying stage, the droplet temperature is assumed uniform, and the two curves coincide. Figure 4.9 shows the droplet vaporization rate, and the integrated liquid mass vaporized normalized by the initial mass of the liquid ( $\int \dot{m}_l dt / m_{l_i}$ ). The peak in the vaporization rate is caused by the consideration of the transient droplet heating, and the dip is a result of the dip in the surface temperature. Later, as the droplet temperature rises, so does the vaporization rate. The total mass vaporized is somewhat linear with time early during the droplet lifetime. This is also reported in the experimental observations of Lee and Law [55]. Figure 4.10 shows the bubble inflow rate and the bubble vaporization/condensation rate. These rates are small compared to the droplet vaporization rate, and ratio of these rates to the droplet vaporization rate is of the order of the ratio of bubble density to liquid density. It is interesting to note that although a fraction of the fuel vapor evaporated from the external surface of the droplet gets initially condensed in the bubble, at a later stage evaporation also occurs inside the bubble. The cumulative vaporized mass approximately balances the cumulative condensed mass.

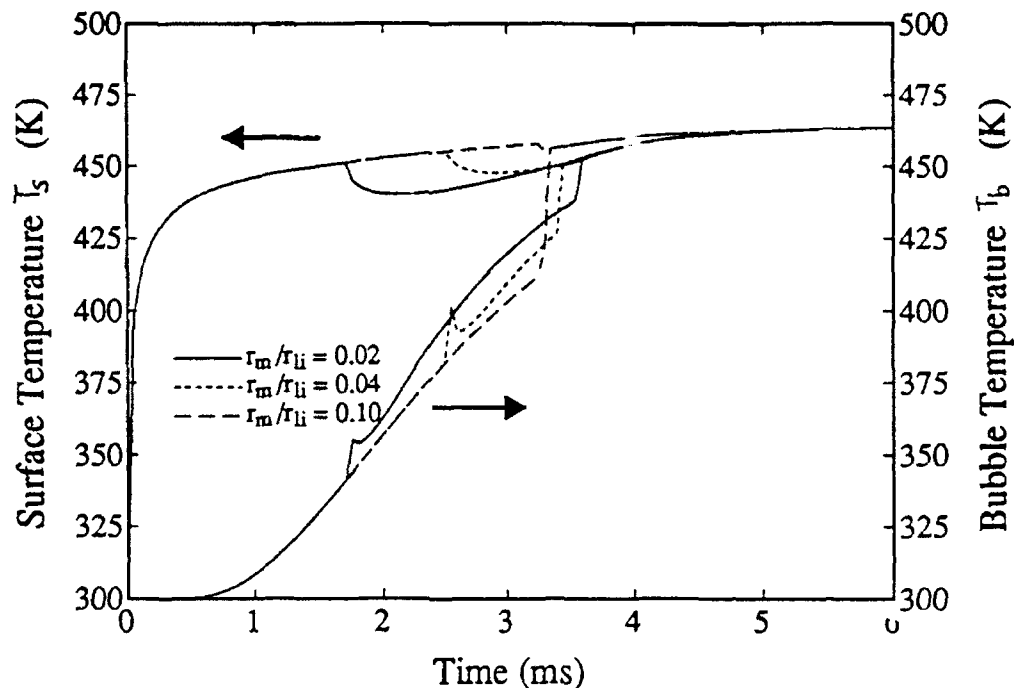


Figure 4.8: Droplet surface temperature and bubble temperature for different metal particle sizes and fixed initial metal volume fraction  $\phi_{m_i} = 0.25$ .

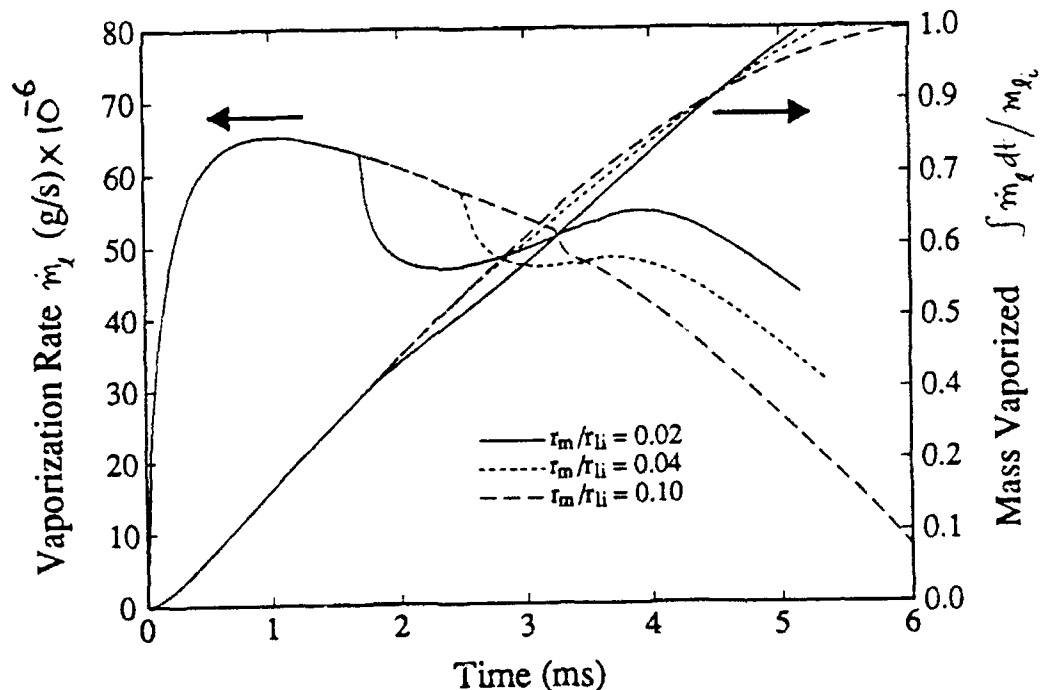


Figure 4.9: Vaporization rate and mass vaporized for different metal particle sizes and fixed initial metal volume fraction  $\phi_{m_i} = 0.25$ .

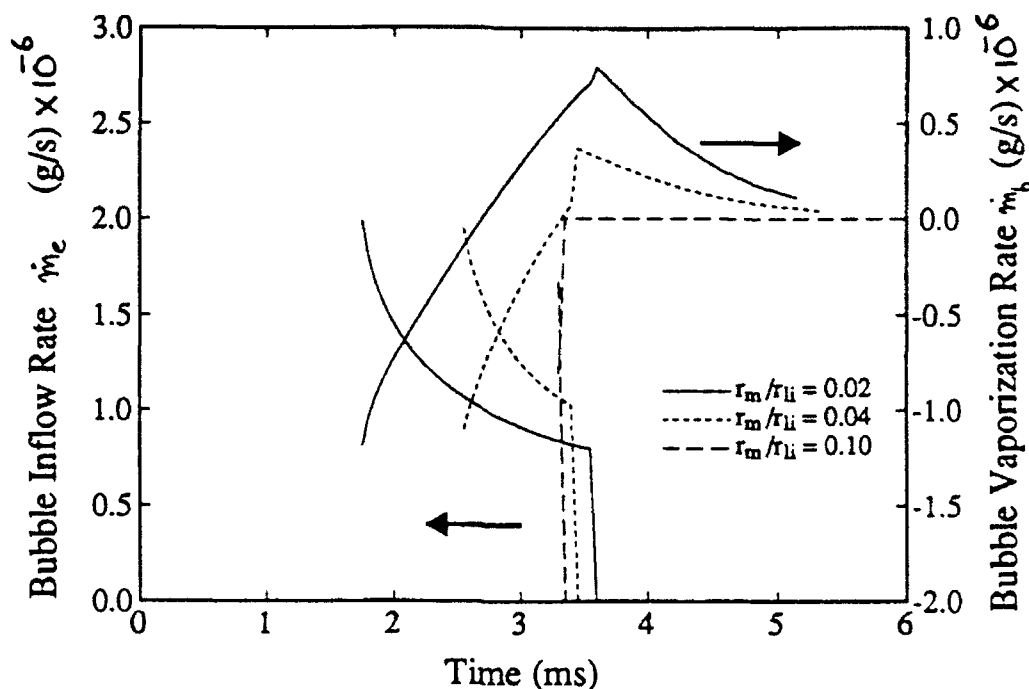


Figure 4.10: Bubble inflow rate and bubble vaporization rate for different metal particle sizes and fixed initial metal volume fraction  $\phi_m = 0.25$ .

Figures 4.11-4.15 show the same set of results, obtained by varying the initial metal volume fractions to 5, 15, 25, and 50%, which correspond to about 14, 36, 51, and 76% metal by weight. The metal particle radius is kept fixed at  $2 \mu\text{m}$ . Figure 4.11 shows the droplet radius and the bubble radius, both normalized by the initial droplet radius. Larger metal volume fractions imply smaller initial liquid mass, and thus smaller liquid vaporization times. For lower initial solid loading of 5%, the final shell thickness reaches its critical thickness at a later time (see Figure 4.12), and most of the liquid vaporization occurs in the surface regression regime. In the case of a slurry droplet with 50% volume loading, the initial packing is very close to the maximum packing ( $\pi/6$ ) allowed. The shell thickness reaches its critical value very early. Here, most of the droplet lifetime consists of liquid vaporization occurring inside of the pores. This shows that relative amount time spent in the three stages of vaporization is dependent upon the initial solid loading. Additionally, in the 50% initial packing case, the liquid surface is found to regress farther into the pores than the cases of intermediate packing. This will result in slower external vaporization rates at a later stage in the droplet lifetime (see Figure 4.14, showing a narrower time span for the 50% packing case). Note that although we have shown the droplet

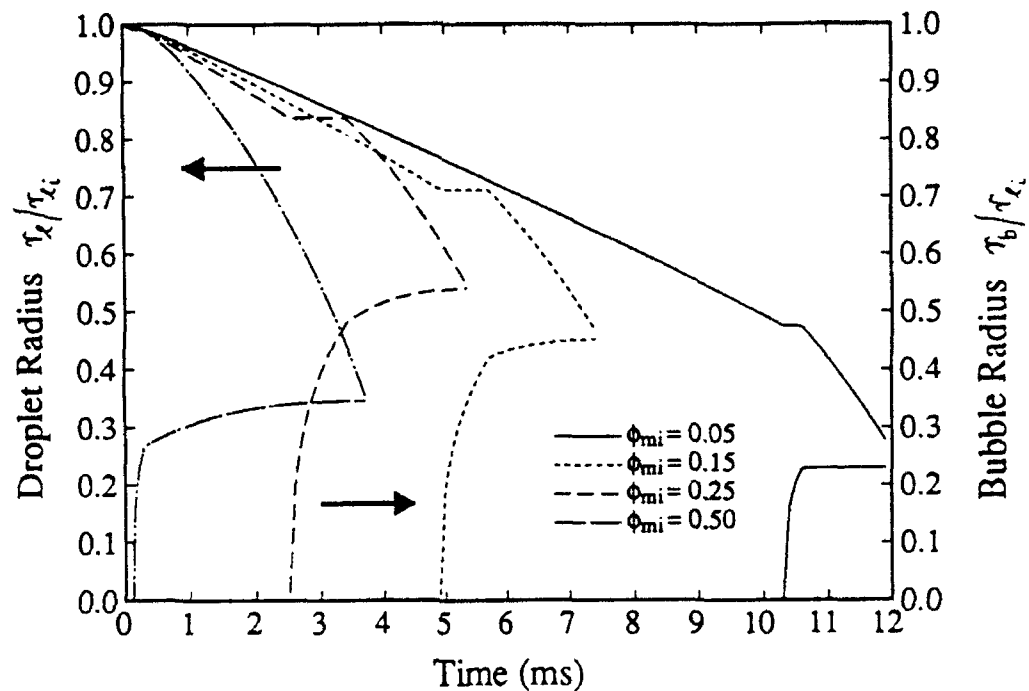


Figure 4.11: Droplet radius and bubble radius for different initial metal loading and fixed metal particle size  $r_m = 2\mu\text{m}$ .

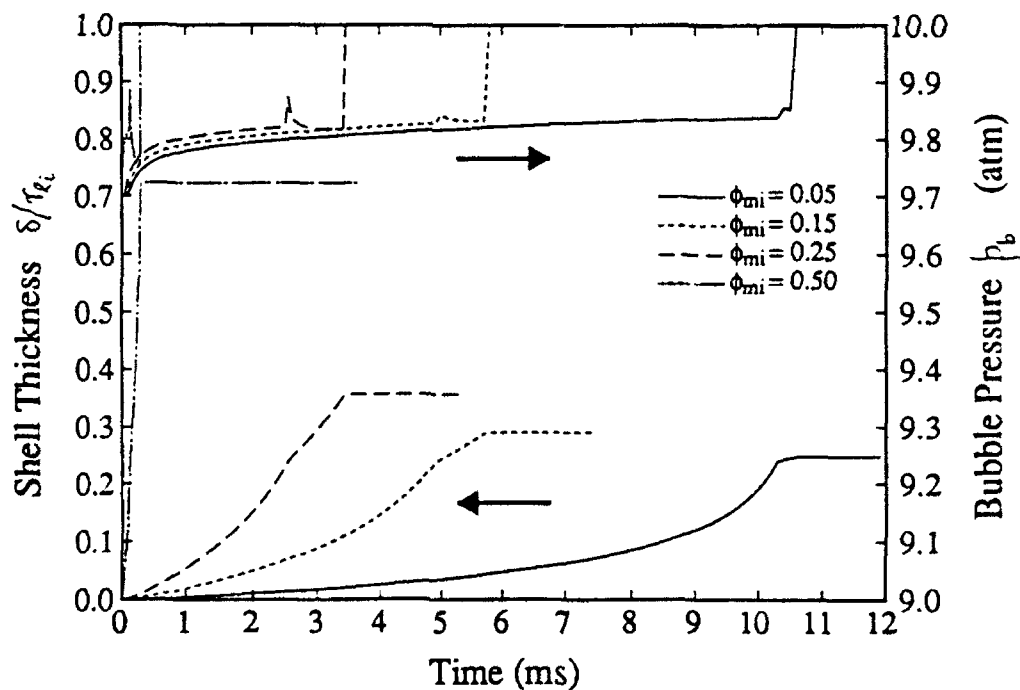


Figure 4.12: Shell thickness and bubble pressure for different initial metal loading and fixed metal particle size  $r_m = 2\mu\text{m}$ .

radius vs time curves, during the surface regression period, and after a short transient time, the  $r_i^{1.5}$  vs time curve is found to be linear because the heat and mass exchange between the gas and the slurry droplet is convection dominated ( $Re \sim O(100)$ ). To check the so called  $d^3$ -law [55], we have also checked  $r_i^3$  curve vs time for the pore-drying stage. In general, it is not linear ( $r_i^2$  vs time is more linear). Figure 4.12 shows the shell thickness, normalized by the initial droplet radius, and the pressure inside the bubble. The droplet surface temperature and the bubble temperature for the four cases are plotted in Figure 4.13. In case of larger initial metal loadings, the mixture conductivity is higher, and the interior of the droplet heats faster. The corresponding droplet vaporization rate, and the integrated liquid mass vaporized are given in Figure 4.14. Figure 4.15 shows the bubble inflow rate and the bubble

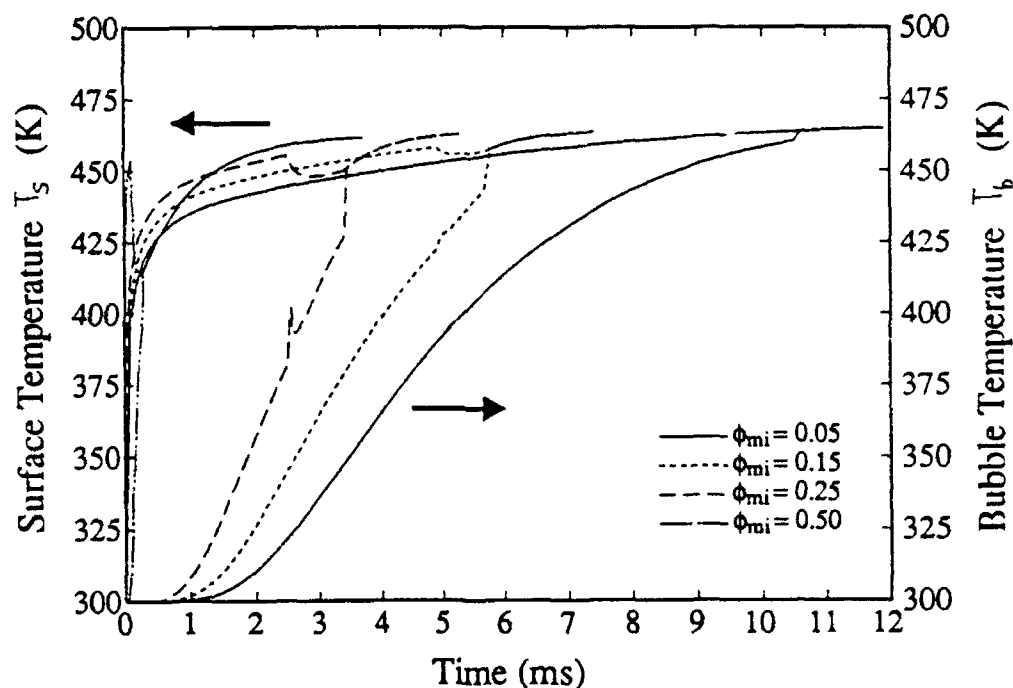


Figure 4.13: Droplet surface temperature and bubble temperature for different initial metal loading and fixed metal particle size  $r_m = 2\mu\text{m}$ .

vaporization/condensation rate. These results are similar to the set shown earlier.

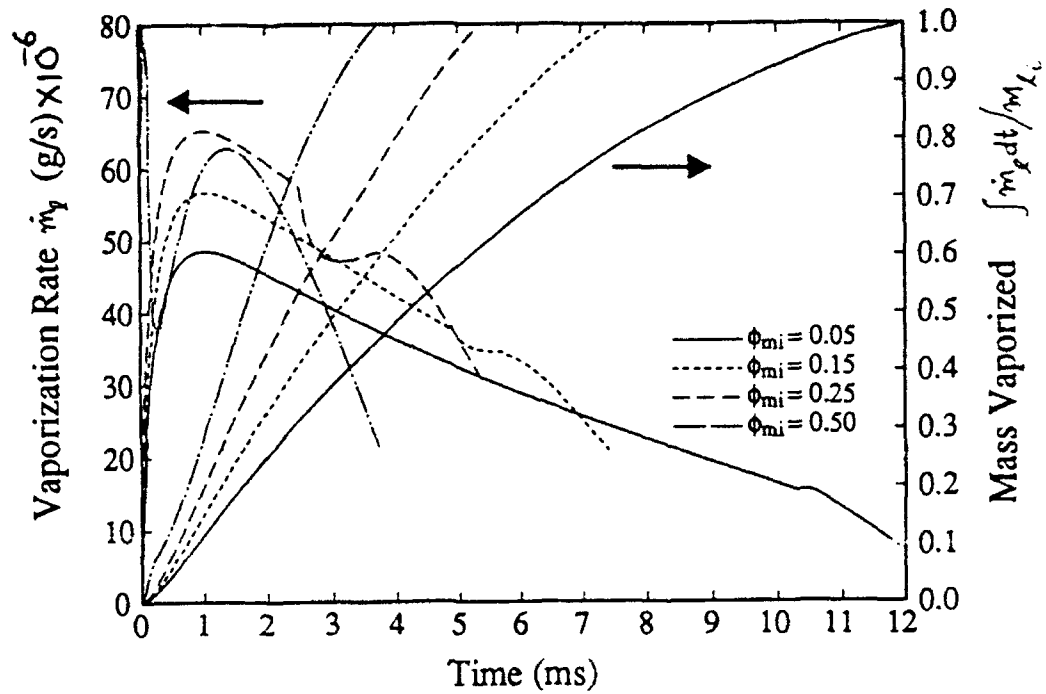


Figure 4.14: Vaporization rate and mass vaporized for different initial metal loading and fixed metal particle size  $r_m = 2\mu\text{m}$ .

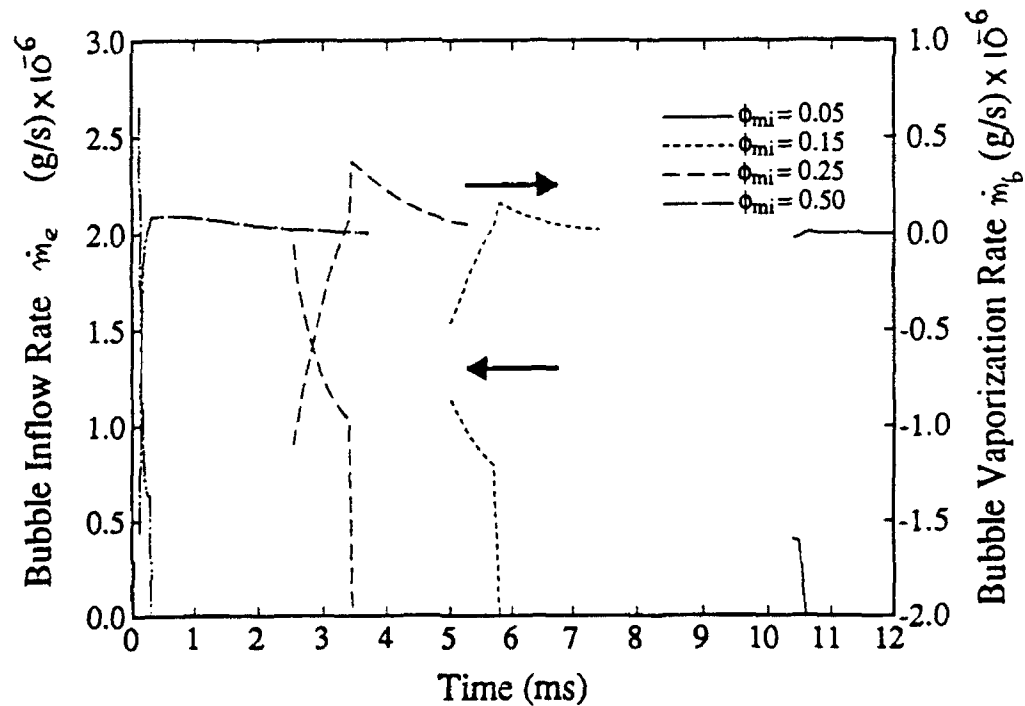


Figure 4.15: Bubble inflow rate and bubble vaporization rate for different initial metal loading and fixed metal particle size  $r_m = 2\mu\text{m}$ .

## 4.5 Conclusions

A simple model has been proposed for liquid vaporization from the metal slurry droplets. The phenomena of transient droplet heating, droplet surface regression, shell and bubble formations, and pore drying of the shell were shown to be salient features of slurry droplet vaporization, and formulations were presented to model these. Various vaporization possibilities were discussed, and a general model proposed. Heat- and mass-transfer numbers in gas phase have been corrected to account for the external gas motion. Lee and Law's experimentally inferred shell rigidization and maximum shell packing criterion were employed to predict transition from surface regressing to constant-radius vaporization regimes. Pore drying was analyzed by an expanding bubble-regressing liquid type of model. Equilibrium conditions were considered for pressure, energy and mass inside the droplet. Gas-phase heat- and mass-transfer solutions were rederived using the film theory approach, and corrections to the transfer numbers were obtained.

Initial droplet radius was kept fixed and results were obtained for two sets of parameters. In the first set, ratio of particle size to droplet size was varied while keeping the initial volume of the solid particles at 25%. In the second set, the particle size was fixed and initial volume fraction varied. It was shown that, depending on particle size and initial volume fraction of solid particles, a shell forms on the droplet surface. Droplet radius rapidly attains a constant value after injection. Upon rigidization of the shell, a bubble consisting of both fuel vapor and external gas is formed. The bubble grows faster initially. The ratio of rate of external gas blowing into the bubble and fuel vaporization rate is of the order of the ratio of bubble to liquid density. This inflow effect is especially important at high pressures. Initially, condensation of fuel vapor occurs in the bubble, and later vaporization occurs. Relative time fractions of vaporization lifetime spent in the three stages of vaporization were dependent on the initial solid loading and the metal particle size. For the same initial metal loading, droplet lifetime increased for larger metal particle size. Higher vaporization times were found in droplets with larger metal particles because of the formation of smaller bubbles, which resulted in smaller final liquid radii in the pore-drying stage, thus causing liquid vaporization rates to fall near the end of the droplet lifetime. The

droplet behavior was transient, and the classical  $d^2$ -law type of analysis could not be used to describe vaporization of liquid fuel from slurry droplets.

*The criterion for the rigidization of the shell and the maximum packing fraction of the metal particles is likely to depend on the slurry additives and the size of the metal particles. Further experimental investigation is necessary to determine the shell rigidization criterion and the maximum packing of the metal particles.*

## Chapter 5

# Metal Particle Combustion With Oxide Condensation

### 5.1 Introduction

Aluminum particle combustion has been extensively studied in the past, both experimentally and analytically, from a viewpoint of determining combustion efficiencies of metalized solid propellants (see Chapter 1). A critical aspect in previous studies has been the neglect of the thermodynamic phase equilibria between condensed and the vapor phases. As a result of this neglect, the condensation is assumed to occur only at fixed radial positions: at the flame and at the droplet surface. In addition, these models require arbitrary specification of the droplet surface temperature and the flame temperature, rather than being determined in the model. Thus, even though it is assumed that the flame temperature is limited by the boiling point of the aluminum oxide, the partial pressure of oxide and the total gas pressure have no role in determining the flame temperature, which is always fixed at 3850 K. In reality, the calculated gas temperatures and oxide vapor-liquid thermodynamic equilibria must determine whether there exists condensed oxide at the flame. As the combustion products move away from the flame, where the temperature is highest, they will undergo condensation at some location beyond the flame.

In an effort to improve upon the understanding of metal combustion, a simplified, analytical, quasi-steady gas-phase model for the burning of an isolated aluminum droplet is presented in this chapter. The important effects of condensation of the oxide

on the particle surface and in the gas phase are included. The radius of the condensation and the condensation temperature are determined in the model. Additionally, we account for the transient heating of the metal particle. A Schvab-Zel'dovich transformation is made to eliminate the source terms resulting from combustion. The resulting conservation equations are integrated to obtain expressions for various fluxes. An iterative solution procedure is used to obtain the system eigenvalues: fuel and oxide mass fluxes at the droplet surface, droplet surface temperature, location and temperature at the oxide condensation point.

## 5.2 Analysis

A schematic of the burning aluminum droplet is shown in Figure 5.1. In a hot

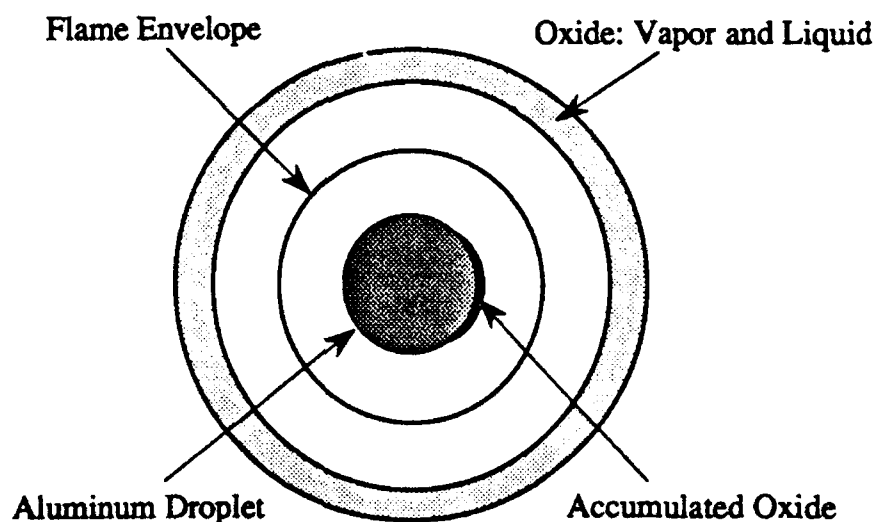


Figure 5.1: Schematic of the aluminum droplet.

oxidizing environment, the metal heats to the melting point of the aluminum (933.1 K), which results in phase change from solid to liquid metal. Continued heating (resulting from convection, radiation and surface oxidation) causes further temperature rise of the metal until the oxide melts (2325 K), and the ignition occurs. Aluminum vapor flows out and reacts with oxygen to form aluminum oxide. In a quiescent atmosphere, the condensed particles (typically  $< 2 \mu\text{m}$  diameter, Price [74], Salita [83]),

concentrate just outside the flame envelope. From single particle tests, it is known that additional oxide is collected at the burning aluminum droplet [98, 83]. A vapor phase diffusion flame results, and the surface oxidation of the aluminum gets inhibited due to the lack of oxidizer available at the droplet surface. The pre-ignition processes for heating of an aluminum particle are modeled in earlier chapters 2 and 3.

Consider a molten aluminum droplet burning in air, with product condensation, as illustrated in Figure 5.2. From stoichiometry, we know that  $(1 + f)$  kg of product (aluminum oxide) are formed by reaction of 1 kg of oxygen with  $f$  kg of fuel vapor. Under usual ambient conditions of low oxidizer mass fractions and moderate gas temperatures, the condensation of oxide occurs. The net or bulk gas flux in the inner zone (near the droplet surface) is primarily controlled by the droplet temperature, which in turn is coupled to the burning rate of the fuel. It will be shown later, in the results section, that when the droplet is relatively cool, the fuel vaporization rate is low, and the bulk gas velocity is negative. This situation persists for about a tenth of the droplet lifetime. Once the droplet gets relatively warm, the bulk gas velocity in the inner zone becomes positive. At the condensation point, the gas velocity becomes discontinuous, due to the sink of the mass resulting from condensation. This "traps" the condensed oxide at the condensation radius. Here, the *thermophoresis effect* may drive the condensed particles outwards. However, since the bulk flow in the outer zone is negative (towards the condensation radius), the particles are swept back by convection. The effect of thermophoresis is discussed in detail in Appendix D.

The key assumptions of the model are:

- (a) The burning process is isobaric, spherically symmetric and quasi-steady.
- (b) Infinite rate kinetics are assumed at the flame.
- (c) The fuel mass transport at the droplet surface is not inhibited by the presence of the condensed oxides.
- (d) The gas-phase condensation occurs in a thin zone, and all the oxide vapor flowing radially outwards from the flame condenses at this location.

Assumptions (a) and (b) are usually made to analyze hydrocarbon droplet combustion, and a discussion on these can be found in the text by Williams [109]. It is

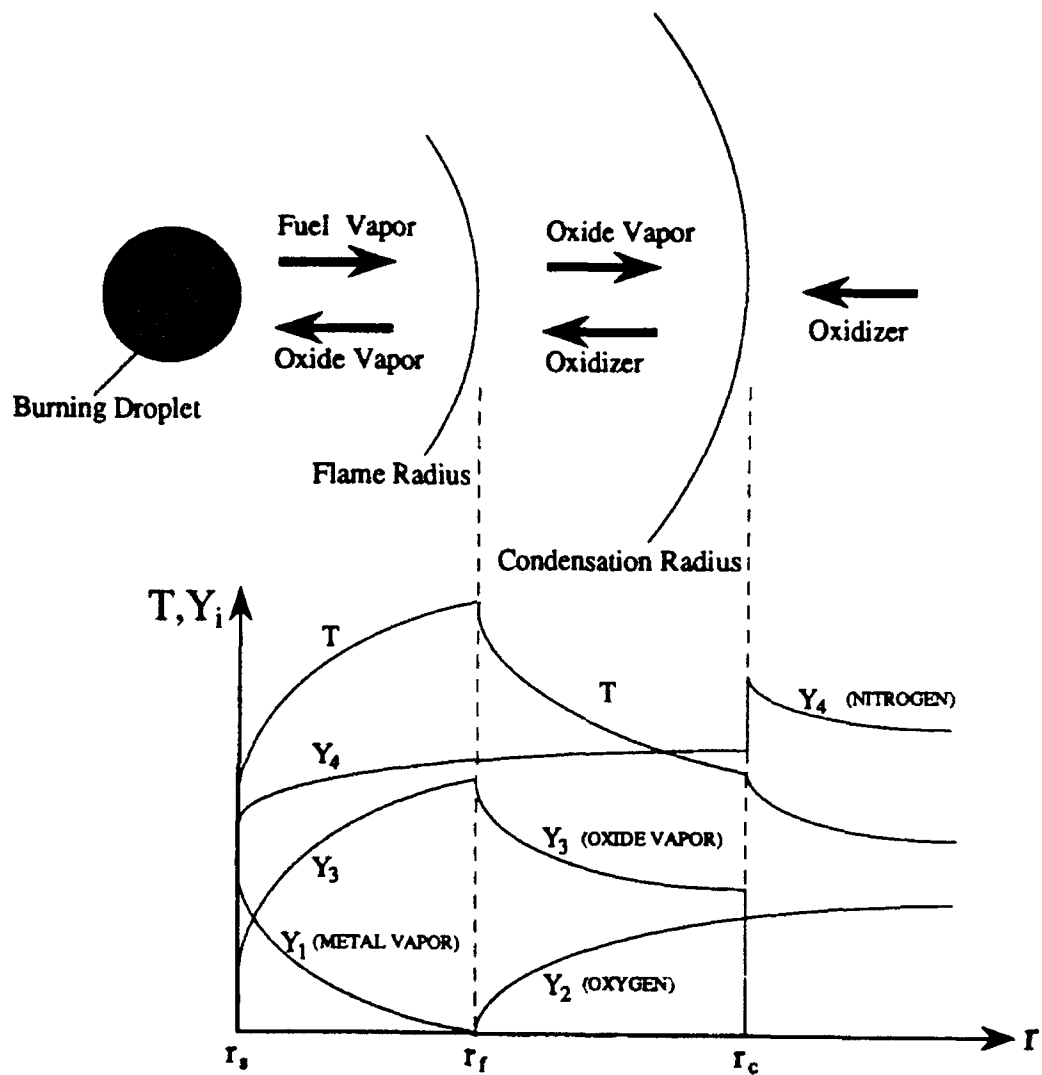


Figure 5.2: Droplet combustion model and schematic mass fractions and temperature profiles.

remarked here that the kinetics for metal vapor combustion are several orders of magnitude faster in comparison to hydrocarbon vapor combustion (Glassman [36], see also a discussion in Chapter 6). Hence, infinite rate kinetics is a good assumption for aluminum vapor combustion. With assumption (c) we are implying that, as the condensed oxides accumulate on the droplet surface, they offer no additional resistance to the transport of metal vapor. Further, the spherical symmetry of the problem is maintained as the liquid metal is depleted from the droplet. Assumption (d) is supported by several experimental observations (Hermsen [43]; Prentice [73], Price [74]; Turns et al. [98]) of "trapping" of the condensed oxide and has been employed by King [48] on the grounds that once condensation occurs, the condensed particles serve as sites for further heterogeneous condensation. The assumption of infinitely fast condensation is relaxed in a model problem described in Appendix C. The calculations of Appendix C reveal that, for the physically realistic rate constants likely to be encountered during the burning of aluminum, the assumption of infinitely fast condensation of the oxide is well justified. It is also remarked that, dependent upon the ambient conditions, the gas-phase condensation occurs relatively far from the droplet surface, and the effect on the fuel vaporization rate is expected to be small.

Properties employed are listed in Table 5.1. Species are represented by the subscripts: fuel 1, oxygen 2, oxide vapor 3, and inerts (nitrogen) 4. It is known that  $\text{Al}_2\text{O}_3(\text{g})$  does not exist (Price [74]; Friedman and Maček [31]; Law [50]); instead  $\text{AlO}$ ,  $\text{Al}_2\text{O}$ , etc. are present. Recently, there has been considerable interest and discussion on the thermodynamic properties of the metal oxides and the combustion phase of burning metals (Steinberg et al. [90, 91], Glassman [38]). The terms boiling temperature, saturation temperature, gasification temperature, dissociation temperature, and flame temperature have been distinguished. When the Gibbs phase rule is applied to a dissociating oxide system, with more than one constituent in the vapor phase, it is clear that the system has more than one degree of freedom. Hence, the Clausius-Clapeyron equation is inadequate to represent phase transitions for these dissociating systems. A comprehensive calculation to represent the phase transitions will involve writing all the chemical reactions for all the species, identifying the involved rate constants, and then considering the conditions for chemical equilibrium (see earlier work on condensation in nozzles by Courtney [22]). Then these equations will have

Property	Al	Al <sub>2</sub> O <sub>3</sub>
Atomic Weight $M$	26.98	101.96
Liquid Density $\rho$ (g/cm <sup>3</sup> , $T$ in K)	$2.879-5.40 \times 10^{-4} T$	$5.630-1.124 \times 10^{-3} T$
Liquid Specific Heat $C_p$ (kcal/kg-K)	0.281	0.340
Saturated Vapor Pressure (atm)	$\exp(13.279-36497/T)$	$\exp(19.285-62829/T)$
Heat of Vaporization $h_{fg}$ (kcal/kg)	2580	1224
Heat of Combustion $\Delta H$ (kcal/kg)	7335	-

The properties were compiled from:

Density: Salita [85].

Specific heat: Stull and Prophet [92].

Vapor pressure: Salita [85]; Hatch [42]; Ride [81]; Green and Maloney [41]; Kaye and Laby [46].

Heat of vaporization: Stull and Prophet [92]. For Al<sub>2</sub>O<sub>3</sub>,  $h_{fg}$  was estimated from the vapor-liquid equilibrium relation.

Heat of combustion: Stull and Prophet [92]; Ride [81]; Green and Maloney [41]; Kaye and Laby [46]; at 298 K, the value was adjusted for appropriate ambient gas temperatures.

Gas  $k$  and  $C_p$ : Were evaluated at an average temperature between  $T_s$  and  $T_f$  from Vargaftik [101].

Table 5.1: Properties of aluminum and aluminum oxide.

to be coupled to the energy and species conservation equations describing the vaporization and burning of aluminum. Note that in the Gordan-McBride computer code [40] description, it is stated that the data for solid and liquid aluminum oxide are not available. Because of absence of thermodynamic data, and added complexity, such a formulation is beyond the scope of this study. We assume that the vapor-liquid equilibrium for aluminum and aluminum oxide is given by Clausius-Clapeyron relations

$$X_{1\text{sat}} = \frac{\exp(A_1 - A_2/T_{\text{sat}})}{p_{\infty}} \quad (5.1)$$

$$X_{3\text{sat}} = \frac{\exp(B_1 - B_2/T_{\text{sat}})}{p_{\infty}} \quad (5.2)$$

Previous experimental studies [11, 15, 24, 27, 107, 67] have been in disagreement on the vapor composition itself over the liquid aluminum oxide. As also noted in the JANAF Thermochemical Tables [45], the mass spectroscopic experiments were performed in tungsten or molybdenum crucibles, which cause a change in the partial pressure of the dissociated species observed in the effusion experiments by reactions between the metallic crucibles and the vapor. There is also uncertainty in the values of accommodation or evaporation coefficients. From the above phase equilibrium relation, the boiling point of  $\text{Al}_2\text{O}_3$  at 1 atm is 3258 K and the latent heat is 1224 kcal/kg. For the latent heat Law [50] uses 1111 kcal/gm, von Wartenberg [107] gives 1471 kcal/kg, Farber et al. [27] give 1716 kcal/kg, Peleg and Alcock [67] give 1746 kcal/kg. The boiling points are given as 3770 K [67], 3300 K [107], and 3248 K [67]. In the absence of any reliable high temperature and uniformly-agreed-to data, we decided to use the CRC Handbook values.

The total gaseous mass flux is given by

$$m_g = m_1 + m_2 + m_3 + m_4, \quad \text{with} \quad Y_1 + Y_2 + Y_3 + Y_4 = 1 \quad (5.3)$$

The equation of continuity, in the two zones, becomes

$$r^2 m_{g,1} = \text{constant} = r_s^2 (m_{1,s} + m_{3,s}) \quad \text{for } r_s < r < r_c \quad (5.4)$$

$$r^2 m_{g,2} = \text{constant} = -r_s^2 m_{1,s} / f \quad \text{for } r_c < r < \infty \quad (5.5)$$

where  $r_s$  is the droplet radius and  $m_{1,s}$  and  $m_{3,s}$  are the fuel and oxide vapor fluxes at the droplet surface. The second relation states that oxygen is the only species in

the outer zone with a net non-zero flux. The general mass conservation for all the species can be written as:

$$\frac{1}{r^2} \frac{d}{dr} \left\{ r^2 m_{g,j} Y_i - r^2 \rho D \frac{dY_i}{dr} \right\} = S_i \quad (5.6)$$

where  $Y_i$  is the mass fraction of species  $i$ ,  $S_i$  is a source term due to combustion, and  $j = I$  or  $II$ , stands for inner or outer zone. Fickian diffusion has been assumed. It is also assumed that the condensed oxide occupies negligible volume. From stoichiometry, we note that  $S_2 = S_1/f$ ,  $S_3 = -(1+f)S_1/f$ ,  $S_4 = 0$ . The energy conservation statement is

$$\frac{1}{r^2} \frac{d}{dr} \left\{ r^2 m_g C_p (T - T_s) - r^2 k \frac{dT}{dr} \right\} = -S_1 \Delta H \quad (5.7)$$

In Eqs. (5.6) to (5.7) the source terms are eliminated using the familiar Schvab-Zel'dovich transformation [109] to obtain (all diffusivities are assumed equal and Lewis number equals one):

$$\frac{d}{dr} \left\{ r^2 m_{g,j} \beta_{FO} - r^2 \rho D \frac{d\beta_{FO}}{dr} \right\} = 0 \quad (5.8)$$

$$\frac{d}{dr} \left\{ r^2 m_{g,j} \beta_{FP} - r^2 \rho D \frac{d\beta_{FP}}{dr} \right\} = 0 \quad (5.9)$$

$$\frac{d}{dr} \left\{ r^2 m_{g,j} \beta_{FT} - r^2 \rho D \frac{d\beta_{FT}}{dr} \right\} = 0 \quad (5.10)$$

where

$$\beta_{FO} \equiv Y_1 - fY_2, \quad \beta_{FP} \equiv \frac{1+f}{f} Y_1 + Y_3, \quad \beta_{FT} \equiv C_p (T - T_\infty) + Y_1 \Delta H \quad (5.11)$$

Writing mass and energy balances at the droplet surface, we have

$$m_{1,s} = Y_{1,s} m_{g,s} - \rho D \left. \frac{dY_1}{dr} \right|_s \quad (5.12)$$

$$m_{2,s} = Y_{2,s} m_{g,s} - \rho D \left. \frac{dY_2}{dr} \right|_s = 0, \text{ no oxidizer crosses the droplet surface} \quad (5.13)$$

$$m_{3,s} = Y_{3,s} m_{g,s} - \rho D \left. \frac{dY_3}{dr} \right|_s \quad (5.14)$$

$$m_{4,s} = Y_{4,s} m_{g,s} - \rho D \left. \frac{dY_4}{dr} \right|_s = 0, \text{ no inerts cross the droplet surface} \quad (5.15)$$

$$k \left. \frac{dT}{dr} \right|_s = m_{1,s} h_{fg,1} + m_{3,s} h_{fg,5} + q_u \quad (5.16)$$

The heat penetrating into the droplet interior  $q_u$ , where the metal has a high thermal conductivity (Biot number  $\ll 1$ ), causes the droplet temperature to rise according to

$$q_u = \frac{(mC_p)_d dT_s}{4\pi r_s^2 dt} \quad (5.17)$$

The  $(mC_p)_d$  term includes the mass of the liquid aluminum and the mass of the oxide condensed at the droplet surface. From these, we can obtain the boundary conditions for the Schvab-Zel'dovich variables ( $\beta$ ) as

$$\rho D \left. \frac{d\beta_{FO}}{dr} \right|_s = -m_{1,s} + m_{g,s} \beta_{FO,s} \quad (5.18)$$

$$\rho D \left. \frac{d\beta_{FP}}{dr} \right|_s = -\frac{1+f}{f} m_{1,s} - m_{3,s} + m_{g,s} \beta_{FP,s} \quad (5.19)$$

$$\rho D \left. \frac{d\beta_{FT}}{dr} \right|_s = m_{1,s}(h_{fg,1} - \Delta H) + m_{3,s} h_{fg,5} + q_u + m_{g,s} \Delta H Y_{1,s} \quad (5.20)$$

where

$$\beta_{FO}(r_s) = Y_{1,s}, \quad \beta_{FP}(r_s) = \frac{1+f}{f} Y_{1,s} + Y_{3,s}, \quad \beta_{FT}(r_s) = Y_{1,s} \Delta H + C_p (T_s - T_\infty) \quad (5.21)$$

The second boundary conditions are obtained at a radius far away from the droplet surface ( $r \rightarrow \infty$ ):

$$\beta_{FO}(\infty) = -f Y_{2,\infty}, \quad \beta_{FP}(\infty) = 0, \quad \beta_{FT}(\infty) = 0 \quad (5.22)$$

The aluminum radius reduction is given by

$$\frac{dr_{Al}}{dt} = -\frac{m_{1,s}}{\rho_{Al}} \quad (5.23)$$

while the droplet radius, which is larger than the aluminum radius due to the accumulation of the condensed oxide, is given by

$$\frac{dr_s}{dt} = -\left\{ \frac{m_{1,s}}{\rho_{Al}} + \frac{m_{3,s}}{\rho_5} \right\} \quad (5.24)$$

Now, we can integrate the conservation equations (5.10) in the two zones to obtain expressions for the various fluxes. Conditions needed to match the solutions in the two zones, at the radius of condensation  $r = r_c$ , are (superscript + and - denote conditions outside and inside of  $r_c$ , respectively) as follows:

## (i) Fuel vapor

$Y_1$  and  $dY_1/dr$  are zero in the neighborhood of  $r = r_c$ .

## (ii) Oxygen

Partial density ( $\rho Y_2$ ) and the flux of oxygen is continuous. Thus

$$r_c^2 m_{2,c} = (r^2 m_{g,I}) Y_{2,c} - r_c^2 \rho D \left. \frac{dY_2}{dr} \right|_{r_c^-} = (r^2 m_{g,II}) Y_{2,c} - r_c^2 \rho D \left. \frac{dY_2}{dr} \right|_{r_c^+} \quad (5.25)$$

## (iii) Oxide vapor

$Y_3$  is a function of  $T_c$  through the Clausius-Clapeyron relation Eq. (5.2) at  $r = r_c^-$ .  $Y_3$  and  $dY_3/dr$  are zero for  $r \geq r_c$  in accordance with our assumption of complete condensation at  $r = r_c$ .

## (iv) Energy

Temperature is continuous. The energy flux is matched as

$$\begin{aligned} (r^2 m_{g,I}) h_{g,1} \Big|_{r_c^-} - r^2 k \left. \frac{dT}{dr} \right|_{r_c^-} &= (r^2 m_{g,II}) h_{g,2} \Big|_{r_c^+} - r^2 k \left. \frac{dT}{dr} \right|_{r_c^+} \\ &\quad - (r^2 m_3^+) \{ h_{fg,3} + (C_{p,l} - C_p)(T_c - T_\infty) \} \end{aligned} \quad (5.26)$$

where  $C_{p,l}$  denotes the specific heat of the liquid oxide.

The partial density of oxygen ( $\rho Y_2$ ) should be continuous at the radius of condensation because oxygen flows towards the flame. Our gas-phase conservation equations are solved assuming a constant density in the radial direction. Later, it will be shown that the mole fraction of the oxide vapor is very low at the radius of condensation. This happens because of dilution of the gas by nitrogen and oxygen. The temperature is continuous across the radius of condensation. Hence, the assumption of  $Y_{2,c} = Y_{2,c}^- \approx Y_{2,c}^+$  is made. The partial density of nitrogen ( $\rho Y_4$ ) need not be continuous at the radius of condensation because diffusion balances convection everywhere for them ( $m_4 = 0$ ); any radial position can have a contact surface discontinuity for nitrogen. Note that in the metal slurry application, the environment might include the products of hydrocarbon combustion (e.g.  $\text{CO}_2$ ,  $\text{H}_2\text{O}$ ). These inert products can be lumped with nitrogen for our purposes. The final results of integration of the conservation equations, and profiles for the Schvab-Zel'dovich variables, are given in a tabular form in Table 5.2. We can also show that

Equation	Inner Zone: $r_s < r < r_c$	Outer Zone: $r_c < r < \infty$
Continuity	$M_{g,I} = \text{constant} = \frac{r^2(m_{1,c} + m_{3,c})}{r_s \rho D}$	$M_{g,II} = \text{constant} = -\frac{r^2 m_{1,c}}{f r_s \rho D}$
Fuel-Oxidizer	$M_{g,I} \left(1 - \frac{r_s}{r_c}\right) = \ln \left\{ 1 + \frac{f Y_{2,c} + Y_{1,c}}{\frac{M_{1,c}}{M_{g,I}} - Y_{1,c}} \right\}$ $\beta_{FO}(r) = \frac{M_{1,c}}{M_{g,I}} + \left( Y_{1,c} - \frac{M_{1,c}}{M_{g,I}} \right) e^{M_{g,I} \left(1 - \frac{r_s}{r_c}\right)}$	$M_{g,II} \frac{r_s}{r_c} = \ln \left\{ 1 + \frac{Y_{2,c} - Y_{2,\infty}}{1 - Y_{2,c}} \right\}$ $\beta_{FO}(r) = \frac{M_{1,c}}{M_{g,II}} - \left( f Y_{2,\infty} + \frac{M_{1,c}}{M_{g,II}} \right) e^{-M_{g,II} \frac{r_s}{r_c}}$
Fuel-Product	$M_{g,I} \left(1 - \frac{r_s}{r_c}\right) = \ln \left\{ 1 + \frac{\frac{1+f}{f} Y_{1,c} + Y_{3,c} - Y_{3,\infty}}{1 + \frac{M_{1,c}}{M_{g,I}} - \frac{1+f}{f} Y_{1,c} - Y_{3,c}} \right\}$ $\beta_{FP}(r) = \frac{M_{1,c}}{M_{g,I}} \left\{ \frac{1+f}{f} + \frac{M_{3,c}}{M_{1,c}} \right\} + \left\{ \left( Y_{1,c} - \frac{M_{1,c}}{M_{g,I}} \right) \frac{1+f}{f} + Y_{3,c} - \frac{M_{3,c}}{M_{g,I}} \right\} e^{M_{g,I} \left(1 - \frac{r_s}{r_c}\right)}$	$Y_3 = 0$ $\beta_{FP} = 0$
Fuel-Energy	$M_{g,I} \left(1 - \frac{r_s}{r_c}\right) = \ln \left\{ 1 + \frac{Y_{1,c} \Delta H + C_p (T_c - T_c)}{\frac{M_{1,c}}{M_{g,I}} q_I - Y_{1,c} \Delta H} \right\}$ $\beta_{FT}(r) = \frac{M_{1,c} q_I}{M_{g,I}} + \left\{ Y_{1,c} \Delta H + C_p (T_c - T_\infty) - \frac{M_{1,c} q_I}{M_{g,I}} \right\} e^{M_{g,I} \left(1 - \frac{r_s}{r_c}\right)}$ $q_I = \Delta H - h_{f,g,1} + \frac{M_{3,c} h_{f,g,2}}{M_{1,c}} - \frac{q_{3,c}}{m_{1,c}}$	$M_{g,II} \frac{r_s}{r_c} = \ln \left\{ 1 + \frac{C_p (T_c - T_\infty)}{\frac{M_{1,c}}{M_{g,II}} q_{II} - C_p (T_c - T_\infty)} \right\}$ $\beta_{FT}(r) = \frac{M_{1,c} q_{II}}{M_{g,II}} \left\{ 1 - e^{-M_{g,II} \frac{r_s}{r_c}} \right\}$ $q_{II} = q_I + \frac{M_{g,I} - M_{g,II}}{M_{1,c}} \left\{ h_{f,g,3} + (C_{p,I} - C_{p,O})(T_c - T_\infty) \right\}$
Nitrogen*	$M_{g,I} \left(1 - \frac{r_s}{r_c}\right) = \ln \left\{ 1 + \frac{Y_{1,c} + Y_{3,c} - Y_{3,\infty} - Y_{3,c}}{1 - Y_{1,c} - Y_{3,c}} \right\}$	$M_{g,II} \frac{r_s}{r_c} = \ln \left\{ 1 + \frac{Y_{2,c} - Y_{2,\infty}}{1 - Y_{2,c}} \right\}$

\*These relations are not independent. They may be obtained by manipulation of fuel-oxidizer and fuel-product relations given above.

Table 5.2: Solution summary of equations governing aluminum combustion.

$$\frac{M_{1,s}}{M_{g,I}} = \frac{Y_{1,s}(1 - Y_{3,c}) + fY_{2,c}(1 - \frac{1+f}{f}Y_{1,s} - Y_{3,s})}{Y_{1,s} + Y_{3,s} - Y_{3,c} - Y_{2,c}} \quad (5.27)$$

Note that the classical burning hydrocarbon droplet solution is recovered from solutions presented in Table 5.2 by using  $\frac{M_{1,s}}{M_{g,I}} = 1$  and letting  $r_c \rightarrow \infty$ . The flame radius can be obtained from the fuel-oxidizer relations by using  $\beta_{FO} = 0$ , at  $r = r_s$ , as:

$$\frac{r_s}{r_f} = 1 - \frac{1}{M_{g,I}} \ln \left\{ 1 + \frac{Y_{1,s}M_{g,I}}{M_{1,s}} \right\} \quad (5.28)$$

The flame temperature ( $T_f$ ) is then obtained from the fuel-oxidizer relation as:

$$C_p(T_f - T_\infty) = \{Y_{1,s}(\Delta H - q_l) + C_p(T_s - T_\infty)\} \frac{\frac{M_{1,s}}{M_{g,I}}}{\frac{M_{1,s}}{M_{g,I}} - Y_{1,s}} \quad (5.29)$$

Calculations indicated that, during early times in the droplet heating period, the net mass flux in the fuel-oxide Zone I could be negative. This situation, depending on the droplet initial temperature and ambient conditions, lasts for about 1/50 to 1/10 of the droplet lifetime. The gas-phase phenomenon during this period is essentially transient in nature, and no quasi-steady theory can correctly model it. Hence, in accordance with our stated objective of developing a simple model, we shall assume no gas-phase condensation during the time it takes for the droplet to warm enough so that the net gas mass flux becomes positive in Zone I. Low ambient temperatures, e.g. 300 K, along with initial droplet temperatures of 2325 K, failed to raise the droplet temperature enough so that the net gas mass flux could become positive.

### 5.3 Solution Procedure

Clearly, the mass and heat transport are coupled, and an iterative procedure is to be employed. The scheme used in our calculations is briefly described below:

- (i) At the advanced time, guess the droplet surface temperature  $T_s$ , condensation temperature  $T_c$ , condensation radius  $r_c$ , and oxygen mass fraction  $Y_{2,c}$ . Obtain  $Y_{1,s}$ ,  $Y_{3,s}$  and  $Y_{3,c}$  from  $T_s$  and  $T_c$  using the Clausius-Clapeyron relations, Eqs. (5.1) and (5.2).

- (ii) Find  $M_{g,I}$  from fuel-oxidizer relation (inner zone) in Table 5.2, and  $M_{1,s}$  from Eq. (5.27). Find  $M_{3,s} = M_{g,I} - M_{1,s}$  and  $M_{g,2} = -M_{1,s}/f$ .
- (iii) Update  $Y_{2,c}$  from fuel-oxidizer relation (outer zone) in Table 5.2. Repeat steps (ii) to (iii) until convergence is reached on  $Y_{2,c}$ .
- (iv) Determine  $q_I$  by equating the transfer number from the fuel-oxidizer relation and the fuel-energy relations for the inner zone, both given in Table 5.2. Find  $q_{II}$ .
- (v) Update condensation radius  $r_c$  using fuel-energy relation for the outer zone given in Table 5.2. Update  $Y_{2,c}$  and  $Y_{3,c}$  using the fuel-oxidizer relation for the outer zone and fuel-oxidizer relation for the inner zone, respectively. Update  $T_c$  using the corrected value of  $Y_{3,c}$  and the inverse Clausius-Clapeyron relation, Eq. (5.2).
- (vi) Repeat steps (i) to (v), until convergence on  $T_c$ .
- (vii) Update the droplet radius  $r$ , using Eq. (5.24), and the droplet surface temperature  $T_s$ , using Eq. (5.17).
- (viii) Repeat steps (i) to (vii), until convergence is reached on  $r$ , and  $T_s$ . Then, advance time.

All variables in our results are converged to a maximum error less than 0.01%. The time step used is normally 0.01 ms. The solution, after initial startup, converges in a minimum number of iterations. The reason is that the gas-phase profiles get established.

## 5.4 Results and Discussion

Results of computations for an aluminum droplet burning in air are presented in Figures 5.3 to 5.9. In all cases, the ambient oxygen mass fraction is  $Y_{2,\infty} = 0.232$  and the initial droplet temperature is 2325 K, corresponding to the melting point of the protective coating of the aluminum oxide that forms over the aluminum particle.

Consider an aluminum particle of nominal size  $25 \mu\text{m}$  at room temperature of 300 K. Using the density-temperature relation in Table 5.2, it can be shown that this corresponds to a particle size of  $30.2 \mu\text{m}$  at 2500 K. An average particle temperature of 2500 K is used to evaluate the liquid and oxide density, and initial particle radius of  $30.2 \mu\text{m}$  employed. Ambient pressures from 1 to 20 atm, and ambient temperatures from 300 to 2500 K, are considered. Wherever possible, results are compared against earlier experimental observations. Direct comparison with existing theoretical models is erroneous, due to the inaccurate assumptions regarding gas-phase velocity and *a priori* knowledge of flame and droplet surface temperatures made in these early modeling efforts.

Figure 5.3 shows typical gas-phase mass fraction and temperature profiles, for an ambient pressure of 10 atm and temperature of 2000 K. After a transient heating period, which usually lasts for about one tenth of the lifetime, the gas-phase profiles become steady in time. In the case shown in Figs. 3 to 5, the transient period lasts for about 0.5 ms, and the droplet lifetime is about 4.5 ms. The flame is located at the peak gas temperature, and the fuel and oxygen mass fractions go to zero here, in accordance with the thin flame assumption. The flame standoff distance is found to be about 2.4 times the droplet radius. Condensation of the aluminum oxide occurs at a non-dimensional radius of about 6.7, and here the oxide mass fraction  $Y_3$  goes to zero. The reason for lower flame standoff distance in the case of aluminum droplets, as compared to liquid hydrocarbon droplets, is that the heat and mass transfer numbers obtained are lower. This results from a lower ratio of heat of combustion to heat of vaporization for aluminum, e.g. for n-hexane to n-decane the ratio  $\Delta H/h_{fg}$  goes from about 131 to 158, while for aluminum it is about 2.8. Also, in the quasi-stage for all of the cases considered, the gas-phase temperatures are higher than the saturation temperatures for the oxide between the radial locations bound by the droplet surface and the condensation radius, which lies beyond the flame. Hence, the region near the droplet surface is condensate free. Based upon experimental observations of condensate free region near the droplet surface, it has been (Brewster [12]) speculated that this is a result of thermophoresis driving the particles from the condensation-flame zone towards the droplet (against strong convection outwards from the droplet surface). We show that the condensation radius results from a consideration of vapor-liquid equilibrium. Vapor oxides generated at

the flame diffuse inwards (and outwards), and this is the reason for the observation of condensate free inner zone. Since the condensation radius lies in a zone of negative

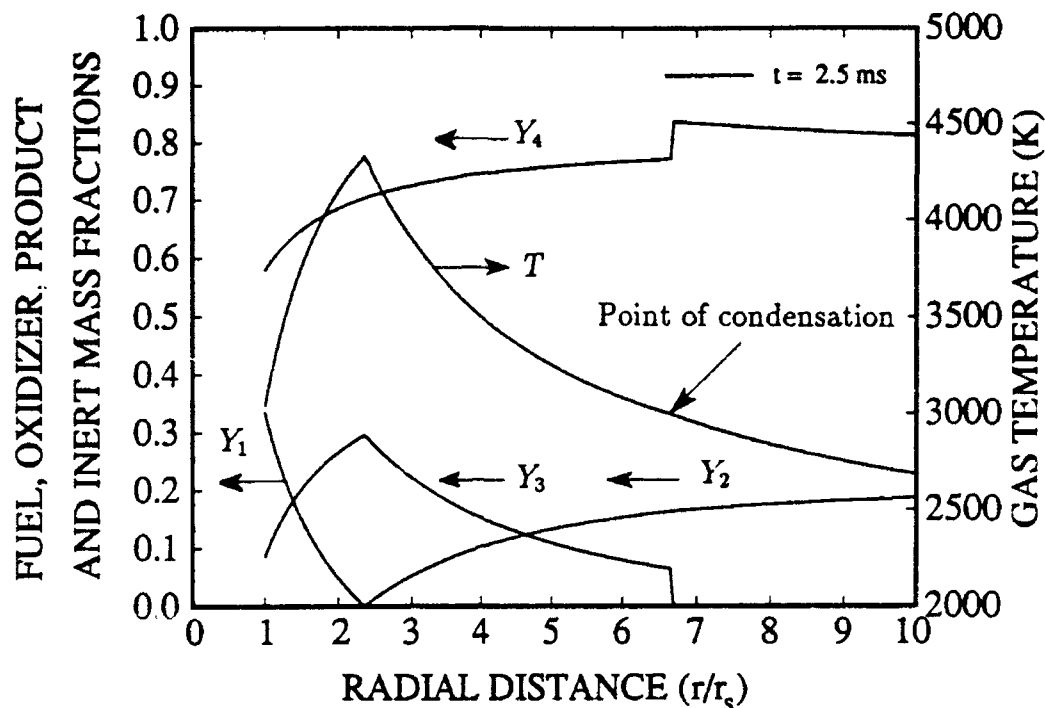


Figure 5.3: Gas-phase profiles of the fuel ( $Y_1$ ), oxygen ( $Y_2$ ), oxide ( $Y_3$ ) and inert ( $Y_4$ ) mass fractions, and the temperature ( $T$ ). The flame is at the peak gas temperature. The point of condensation is given by  $Y_3 = 0$ . In these calculations:  $Y_{2,\infty} = 0.232$ ,  $p_\infty = 10$  atm,  $T_\infty = 2000$  K,  $r_{s,i}|_{T=300K} = 25$   $\mu\text{m}$ .

thermal gradient, the thermophoretic velocity is directed radially outwards. For the above case, with the gas-phase temperature profile established, the thermophoretic velocity for a condensed particle of  $\text{Al}_2\text{O}_3$  of diameter  $1$   $\mu\text{m}$  is estimated as  $+3.7$  cm/s. The gas velocity just outside of the radius of condensation is obtained as  $-7.3$  cm/s. As these velocities are of the same order, the thermophoresis may result in some thickening of the zone of condensation. However, as the condensed particles are pushed to lower temperatures, the gas momentum will drag them back in the opposite direction. Thus, thermophoresis will have a limited effect, only. Further details on the thermophoretic effect are presented in Appendix D. It is apparent that the heat release due to gas-phase condensation occurs relatively far from the droplet surface.

Figure 5.4 shows the time evolution of the non-dimensional fuel and oxide mass fluxes in the inner zone, and the net gas fluxes in the inner and outer zones. After the initial droplet heating transient, the fluxes become constant. This happens because all of the heat from the flame and the surface condensation of the oxide goes into vaporization of the fuel, and the droplet temperatures remain fixed. The fuel mass flux is always positive, thus indicating fuel vaporization at the droplet surface. The oxide mass flux at the droplet surface is always negative, indicating oxide condensation. The net gas flux in the inner zone begins negative as the droplet is relatively cold, and becomes positive when the droplet becomes relatively warm. The net gas mass flux in the outer region is of course just the flux of oxygen, and is in stoichiometric proportion to the fuel flux. The outer net gas flux is negative so that a discontinuity and change of direction in the net gas flux occurs because of the oxide condensation. Figure 5.4 also shows the cumulative mass of aluminum vaporized from the droplet. This is obtained by taking the ratio of the total amount of fuel vaporized  $\int_0^t m_{1,s} dt'$  to the initial droplet mass. We note that the fluxes shown in the Figure 5.4 are defined as  $M_{i,s} = r_s m_{i,s} / \bar{\rho} \bar{D}$ . Thus, it is not the fuel flux, for example, that is constant with time, rather the product of the droplet radius and the flux which becomes steady in time. Figure 5.5 shows the squared droplet radius  $(r_s/r_{s,i})^2$ , the fuel radius  $(r_{Al}/r_{s,i})$ , the oxide radius  $(r_{ox}/r_{s,i})$ , the flame standoff distance  $(r_f/r_s)$ , and the condensation distance  $(r_c/r_s)$ . As expected, with the diffusion controlled mass and heat transport employed in the model,  $\frac{dr_s^2}{dt}$  is found to be constant, after the initial transient droplet heating time. The oxide radius denotes a fictitious radius corresponding to a sphere of accumulated oxide on the droplet. Upon completion of the vaporization of the fuel, the droplet radius and the oxide radius become equal. During the period of transient heating, the condensation occurs nearer to the flame, and then  $r_c/r_s$  becomes a constant. The reason for this is that the gas-phase temperatures become steady. The location of the condensation radius is extremely sensitive to the ambient temperature, as will be shown in Figure 5.7.

In Figures 5.6 to 5.9, we summarize the results of our calculations under varying ambient conditions. Figure 5.6 shows the droplet, condensation, and the flame temperatures for the different ambient pressures and temperatures. In the range of calculations, the ambient pressure has a large effect on the droplet temperature, and the ambient temperature has a small effect. At a pressure of 1 atm, we obtain droplet

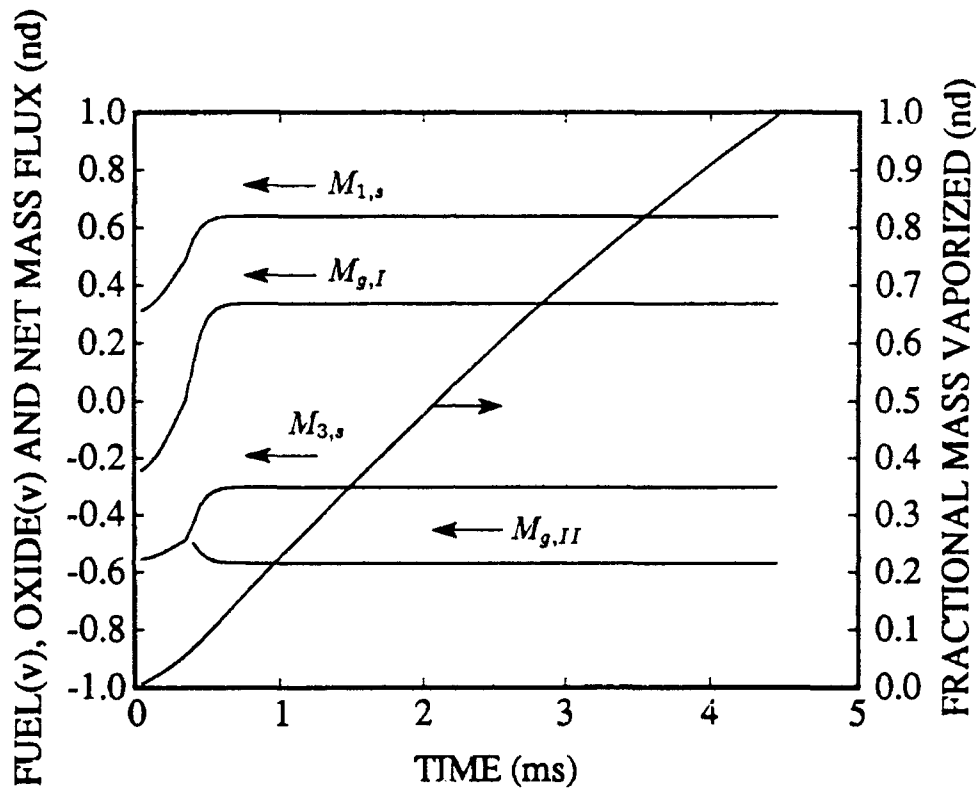


Figure 5.4: Time evolution of the fuel vapor ( $M_{1,s}$ ), oxide vapor ( $M_{3,s}$ ), and the net gas fluxes in the inner ( $M_{g,I}$ ) and outer ( $M_{g,II}$ ) zones. Also shown is the fractional mass vaporized, which is the ratio of time integration of the flux of the fuel vaporized to the initial droplet mass. In these calculations:  $Y_{2,\infty} = 0.232$ ,  $p_\infty = 10$  atm,  $T_\infty = 2000$  K,  $r_{s,i}|_{T=300K} = 25$   $\mu\text{m}$ .

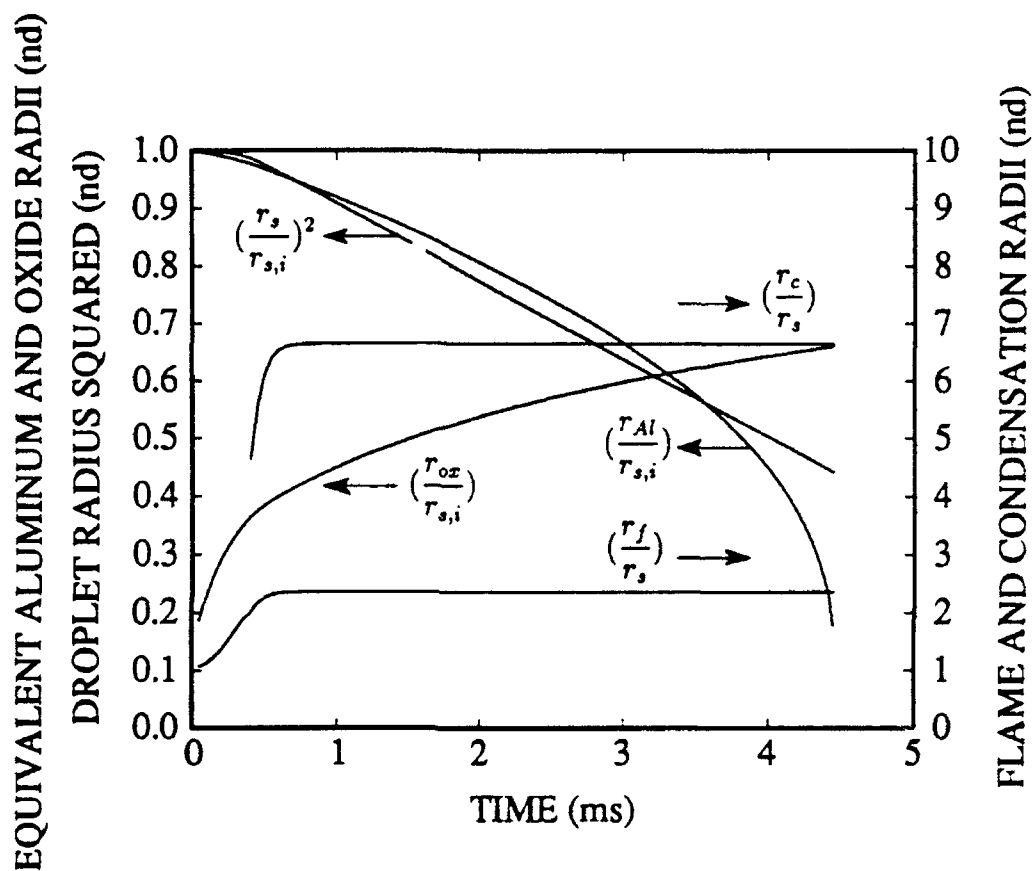


Figure 5.5: Time evolution of the droplet surface radius  $(r_s/r_{s,i})^2$ , fuel radius  $(r_{Al}/r_{s,i})$ , and oxide radius  $(r_{ox}/r_{s,i})$ . Also shown are the flame  $(r_f/r_s)$  and condensation  $(r_c/r_s)$  radii. In these calculations:  $Y_{2,\infty} = 0.232$ ,  $p_\infty = 10$  atm,  $T_\infty = 2000$  K,  $r_{s,i}|_{T=300K} = 25$   $\mu\text{m}$ .

temperatures in the range 2536 to 2602 K; for  $p_\infty = 10$  atm,  $T_s = 3005$  to 3058 K; and for  $p_\infty = 20$  atm,  $T_s = 3181$  to 3243 K. The boiling point of the aluminum may be found from Eq. (5.1) as 2748, 3325 and 3549 K, respectively for total pressures of 1, 10 and 20 atm. The droplet surface temperature (Figure 5.6) is found

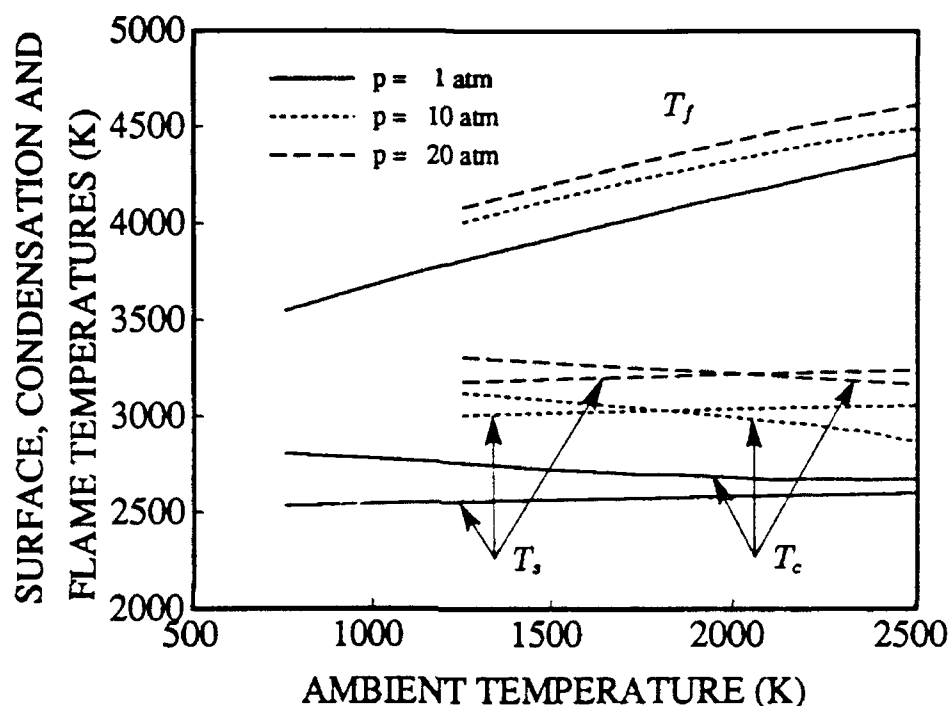


Figure 5.6: Effect of varying ambient pressure and temperature on the droplet surface ( $T_s$ ), condensation ( $T_c$ ), and flame ( $T_f$ ) temperatures. Note the closeness of  $T_s$  and  $T_c$ . In these calculations:  $Y_{2,\infty} = 0.232$ ,  $r_{s,i}|_{T=300K} = 25 \mu\text{m}$ .

to be much lower than the prevalent boiling point temperature. This fact has been reported earlier by Brzustowski and Glassman [13, 14]. For  $10 \mu\text{m}$  radius particles, they report surface temperatures of about 2450 K at 1 atm, and 2800 K at 10 atm. Also, Ermakov et al. [26] report temperature of burning aluminum droplets at 1 atm to be in the range 2430 to 2540 K, depending upon the rate of heat input. This results in  $Y_{1,s}$ , the aluminum mass fraction at the droplet surface, to be far lower than 1.0. The flame temperatures are obtained from a frozen equilibrium calculation. In reality, dissociation of the oxide will limit these temperatures. Nevertheless, results from a NASA code (Gordon, McBride and Zeleznik [40]) for pressures of 1, 10 and 20 atm, and an ambient temperature of 2000 K, give adiabatic flame temperatures of

3680, 4139 and 4296 K, respectively. We find the corresponding flame temperatures as 4150, 4331 and 4428 K. The difference with the equilibrium code is lower at higher pressures, since the dissociation is suppressed. Under any circumstances, the comparison between a diffusion flame temperature and an adiabatic flame temperature can only be very crude since the diffusion film is not adiabatic. In view of the approximations inherent in the model, viz. approximation of products as generic  $\text{Al}_2\text{O}_3$ , lack of an equilibrium calculation and the non-adiabatic character, the agreement may be deemed satisfactory. Note that earlier models have assumed that the flame temperature is known (Law [50]) and the condensation temperature is known (King [48]) *a priori*. Additionally, the droplet and condensation temperatures are found to be in the same approximate range. This questions the importance of radiative heat transfer from the condensed oxide to the droplet, in comparison to convection (Brewster [12]).

In Figure 5.7, we report the final droplet sizes resulting upon vaporization of all of the aluminum and accumulation of oxide. The figure also shows the flame and condensation radii. Note that, as different ambient conditions result in different droplet radius reduction rates, to facilitate comparisons, all radii in the Figure 5.7 have been normalized by the initial droplet radius. Increasing the ambient pressure has a small effect on the flame radius and final droplet size. However, it has a profound effect on the radius of condensation, via the vapor-liquid equilibrium. The exponential dependence of vapor-liquid equilibrium with temperature is also the reason for the rapid rise in the radius of condensation with ambient temperature. In all the cases examined, the final droplet radius is found to be in the narrow range of 65 to 75% of the initial particle size. This matches very well with the reported experimental observations. Turns et al. [98] report final sizes of 60 to 80%. Salita [83] estimates the diameter of the residual aluminum oxide at about 70%. This also shows a limitation of the present model, i.e. the assumed spherical symmetry may be destroyed as the oxide accumulates on the droplet surface. This is generally true for all simple models. Turns et al. suggest usage of a spherical cap, with spherical symmetry maintained in the ratio of exposed metal to total surface area. Increasing total pressure causes a slight reduction in the flame standoff distance, and ambient temperature has very small effect on the flame standoff distance. In our results, the flame standoff ratios ( $r_f/r_s$ ) are obtained in the range of 2.0 to 3.1. These ratios are somewhat lower than the range reported by Wilson and Williams [110], 2.8 to 5.0. In their study, the extremum in the

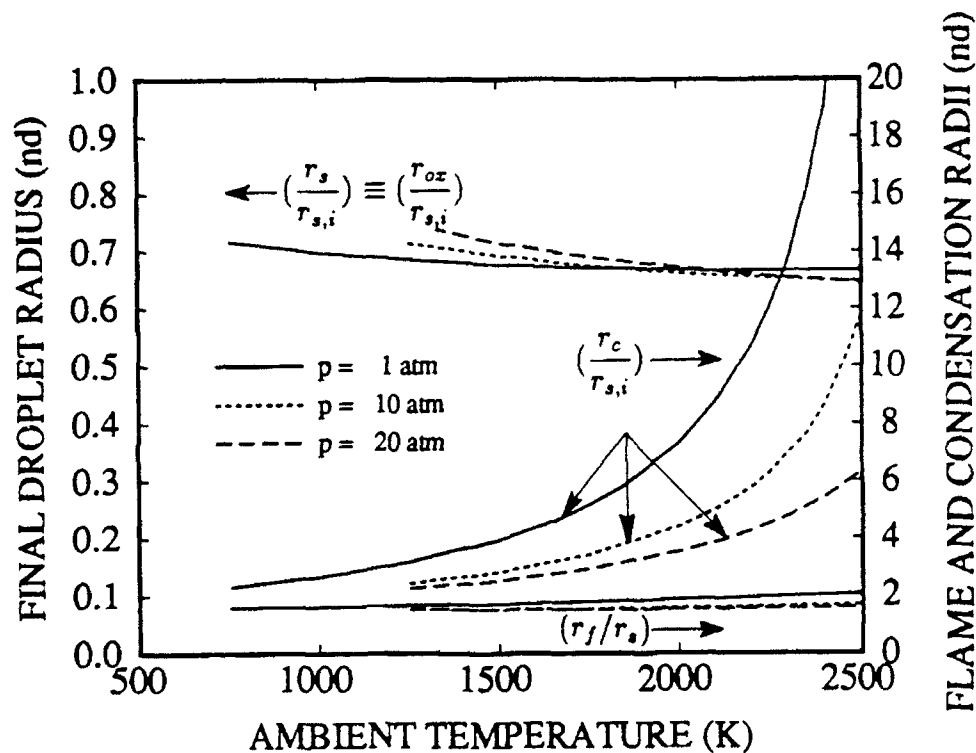


Figure 5.7: Effect of varying ambient pressure and temperature on the flame ( $r_f/r_{s,i}$ ), condensation ( $r_c/r_{s,i}$ ), and final droplet ( $r_s/r_{s,i} \equiv r_{ox}/r_{s,i}$ ) radii. Since different values of  $r_s$  result for different ambient conditions, the radii in this figure are non-dimensionalized by  $r_{s,i}$ , to facilitate comparison. Pressure has small effect on the final size, but a large effect on the condensation radius. In these calculations:  $Y_{2,\infty} = 0.232$ ,  $r_{s,i}|_{T=300K} = 25 \mu\text{m}$ .

flame radial intensity was taken as the “flame” radius. The authors themselves note that the “locus of maximum intensity in a flame zone laden with condensed products is not necessarily where the reactants melt and react stoichiometrically”. Comparison of our results with their experimental results is difficult because they impulsively heat with a laser while we rely on higher ambient temperatures to obtain ignition. Interestingly, when we compare our condensation radius,  $r_c/r_s$  (at lower ambient temperatures, say  $\sim 1000$  K), we find good match with their “flame” standoff distance (which was obtained with normal room temperature as the ambient condition). For comparison purposes: for  $p_\infty = 1$  atm,  $Y_{2,\infty} = 0.232$  and  $T_\infty = 1000$  K, we find  $r_f/r_s = 2.29$  and  $r_c/r_s = 3.78$ ; for  $p_\infty = 5$  atm,  $Y_{2,\infty} = 0.232$  and  $T_\infty = 1000$  K, we find  $r_f/r_s = 2.25$  and  $r_c/r_s = 4.28$ ; for  $p_\infty = 5$  atm,  $Y_{2,\infty} = 0.33$  and  $T_\infty = 500$  K, we find  $r_f/r_s = 2.24$  and  $r_c/r_s = 4.10$ . These  $r_f/r_s$  and  $r_c/r_s$  ratios are independent of the initial particle size, and the  $r_c/r_s$  ratios are in good ‘match’ with the corresponding values of about 3.9, 4.0 and 4.2 reported in the Wilson and Williams study. It is possible that the experimentalists have misinterpreted the radius of condensation, definitely the most intense region in the flame, to be the “flame” radius.

Figure 5.8 presents the effect of ambient pressure and temperature on the fuel, oxide and net gas fluxes in the inner zone. Again note that, as different ambient conditions result in different droplet radius reduction rates, to facilitate comparison, the non-dimensional fluxes in this figure are defined as  $M_i = \frac{r^2 \dot{m}_i}{r_s \rho D}$ , rather than the usual  $M_i = \frac{r^2 \dot{m}_i}{r_s \rho D}$ . An increase in ambient temperature results in slight increase of the fluxes. An increase in the ambient pressure results in slight lowering of the fuel and oxide mass fluxes. The net gas mass flux shows little dependence on pressure, as these effects tend to cancel. The burning times obtained are also shown in the Figure 5.8. The behavior of decrease of burning time with increasing ambient temperature and decreasing pressure is consistent with observations on hydrocarbon droplets (see Chapter 2). A comparison of our model predictions of droplet burning times with the previous experimental results is shown in Figure 5.9. This figure, along with the data points from various authors, is taken from Turns et al. [98]. The solid lines are calculated times for three ambient oxygen mole fractions: 0.10, 0.15 and 0.25. In these calculations,  $T_\infty = 1660$  K, which represents a mean value in their range (1510 to 1809 K) of experiments, and  $p_\infty = 1$  atm. Excellent agreement is found between the experimental values from Turns et al. and theoretical values at

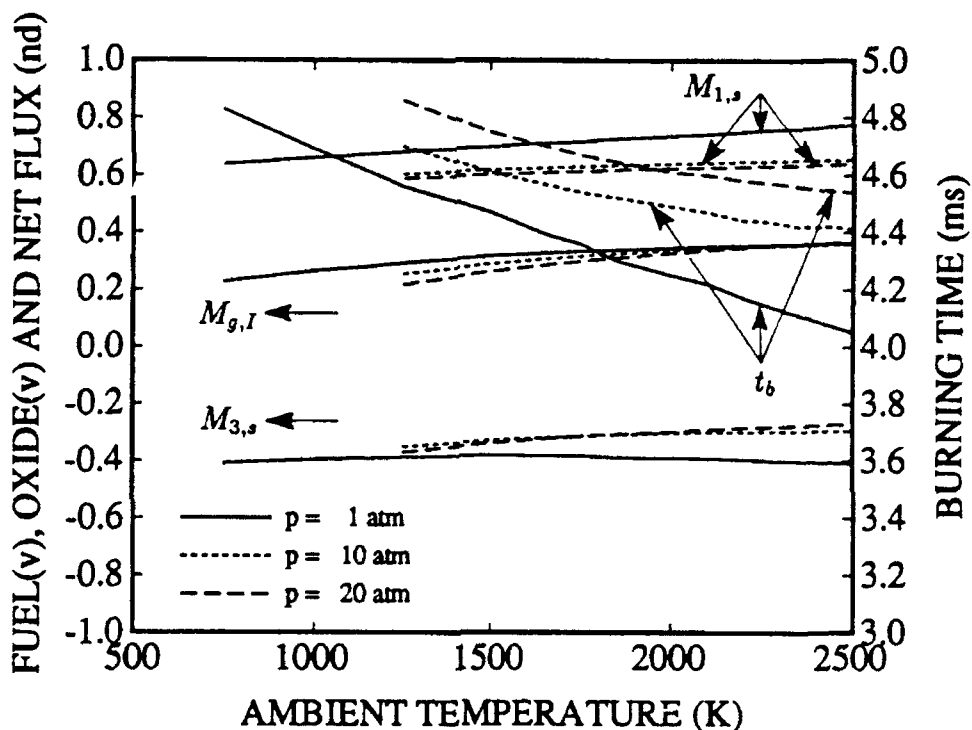


Figure 5.8: Effect of varying ambient pressure and temperature on the fuel vapor ( $M_{1,s}$ ), oxide vapor ( $M_{3,s}$ ) and net gas ( $M_{g,I}$ ) fluxes in the gas phase. Effect on the droplet burning time is also shown. To facilitate comparison, the non-dimensional fluxes in this figure are defined as  $M_i = \frac{r^2 m_i}{r_{s,i} \rho D}$ , rather than the usual  $M_i = \frac{r^2 m_i}{r_{s,i} \rho D}$ . In these calculations:  $Y_{2,\infty} = 0.232$ ,  $r_{s,i}|_{T=300K} = 25 \mu\text{m}$ .

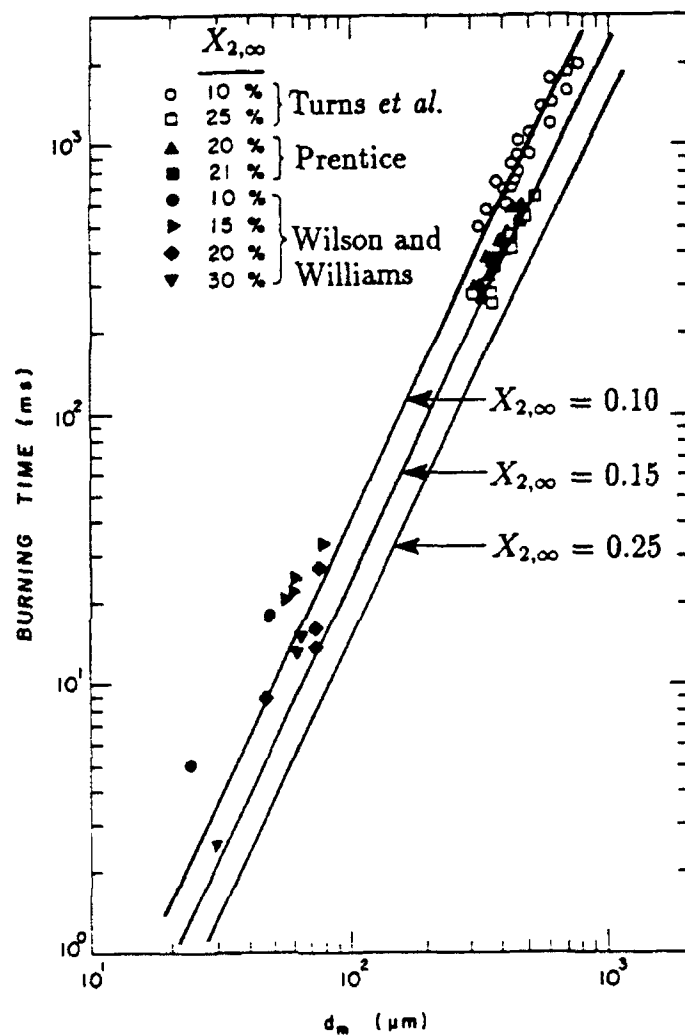


Figure 5.9: Comparison of predicted and experimental values of the droplet burning time. The figure is taken from Turns *et al.*[74]. Solid lines represent analytical results for three ambient oxygen mole fractions:  $X_{2,\infty} = 0.10$ ,  $0.15$  and  $0.25$ . In these calculations  $T_\infty = 1660$  K and  $p_\infty = 1$  atm.

lower oxygen mole fractions, and fair agreement is found at higher mole fractions. It is to be noted here that the data by Turns et al. has been presumably obtained at  $p_{\infty} = 1$  atm, while that from the study by Wilson and Williams includes values at higher ambient pressures. Additionally, experiments of Wilson and Williams utilized a laser pulse ignition of aluminum particles. For comparing with our calculations, the corresponding initial droplet temperature could be different than the value of 2325 K used by us. Also, we have used an ambient temperature of 1660 K, as against the room temperature gases used by them. The lower ambient temperatures and higher pressures would result in higher burning times, *cf.* Figure 5.8.

## 5.5 Summary

A simple model has been constructed to describe the vapor-phase combustion of metal particles in air. The advantage of the present model over earlier theoretical work is that a knowledge of the droplet, flame and condensation temperatures is not needed *a priori*. Proper vapor-liquid phase-equilibrium relations for the fuel and the oxide are incorporated into the model.

It is found that, for all the cases analyzed, in a zone bounded by the droplet radius and a radius greater than the flame radius, the gas temperatures are higher than the saturation temperatures of the oxide vapor, and hence, contrary to previous theory, this high temperature zone is condensate-free, and the flame temperature exceeds the oxide boiling point. The radius reduction followed a  $d^2$ -law, with the ratio of flame to droplet radius being constant. With the accumulation of the oxide on the droplet surface, the final droplet radius goes to about 70% of the initial particle radius. Good agreement with published experimental results for droplet temperature, final droplet size, flame temperatures and burning times is obtained. The temperatures near the flame are high, resulting in no condensation of oxide at the flame. It is found that for particles burning in air, there exists a condensate-free zone near the droplet surface. Condensation of oxide occurred in a finite zone that exists outside of the flame radius. Earlier models are incapable of predicting the droplet temperature, flame temperature and radius of condensation, or of explaining the observation of condensate-free zone near the droplet surface. The previous theories assume that

the oxide boiling point is a limit on the flame temperature, because that conclusion follows from a premixed adiabatic flame computation. This assumption erroneously ignores the difference between a premixed flame and a diffusion flame and the effect of ambient temperature. Our results show that the assumption is poor one for the wide range of ambient temperatures studied. Increasing ambient pressure and decreasing ambient temperature moved the condensation radius closer to the flame radius. The condensation radius is found to have an exponential dependence on the ambient temperature, which results from the exponential dependence of the vapor-liquid equilibrium upon temperature. The calculations have resulted in a better understanding of the combustion of aluminum particles.

# Chapter 6

## Flame Propagation In Metal Slurry Sprays

### 6.1 Introduction

Earlier, in Chapter 4, we have found that the metal particle can not be ignited by the heat released from the liquid fuel burning of the same droplet, unless the ambient air is preheated to sufficiently large temperature values. Heat released from the burning of other liquid fuel droplets and metal combustion in the spray is necessary to ignite the metal in the slurry droplet with a significant metal mass loading. Hence, to examine the ignition and combustion characteristics of the slurry droplets, a spray calculation is necessary. No previous analytical or computational studies could be found on the topic of spray combustion of the metal slurry droplets. However, spray combustion of hydrocarbon droplets has been extensively studied. Comprehensive reviews on spray combustion are available (e.g., Sirignano [88], and Faeth [28]).

From a practical point of view, theoretical and numerical calculations of realistic spray combustion are quite complex due to the probabilistic character of initial conditions, and, strong and nonlinear coupling between the gas and liquid phases. Numerically accurate representation of ignition and flame characteristics in sprays will require resolution on a scale smaller than typical droplet spacing. The ignition characteristics, existence of individual or group flames, and rate of propagation of chemical reaction, are all influenced by space and size distributions of the spray. These distributions can only be represented in a statistical manner, thereby imposing

restrictions on the spray combustion model. In recent years, there has been extensive numerical and experimental work on flame propagation studies in orderly arrays of fuel droplets (Aggarwal and Sirignano [3, 4], Rangel and Sirignano [77, 78, 80], Umemura [100], Tsai and Sterling [97], Queiroz et al. [75, 76], Miyasaka and Law [60], Sangiovanni and Kesten [86], Twardus and Brzustowski [99]). The simplified one- or two-dimensional models are not able to account for many important phenomenon, such as turbulence, three dimensionality, random size and space distributions, and detailed chemical kinetics. However, the simplified models do help identify important features of gas and liquid interactions and the flame structure. From the studies mentioned above, it is apparent that an interactive system of premixed and diffusion flames can exist and that the assumption of a single propagating flame front is too simplistic [15, 16, 18, 22]. The flame simultaneously exhibits both premixed-like and diffusion-like character. The premixed character becomes more important due to the vaporization ahead of the flame, the combustion does not occur with the flame surrounding each individual droplet, and nearly all the vaporization occurs with droplets behind or ahead of the propagating flame [16]. The minimum ignition energy and the ignition delay time are found to be lower in a range of finite initial droplet sizes than for the premixed case (corresponding to zero initial droplet radius) [15]. The gas-droplet interactions for a metal slurry droplet are even more complex because of the expected ignition delay of the metal part.

As a first step in understanding of the complex phenomenon of spray combustion of metal slurry droplets, this investigation seeks to understand the heat and mass transfer interactions between the slurry droplets and the gas flow. This calculation has to be made in order to investigate the manner in which one or more reaction zones spread from one group of droplets to another; it is a logical first step before fully randomized parcels of droplets are explored. In this study, the gas-phase equations are modeled after the configuration developed by Rangel and Sirignano [77, 78, 80].

## 6.2 Analysis

Figure 6.1 shows a schematic of the parallel stream system. A number of parallel droplet streams are injected at the channel inlet, where the droplet composition,

temperature, size, velocity, and spacing of the slurry streams are specified. When the slurry droplets are exposed to a hot oxidizing environment, the liquid fuel vaporizes and burns, leaving behind a dry metal agglomerate. The metal then heats to the melting point of the aluminum (933.1 K). The model assumes that during the phase change, due to the formation of a thin oxide coating, the individual particle shape remains spherical. Continued heating causes further temperature rise of the metal until the oxide melts (2325 K), at which point ignition is presumed to occur. At this temperature, the individual aluminum particles forming the agglomerate coalesce into a molten droplet and vapor-phase burning of aluminum follows. The calculations are terminated after all the aluminum has vaporized and burnt.

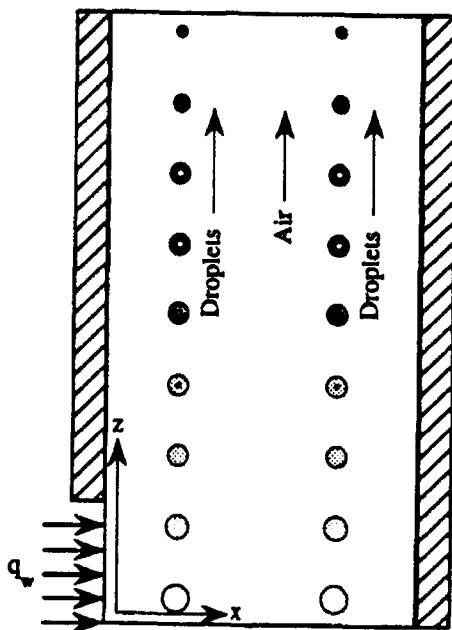


Figure 6.1: Schematic of the parallel slurry droplet stream combustion model and coordinate system.

### 6.2.1 Gas-Phase Analysis

The parallel droplet stream concept, introduced by Rangel and Sirignano [78] is used to analyze the gas phase. This model considers a two-dimensional constant property gas which flows in a rectangular channel of length  $L$  and width  $W$  (Figure 6.1). The side walls are adiabatic except for a portion that receives a uniform heat flux per unit area  $\dot{q}_w$ . There is no dependence on the  $y$  coordinate, which is perpendicular to the axial  $z$  and the transverse  $x$  coordinates. The governing steady, constant thermophysical property equations governing the transport of energy and species of the gas flow in a two-dimensional coordinate system may be stated as:

$$\frac{\partial}{\partial x}(\rho v) + \frac{\partial}{\partial z}(\rho u) = \sum_{j=1}^N n_j \dot{m}_{l,j} - \sum_{j=1}^N n_j \dot{m}_{o,j} \quad (6.1)$$

$$\frac{\partial}{\partial x}(\rho v Y_F) + \frac{\partial}{\partial z}(\rho u Y_F) = \bar{\rho} \bar{D} \left( \frac{\partial^2 Y_F}{\partial x^2} + \frac{\partial^2 Y_F}{\partial z^2} \right) + \sum_{j=1}^N n_j \dot{m}_{l,j} - \dot{W}_F \quad (6.2)$$

$$\frac{\partial}{\partial x}(\rho v Y_O) + \frac{\partial}{\partial z}(\rho u Y_O) = \bar{\rho} \bar{D} \left( \frac{\partial^2 Y_O}{\partial x^2} + \frac{\partial^2 Y_O}{\partial z^2} \right) - \sum_{j=1}^N n_j \dot{m}_{o,j} - \dot{W}_O \quad (6.3)$$

$$\begin{aligned} & \frac{\partial}{\partial x}(\rho C_p v (T - T_s)) + \frac{\partial}{\partial z}(\rho C_p u (T - T_s)) = \\ & k \left( \frac{\partial^2 T}{\partial x^2} + \frac{\partial^2 T}{\partial z^2} \right) - \sum_{j=1}^N n_j \dot{m}_{l,j} \mathcal{L}_{eff} - \sum_{j=1}^N n_j \dot{m}_{o,j} \mathcal{L}_{o,j} + \Delta H \dot{W}_F \end{aligned} \quad (6.4)$$

The momentum equations are bypassed by assuming isobaric and inviscid (except for droplet drag effects) flow. In the above equations,  $n_j$  is the droplet number density,  $\dot{m}_{l,j}$  is the hydrocarbon fuel vaporization rate from the  $j$ th droplet group, and  $\dot{m}_{o,j}$  is the oxidizer consumption rate which occurs in two situations:

- (a) During the heating of the dry agglomerate, oxygen is consumed at the agglomerate surface due to the surface oxidation of aluminum;
- (b) The agglomerate heats, and above temperatures of 2325 K, a detached aluminum vapor-oxygen flame results. Oxygen is consumed at the flame and not at the droplet surface.

Note that the oxygen flux is non-zero only after the complete vaporization of the liquid hydrocarbon from the droplet, and consequently  $\dot{m}_{o,j} = 0$  for  $\dot{m}_{l,j} > 0$ . Also, if

$\dot{m}_{o,j} > 0$ , then  $\dot{m}_{l,j} = 0$ .  $\dot{W}_F$  and  $\dot{W}_O$  are the hydrocarbon fuel and oxygen reaction rates.  $\mathcal{L}_{\text{eff}}$  represents an effective heat of vaporization, which is the latent heat of vaporization of liquid hydrocarbon and the heat penetrating the droplet interior.  $\mathcal{L}_{o,j}$  represents the sink/source term due to:

- (a) For surface oxidation of aluminum agglomerate, the sink term arises from convective heating of the agglomerate by the gas and is given by

$$\mathcal{L}_{o,j} = \frac{A_F 4\pi R^2 h (T - T_{s,j})}{\dot{m}_{o,j}} \quad (6.5)$$

- (b) For vapor-phase burning of aluminum, the source term represents the net heat flux into the gas and is given by

$$\mathcal{L}_{o,j} = - \frac{\dot{m}_{Al} \Delta H_{Al} + \dot{m}_{ox} h_{fg,ox} - \dot{m}_{Al} h_{fg,Al} - \dot{q}_d}{\dot{m}_{o,j}} \quad (6.6)$$

Here,  $\dot{m}_{Al}$  is the vaporization/burning rate of aluminum and  $\dot{m}_{ox}$  is the rate of condensation of the aluminum oxides. Using the stoichiometry of the reaction  $2 \text{Al} + 1.5 \text{O}_2 \rightarrow \text{Al}_2\text{O}_3$ , we can write the preceding equation as

$$\mathcal{L}_{o,j} = - \left\{ \frac{8}{9} (\Delta H_{Al} - h_{fg,Al}) + \frac{17}{8} h_{fg,ox} - \frac{\dot{q}_d}{\dot{m}_{o,j}} \right\} \quad (6.7)$$

Models for determining  $\dot{m}_l$ ,  $\dot{m}_o$ ,  $\mathcal{L}_{\text{eff}}$ ,  $\mathcal{L}_{o,j}$ , and  $\dot{q}_d$  are presented under the heading Droplet Analysis.

In the above formulation, it is implicitly assumed that the aluminum vapor-oxygen kinetics are infinitely fast. Recently, some studies (Fontijn [29], Garland, et al. [33]) have reported the kinetics rate as (moles/cm<sup>3</sup>-s)

$$\frac{d[Al]}{dt} = -9.756 \times 10^{13} [Al]^1 [O_2]^1 \exp(-160/RT) \quad (6.8)$$

Comparing this to *n*-octane reaction rate from Westbrook and Dryer [108]

$$\frac{d[C_8H_{18}]}{dt} = -4.6 \times 10^{11} [C_8H_{18}]^{0.25} [O_2]^{1.5} \exp(-30000/RT) \quad (6.9)$$

we can evaluate the two rate constants as: for  $T = 2000 \text{ K}$

$$k|_{C_8H_{18}} = 2.4 \times 10^8, \quad k|_{Al} = 9.37 \times 10^{13}$$

and for  $T = 3000$  K

$$k|_{C_8H_{18}} = 3.0 \times 10^9, \quad k|_{Al} = 9.5 \times 10^{13}$$

We see that the oxidation of aluminum is at least four orders of magnitude faster than that of *n*-octane. Hence, the assumption of infinitely fast aluminum kinetics is justified.

The assumptions used in the simplification of the gas-phase governing equations are: transverse motion is neglected by assuming  $v$  is zero, heat conduction and species diffusion are neglected in the streamwise direction, the equation of state is taken as  $\rho T = \text{constant}$ , the Lewis number is unity, i.e.,  $\overline{\rho D} = k/C_p$ , and one-step finite-rate kinetics is assumed for the hydrocarbon vapor and oxygen. It is assumed that  $\rho u$  varies only in the streamwise direction and is constant with transverse position. In spite of these simplifications, the model retains the important physics of diffusion and finite chemical kinetics. Then, the continuity equation becomes

$$\frac{\partial}{\partial z}(\rho u) = \sum_{j=1}^N n_j \dot{m}_{l,j} - \sum_{j=1}^N n_j \dot{m}_{o,j} \quad (6.10)$$

and using this in the species and energy conservation equations, we obtain

$$\rho u \frac{\partial Y_F}{\partial z} - \overline{\rho D} \frac{\partial^2 Y_F}{\partial x^2} = \sum_{j=1}^N \{n_j \dot{m}_{l,j}(1 - Y_F) + n_j \dot{m}_{o,j} Y_F\} - \dot{W}_F \quad (6.11)$$

$$\rho u \frac{\partial Y_O}{\partial z} - \overline{\rho D} \frac{\partial^2 Y_O}{\partial x^2} = \sum_{j=1}^N \{n_j \dot{m}_{l,j}(-Y_O) - n_j \dot{m}_{o,j}(1 - Y_O)\} - \dot{W}_O \quad (6.12)$$

$$\begin{aligned} & \rho u C_p \frac{\partial (T - T_s)}{\partial z} - k \frac{\partial^2 T}{\partial x^2} = \\ & - \sum_{j=1}^N \{n_j \dot{m}_{l,j} (C_p (T - T_s) + \mathcal{L}_{\text{eff}}) - n_j \dot{m}_{o,j} (C_p (T - T_s) - \mathcal{L}_{o,j})\} + \Delta H \dot{W}_F \end{aligned} \quad (6.13)$$

The above gas-phase governing equations are non-dimensionalized by using

$$\xi = z/z_{\text{ref}}, \quad z_{\text{ref}} = \frac{m_{l,i} u_{l,i}}{4\pi R_i \overline{\rho D}} = \frac{R_i^2 \rho_l (1 - \phi_{m,i}) u_{l,i}}{3\overline{\rho D}},$$

$$\chi = x/L$$

to obtain the general relation

$$\frac{\partial J_k}{\partial \xi} - P_1 \frac{\partial^2 J_k}{\partial \chi^2} = \sum_{j=1}^N P_2 (S_{v,j,k} - S_{o,j,k}) + P_5 S_c \quad (6.14)$$

for  $k = 1, 2$  and  $3$ . In the preceding equation,  $J_1$ ,  $J_2$  and  $J_3$  are quantities proportional to the fuel mass fraction, oxygen mass fraction and gas temperature, respectively. In the calculations, the continuity equation is not solved and  $\rho u$  is assumed constant throughout. Thus, the thermal expansion is related to gas acceleration in the streamwise direction. The boundary conditions for Eqs. (6.14) are: impermeable and adiabatic walls ( $\partial T/\partial x = \partial Y_F/\partial x = \partial Y_O/\partial x = 0$ ), except for the region of constant heat flux at the left wall  $x = 0$ , as shown in Figure 6.1, and, specified fuel and oxygen mass fractions and gas temperature at the inlet  $\xi = 0$ .

## 6.2.2 Solution of the Gas-Phase Equations

The gas-phase conservation equations (6.14) are solved by a procedure similar to the one employed by Rangel and Sirignano [78] and hence only a brief outline is presented here. The appropriate Green's function needed to solve Eqs. (6.14) is first constructed by solving an auxiliary problem (see Özişik[65]) as:

$$G(\chi, \xi | \chi', \xi') = 1 + 2 \sum_{n=1}^{\infty} e^{-P_1 n^2 \pi^2 (\xi - \xi')} \cos(n\pi\chi') \cos(n\pi\chi) \quad (6.15)$$

The solution for  $J_k$  is then obtained as:

$$J_k(\chi, \xi) = \int_0^1 J_{k,i}(\xi') G(\chi, \xi | \chi', \xi') |_{\xi'=0} d\chi' + \int_0^{\xi} \sum_{j=1}^N P_2 (S_{v,j,k} - S_{o,j,k}) |_{\chi'=\chi_j} d\xi' \\ + \int_0^{\xi} \int_0^1 P_5 S_c G(\chi, \xi | \chi', \xi') d\chi' d\xi' + \int_0^{\xi} P_8 \dot{q}_w G(\chi, \xi | \chi', \xi') |_{\chi'=0} d\xi' \quad (6.16)$$

In the above equation, the four integrals represent the effects of the inlet conditions (at  $\xi = 0$ ), the vaporization/oxidation point sources located at  $\chi = \chi_j$ , the effects of energy release due to burning of the hydrocarbon, and the external heat flux imposed on the system, respectively. The last term does not exist for the species equations, i.e., for  $k = 1$  and  $2$ . As the source terms  $S_{v,k}$ ,  $S_{o,k}$ , and  $S_c$  are functions

of the dependent variables  $J_k$ , as well as the droplet variables, the integrals must be evaluated numerically. Noting the series nature of the Green's function, we let

$$J_k(\chi, \xi) = 1 + 2 \sum_{n=1}^{\infty} J_{kn}(\xi) \cos(n\pi\chi) \quad (6.17)$$

where the functions  $J_{kn}$  have to be determined. On substituting Eq. (6.15) in Eq. (6.16) and comparing with Eq. (6.17), we can get

$$\begin{aligned} J_{kn}(\xi) = & e^{-P_1 n^2 \pi^2 \xi} \int_0^1 J_{k,i}(\chi') \cos(n\pi\chi') d\chi' + \\ & \sum_{j=1}^N e^{-P_1 n^2 \pi^2 \xi} \int_0^{\xi} P_2 (S_{v,k} - S_{o,k}) e^{P_1 n^2 \pi^2 \xi'} d\xi' \cos(n\pi\chi_j) \\ & + e^{-P_1 n^2 \pi^2 \xi} \int_0^{\xi} e^{+P_1 n^2 \pi^2 \xi'} \int_0^1 P_5 S_c \cos(n\pi\chi') d\chi' d\xi' + e^{-P_1 n^2 \pi^2 \xi} \int_0^{\xi} e^{+P_1 n^2 \pi^2 \xi'} P_8 \dot{q}_w d\xi' \end{aligned} \quad (6.18)$$

By differentiating the above with respect to  $\xi$ , we obtain

$$\frac{dJ_{kn}}{d\xi} = \sum_{j=1}^N P_2 (S_{v,k} - S_{o,k}) \cos(n\pi\chi_j) + \int_0^1 P_5 S_c \cos(n\pi\chi') d\chi' + P_8 \dot{q}_w - P_1 n^2 \pi^2 J_{kn} \quad (6.19)$$

which is subject to the boundary conditions

$$J_{kn}(\xi = 0) = \int_0^1 J_{k,i}(\chi') \cos(n\pi\chi') d\chi' \quad (6.20)$$

for  $n = 0, 1, 2, \dots$ . A total of  $n$  numerical integrations must be performed at each axial step, and the choice of  $n$  is dependent upon desired accuracy. The results presented have been obtained with  $n = 16$ .

### 6.3 Droplet Analysis

The liquid-phase analysis uses the slurry droplet vaporization model developed in Chapter 4 and the aluminum burning droplet model developed in Chapter 5. The metal slurry is conceptualized as consisting of a suspension of small metal particles in a spherical liquid droplet (Figure 6.2). Figure 6.2 shows the vaporization sequence of the slurry droplet as proposed in Chapter 4. Stage I is characterized by surface regression;

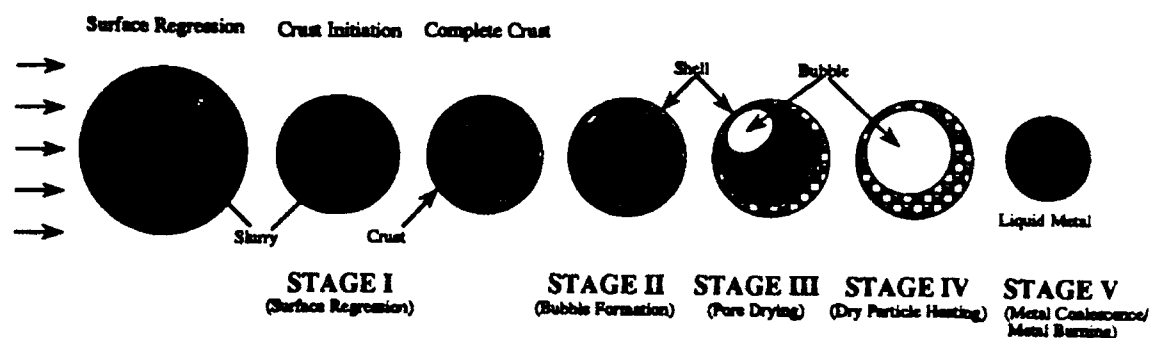


Figure 6.2: Schematic of the life history of the slurry droplets.

here the vaporization proceeds in a manner similar to that for pure liquid droplets (with modified droplet properties). The manner of further vaporization depends on the permeability and strength of the shell. The onset of shell formation (Stage II) is given by the appearance of a thin crust of solid particles forming on the droplet surface. The manner of liquid vaporization depends on the permeability, the effective pore radius, and the strength of the shell and, depending on these, several models exist (refer to Chapter 4). We employ the most general shell-bubble vaporization model. Further vaporization causes the shell thickness to grow, with formation of a bubble in the interior of droplet. The bubble is attached to the droplet surface and its diameter increases with time. When the shell thickness is at the maximum value, the drying of the pores starts (Stage III). Stage III involves the dry agglomerate heating and begins when all the liquid has evaporated. Stage V, is the metal coalescence and burning stage, and is characterized by the coalescence of the individual solid particles into a single molten droplet. A detached aluminum-oxygen flame then follows. The models for each of these stages have been described in previous chapters, and will be briefly mentioned here.

### Stage I: Surface Regression

The regression history of the slurry diameter due to hydrocarbon vaporization is dependent upon the initial solid loading. For higher initial solid loadings (with solid volume fractions close to  $\pi/6$ ), the slurry diameter may not regress at all. We shall consider the general case of low initial solid loading. A critical stage is reached

when the solids in the outermost layer cannot be compacted anymore and Stage II follows. We assume that the critical solid volume fraction corresponds to that for the most open packing (i.e.,  $\phi_{max} = \pi/6$ ) and the corresponding critical shell thickness is three times the solid particle diameter. The droplet density, conductivity, and specific heat have to be modified to reflect the solid-liquid mixture properties and they become dependent upon the radial position inside the droplet. During the surface regression stage, the droplet radius shrinks to a constant value, the droplet heats and the maximum temperature (which occurs at the surface) is limited by the liquid hydrocarbon boiling point, the hydrocarbon vaporization rate  $\dot{m}_{l,j} > 0$ , the oxygen consumption rate  $\dot{m}_{o,j} = 0$ , the sink/source terms  $\mathcal{L}_{eff} > 0$  and  $\mathcal{L}_{o,j} = 0$ . Details of the model can be found in Chapter 4.

### Stage II: Liquid Vaporization through the Shell

The phenomena during this stage are dependent upon the ambient pressure and temperature, the type of the liquid fuel, and the particle size. The porous shell is assumed to contain the solid particles in the shell thickness and the volume swept away due to vaporization. Here, we consider the more general permeable shell case with high ambient pressure, with the gas bubble consisting of fuel vapor and ambient gas attached to the droplet surface, whose diameter increases with hydrocarbon vaporization. The metal particles inside the droplet get further compacted and when the shell thickness reaches the maximum value Stage III vaporization commences. The dynamic and thermodynamic equilibria inside the droplet are satisfied by making pressure and energy balances on the bubble. For the purpose of heat transport calculations inside the slurry droplet, the bubble is placed spherically symmetric with respect to the droplet center. Thus, we can make a one-dimensional heat transfer calculation inside the droplet to determine the temperature profile. During the liquid vaporization though the shell stage, the external droplet radius remains constant, the bubble radius increases to a critical value, the droplet surface temperature is limited by the liquid hydrocarbon boiling point, the hydrocarbon vaporization rate  $\dot{m}_{l,j} > 0$ , the oxygen consumption rate  $\dot{m}_{o,j} = 0$ , the sink/source terms  $\mathcal{L}_{eff} > 0$  and  $\mathcal{L}_{o,j} = 0$ . Details of the model can be found in Chapter 4.

### Stage III: Pore Drying

Depending on the thickness of the shell, in general, there is still a substantial mass of liquid trapped in the pores of the agglomerate. We employ an expanding bubble-regressing liquid model. The bubble is allowed to expand in response to the effects of temperature increase, which changes gas density and the fuel mass fraction equilibrium inside the bubble. The liquid surface also regresses in the interior of the agglomerate pores. The thermal conductivity of the agglomerate is high; hence, the droplet temperature is assumed to be uniform. During the pore drying stage, the external and internal droplet radii remain constant, the droplet temperature (uniform) is limited by the liquid hydrocarbon boiling point, the hydrocarbon vaporization rate  $\dot{m}_{l,j} > 0$ , the oxygen consumption rate  $\dot{m}_{o,j} = 0$ , the sink/source terms  $\mathcal{L}_{\text{eff}} > 0$  and  $\mathcal{L}_{o,j} = 0$ . Details of the model can be found in Chapter 4.

#### Stage IV: Dry Agglomerate Heating

This stage commences on the complete vaporization of all the hydrocarbon fuel from the slurry droplet and so a dry agglomerate is left. The agglomerate heats rapidly, mostly due to strong convective heat flux from surrounding hot gases, until the phase change of aluminum occurs (at 933.1 K). During the phase change of aluminum, the particle temperature remains fixed. Melting of aluminum particles does not cause the individual particles to lose their identity, as the aluminum particles are enveloped by a protective coating of aluminum oxide, until the melting point of the oxide is reached,  $\sim 2325$  K, beyond which a detached aluminum vapor-oxygen flame results (Stage V). During the dry agglomerate heating stage, the external droplet radius shows a very small growth (due to surface oxidation of aluminum), the droplet temperature increases to the oxide melting point, the hydrocarbon vaporization rate  $\dot{m}_{l,j} = 0$ , the oxygen consumption rate  $\dot{m}_{o,j} > 0$ , the sink/source terms  $\mathcal{L}_{\text{eff}} = 0$  and  $\mathcal{L}_{o,j} > 0$ . Details of the model can be found in Chapters 2 and 3. To account for the enhanced surface area of an agglomerate in comparison to a smooth sphere, a surface area factor  $A_F = 2$  is employed, see Eq. (6.5). This factor represents the ratio of surface area of a hemisphere to its projected area.

#### Stage V: Coalescence and Metal Burning

At the aluminum oxide melting point, 2325 K, the protective coating enveloping the individual molten aluminum particles melts and retracts. The aluminum particles coalesce into a single droplet of molten aluminum. Aluminum vaporizes from the

droplet surface and the vapor reacts with oxygen in the gas phase. The aluminum burning phenomenon is similar to that of a hydrocarbon droplet burning, with the notable difference of product condensation. Aluminum oxides, diffusing in radially inwards and outwards direction from the detached flame, condense on the droplet surface and in form of "smoke" in the gas phase. A result is that the final droplet radius, which occurs when all the aluminum is vaporized and burnt, does not go to zero and is an outcome of continuous accumulation of aluminum oxide on the droplet surface. The model details for aluminum burning in oxygen environment can be found in Chapter 5. During the dry agglomerate heating stage, the external droplet radius shows a net decrease resulting from vaporization of aluminum and accumulation of aluminum oxide, the droplet temperature increases to a value significantly less than the prevailing aluminum boiling point, the hydrocarbon vaporization rate  $\dot{m}_{i,j} = 0$ , the oxygen consumption rate  $\dot{m}_{o,j} > 0$ , the sink/source terms  $\mathcal{L}_{eff} = 0$  and  $\mathcal{L}_{o,j} < 0$ .

#### Stage VI: Residual Particle Heating/Cooling

On completion of aluminum vaporization, due to accumulation of condensed oxides on the particle surface, the particle radius remains finite and this residual particle exchanges heat with the gas-phase. Depending on the particle and gas temperatures, the particle can heat or cool. To keep the analysis simple, we assume that no mass interactions occur between the particle and gas-phase.

## 6.4 Results and Discussion

Slurry droplets with initial radius  $50 \mu\text{m}$  and at  $300 \text{ K}$ , are injected into the combustion chamber with an initial velocity of  $40 \text{ m/s}$ . At the inlet, the air is at  $1 \text{ atm}$  and  $1000 \text{ K}$  with an oxygen mass fraction of  $0.23$  and velocity  $1 \text{ m/s}$ . The side walls of the channel of width  $1.5 \text{ cm}$  are insulated, except for a  $2 \text{ cm}$  long segment on the left wall (Figure 6.1) where a  $10 \text{ W/cm}^2$  flux is applied to serve as an ignition source. The liquid equivalence ratio, the metal particle radius, and the metal loading are amongst the parameters studied. The equivalence ratios stated are based upon the liquid content of the slurry droplet. The geometric arrangements include injection of one, three, or five streams of droplets.

We first study the general ignition characteristics of the slurry droplets injected in a single stream, at  $\chi = 0.5$ , which is mid-way in the transverse direction. Figure 6.3 shows the temperature contours for a liquid equivalence ratio of 0.3, initial gas temperature of 600 K, and solid loading of 10% by volume. A premixed hydrocarbon flame is seen to propagate from the left wall (see also temperature contour plots for injection of three or five streams, Figures 6.9 and 6.10). The flame depletes the fuel produced ahead of it and, as the droplets cross this reaction zone, further rapid vaporization occurs which results in this additional fuel vapor reacting in a diffusional manner. The mixture is more fuel rich at the stream location and oxygen is depleted first (also see Figure 6.5). The premixed flame results in local higher temperatures, as can be seen in Figure 6.6. The local gas temperature values reach about 3550 K. There are two reasons for this: first, the inlet gas temperature is high (1000 K) and, second, the wall heat flux results in higher temperatures than stoichiometrically attainable. The locally high temperature has been discussed in the earlier study by Rangel and Sirignano [79]. On completion of the liquid hydrocarbon vaporization, the hydrocarbon vapor (due to the finite rate chemistry) continues to react with the gas-phase oxygen, and the gas temperature at the plane of the stream keeps rising. From that plane, heat is lost by diffusion to the rest of the combustor and by convection to raise the temperature of the dry agglomerate. A maximum is reached at about  $\xi = 0.65$ . At this equivalence ratio, the rise in the gas-phase temperatures is insufficient to result in the ignition of the metal particle even though the local gas-phase temperatures can be significantly larger than the melting point of the oxide, which is the ignition criteria. The temperature then falls and would ultimately become uniform for large values of  $\xi$  (Figures 6.6, 6.11, and 6.12). The phenomenon of vaporization of the liquid hydrocarbon, and its subsequent oxidation, in case of slurry droplets is very similar to that for all-liquid droplets. For comparative results from all-liquid droplets, please refer to citeAgg84, Agg85, Ran86, Ran88, Ran89.

By varying the inlet gas temperature ( $T_\infty$ ) and the liquid equivalence ratio ( $\Phi_l$ ), it was found that, for a  $T_\infty = 600$  K, a minimum  $\Phi_l \approx 0.55$  is needed to cause the ignition of the metal agglomerate. For a  $T_\infty = 1000$  K, a minimum  $\Phi_l \approx 0.4$  is needed. All subsequent results are obtained with a  $T_\infty$  of 1000 K. Figure 6.4 shows the temperature contours for  $\Phi_l = 0.5$ , metal particle to initial droplet radius ratio of 0.04, and 10% initial loading of metal by volume. The difference between Figures 6.3

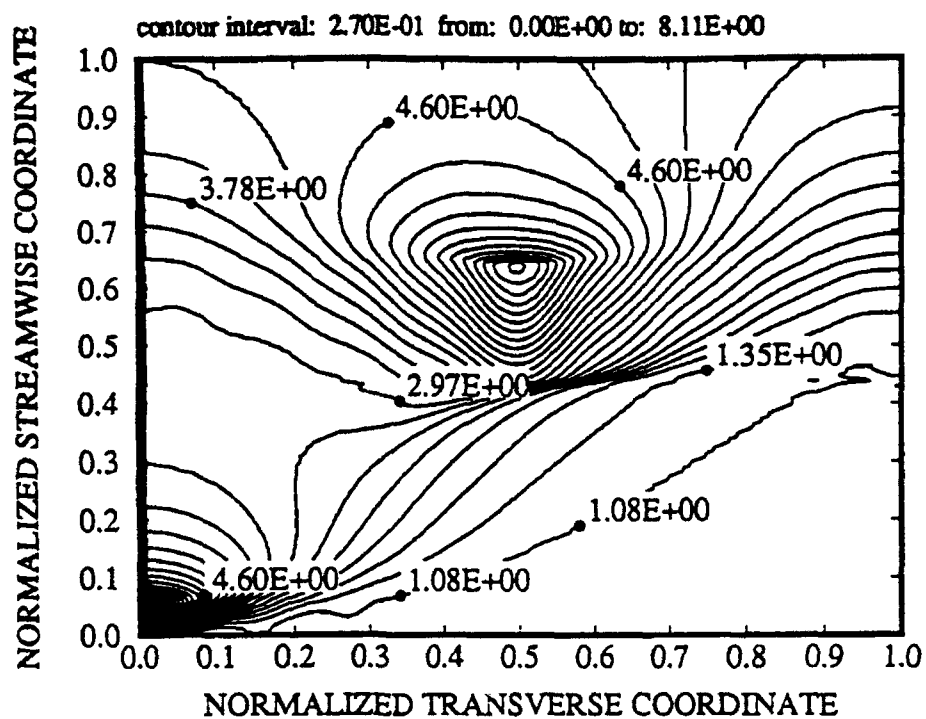


Figure 6.3: Gas-phase temperature contours for one stream injected at  $\chi = 0.5$ , liquid equivalence ratio  $\Phi_l = 0.3$ , and  $T_\infty = 600$  K.

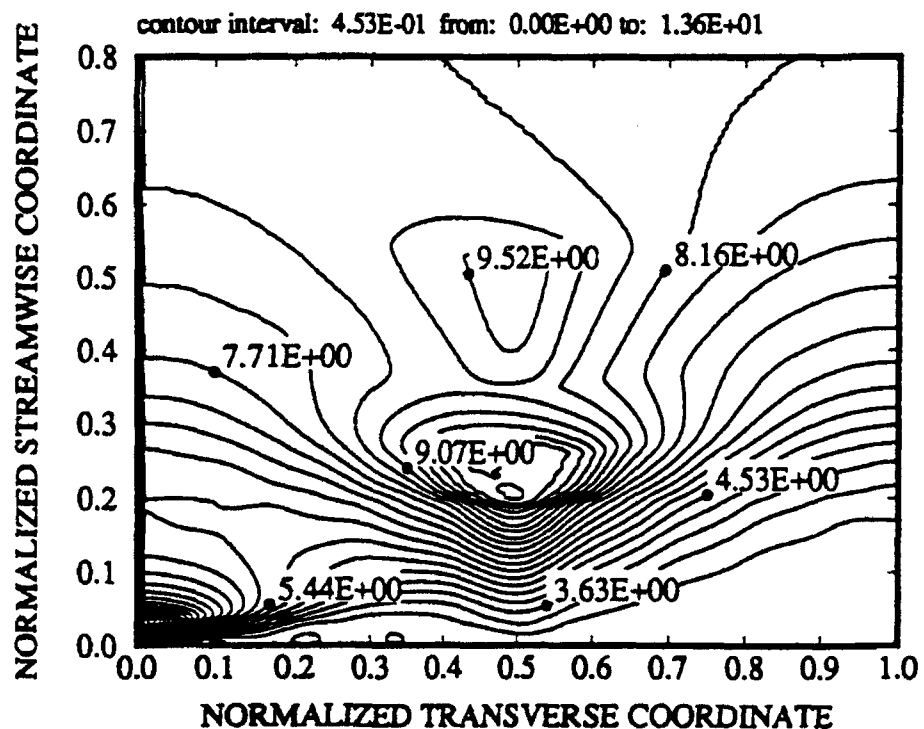


Figure 6.4: Gas-phase temperature contours for one stream injected at  $\chi = 0.5$ , liquid equivalence ratio  $\Phi_l = 0.5$ , and  $T_\infty = 1000$  K.

and 6.4 lies in the ignition and burning of the aluminum particle. A second peak results in the later figure, due to the burning of the aluminum particle. However, as the aluminum kinetics is very fast, only a diffusional flame is present, in contrast with the premixed-diffusional burning characteristic of the hydrocarbon fuel. In this case, the first peak occurs at about  $\xi = 0.25$  which corresponds to the end of hydrocarbon vaporization from the droplet, and the second peak occurs at about  $\xi = 0.52$  which corresponds to the end of aluminum burning.

Figures 6.5 and 6.6 show the transverse profiles of the gas-phase oxygen mass fraction and temperature, at various streamwise locations in the combustor.  $\xi = 0.1$  corresponds to about 5.9 cm streamwise length. Lower streamwise locations are closer to the fuel injection plane. Hence, relatively smaller amount of oxygen is consumed at these locations (Figure 6.5). Since our model accounts for the droplet transient heating, the thermal inertia of the droplets causes the fuel mass fractions to be lower near the plane of injection (not shown). The lower oxygen mass fractions are always located at the injection plane. By about  $\xi = 0.6$ , most of the reaction is completed, and the oxygen mass fraction, and the gas-phase temperature in Figure 6.6, have become approximately uniform. The temperature curves, Figure 6.6, are in trend opposite to those for oxygen, as higher temperatures result from increased consumption of oxygen. The temperatures near the left wall are higher due to the presence of the ignition source. The temperature rises along the streamwise direction due to the reaction of the octane vapor with oxygen, and also heat diffusion from the ignition source.

Figure 6.7 shows the droplet radius as a function of the streamwise coordinate, which is related to time by a Lagrangian formulation involving droplet velocity. Since the initial solid volumetric loading is 10%, there occurs a significant period of radius regression, after which the droplet external radius becomes constant. During the period of the heating of the dry agglomerate, from  $\xi = 0.26$  to 0.34, the agglomerate radius remains essentially fixed. At  $\xi = 0.34$ , the agglomerate ignites, the radius decreases as a result of the individual particles coalescing into a single molten aluminum droplet. Burning of the aluminum causes further radius reduction, until  $\xi = 0.53$ . Finally, as noted earlier, a fixed particle radius results from the accumulation of liquid aluminum oxide on the droplet. The final residual particle size, as noted in detailed modeling of a burning of a single aluminum particle in Chapter 5, has been

experimentally observed to be about 70% of the initial aluminum particle size. Here too, the same is observed. Figure 6.8 shows the droplet surface and the gas-phase temperatures at the injection plane. The droplet temperature is initially limited by the hydrocarbon wet bulb temperature and then rises to about 2500 K, which is the temperature at which most of the aluminum vaporizes. The flat portion at 933 K corresponds to the phase change of solid to liquid aluminum. After  $\xi = 0.53$ , the residual particle heats to an equilibrium temperature with the gas phase.

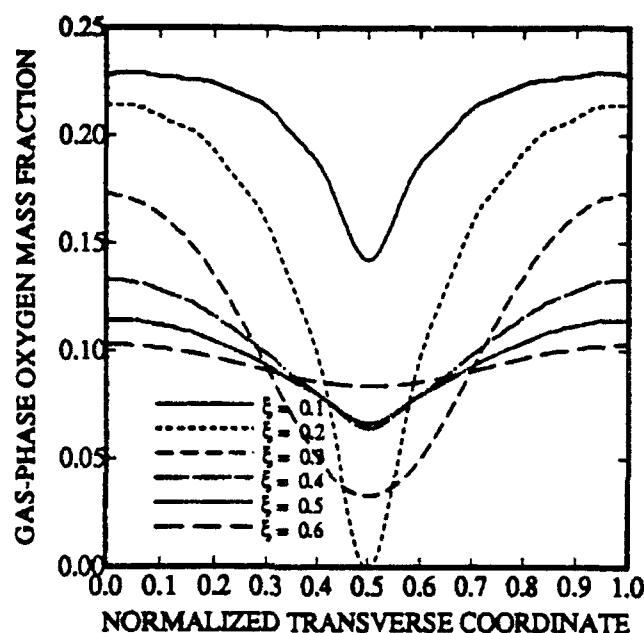


Figure 6.5: Gas-phase oxygen mass fraction versus normalized transverse coordinate ( $\chi$ ) at various streamwise locations ( $\xi$ ), for one stream injected at  $\chi = 0.5$ .

In the three streams case, the fuel injection locations are at  $\chi = 0.25, 0.50,$  and  $0.75$ . For five streams case, the fuel injection locations are  $\chi = 0.16, 0.32, 0.48, 0.64,$  and  $0.80$ . The temperature contours are shown in Figures 6.9 and 6.10. The stream closest to the left wall, where the heating source is, ignites first. Ignition occurs relatively early here, as the first stream is closer to the ignition source, and hence, the oxygen is consumed near the left wall first. The liquid equivalence ratio and the initial solid loading is kept the same, i.e., 0.5 and 10%, respectively. Increasing the number of streams results in a more even distribution of fuel and the premixed flame limit is approached. Almost all the fuel is depleted by  $\xi = 0.5$ . The resulting temperature profiles are flatter, compared to the single stream case, as shown by

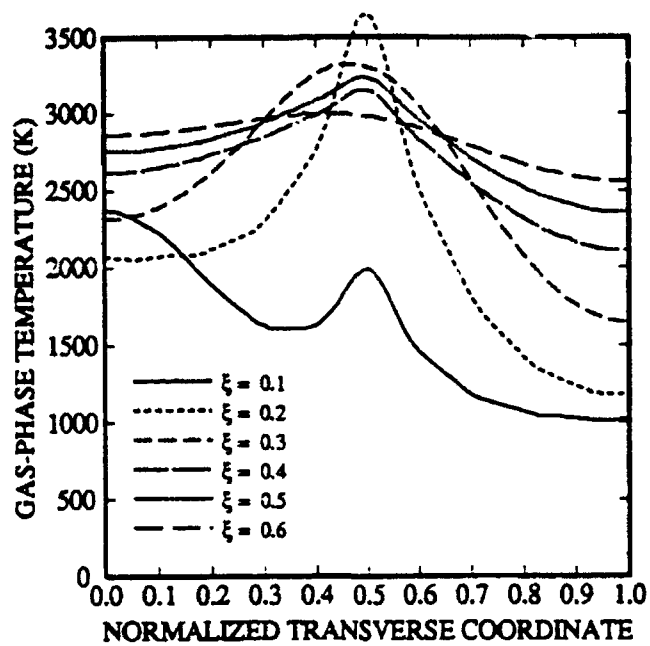


Figure 6.6: Gas-phase temperature versus normalized transverse coordinate ( $\chi$ ) at various streamwise locations ( $\xi$ ), for one stream injected at  $\chi = 0.5$ .

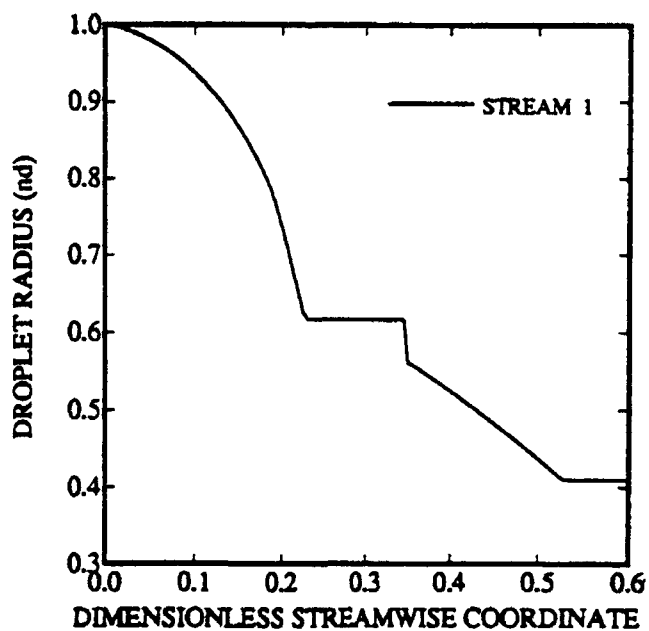


Figure 6.7: Droplet radius versus normalized streamwise coordinate ( $\xi$ ), for one stream injected at  $\chi = 0.5$ , liquid equivalence ratio  $\Phi_l = 0.5$ , and  $T_\infty = 1000$  K.

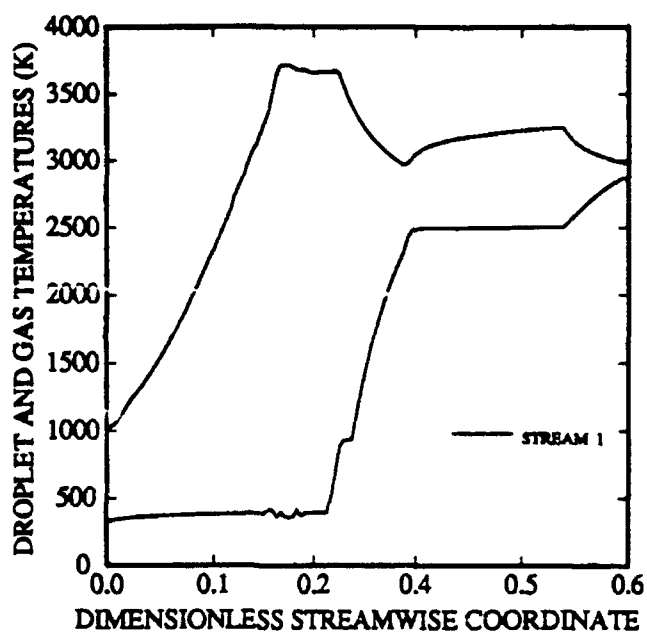


Figure 6.8: Droplet and gas-phase temperatures at  $\chi = 0.5$ , for one stream injected at  $\chi = 0.5$ , liquid equivalence ratio  $\Phi_l = 0.5$ , and  $T_\infty = 1000$  K.

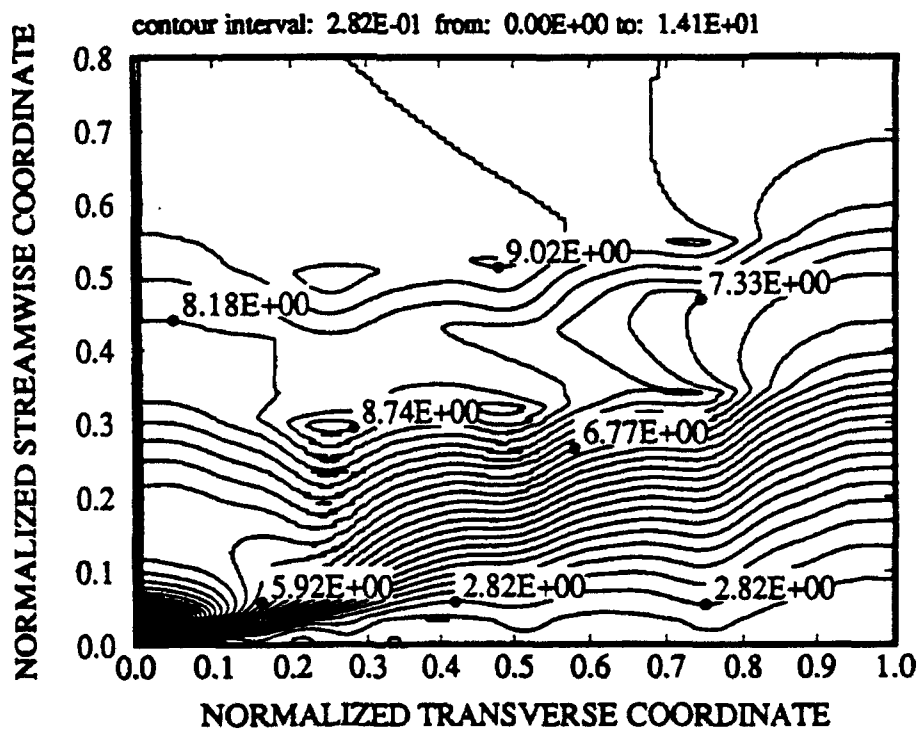


Figure 6.9: Gas-phase temperature contours for injection of three streams at  $\chi = 0.25, 0.50, \text{ and } 0.75$ ; and  $\Phi_l = 0.5, T_\infty = 1000$  K,  $\phi_{m,i} = 10\%$ , and  $r_m/r_{l,i} = 0.04$ .

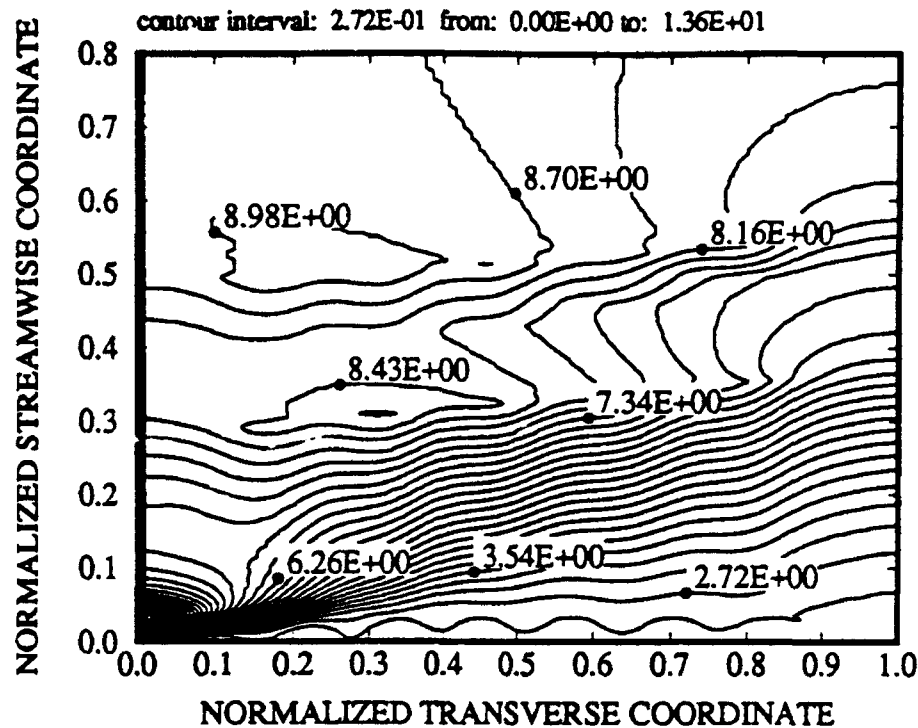


Figure 6.10: Gas-phase temperature contours for injection of five streams at  $\chi = 0.16$ , 0.32, 0.48, 0.64, and 0.80; and 0.75,  $\Phi_t = 0.5$ ,  $T_\infty = 1000$  K,  $\phi_{m,i} = 10\%$ , and  $r_m/r_{t,i} = 0.04$ .

Figures 6.11 and 6.12. The location and propagation of the premixed flame is evident from the contour plots in Figures 6.9 and 6.10. Similar results for hydrocarbon droplets are reported by Rangel and Sirignano [78, 79, 80] and also experimentally observed [75]. Ignition delay, reaction rates, and interaction between the premixed and diffusional flame structure are analyzed by them, and hence, not repeated here. We also find that the reactive flow is characterized by an inlet preignition zone followed by a premixed flame that acts as the overall global ignition source for the fuel streams. Downstream to this premixed flame, depending upon the number of streams being employed, a pattern of diffusion flames surrounding individual streams or groups emerges. This helps in rapid heating of the metal part subsequent to the completion of liquid fuel vaporization from the slurry droplet. Note that minimum gas inlet temperature/liquid fuel equivalence ratio requirements are not affected by the number of streams. Only small differences are seen on comparing the liquid hydrocarbon vaporization, agglomerate heating, and metal burning times for the multiple stream arrangement with those times for the single stream arrangement. In a practical sense, this means that it might suffice to study experimentally/analytically the single stream configuration in order to investigate the metal ignition characteristics. The

observation of the independence of the ignition delay and the burning of the metal part from the stream arrangement is in agreement with the known flame characteristics in these sprays, i.e., even though the initiation of the chemical reaction at a location is controlled by the local conditions, the overall ignition is dependent upon the global conditions of the spray [78].

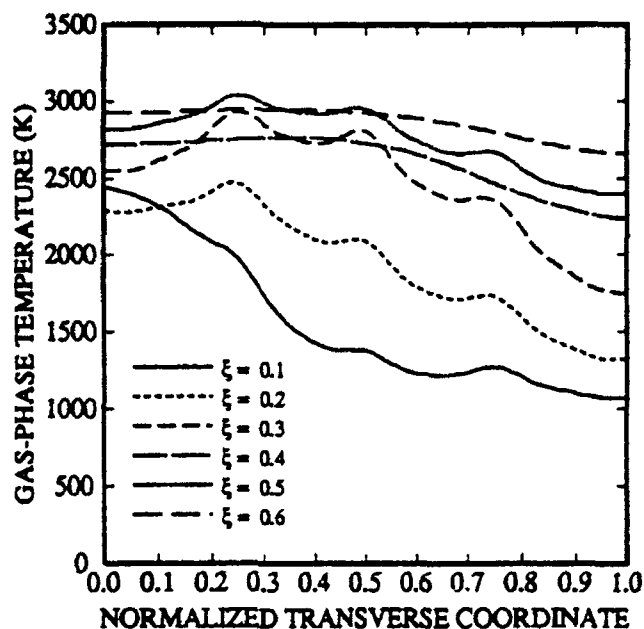


Figure 6.11: Gas-phase temperature versus normalized transverse coordinate ( $\chi$ ) at various streamwise locations ( $\xi$ ), for three stream injection.

The liquid hydrocarbon vaporization time, and additional times required to heat the dry agglomerate to ignition and burning of the metal, are shown in Figures 6.13 and 6.14. The times shown are cumulative. In Figure 6.13, we show the effect of increasing the solid loading, for  $\Phi_l = 0.5$ ,  $T_\infty = 1000$  K, one stream injection, and a fixed particle to initial droplet radius ratio of 0.02. Note that a 10% aluminum loading by volume corresponds to 30% loading by weight, and 25% by volume equals about 51% by weight. As expected, as the solid loading increases, the amount of liquid content of the slurry droplet is less, and it takes relatively less time to vaporize the liquid fuel from a slurry droplet with larger metal content. And for the same reason, the times taken to heat the agglomerate and burn the metal particle increase. The effect of varying the particle size while keeping the metal loading constant is shown in the Figure 6.14. As the relative particle size is increased, the external radius of the droplet that is attained in Stages II to IV, is smaller. Hence, the effective surface

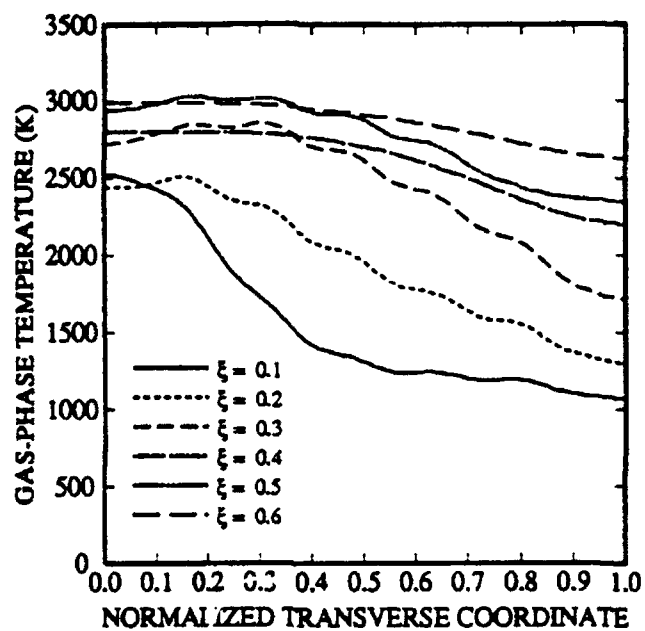


Figure 6.12: Gas-phase temperature versus normalized transverse coordinate ( $\chi$ ) at various streamwise locations ( $\xi$ ), for five stream injection.

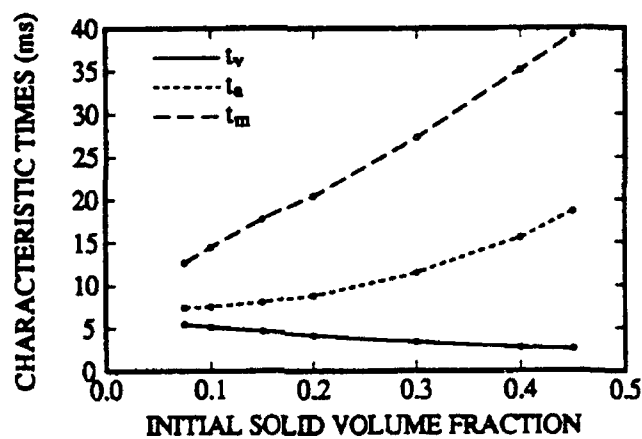


Figure 6.13: Comparison of liquid hydrocarbon vaporization time ( $t_v$ ), dry agglomerate heating time ( $t_a$ ), and the metal burning time ( $t_m$ ), for  $\Phi_l = 0.5$ ,  $T_\infty = 1000$  K, and  $r_m/r_{l,i} = 0.02$ .

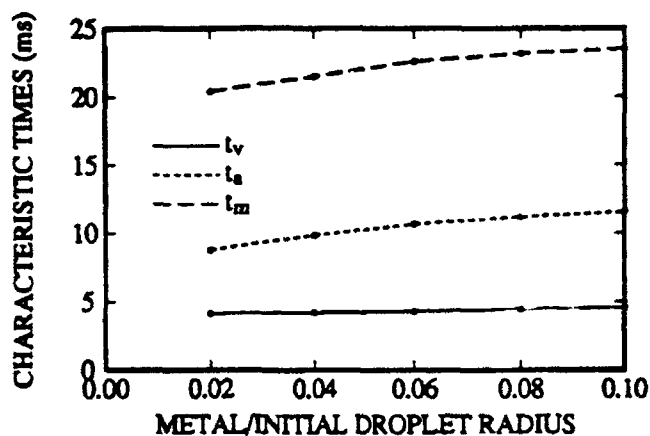


Figure 6.14: Comparison of liquid hydrocarbon vaporization time ( $t_v$ ), dry agglomerate heating time ( $t_a$ ), and the metal burning time ( $t_m$ ), for  $\Phi_i = 0.5$ ,  $T_\infty = 1000$  K, and initial metal loading  $\phi_{m,i} = 20\%$  by volume.

area is smaller and this results in a small increase in the time needed to heat the dry agglomerate to the ignition temperature of the aluminum agglomerate. The time required for burning of the metal is practically unaffected. Figures 6.13 and 6.14 also show that, depending upon equivalence ratio, gas inlet temperature, and slurry metal loading, the ignition and burning times for metal can be several times larger than the hydrocarbon vaporization time. Similar observations about the metal ignition and burning times have been known in past [111, 112, 98] and seen by us in Chapters 2 and 3. However, the preceding studies only analyzed isolated slurry droplets, hence to reach better quantitative numbers a spray calculation is essential. In Chapter 2, we found that for the isolated slurry droplets, the ambient air must be preheated to temperatures close to the melting point of the aluminum oxide ( $\sim 2315$  K) in order to ignite aluminum. Hence, the observation was made that typically the heat released from burning of the hydrocarbon from the *same* slurry droplet is insufficient to result in ignition. Heat released from the burning of the *other* droplets is necessary, thus making the spray calculation essential. Not surprisingly, in the Chapter 2, minimum inlet gas temperatures of about 2000 K were required to result in ignition, while in this study we have seen that the metal part can be ignited with inlet gas temperatures of about 1000 K.

## 6.5 Summary

An analytical and computational model of flame propagation in a two-dimensional arrangement of parallel slurry droplet streams injected into a hot gas has been presented. Using the simplifying assumptions of uniform pressure and neglect of transverse motion, the governing gas-phase equations are analytically integrated by using the Green's function approach and a resulting set of first order nonlinear ordinary differential equations is numerically solved. The droplet model included transient heating and particle drag, a shell-bubble formulation, and heating and ignition of the metal agglomerate subsequent to the vaporization of the liquid fuel, and burning of the metal.

Results obtained show that, at different combustor locations, interacting and distinct premixed and diffusion type reaction zones for the hydrocarbon are present. A premixed hydrocarbon vapor-air premixed flame is established close to the channel inlet and then acts as the ignition source for the droplets which cross it. Two diffusional flames then follow: first, for the burning of the remainder of the hydrocarbon fuel, and second, for the metal burning. The metal burns in a diffusional manner due to the faster aluminum-oxygen kinetics. Better mixing is obtained with arrangements using multiple injection streams. However, the effects of multiple streams on the ignition and burning characteristics of the slurry droplets are small, in comparison to single stream injection. The metal ignition and burning times are observed to be practically independent of the stream arrangement, thus implying that it might suffice to study experimentally/analytically the single stream configuration in order to investigate the metal ignition and burning characteristics. It is also found that the metal burning times increase with increased metal loading in the slurry, and on increasing the particle to initial droplet radius ratio. The spray calculation clearly demonstrates that, for a stream of slurry droplets, the minimum ambient temperature requirements to result in metal ignition are altogether different than those for a single isolated slurry droplet.

# Bibliography

- [1] Abraham, F. F., *Homogeneous Nucleation Theory*, Academic Press, New York, 1974.
- [2] Abramzon, B. and Sirignano, W. A., "Droplet Vaporization Model for Spray Combustion Calculations," *Int. J. Heat Mass Transfer*, Vol. 32, No. 9, 1989, pp. 1605-1618.
- [3] Aggarwal, S. K. and Sirignano, W. A., "Ignition of Fuel Sprays: Deterministic Calculations for Idealized Droplet Arrays," *Twentieth Symposium (International) on Combustion*, The Combustion Institute, Pittsburgh, 1984, pp. 1773-1780.
- [4] Aggarwal, S. K. and Sirignano, W. A., "Unsteady Flame Propagation in a Closed Volume," *Combust. and Flame*, Vol. 62, 1985, pp. 69-84.
- [5] Antaki, P. J., "Transient Process in a Rigid Slurry Droplet During Liquid Vaporization and Combustion," *Combust. Sci. and Tech.*, Vol. 46, 1986, pp. 113-135.
- [6] Antaki, P. J. and Williams, F. A., "Transient Process in a Non-Rigid Slurry Droplet During Liquid Vaporization and Combustion," *Combust. Sci. and Tech.*, Vol. 49, 1986, pp. 289-296.
- [7] Antaki, P. J. and Williams, F. A., "Observations on the Combustion of Boron Slurry Droplets in Air," *Combust. and Flame*, Vol. 67, 1987, pp. 1-8.
- [8] Aylmore, D. W., Gregg, S. J., and Jepson, W. B., "The Oxidation of Aluminum in Dry Oxygen in the Temperature Range 400-650 °C," *J. Inst. Metals*, Vol. 88, 1960, pp. 205-208.
- [9] Batchelor, G. K., *An Introduction to Fluid Dynamics*, Cambridge University Press, Cambridge, 1967.
- [10] Bird, R. B., Stewart, W. E. and Lightfoot, E. N. *Transport Phenomenon*, John Wiley & Sons, Inc., New York, 1960.
- [11] Brewer, L., and Searcy, A. W., "The Gaseous Species of the Al-Al<sub>2</sub>O<sub>3</sub> System," *Journal of American Chemical Society*, Vol. 73, 1951, pp. 5308-5314.

- [12] Brewster, M. Q., "Heat Transfer in Heterogeneous Propellant Combustion Systems," *Annual Review of Heat Transfer*, (C. L. Tien, Ed.), Vol. 4, 1992, pp. 287-330.
- [13] Brzustowski, T. A. and Glassman, I., "Vapor-Phase Diffusion Flames in the Combustion of Magnesium and aluminum: I. Analytical Developments," *Progress in Astronautics and Aeronautics* (H. G. Wolfhard, I. Glassman and L. Green Jr., Eds.), Academic Press, Vol. 15, 1964, pp. 75-115.
- [14] Brzustowski, T. A. and Glassman, I., "Vapor-Phase Diffusion Flames in the Combustion of Magnesium and Aluminum: II. Experimental Observation in Oxygen Atmospheres," *Progress in Astronautics and Aeronautics* (H. G. Wolfhard, I. Glassman and L. Green Jr., Eds.), Academic Press, Vol. 15, 1964, pp. 117-158.
- [15] Burns, R. P., "Systematics of Evaporation Coefficient  $\text{Al}_2\text{O}_3$ ,  $\text{Ga}_2\text{O}_3$ ,  $\text{In}_2\text{O}_3$ ," *Journal of Chemical Physics*, Vol. 44, No. 9, 1966, pp. 3307-3319.
- [16] Carey, V. P., *Liquid-Vapor Phase-Change Phenomena*, Hemisphere Publishing Company, Washington, 1992.
- [17] Charlesworth, D. H. and Marshall Jr., W. R., "Evaporation from Drops Containing Dissolved Solids," *A.I.Ch.E. Journal*, Vol. 6, No. 1, 1960, pp. 9-23.
- [18] Chervinsky, A., "Transient Burning of Spherical Symmetric Fuel Droplets," *Israel J. of Tech.*, Vol. 7, Nos. 1-2, 1969, pp. 35-42.
- [19] Cho, S. Y., Takahashi, F., and Dryer, F. L., "Some Theoretical Considerations on the Combustion and Disruption of Free Slurry Droplets," *Combust. Sci. and Tech.*, Vol. 67, 1989, pp. 37-57.
- [20] Chung, J. N., "The Motion of Particles Inside a Droplet," *J. Heat Transfer*, Vol. 104, 1982, pp. 438-445.
- [21] Clift, R., Grace, J. R., and Weber, M. E., *Bubbles, Drops and Particles*, Academic Press, New York, 1978.
- [22] Courtney, W. G., "Condensation in Nozzles," *Ninth Symposium (International) on Combustion*, The Combustion Institute, Pittsburgh, 1963, pp. 799-810.
- [23] Crespo, A. and Liñan, A., "Unsteady Effects in Droplet Evaporation and Combustion," *Combust. Sci. and Tech.*, Vol. 11, 1975, pp. 9-18.
- [24] Drowart, J., DeMaria, G., Burns, R. P. and Inghram, M. G., "Thermodynamic Study of  $\text{Al}_2\text{O}_3$ ," *Journal of Chemical Physics*, Vol. 32, No. 5, 1960, pp. 1366-1372.
- [25] Dwyer, H. A. and Sanders, B. R., "A Detailed Study of Burning Fuel Droplets," *Twenty-First Symposium (International) on Combustion*, The Combustion Institute, Pittsburgh, 1986, pp. 633-639.

- [26] Ermakov, V. A., Razdobreev, A. A., Skorik, A. I., Pozdeev, V. V., and Smollyakov, S. S., "Temperature of Aluminum Particles at the Time of Ignition and Combustion," *Comb. Expl. and Shockwaves*, Vol. 18, No. 2, 1982, pp. 256-257.
- [27] Farber, R. D., Srivastava, R. D. and Uy, O. M., "Mass Spectrometric Determination of the Thermodynamic Properties of Vapour Species from Alumina," *Journal of Chemical Society, Faraday Trans.*, Vol. 68, 1971, pp. 249-258.
- [28] Faeth, G. M., "Evaporation and Combustion of Sprays," *Prog. Energy and Combust. Sci.*, Vol. 9, 1983, pp. 1-76.
- [29] Fontijn, A. (Ed.) *Gas-Phase Metal Reactions*, North-Holland, Amsterdam, 1992.
- [30] Friedman, R., and Maček, A., "Ignition and Combustion of Aluminum Particles in Hot Ambient Gases," *Combust. and Flame*, Vol. 6, 1962, pp. 9-19.
- [31] Friedman, R., and Maček, A., "Combustion Studies of Single Aluminum Particles," *Ninth Symposium (International) on Combustion*, The Combustion Institute, Pittsburgh, 1963, pp. 703-712.
- [32] Fu, W.-B., Wei, J.-B., Han, H.-Q., and Zhang Y.-P., "A Study of the Evaporation and Ignition of a Single Coal-Water Slurry (CWS) Droplet," *Combust. Sci. and Tech.*, Vol. 43, 1985, pp. 67-83.
- [33] Garland, N. and Nelson, H. H., "Temperature Dependence of the Kinetics of the Reaction  $\text{Al} + \text{O}_2 \rightarrow \text{AlO} + \text{O}$ ," *Chemical Physics Letters*, Vol. 191, Nos. 3-4, 1992, pp. 269-272.
- [34] Glassman, I., "Combustion of Metals - Physical Considerations," *Progress in Astronautics and Aeronautics* (M. Summerfield, Ed.), Academic Press, Vol. 1, 1960, pp. 253-258.
- [35] Glassman, I., *Combustion*, 2nd Ed., Academic Press, Orlando, 1987.
- [36] Glassman, I. Personal communication, 1991.
- [37] Glassman, I. and Law, C. K., "Sensitivity of Metal Reactivity to Gaseous Impurities in Oxygen Environments," *Combust. Sci. and Tech.*, Vol. 80, 1991, pp. 151-157.
- [38] Glassman, I., "The Combustion Phase of Burning Metals," *Combust. and Flame*, Vol. 93, 1993, pp. 338-342.
- [39] Gomez, A. and Rosner, D. E., "Thermophoretic Effects on Particles in Counterflow Diffusion Flames," *Combust. Sci. and Tech.*, Vol. 89, 1993, pp. 335-362.

- [40] Gordon, S., McBride, B. J., and Zeleznik, F. J., "Computer Program for Calculation of Complex Chemical Equilibrium Compositions and Applications," NASA SP-273, 1976.
- [41] Green, D. W. and Maloney, J. O. (Eds.), "Perry's Chemical Engineers' Handbook," 6th Ed., McGraw-Hill, New York, 1984.
- [42] Hatch, J. E. (Ed.), "Aluminum Properties and Physical Metallurgy," American Society for Metals, Metals Park, OH, Ch. 1, 1984.
- [43] Hermsen, R. W., "Aluminum Combustion Efficiency in Solid Rocket Motors," *19th Aerospace Sciences Meeting*, St. Louis, AIAA Paper 81-0038, 1981.
- [44] Hinds, W. C. *Aerosol Technology: Properties, Behavior, and Measurement of Airborne Particles*, John Wiley & Sons, Inc., New York, 1982.
- [45] *JANAF Thermochemical Tables*, 3rd Ed., (R. C. West Ed.), American Chemical Society and American Institute of Physics, New York, 1985, Vo. 14.
- [46] Kaye, G. W. C. and Laby, T. H., "Tables of Physical and Chemical Constants," 15th Ed., Longman, London, 1986.
- [47] Kanury, A. M., "Introduction to Combustion Phenomenon," Gordon and Breach Science Publishers, New York, Ch. 5, 1975.
- [48] King, M. K., "Modeling of Single Particle Aluminum Combustion in CO<sub>2</sub>-N<sub>2</sub> Atmospheres," *Twelfth Symposium (International) on Combustion*, The Combustion Institute, Pittsburgh, 1978, pp. 1317-1328.
- [49] Kumagai, S., Sakai, T., and Okajima, S., "Combustion of Free Fuel Droplets in a Freely Falling Chamber," *Thirteenth Symposium (International) on Combustion*, The Combustion Institute, Pittsburgh, 1971, pp. 779-785.
- [50] Law, C. K., "A Simplified Theoretical Model for the Vapor-Phase Combustion of Metal Particles," *Combust. Sci. and Tech.*, Vol. 7, 1973, pp. 197-212.
- [51] Law, C. K., "Models for Metal Particle Combustion with Extended Flame Zones," *Combust. Sci. and Tech.*, Vol. 12, 1976, pp. 113-124.
- [52] Law, C. K., Chung, S. H., and Srinivasan, N., "Gas-Phase Quasi-Steadiness and Fuel Vapor Accumulation Effects in Droplet burning," *Combust. and Flame*, Vol. 38, 1980, pp. 173-198.
- [53] Law, C. K., "Recent Advances in Droplet Vaporization and Combustion," *Prog. Ener. Combust. Sci.*, Vol. 8, 1982, pp. 171-201.
- [54] Lee, A., Law, C. K., and Randolph, A. L., "Aerothermochemical Studies of Energetic Liquid Materials: 2. Combustion and Microexplosion of Droplets of Organic Azides," *Combust. and Flame*, Vol. 71, 1988, pp. 123-136.

- [55] Lee, A. and Law, C. K., "Gasification and Shell Characteristics in Slurry Droplet Burning," *Combust. and Flame*, Vol. 85, 1991, pp. 77-93.
- [56] Marcus, B. D., "Theory and Design of Variable Conductance Heat Pipes," NASA CR-2018, 1972.
- [57] Maček, A., "Fundamentals of Combustion of Single Aluminum and Beryllium Particles," *Eleventh Symposium (International) on Combustion*, The Combustion Institute, Pittsburgh, 1967, pp. 203-217.
- [58] Megaridis, C. M. and Sirignano, W. A., "Numerical Modeling of a Vaporizing Slurry Droplet," *AIAA Paper 90-0362*, 28<sup>th</sup> Aerospace Sciences Meeting, Reno, 1990.
- [59] Merzhanov, A. G., Grigorjev, Yu. M., and Gal'chenko, Yu. A., "Aluminum Ignition," *Combust. and Flame*, Vol. 29, 1977, pp. 1-14.
- [60] Miyasaka, K., and Law, C. K., "Combustion of Strongly-Interacting Droplet Arrays," *Eighteenth Symposium (International) on Combustion*, The Combustion Institute, Pittsburgh, PA, 1981, pp. 787-799.
- [61] Mikami, H., "Numerical Simulation of Nonequilibrium Condensation in Gas Dynamic Expansion," *PhysicoChemical Hydrodynamics*, Vol. 11, No. 4, 1989, pp. 441-453.
- [62] Mills, A. F. Personal communication, 1990.
- [63] Newton, G. H., Kramlich, J., and Payne, R., "Modeling the SO<sub>2</sub>-Slurry Droplet Reaction," *AIChE Journal*, Vol. 36, No. 12, 1990, pp. 1865-1872.
- [64] Nielsen, L. E., "Predicting the Properties of Mixtures: Mixture Rules in Science and Engineering," Marcel Dekker, Inc., New York, Ch. 3, 1978.
- [65] Ozişik, M. N., "Heat Conduction," John Wiley and Sons, New York, Ch. 6, 1980.
- [66] Patankar, S. V., "Numerical Heat Transfer and Fluid Flow," Hemisphere, New York, 1980, p. 44.
- [67] Peleg, M. and Alcock, C. B., "The Mechanism of Vaporization and the Morphological Changes of Single Crystals of Alumina and Magnesia at High Temperatures," *High Temperature Science*, Vol. 6, 1974, pp. 52-63.
- [68] Peleg, I. and Timnat, Y. M., "Combustion of Aluminum and Boron Slurry Fuels in a Dump Combustor," *Sixteenth Symposium (International) on Combustion*, The Combustion Institute, Pittsburgh, PA, 1982, pp. 557-563.
- [69] Petela, R., "Combustion of Mono-Fractional Droplets of Coal-Oil Mixtures," *Fuel*, Vol. 64, 1985, pp. 692-696

- [70] Polishchuk, D. I., Shevchuk, V. G., Velikanova, V. L., Goroshin, S. V., and Nechitailo, I. N., "Critical Ignition Conditions for Conglomerates of Aluminum Particles," *Combust. Expl. Shockwaves*, Vol. 14, No. 2, 1978, pp. 175-178.
- [71] Prakash, S., and Sirignano, W. A., "Theory of Convective Droplet Vaporization with Unsteady Heat Transfer in the Circulating Liquid Phase," *Int. J. Heat Mass Transf.*, Vol. 23, 1980, pp. 253-268.
- [72] Pratt, B. S. and Pratt, T. P., "An Interactive Computer Code for Calculation of Gas-Phase Chemical Equilibrium (EQLBRM)," NASA CR-168337, 1984.
- [73] Prentice, J. L., "Aluminum Droplet Combustion," Naval Weapons Center, China Lake, CA, Report No. TP 5569, 1974.
- [74] Price, E. W., "Combustion of Metalized Propellants," *Progress in Astronautics and Aeronautics* (K. K. Kuo and M. Summerfield, Eds.), Academic Press, Vol. 90, 1984, pp. 479-513.
- [75] Queiroz, M., "The Effect of Lateral Spacing on the Combustion Dynamics and Thermal Structure of an Array of Burning Droplet Streams," *Combust. Sci. and Tech.*, Vol. 72, 1990, pp. 1-16.
- [76] Queiroz, M., and Yao, S. C., "Experimental Exploration of the Thermal Structure of an Array of Burning Droplet Streams," *Combust. and Flame*, Vol. 82, 1990, pp. 346-360.
- [77] Rangel, R. H. and Sirignano, W. A., "Rapid Vaporization and Heating of Two Parallel Fuel Droplet Streams," *Twenty-First Symposium (International) on Combustion*, The Combustion Institute, Pittsburgh, PA, 1986, pp. 618-624.
- [78] Rangel, R. H. and Sirignano, W. A., "Two-Dimensional Modeling of Flame Propagation in Fuel Stream Arrangements," *Progress in Astronautics and Aeronautics* (A. L. Kuhl, R. J. Bowen, J. C. Leyer and A. Borisov, Eds.), Academic Press, Vol. 113, 1988, pp. 128-150.
- [79] Rangel, R. H. and Sirignano, W. A., "Unsteady Flame Propagation in a Spray with Transient Droplet Heating," *Twenty-Second Symposium (International) on Combustion*, The Combustion Institute, Pittsburgh, PA, 1988, pp. 1931-1939.
- [80] Rangel, R. H. and Sirignano, W. A., "Combustion of Parallel Fuel Droplet Streams," *Combust. and Flame*, Vol. 51, 1989, pp. 241-254.
- [81] Ride, D. R. (Ed. in Chief), "CRC Handbook of Chemistry and Physics," 72nd Ed., CRC Press, Boca Raton, 1991.
- [82] Sabnis, J. S., de Jong, F. J., and Gibeling, H. J., "A Two-Phase Distributed Combustion Model for Metalized Solid Propellants," *28th JANNAF Combustion Meeting*, San Antonio, 1991.

- [83] Salita, M., "Quench Bomb Investigation of  $\text{Al}_2\text{O}_3$  Formation from Solid Rocket Propellants (part II): Analysis of Data," *25th JANNAF Combustion Meeting*, CPIA 498, 1, pp. 185-197.
- [84] Sakai, T. and Saito, M., "Single Droplet Combustion of Coal Slurry Fuels," *Combust. and Flame*, Vol. 51, 1983, pp. 141-154.
- [85] Salita, M. Personal communication, 1991.
- [86] Sangiovanni, J. J., and Kesten, A. S., "Effect of Droplet Interaction on Ignition in Monodispersed Droplet Streams," *Sixteenth Symposium (International) on Combustion*, The Combustion Institute, Pittsburgh, PA, 1977, pp. 577-592.
- [87] Schlichting, H., "Boundary Layer Theory," 7th Edition, McGraw-Hill, New York, 1979, pp. 157-158.
- [88] Sirignano, W. A., "Fuel Droplet Vaporization and Spray Combustion Theory," *Prog. Energy and Combust. Sci.*, Vol. 9, 1983, pp. 291-322.
- [89] Spalding, D. B., "Theory of Particle Combustion at High Pressures," *ARS Journal*, Vol. 29, 1959, pp. 828-835.
- [90] Steinberg, T. A., Wilson, D. B. and Benz F., "The Combustion Phase of Burning Metals," *Combust. and Flame*, Vol. 91, 1992, pp. 200-248.
- [91] Steinberg, T. A., Wilson, D. B. and Benz F., "The Combustion Phase of Burning Metals - Response," *Combust. and Flame*, Vol. 93, 1993, pp. 343-347.
- [92] Stull, D. R. and Prophet, H., "JANNAF Thermochemical Tables," 2nd Edition, NSRDS-NBS 37, 1971.
- [93] Szekely, Jr., G. A. and Faeth, G. M., "Combustion Properties of Carbon Slurry Drops," *AIAA J.*, Vol. 20, 1982, pp. 422-429.
- [94] Szekely, Jr., G. A. and Faeth, G. M., "Effects of Carbon-Black Properties on Combustion of Carbon-Black Slurry Agglomerates," *Combust. and Flame*, Vol. 58, 1984, pp. 31-43.
- [95] Takahashi, F., Dryer, F. L., and Williams, F. A., "Combustion Behavior of Free Boron Slurry Droplets," *Twenty-First Symposium (International) on Combustion*, The Combustion Institute, Pittsburgh, 1983, pp. 1983-1991.
- [96] Takahashi, F., Heilweil, I. J., and Dryer, F. L., "Disruptive Burning Mechanism of Free Slurry Droplets," *Combust. Sci. and Tech.*, Vol. 65, 1989, pp. 151-165.
- [97] Tsai, J. H., and Sterling, A. M., "The Combustion of Linear Droplet Arrays in a Convective, Coaxial Potential Flow," *Combust. and Flame*, Vol. 86, 1991, pp. 189-202.

- [98] Turns, S. R., Wong, S.-C., and Ryba, E., "Combustion of Aluminum-based Slurry Agglomerates," *Combust. Sci. and Tech.*, Vol. 54, 1987, pp. 299-318.
- [99] Twardus, E. M., and Brzustowski, T. A., "An Experimental Study of Flame Speed and Burning in Arrays of Monosize Hydrocarbon Droplets," *Combust. Sci. and Tech.*, Vol. 17, 1978, pp. 215-222.
- [100] Umemura, A., "A Theoretical Study on the Unsteady, Interactive Combustion of a Linear Droplet Stream," *Twenty-Third Symposium (International) on Combustion*, The Combustion Institute, Pittsburgh, PA, 1990, pp. 1445-1453.
- [101] Vargaftik, N. B., "Tables on the Thermophysical Properties of Liquids and Gases," 2nd Edition, Hemisphere, New York, 1975.
- [102] Velikanova, V. L., Polishchuk, D. I., and Nechitailo, I. N., "Ignition Temperature of Conglomerates Formed After Burning-up of the Binder from Suspensions of Aluminum Powder in Kerosene," *Advances in Aerosol Physics*, Vol. 7, 1973, pp. 100-105.
- [103] Vilyunov, V. N., Vorozhtsov, A. B., and Feshchenko, Y. V., "Modeling of Two-Phase Flow of a Gas Mixture with Burning Metal Particles in a Semienclosed Channel," *Comb. Expl. and Shockwaves*, Vol. 25, No. 3, 1989, pp. 296-300.
- [104] Young, N. O., Goldstein, J. S., and Block, M. J., "The Motion of Bubbles in a Vertical Temperature Gradient," *J. Fluid Mech.*, Vol. 6, 1959, pp. 350-356.
- [105] Yuasa, S. and Takeno, T., "Ignition and Combustion of Magnesium-Aluminum Alloy Particle Clouds in a Hot Gas Stream," *Nineteenth Symposium (International) on Combustion*, The Combustion Institute, Pittsburgh, 1982, pp. 741-748.
- [106] Yuen, M. C. and Chen, L. W., "On Drag of Evaporating Liquid Droplets," *Combust. Sci. and Tech.*, Vol. 14, 1976, pp. 147-154.
- [107] Wartenberg, von H. v., "Zur Kenntnis der Tonerde," *Z. Anorg. Chem.*, Vol. 269, 1952, pp. 76-85
- [108] Westbrook, C. K. and Dryer, F. L., "Chemical Kinetic Modelling of Hydrocarbon Combustion," *Prog. Energy and Combust. Sci.*, Vol. 10, 1984, pp. 1-57.
- [109] Williams, F. A., "Combustion Theory," 2nd Edition, Benjamin/Cummings, Menlo Park, California, 1985.
- [110] Wilson Jr., R. P. and Williams, F. A., "Experimental Study of the Combustion of Single Aluminum Particles in O<sub>2</sub>/Ar," *Thirteenth Symposium (International) on Combustion*, The Combustion Institute, Pittsburgh, 1971, pp. 833-845.

- [111] Wong, S.-C. and Turns, S. R., "Ignition of Aluminum Slurry Droplets," *Combust. Sci. and Tech.*, Vol. 52, 1987, pp. 221-242.
- [112] Wong, S.-C. and Turns, S. R., "Disruptive Burning of Aluminum/Carbon Slurry Droplets," *Combust. Sci. and Tech.*, Vol. 66, 1989, pp. 75-92.

# Appendix A

## Ignition of Aluminum and Diffusivity of Oxygen through $\text{Al}_2\text{O}_3$

Several studies are available in the literature on the ignition of aluminum particles. Aylmore et al. [8] present results for oxidation of aluminum strips ( $3.5 \times 1 \times 0.08 \text{ cm}^3$ ) in dry oxygen in the temperature range 400–650 C. The oxidation rate is seen to decrease initially, then is constant, and then decrease again. They reach the conclusion that, even in the range 400–650 C, no quantitative analysis of the oxidation curves for aluminum can be given. Maček et al., in a series of papers (Friedman and Maček [30, 31]; Maček [57]), examine the ignition characteristics of small ( $< 100 \mu\text{m}$ ) aluminum particles, burning under varying oxygen concentrations, total pressure, and water vapor content. They reach the conclusion that ignition occurs when the layer of aluminum oxide formed by the surface reaction of aluminum breaks down by melting, which occurs at temperatures of  $\sim 2300 \text{ K}$ . They add that the dominant mode of heat transfer between the particle and the gaseous environment is heat conduction from the gas to the particle. Radiation effects are shown to be negligible during the pre-ignition process, surface heating effects are shown to be small, and it is experimentally concluded:

$$2300 - T_{\infty, i} = K p_{O_2}^n \quad (\text{A.1})$$

where  $T_{\infty, i}$  is the minimum ambient gas temperature for ignition,  $p_{O_2}$  is the partial pressure of oxygen (atm), and  $K$  and  $n$  are experimentally obtained as 140 and 0.41. The minimum ambient temperature is found to be practically independent of the particle size. This minimum ambient temperature requirement is further confirmed by Merzhanov et al. [59], who present an experimental study on the ignition of aluminum wires subjected to programmed electrical heating in a flow of gaseous oxidant. Their conclusion is that two different regimes of aluminum ignition are possible, one in which

the chemical interaction between the aluminum and oxidant is low (characterized by weak oxidants, thick initial films; and the minimum ambient temperatures are given by the equation above), and the second in which the chemical interaction is large. In the later case, the reaction rate is dependent upon the film thickness, and the film thickness growth for aluminum oxidation in pure  $O_2$  in the temperature range 1600–2000 C and 1 atm pressure is described by a parabolic model:

$$\frac{d\delta}{dt} = \frac{1.9 \times 10^{-5}}{\delta} \exp\left(-\frac{17000}{\mathcal{R}_g T}\right) \text{ cm/s}; \quad \mathcal{R}_g = 1.987 \text{ cal/mole-K} \quad (\text{A.2})$$

Transport of oxygen across the aluminum oxide is a complex process, involving ion transport. To obtain a diffusion coefficient for oxygen through the aluminum oxide, we use the Merzhanov's experimental data in the following manner. As the film growth rate can be expected to be proportional to the partial pressure of oxygen, in the absence of any better information, we assume that for aluminum oxidation in air

$$\frac{d\delta}{dt} \approx \frac{1.9 \times 10^{-5}}{\delta} \exp\left(-\frac{17000}{\mathcal{R}_g T}\right) X_{o_s} \text{ cm/s} \quad (\text{A.3})$$

where  $X_{o_s}$  denotes the oxygen mole fraction at the oxide-gas interface. The molecular weights of oxygen and the inerts are nearly identical, hence

$$X_{o_s} \approx Y_{o_s} \quad (\text{A.4})$$

where  $Y_{o_s}$  denotes the oxygen mass fraction at the oxide-gas interface. Now, consider the geometry of the problem as shown in the Figure 2.1. If we assume steady 1-dimensional Fickian diffusion of oxygen through the oxide layer, we will have

$$\frac{1}{r^2} \frac{d}{dr} \left( r^2 (\rho D)_{ox} \frac{dY_{o_s}}{dr} \right) = 0 \quad (\text{A.5})$$

with the boundary conditions:

$$\text{at } r = r_{Al}, Y_o = 0; \quad \text{and at } r = r_s, Y_o = Y_{o_s} \quad (\text{A.6})$$

Solution of the above equation yields

$$\dot{m}_o = 4\pi r_s^2 (\rho D)_{ox} \frac{dY_{o_s}}{dr} = \frac{4\pi (\rho D)_{ox} Y_{o_s}}{\frac{1}{r_{Al}} - \frac{1}{r_s}} \quad (\text{A.7})$$

Now, using Eq. 2.40, we assume: that  $r_s \approx r_m$ , where  $r_m$  is the initial metal radius; and further, that the change in the outer radius is small, to obtain

$$\dot{m}_o = \frac{32}{17} \pi \rho_{ox} r_m^2 \frac{d\delta}{dt} \quad (\text{A.8})$$

Eliminating  $\dot{m}_o$  from the last two equations gives

$$\delta \frac{d\delta}{dt} = \frac{17}{8} \mathcal{D}_{ox} Y_{o_s} \quad (\text{A.9})$$

Combining this with Eq. (A.3) yields

$$\mathcal{D}_{ox} = \frac{8}{17} 1.9 \times 10^{-5} \exp\left(-\frac{17000}{\mathcal{R}_g T}\right) \text{ cm}^2/\text{s} \quad (\text{A.10})$$

It is obvious that better data are needed to model the diffusivity. We checked the sensitivity of our calculations in Chapter 2 with regard to the above relation. It is found that increasing  $\mathcal{D}_{ox}$  by a factor of two increases the particle temperature by no more than 10%, and increasing the coefficient in the exponential term by a factor of two reduces the particle temperature by less than 10%.

## Appendix B

# Comments on "Sensitivity of Metal Reactivity to Gaseous Impurities in Oxygen Environments"

Glassman and Law [37], in a paper on metal reactivity, analyze the reactivity of aluminum with ambient oxygen concentration. They show that the metal reactivity can be very sensitive to the presence of small gaseous impurities in oxygen environment. Consider a spherical metal particle, such as aluminum, undergoing surface oxidation in an oxygen environment that also contains "impurity", i.e. an inert. For spherically-symmetric, quasi-steady, isobaric convection-diffusion of oxygen through the gas phase (see Fig. 2.1), we can show that the oxygen flow rate  $m_o$  is given by:

$$m_o = 4\pi(\rho\mathcal{D})_g r_s \ln \left\{ 1 + \frac{Y_{o,\infty} - Y_{o,s}}{1 - Y_{o,\infty}} \right\} \quad (\text{B.1})$$

where  $Y_o$  is the oxygen mass fraction and subscripts  $s$  and  $\infty$  denote the conditions at the droplet surface and far away. From stoichiometry, if  $\sigma$  denotes the stoichiometric coefficient, we have the metal consumption rate as:

$$m_o = \sigma m_F = \sigma 4\pi r_s^2 \rho_{Al} Y_{o,s} k_s \quad (\text{B.2})$$

where the assumption of first order reaction for  $Y_{o,s}$  is made and  $k_s$  is an unknown rate constant that is varied as a parameter. Eliminating  $Y_{o,s}$  in between above two relations, we get:

$$\bar{m}_o = \frac{m_o}{4\pi(\rho\mathcal{D})_g r_s} = \ln \left\{ 1 + \frac{Y_{o,\infty} - \frac{m_o}{\sigma 4\pi r_s^2 \rho_{Al} k_s}}{1 - Y_{o,\infty}} \right\} \quad (\text{B.3})$$

The above equation is solved iteratively for  $m_o$  and  $Y_{o,s}$ . The solution shows that  $Y_{o,s}$  increases exponentially, for high values of  $k_s$ , as  $Y_{o,\infty} \rightarrow 1$ .

Above formulation considers only the the gas-phase resistance to the mass transfer. For aluminum particles, at temperatures below the oxide melting point ( $\sim 2315$  K), the growth of the oxide film on the particle surface resists further oxidation. Refer to Fig. 2.1, which shows the oxide film growing on the surface of an aluminum particle. The gas-phase oxygen conservation yields Eq. (1). Diffusion of oxygen through the shell of the solid aluminum oxide yields:

$$m_o = 4\pi(\rho D)_{ox} \frac{r_s r_{Al}}{r_s - r_{Al}} Y_{o,s} \quad (\text{B.4})$$

Elimination of  $Y_{o,s}$  gives:

$$\bar{m}_o = \frac{m_o}{4\pi(\rho D)_g r_s} = \ln \left\{ 1 + \frac{Y_{o,\infty} - \frac{m_o(r_s - r_{Al})}{4\pi r_s r_{Al}(\rho D)_{ox}}}{1 - Y_{o,\infty}} \right\} \quad (\text{B.5})$$

which can be solved iteratively for  $m_o$ . The rate of growth of the oxide film can be obtained by stoichiometry of the reaction  $2 \text{Al} + 3 \text{O} \rightarrow \text{Al}_2\text{O}_3$ , requiring that 9 kg of aluminum are consumed for each 8 kg of oxygen, such that:

$$\frac{d}{dt} \left\{ \frac{4}{3} \pi \rho_{Al} r_{Al}^3 \right\} = -\frac{9}{8} m_o \quad (\text{B.6})$$

Similarly, as 17 kg of oxide shell are formed for each 8 kg of oxygen consumed, the outer radius of the particle is given by:

$$\frac{d}{dt} \left\{ \frac{4}{3} \pi \rho_{ox} (r_s^3 - r_{Al}^3) \right\} = \frac{17}{8} m_o \quad (\text{B.7})$$

The diffusivity of oxygen through the solid oxide is given by:

$$\mathcal{D}_{ox} = \frac{8}{17} 1.9 \times 10^{-5} \exp \left( -\frac{17,000}{\mathcal{R}_g T} \right) \text{ cm}^2/\text{s} \quad (\text{B.8})$$

This result for diffusivity is based on experimental data of Merzhanov [59]. Presumably, it contains the effects of both chemical oxidation and diffusion through the oxide with discontinuity of oxygen concentration across the gas-oxide interface (phase equilibrium). To determine the surface temperature, an ordinary differential equation may be solved for energy transport in the gas phase, with the particle temperature assumed to be uniform.

This approach, for particle temperatures below the oxide melting point, eliminates the need to assume a rate constant  $k_s$  and includes the resistance to oxygen transport due to the film growth (in addition to the gas-phase resistance). The main conclusion of reactivity increasing exponentially with  $Y_{o,\infty}$  is probably not affected.

# Appendix C

## Solution of a Model

### One-Dimensional Transpiration

### Problem

This section concerns the model assumption of rapid condensation of the aluminum oxide vapor formed during the combustion of the aluminum particles, made in Chapter 5. The condensation results in "smoke," experimentally observed suspension of about  $1 \mu m$  particles of liquid aluminum oxide which are ultimately convected by the carrier gas flow.

We consider a model transpiration problem where one phase condenses amidst a non-condensable gas flow in counter-current direction. A schematic of the problem is shown in Figure C.1. Consider two parallel walls held at specified fixed temperatures  $T_L$  and  $T_R$ , with  $T_L > T_R$ . At the left boundary, the bulk temperature is higher than the saturation temperature of the oxide vapor, under prevalent physical conditions. This prevents the condensation of the oxide at the left wall. Oxygen flows from the right wall towards the left wall where it gets consumed. The mass flux of the oxygen is constant. The condensable oxide vapor flows from the left wall towards the right wall. Nitrogen is also present in the system and it is stationary. In the near left wall region, the mass flux of the oxide is greater than the mass flux of oxygen, so that the net mass flux or the gas velocity is positive. After some distance  $x_c$  from the left wall, the saturation conditions are such that condensation starts. As condensation occurs, the oxide vapor mass flux drops and the oxide liquid mass flux increases. The gas velocity in the near right wall region could become negative if sufficient vapor condenses. The left wall is a crude approximation to a diffusion flame resulting from the reaction of aluminum vapor and oxygen, and the right wall represents conditions far away from the flame.

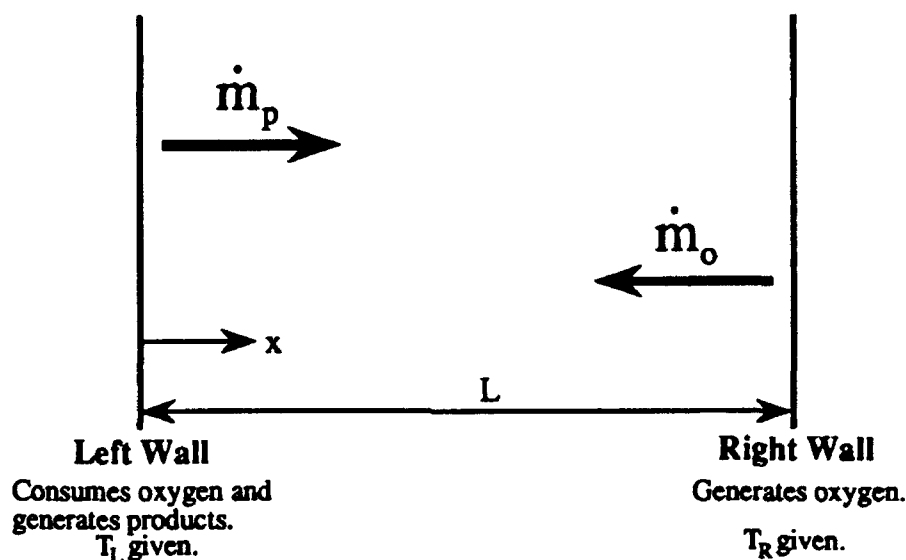


Figure C.1: A model transpiration problem. Oxide vapor flows from left to right, and oxygen flows from right to left.

In our context, condensation is usually of two kinds: (i) heterogeneous, where a large concentration of particles or ions ("seed") is present; condensation occurs on the existing particles without formation of a new nuclei, and (ii) homogeneous nucleation, where no foreign particles or ions are present. Homogeneous nucleation requires that the oxide vapor be supersaturated, small clusters of molecules or embryos form, and vapor condense on these embryos so that it grows into a nucleus and ultimately a droplet. In heterogeneous condensation, vapor condenses on the seed particles to make a nucleus, and lower supersaturations are needed. No studies of Wilson cloud chamber type on the condensation of aluminum oxide vapor could be found. It has been well known that for water vapor, supersaturations of 2 to 5 have been obtained under different experimental conditions [1, 16]. In our model problem, by prescribing a large temperature difference between the two walls, we impose a large thermal gradient. Hence, the saturation values increase very rapidly in a very short distance, and we make the assumption that condensation commences upon saturation conditions being met.

We seek to resolve the mass fractions and fluxes of various species in the core region where the condensation occurs. A Damköhler number governing the phenomenon is identified. The model assumption used in constructing the burning model for an aluminum particle, i.e., the assumption of complete oxide condensation at the saturation conditions, is equivalent to an infinite Damköhler number. An analytical solution

is obtained for the infinite Damköhler number problem and the results for different rate constants are compared.

Here, we are interested in the steady-state solution. The governing equations for the one-dimensional problem are

$$\frac{\partial}{\partial x}\{\rho u\} = -\dot{w}_c \quad (\text{C.1})$$

$$\frac{\partial}{\partial x}\left\{\rho u Y_o - \rho \overline{D} \frac{\partial Y_o}{\partial x}\right\} = 0 \quad (\text{C.2})$$

$$\frac{\partial}{\partial x}\left\{\rho u Y_p - \rho \overline{D} \frac{\partial Y_p}{\partial x}\right\} = -\dot{w}_c \quad (\text{C.3})$$

$$\frac{\partial}{\partial x}\left\{\rho u Y_n - \rho \overline{D} \frac{\partial Y_n}{\partial x}\right\} = 0 \quad (\text{C.4})$$

$$\frac{\partial}{\partial x}\left\{\rho u C_p T - k \frac{\partial T}{\partial x}\right\} = -\dot{w}_c h_{fg} \quad (\text{C.5})$$

$$\dot{w}_c = kS(Y_p - Y_{p,sat}) \quad (\text{C.6})$$

$$\rho = p\overline{M}/\mathcal{R}_u T \quad (\text{C.7})$$

In the above equations  $\rho$  and  $u$  are the bulk gas density and velocity,  $\dot{w}_c$  is the volumetric rate of condensation the oxide vapor,  $Y_o$ ,  $Y_p$ , and  $Y_n$  are the oxygen, oxide vapor, and nitrogen (inert gases) mass fractions respectively,  $T$  is the gas temperature and  $h_{fg}$  is the heat of vaporization of the oxide vapor. Quantity  $k$  represents a rate constant for the condensation and  $S$  is the surface area of condensation per unit volume of the two-phase mixture. Quantities  $k$  and  $S$ , assumed constant for the purpose of this illustrative problem, do themselves depend upon the physical properties of the substances and the prevalent conditions in a complicated and not well understood manner (e.g., refer to [1, 16, 22, 61]).

For our purposes, as the bulk velocity of the carrier gas is very low as compared to a supersonic expansion in a nozzle, say, the characteristic residence time is very large. This feature results in larger Damköhler numbers and thus the assumption of constant  $kS$  becomes justified in the sense that the results obtained are expected to be independent of Damköhler number for the large Damköhler number values. The Lewis number is assumed to be unity. The above equations are nondimensionalized by using  $\xi = x/L$ , and the nondimensional fluxes are then  $M_g = \rho u L / \overline{\rho D} = M_p + M_o$ ,  $M_p = \dot{m}_p L / \overline{\rho D}$ , and  $M_o = \dot{m}_o L / \overline{\rho D}$ . The Damköhler number is  $Da = kSL^2 / \overline{\rho D}$ . The nondimensional equations are

$$\frac{dM_g}{d\xi} + Da(Y_p - Y_{p,sat}) = 0 \quad (\text{C.8})$$

$$\frac{dY_o}{d\xi} - M_g Y_o + M_o = 0 \quad (\text{C.9})$$

$$\frac{d(1 - Y_p)}{d\xi} - M_g(1 - Y_p) + M_o = 0 \quad (\text{C.10})$$

$$\frac{d^2\beta}{d\xi^2} - M_g \frac{d\beta}{d\xi} + Da(Y_p - Y_{p, sat})\beta = 0 \quad (C.11)$$

where  $\beta = \frac{c_p(T-T_R)}{h_{fg}} + Y_p$ . The subscripts  $L$  and  $R$  refer to conditions at the left and the right wall respectively. The boundary conditions for the above equations are:

- (a) for oxygen conservation, the mass flux  $\dot{m}_o$  is specified at the right wall along with the mass fraction at the right wall  $Y_{o,R}$ . Note that  $\dot{m}_o$  is constant everywhere.
- (b) for vapor oxide conservation, the mass flux  $\dot{m}_p$  is specified at the left wall along with the mass fraction at the left wall  $Y_{p,L}$ .  $\dot{m}_p$  goes down in axial direction as the oxide condenses.
- (c) for energy conservation, the temperatures  $T_L$  and  $T_R$  are specified.

Equations (C.8) to (C.10) are solved by a fourth-order accurate Runge-Kutta scheme. Eq. (C.11) is solved by second-order accurate finite differences. An analytical solution without vapor oxide condensation is constructed, and the initial temperature and mass fraction profiles are obtained, and are then iterated upon. The solution converges within a few (say 5) iterations.

The results from the above calculations are shown in Figures C.2 to C.9. The figures show the temperature and mass fraction profiles, nondimensional mass fluxes and dimensional bulk gas velocity. For the cases of small Damköhler numbers, Figures C.2 and C.3 for  $Da = 1$ , and Figures C.2 and C.3 for  $Da = 10$ , only a small amount of oxide vapor condenses. For  $Da = 1$ , very little oxide condenses, and the profiles are diffusion controlled, as the convection is very weak. On increasing the  $Da$  to 10, somewhat more, but still not all, of the oxide vapor condenses.

Physically we can expect the Damköhler number to be very large, i.e., the condensation occurs very rapidly. At  $Da = 100$ , shown in Figures C.6 and C.7, all of the oxide vapor condenses in the problem width. The condensation starts at about  $\xi = 0.68$  and all of the oxide has condensed by  $\xi = 0.78$ . The oxide mass fraction terminates at this point, as virtually no more oxide exists in the gas phase. Note that liquid droplets, which essentially are at the local gas velocity, will accumulate at the point of zero velocity at  $\xi = 0.76$ . Upon increasing the  $Da$  number to 1000 similar profiles are observed, as shown in Figures C.8 and C.9. The condensation zone has a much shorter width. The temperature and mass fraction profiles show very little change, from the case for  $Da = 100$ .

To compare the finite Damköhler number cases with the assumption of infinitely fast condensation made in developing the aluminum burning model, an analytical solution was found in a manner similar to the one used in Chapter 5. All the condensation is assumed to occur at the location ( $\xi_c$ ) where the gas temperature is equal

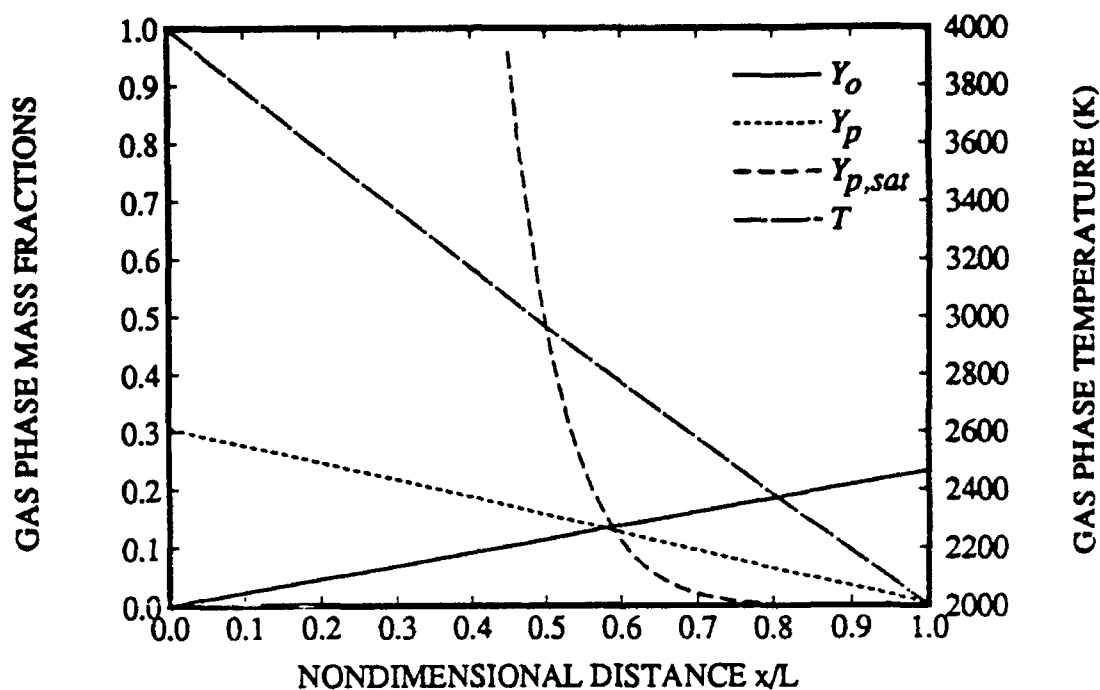


Figure C.2: Oxygen  $Y_o$  and vapor oxide  $Y_p$  mass fractions and gas temperatures  $T$  for  $Da = 1.0$ . Also shown is saturation oxide mass fraction  $Y_{p,sat}$ .

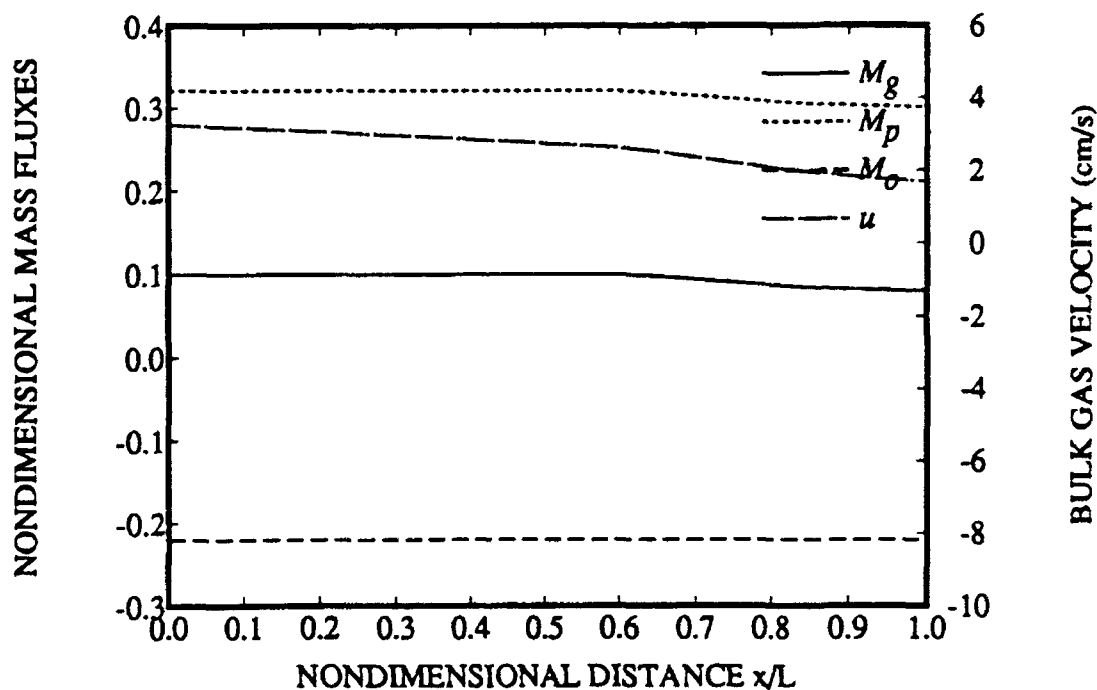


Figure C.3: Nondimensional mass fluxes of oxygen  $M_o$ , oxide vapor  $M_p$  and bulk gas  $M_g = M_o + M_p$  for  $Da = 1.0$ . Also shown is dimensional gas velocity  $u$ .

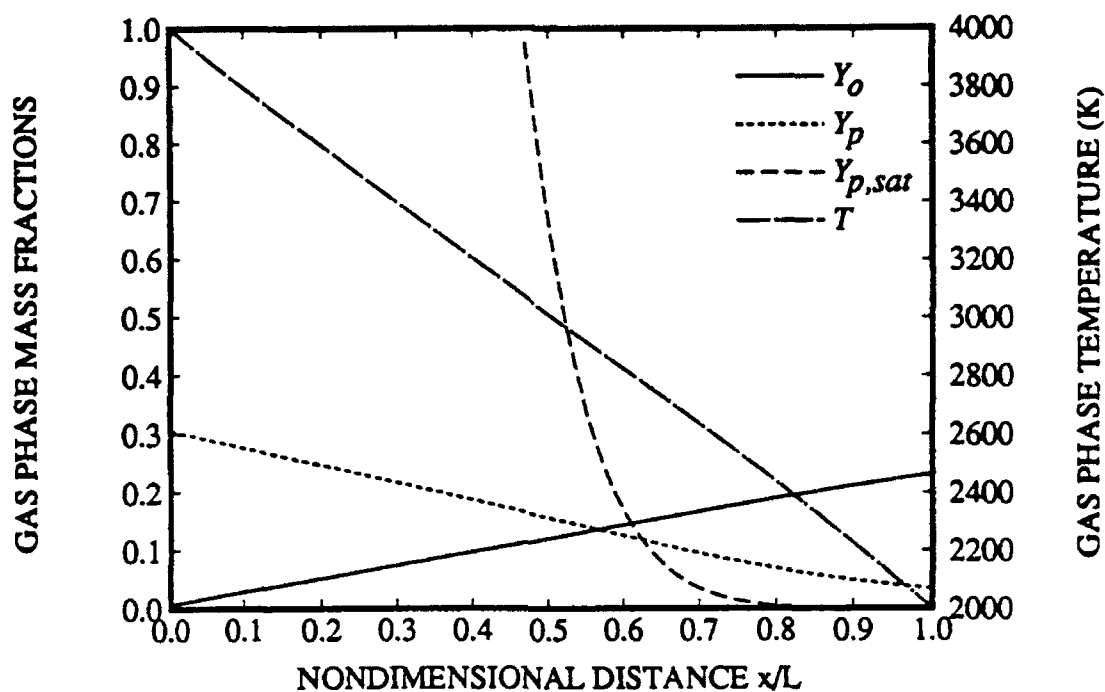


Figure C.4: Oxygen  $Y_o$  and vapor oxide  $Y_p$  mass fractions and gas temperatures  $T$  for  $Da = 10.0$ . Also shown is saturation oxide mass fraction  $Y_{p,sat}$ .

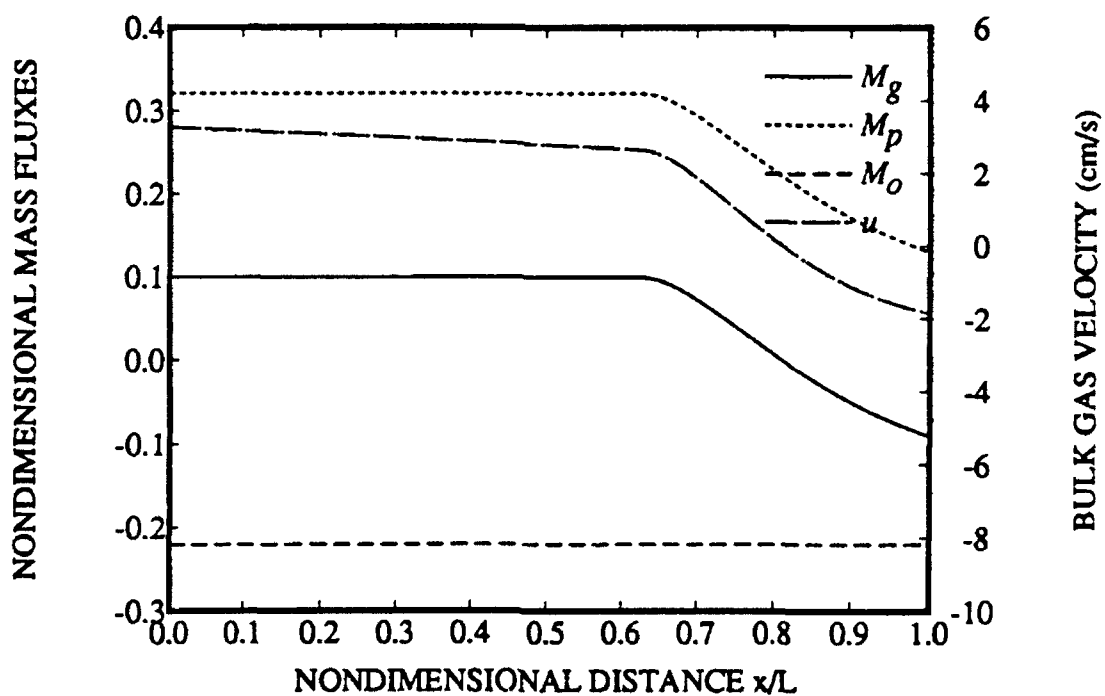


Figure C.5: Nondimensional mass fluxes of oxygen  $M_o$ , oxide vapor  $M_p$  and bulk gas  $M_g = M_o + M_p$  for  $Da = 10.0$ . Also shown is dimensional gas velocity  $u$ .

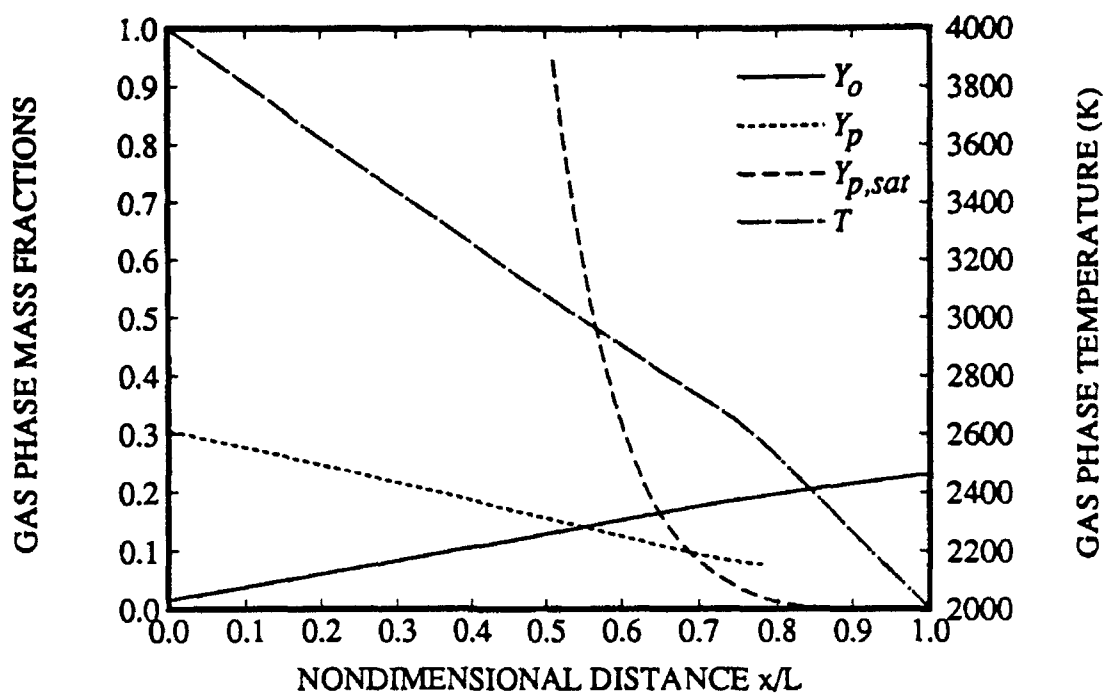


Figure C.6: Oxygen  $Y_o$  and vapor oxide  $Y_p$  mass fractions and gas temperatures  $T$  for  $Da = 100.0$ . Also shown is saturation oxide mass fraction  $Y_{p,sat}$ .

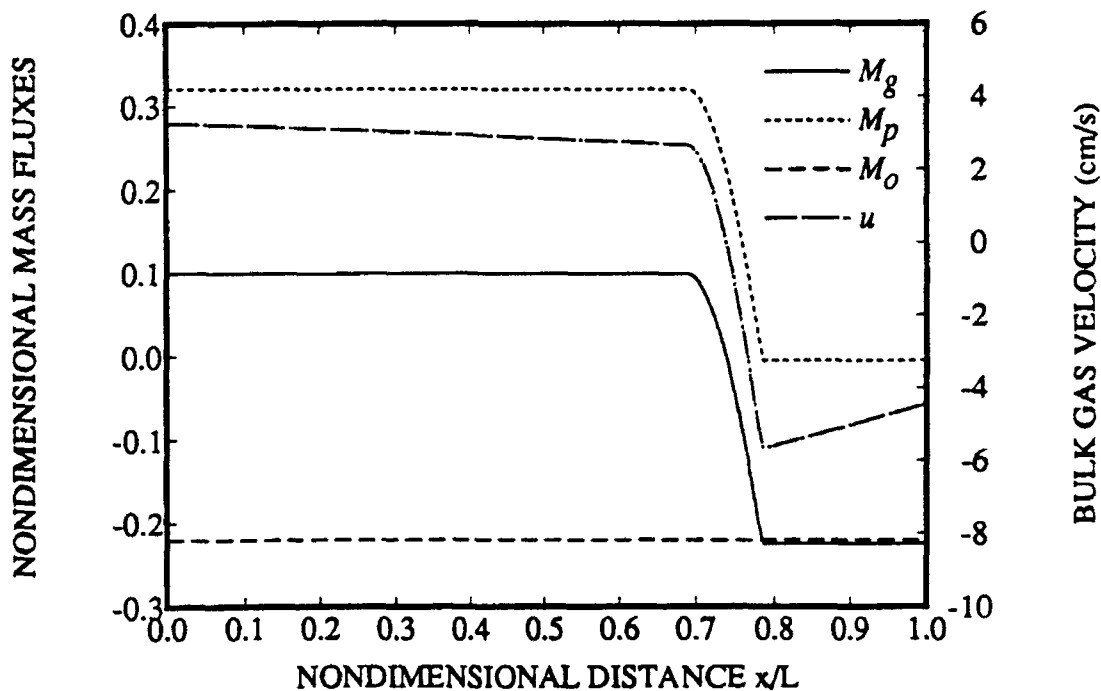


Figure C.7: Nondimensional mass fluxes of oxygen  $M_o$ , oxide vapor  $M_p$  and bulk gas  $M_g = M_o + M_p$  for  $Da = 100.0$ . Also shown is dimensional gas velocity  $u$ .

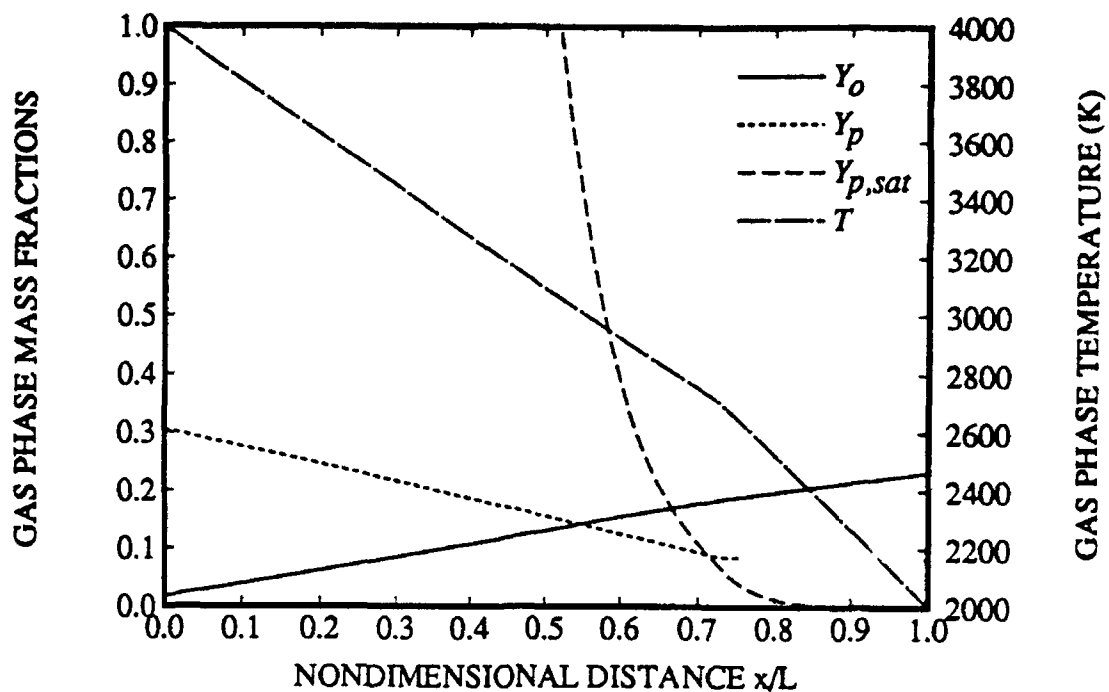


Figure C.8: Oxygen  $Y_o$  and vapor oxide  $Y_p$  mass fractions and gas temperatures  $T$  for  $Da = 1000.0$ . Also shown is saturation oxide mass fraction  $Y_{p,sat}$ .

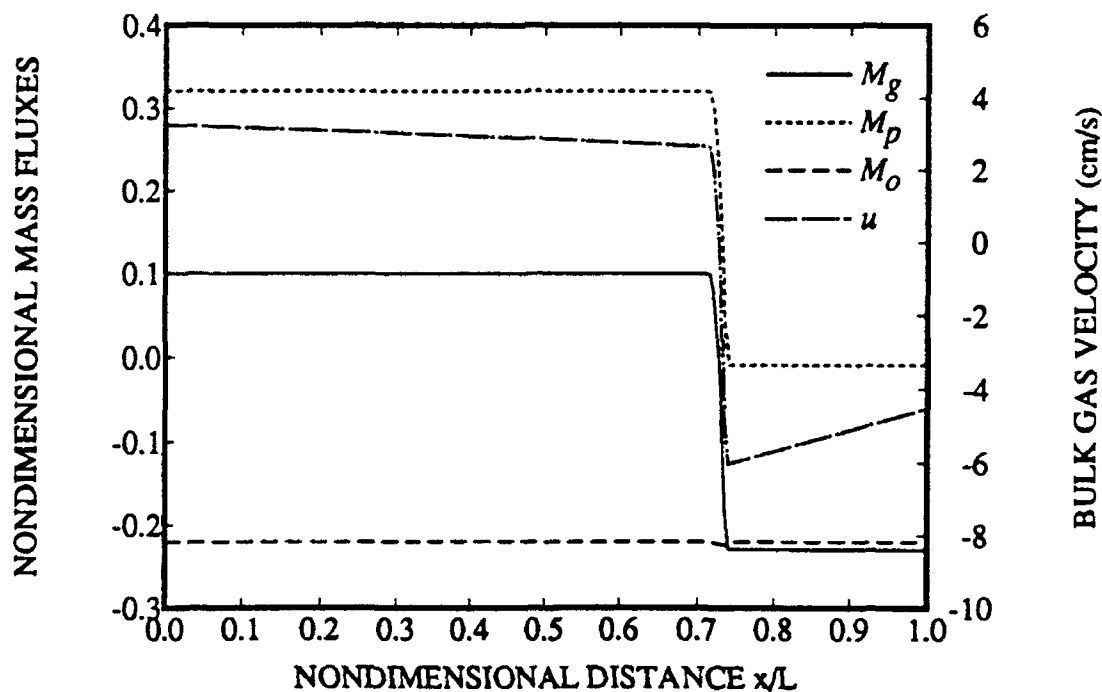


Figure C.9: Nondimensional mass fluxes of oxygen  $M_o$ , oxide vapor  $M_p$  and bulk gas  $M_g = M_o + M_p$  for  $Da = 1000.0$ . Also shown is dimensional gas velocity  $u$ .

to the oxide vapor saturation temperature. The analytical solution to the problem of the rapid ( $Da \rightarrow \infty$ ) condensation is given by the following equations:

(a) For  $0 < \xi < \xi_c$

$$M_g \equiv M_p + M_o = \text{constant} \quad (\text{C.12})$$

$$\ln \left\{ 1 + \frac{Y_o - Y_{o,L}}{Y_{o,L} - M_o/(M_p + M_o)} \right\} = (M_p + M_o)\xi \quad (\text{C.13})$$

$$\ln \left\{ 1 + \frac{Y_p - Y_{p,L}}{Y_{p,L} - M_p/(M_p + M_o)} \right\} = (M_p + M_o)\xi \quad (\text{C.14})$$

$$\ln \left\{ 1 + \frac{\theta - \theta_L}{\theta_L - q_I/(M_p + M_o)} \right\} = (M_p + M_o)\xi \quad (\text{C.15})$$

(b) For  $\xi_c < \xi < 1$

$$M_g = M_o = \text{constant} \quad (\text{C.16})$$

$$\ln \left\{ 1 + \frac{Y_o - Y_{o,c}}{Y_{o,c} - 1} \right\} = M_o(\xi - \xi_c) \quad (\text{C.17})$$

$$Y_p \text{ and } M_p = 0 \quad (\text{C.18})$$

$$\ln \left\{ 1 + \frac{\theta - \theta_c}{\theta_c - q_{II}/(M_o)} \right\} = M_o(\xi - \xi_c) \quad (\text{C.19})$$

where  $\theta$  is the nondimensional temperature  $\theta = C_p(T - T_R)/h_{fg}$ , and  $q_I$  is a nondimensional constant involving temperature gradient at the left wall and is initially unknown. By matching the temperature and the heat fluxes at the condensation point  $\xi_c$  we can show that

$$q_{II} = q_I + M_p \quad (\text{C.20})$$

The results from this analytical solution are obtained by assuming a value for  $\xi_c$  and solving the preceding equations in an iterative manner. Figures C.10 and C.11 show the results for this solution. There is very little difference between the infinite  $Da$  number solution and the higher  $Da$  number ( $Da = 100$  or  $1000$ ) solutions shown in Figures C.6 to C.9. The reason is that the characteristic time for condensation is much shorter than that for thermal or mass diffusion. The solution is independent of the rate of condensation. Thus, the assumption of infinitely fast condensation made while modeling the aluminum burning problem is well justified. The above results showing a thin condensation zone are also supported by several experimental observations (Hermesen [43]; Prentice [73], Price [74]; Turns et al. [98]) of "trapping" of the condensed oxide, which clearly will occur at the point of zero gas velocity.

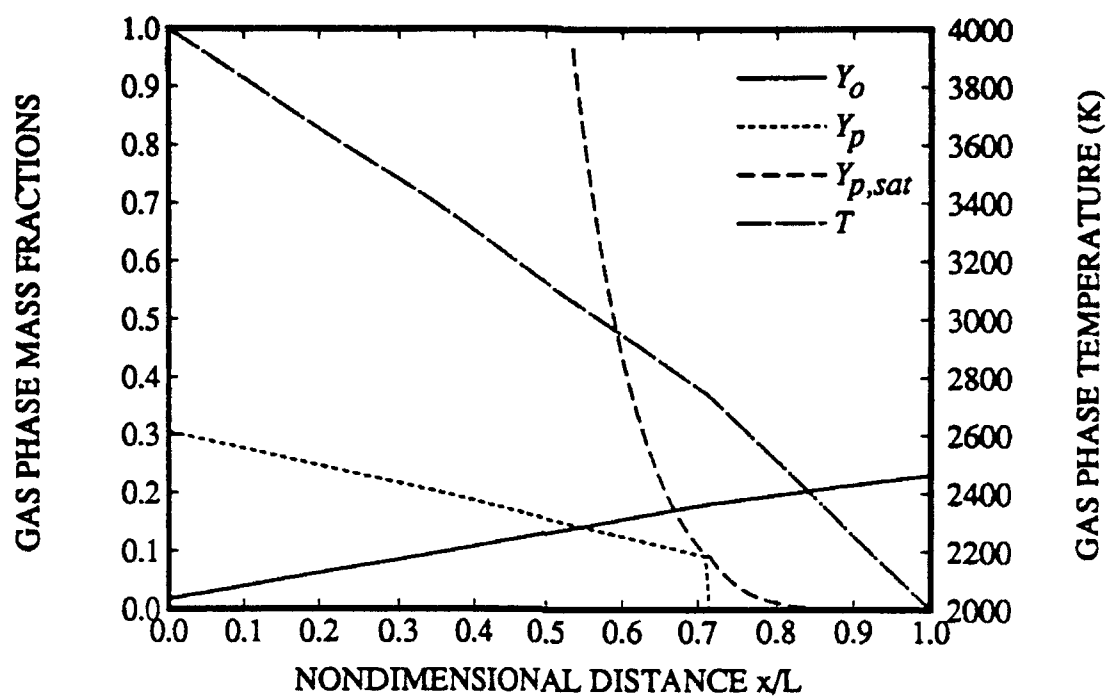


Figure C.10: Oxygen  $Y_o$  and vapor oxide  $Y_p$  mass fractions and gas temperatures  $T$  for  $Da \rightarrow \infty$ . Also shown is saturation oxide mass fraction  $Y_{p,sat}$ .

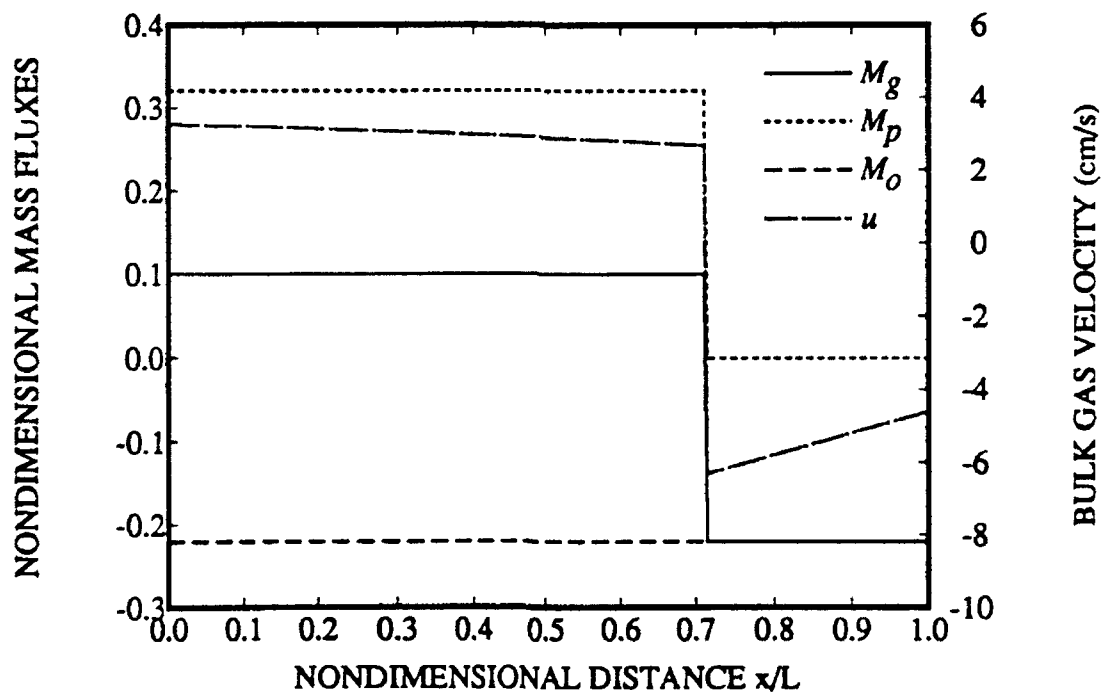


Figure C.11: Nondimensional mass fluxes of oxygen  $M_o$ , oxide vapor  $M_p$  and bulk gas  $M_g = M_o + M_p$  for  $Da \rightarrow \infty$ . Also shown is dimensional gas velocity  $u$ .

# Appendix D

## Effect of Thermophoresis on the Oxide Condensation

In this section, the thermophoretic effects on the condensation region are examined. By using an approximate analysis it is shown that, under the range of ambient conditions studied, the thermophoresis velocity is smaller than the bulk gas velocity and the drag forces overwhelm the thermophoretic force.

Figures 5.1 and 5.2 schematically show the condensation zone enveloping a burning aluminum droplet. Since a thermal gradient exists in the gas phase, the condensed oxide droplets will experience thermophoresis, or a force in the direction of decreasing temperature. A schematic of the problem is shown in Figure D.1. The figure shows a condensed oxide droplet "trapped" at the condensation radius and subjected to thermophoretic and external gas velocities.

Following Hinds [44], the thermophoretic velocity ( $v_{th}$ ) for a particle of diameter  $d_p > \lambda$  (the mean free path) can be given by:

$$v_{th} = \frac{-3\mu C_c H \nabla T}{2\rho_e T_e} \quad (D.1)$$

$\nabla T$  is the thermal gradient, and  $\rho_e$  and  $T_e$  are the gas density and temperature, respectively. The coefficient  $H$  is given by:

$$H \approx \left\{ \frac{1}{1 + 6\lambda/d_p} \right\} \left\{ \frac{k_g/k_p + 4.4\lambda/d_p}{1 + 2k_g/k_p + 8.8\lambda/d_p} \right\} \quad (D.2)$$

The mean free path  $\lambda$  is estimated from Bird et al. [10], as

$$\lambda = \frac{1}{\sqrt{2} \pi d^2 n} \quad (D.3)$$

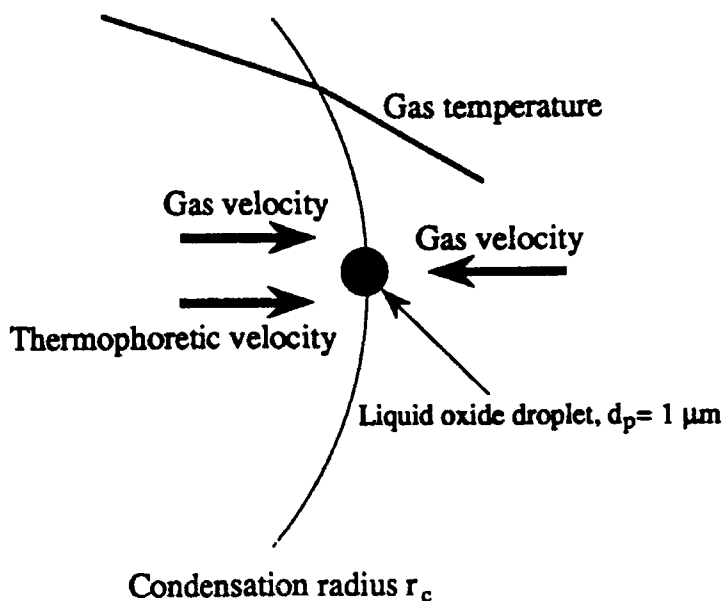


Figure D.1: Effect of thermophoretic velocity on a condensed oxide particle.

$n$  is the molecular number density, and the collision diameter  $d$  may be determined from the viscosity relation

$$\mu = \frac{2}{3\pi^{3/2}} \frac{\sqrt{mkT}}{d^2} \quad (\text{D.4})$$

where  $m$  is the molecular mass, and  $k$  is the Boltzmann constant. The Cunningham slip correction factor  $C_c$  to the Stokes drag is given by

$$C_c = 1 + \frac{2.52\lambda}{d_p} \quad \{\text{good for } d_p > 0.1 \mu\text{m}\} \quad (\text{D.5})$$

To evaluate the thermal gradient, we revisit the theoretical development of Chapter 5. At the radius of condensation, the gas velocity goes through a step. Just left of the condensation radius ( $r_c$ ), the velocity is positive and changes to negative at a radius just larger than  $r_c$ . The thermal gradient in the outer zone differs from the thermal gradient in the inner zone by approximately the amount of heat released from oxide condensation. Since the thermophoretic velocity is always positive, it is more important to evaluate the thermal gradient in the outer zone. This thermal gradient will control any plausible broadening of the condensation zone due to thermophoresis. From the equations presented in Table 5.2, we have

$$\beta_{FT}(r) = \frac{M_{1,2}q_{II}}{M_{g,II}} \left\{ 1 - e^{-M_{g,II} \frac{r_c}{r}} \right\} \quad (\text{D.6})$$

$$q_{II} = q_I + \frac{M_{g,I} - M_{g,II}}{M_{1,s}} \{h_{fg,3} + (C_{p,t} - C_p)(T_c - T_\infty)\} \quad (D.7)$$

$$q_I = \Delta H - h_{fg,1} + \frac{M_{3,s}}{M_{1,s}} h_{fg,3} - \frac{q_u}{m_{1,s}} \quad (D.8)$$

$$M_{g,II} \frac{r_s}{r_c} = \ln \left\{ 1 + \frac{Y_{2,c} - Y_{2,\infty}}{1 - Y_{2,c}} \right\} \quad (D.9)$$

In the above equations,  $M_{1,s}$  is the nondimensional fuel (aluminum) mass flux,  $M_{g,II}$  is the nondimensional gas mass flux in the outer zone,  $r_s$  is the droplet radius,  $Y_{2,c}$  and  $Y_{2,\infty}$  are the mass fractions of oxygen at the condensation radius and infinity, and  $q_I$  and  $q_{II}$  are the constants in the energy conservation relations. The Schvab-Zel'dovich variable  $\beta_{FT} = C_p(T - T_\infty) + Y_1 \Delta H$ . Since the fuel mass fraction  $Y_1$  is zero for any radial location greater than flame radius, and the condensation occurs at a radius larger than the flame radius,  $Y_1 = 0$ . It follows that

$$\nabla T = \left. \frac{dT}{dr} \right|_{r_c^+} = -\frac{M_{1,s} q_{II} r_s}{C_p r_c^2} \left\{ \frac{1 - Y_{2,c}}{1 - Y_{2,\infty}} \right\} \quad (D.10)$$

and

$$v_{th,c} = \frac{-3\mu C_c H}{2\rho_c T_c} \frac{M_{1,s} q_{II} r_s}{C_p r_c^2} \left\{ \frac{1 - Y_{2,c}}{1 - Y_{2,\infty}} \right\} \quad (D.11)$$

We need to compare this velocity to the local bulk gas velocity ( $v_c$ ). From the definition of the nondimensional gas mass flux (see Table 5.2) in the outer zone, we obtain

$$v_c = \frac{r^2 m_{g,II}}{r_c^2 \rho_c} = -\frac{r_s \overline{\rho D} M_{1,s}}{f r_c^2 \rho_c} \quad (D.12)$$

It is seen that both  $v_c$  and  $v_{th,c}$  continuously change as aluminum gets depleted from the burning droplet. It is interesting to divide the two preceding equations to obtain the velocity ratio

$$\frac{-v_c}{v_{th,c}} = \frac{2C_p T_c \overline{\rho D}}{3\mu C_c H f q_{II}} \left\{ \frac{1 - Y_{2,\infty}}{1 - Y_{2,c}} \right\} \quad (D.13)$$

$$\approx \frac{2C_p T_c \overline{\rho D}}{3\mu C_c H f q_{II}} \quad (D.14)$$

which shows that as aluminum is depleted from the burning droplet, the ratio of the local gas velocity to the thermophoretic velocity remains constant. The fundamental reason for this constant value of the velocity ratio is that the droplet burning is diffusion controlled, and thus at any radial location, both the thermal gradient and the local gas velocity are inversely proportional to  $r^2$ .

For air at 3000 K, 10 atm and a typical oxide droplet size of  $1 \mu\text{m}$ ,  $\mu = 949 \times 10^{-7} \text{ N/s}\cdot\text{m}^2$ , and  $\lambda \approx 0.16 \mu\text{m}$ . The ratio  $k_g/k_p = 1.2 \times 10^{-3}$  and makes little difference. Then  $H = 0.15$  and  $v_{th} = -8.59 \times 10^{-5} \nabla T$  ( $\text{cm}^2/\text{s}\cdot\text{K}$ ) ( $\text{K}/\text{cm}$ ),  $q_{II} \approx 7 \times 10^4 \text{ K}/\text{cm}$ , and  $v_{th,c} = 5.9 \text{ cm/s}$ . Similar thermophoretic velocities [39] have recently been observed, though for different experimental conditions. Also  $v_c \approx -9 \text{ cm/s}$  and the velocity ratio is 1.5. A better calculation from the numerical code reveals that over the droplet lifetime,  $v_{th,c}$  varies from 5.3 to 7.2 cm/s and  $v_c$  varies from -7.6 to -10.3 cm/s. The ratio of  $v_c$  to  $v_{th,c}$  is constant over the droplet lifetime and equals 1.6. Over the range of calculations in Chapter 5, the velocity ratio is always greater than one.

To consider the broadening of the condensation zone by thermophoresis, consider the drag on the individual condensed oxide droplets. The Reynolds number for the gas flow is

$$Re = \frac{\rho_c \Delta v d_p}{\mu} \quad (\text{D.15})$$

and  $Re \approx 3.7 \times 10^{-4}$  for a small  $\Delta v = 3 \text{ cm/s}$ . Thus using the creeping flow assumption, the drag over the particles is given by the Stokes relation

$$F_D = 6\pi\mu\Delta v d_p/2 \quad (\text{D.16})$$

Then the particle acceleration is given by

$$\frac{dv}{dt} = \frac{18\mu\Delta v}{\rho_p d_p^2} \approx 400 \text{ m/s}^2 \quad (\text{D.17})$$

Now we can estimate the characteristic relaxation and residence times. The characteristic relaxation time is given by

$$\frac{1}{\tau_{\text{relax}}} = \frac{1}{\Delta v} \frac{dv}{dt} \approx 13,000/\text{s} \quad (\text{D.18})$$

The characteristic residence time is given by

$$\frac{1}{\tau_{\text{residence}}} \approx \frac{v_c}{r_c} = \frac{200 \times 10^{-6}}{0.09} = 2.2 \times 10^{-3} \text{ s} \quad (\text{D.19})$$

Comparing the residence time in the metal droplet film to the relaxation time for condensation, we have

$$\frac{\tau_{\text{residence}}}{\tau_{\text{relax}}} \approx 30 \gg 1 \quad (\text{D.20})$$

Thus the particles, due to their extremely small size, will be opposed by a large drag force if they are ejected outwards by the thermophoretic force. In conclusion, we can state that thermophoretic broadening of the condensation zone may be neglected for the present conditions.

# Appendix E

## Numerical Modeling of a Slurry Droplet Containing a Spherical Particle

### E.1 Introduction

This section focuses on understanding the details of the early post-atomization stage of slurry droplet combustion, i.e., the dynamic interaction between solid and liquid phases, as well as the vaporization of the liquid carrier fuel. The details of the early stages of a slurry droplet lifetime are unraveled through quantitative, time varying, spatially resolved data in all three phases involved. An improved knowledge of the related processes would provide some important information on the practical implications involved.

### E.2 Physical Description

The study investigates the fluid mechanics along with the heating and vaporizing behavior of an isolated liquid droplet that contains a spherical particle in its core and is suddenly injected in a high-temperature, laminar, convective environment. This idealized configuration, which is depicted in Fig. E.1, may be viewed as an approximation to a slurry droplet which contains a large solid particle or a small amount of liquid-carrier fluid. The flow considered is laminar and axisymmetric with initially uniform ambient conditions specified by  $U'_{\infty,0}$ ,  $T'_{\infty}$ ,  $p'_{\infty}$  and  $Y_{f,\infty} = 0$  (no fuel

vapor in the incoming free stream). The solid particle, which is concentric with the surrounding liquid at the beginning of the simulation, is free to move along the axis of symmetry as a result of its dynamic interaction with the liquid carrier.

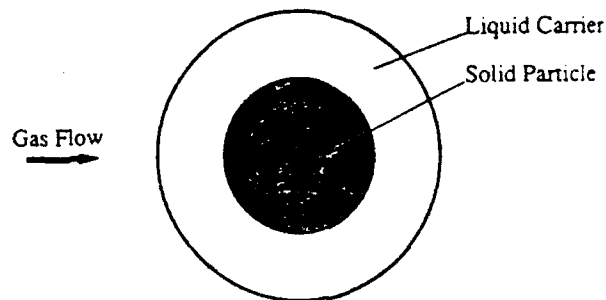


Figure E.1: Schematic of slurry-droplet flow configuration.

Soon after a slurry droplet with uniform temperature is injected into the hot gas stream, a thin boundary layer is developed near the gas/liquid interface and a recirculation zone appears in the droplet wake. The shear stress at the gas/liquid interface causes the gradual development of internal circulation within the liquid phase. The liquid is accelerated by the gas flow, and as it flows over the solid, exerts an axial force on the particle. The resulting relative motion of the solid particle and the carrier fluid has a very significant effect on the liquid-phase flow pattern. As the gas flow gradually adjusts to the presence of the droplet, the induced drag force effectively reduces the relative velocity between the droplet and the free flow, while the droplet size is simultaneously reduced due to vaporization. These combined events cause a gradual reduction of the droplet Reynolds number with time. The details of the solid particle motion with respect to the liquid-carrier fluid eventually determine the possibility for secondary atomization of the slurry droplet resulting from penetration of the particle through the liquid/gas interface. Such an event can be very desirable since it effectively reduces the time required for complete vaporization and combustion of the slurry droplet components.

Since the above momentum, heat, and mass transfer processes occur simultaneously, special care must be taken for their adequate representation in a detailed model configuration. Our model accounts for axial motion of the solid particle, variable thermophysical properties in the gas phase, variable viscosities and latent heat in the liquid phase, internal liquid circulation with transient droplet heating, droplet surface regression due to vaporization, and droplet deceleration with respect to the free flow. The current work extends the model of Chiang et al.[21] which was developed for an isolated, single-component, all-liquid droplet vaporizing inside a high-temperature

convective environment. However, in the case of a slurry droplet such as the one studied herein, the dynamic interaction of the solid particle and the liquid-carrier fluid introduces an additional degree of complexity on which the current study is mainly focused.

### E.3 Assumptions and Governing Equations

The problem is physically viewed as an impulsively started, high-temperature flow over a fixed slurry droplet containing a concentric solid particle. Both liquid and solid components are initially at uniform temperatures. Instead of describing the droplet motion through the gas using an Eulerian formulation, we change the reference frame from a stationary laboratory coordinate system to a system moving with the geometric center of the droplet. As a result of the induced drag force, the relative velocity between the free stream and the droplet varies with time. In order to account for this change, an adjustment of the surrounding gas flow field is necessary throughout the calculation. In addition, the drag force on the solid particle induced by the liquid phase motion around it, necessitates the monitoring of the particle location with respect to the geometric center of the slurry droplet throughout the calculation.

Since the flow studied herein is characterized by a low Mach number, the viscous dissipation terms have been neglected. The contributions of pressure and thermal gradients in gas-phase species diffusion have also been neglected. The very low pressure gradients associated with open systems, as the one under investigation, as well as the low values of the ratio of thermal diffusion coefficients to the product  $\rho_g \mathcal{D}_g$  for most gaseous mixtures justify our assumption. Gravity effects and radiative heat flux have also been neglected. The droplet deformation was not modeled since the droplets considered herein are characterized by low Weber numbers. In addition, the effects of surface tension have been neglected in the current formulation. The behavior of the gaseous mixture surrounding the droplet was assumed to be ideal, while all thermophysical properties (except viscosities and latent heat) in the liquid phase were considered invariant.

In the following we describe the additional considerations and adjustments to the all-liquid droplet model of Chiang et al.[21] that are needed to describe the slurry droplet and the motion of the solid particle. The non-dimensional formulation introduced in Ref. [21] has been maintained in the current study. The initial droplet radius, free stream velocity and physical properties were used to non-dimensionalize the variables. A cylindrical coordinate system  $(r, z)$  was employed to describe the axisymmetric geometry of the problem under investigation.

The detailed form of the applicable gas and liquid-phase equations, along with the appropriate boundary and initial conditions has been reported elsewhere [21] and will not be repeated here. The continuity, momentum, energy and species equations were solved in the gas phase. The liquid phase surrounding the solid particle was described through a vorticity-stream function formulation [28, 29] along with the energy equation. The addition of the solid-phase energy equation was necessary in order to account for the presence of the solid particle core within a slurry droplet

$$\frac{\partial}{\partial \tau E_s}(rT) = \frac{\partial}{\partial r} \left( r \frac{\partial T}{\partial r} \right) + \frac{\partial}{\partial z} \left( r \frac{\partial T}{\partial z} \right) \quad (\text{E.1})$$

## E.4 Gas/Liquid and Solid/Liquid Interface Conditions

The overall behavior of the slurry droplet is highly sensitive to the gas/liquid interface conditions. The vapor pressure above the liquid surface was calculated using Wagner's equation[85] in the form

$$\ln \left( \frac{p'_v}{p'_c} \right) = \frac{\alpha_1 \chi + \alpha_2 \chi^{1.5} + \alpha_3 \chi^3 + \alpha_4 \chi^6}{1 - \chi} \quad (\text{E.2})$$

where  $\chi = 1 - T/T_c$  and  $\alpha_i; i=1,4$  are coefficients [85] characteristic of the liquid compound. For n-octane,  $\alpha_1 = -7.912$ ,  $\alpha_2 = 1.380$ ,  $\alpha_3 = -3.804$  and  $\alpha_4 = -4.501$ . The above equation has been shown [85] to give very good estimates of actual vapor pressure values determined in a wide range of experimental investigations, and was chosen instead of the most commonly employed but less accurate Clapeyron equation for phase equilibrium. In addition, the principles of continuity for shear stress, tangential velocity, mass flux, temperature, energy and species fluxes were expressed in terms of the relevant variables as a system of equations[21] solved sequentially within the overall iterative solution procedure. This system relates the events occurring in the gas phase to those within the droplet.

The continuity of temperature and heat flux on the solid/liquid interface was expressed in spherical coordinates ( $n, \theta$ ) as

$$T_p|_m = T_l|_m, \quad \kappa'_p \frac{\partial T_p}{\partial n}|_m = \kappa'_l \frac{\partial T_l}{\partial n}|_m \quad (\text{E.3})$$

The liquid-phase vorticity over the solid-particle surface, also expressed in spherical coordinates, is given by

$$\omega = -\frac{\partial V_{l,\theta}}{\partial n} - \frac{V_{l,\theta}}{a_p} + \frac{1}{a_p} \frac{\partial V_{l,n}}{\partial \theta}. \quad (\text{E.4})$$

Finally, the liquid-phase stream function over the solid-particle surface is given by

$$\psi = \frac{r^2}{2}(V_d - V_p) \quad (\text{E.5})$$

where the axial velocities of the geometric center of the droplet  $V_d$  and the solid particle  $V_p$  are expressed with respect to a stationary frame. It is important to note that the substantial relative motion of the solid particle and the geometric center of the slurry droplet results in non-zero values of the stream function on the particle surface. This is apparent from the boundary condition for the stream function as defined by Eq. (E.5).

## E.5 Solid Particle Drag

The determination of the drag force which is exerted on the solid particle as a result of the liquid motion, requires knowledge of the velocity and pressure distributions within the liquid phase directly above the particle surface. The required velocities are readily calculated from the liquid-phase stream function values. However, since the pressure in the liquid phase is not calculated directly, we need to solve the tangential component of the liquid momentum equation on the particle surface. This equation, expressed in spherical coordinates with respect to a reference frame based on the center of the solid particle and moving with the velocity of the center of the droplet, is given by

$$\frac{\partial p_l}{\partial \theta} = \frac{2\mu_l}{Re_l} \left[ a_p \frac{\partial^2 V_\theta}{\partial n^2} + \frac{1}{3} \frac{\partial^2 V_n}{\partial n \partial \theta} + 2 \frac{\partial V_\theta}{\partial n} - \frac{2}{3} \cot \theta \frac{\partial V_n}{\partial n} \right] - \frac{2a_p \sin \theta}{Re_g} \gamma_p - a_p (V_n - V_d \cos \theta) \frac{\partial V_\theta}{\partial n} \quad (\text{E.6})$$

Low spatial variations of the liquid viscosity were assumed in the derivation of Eq. (E.6). The first term of the right-hand side of the above equation arises from the viscous terms of the momentum equation, while the second describes an external body force due to the solid particle acceleration at a rate  $\gamma_p$ . The third term on the right-hand side of Eq. (E.6) arises from the convective terms of the momentum equation and includes the velocity of the geometric center of the droplet  $V_d$  as a result of a change in the reference frame.

Equation (E.6) gives the pressure distribution on the solid particle surface by a simple integration along  $\theta$ , when the pressure at  $\theta = 0$  is used as a reference value. The acceleration of the solid particle with respect to a stationary frame, which results from the induced drag force, may then be expressed as a sum of the pressure and friction contributions given by

$$\gamma_p = \frac{3Re_g}{4a_p^3} \frac{\rho_l'}{\rho_p'} \int_0^\pi p_l(\epsilon - z) r d\theta + \frac{3}{2a_p^3} \frac{\mu_{l,0}' \rho_\infty'}{\mu_\infty' \rho_p'} \int_0^\pi \left( r \frac{\partial V_\theta}{\partial n} + \frac{4}{3} (z - \epsilon) \frac{\partial V_n}{\partial n} \right) \mu_l r d\theta \quad (\text{E.7})$$

Table E.1: Physical Parameters Used in Base Case Slurry Droplet Simulation

Parameter	Value
Initial Reynolds number, gas phase $Re_g = 2a'_0 U'_{\infty,0} \rho'_{\infty} / \mu'_{\infty}$	50
Solid particle radius	$a'_0/2$
Free stream temperature, [K]	1250
Ambient pressure, [atm]	10
Initial slurry droplet temperature, [K]	300
Prandtl number $Pr_g$ , gas phase	0.74
Prandtl number $Pr_l$ , liquid phase	9.38
Lewis number $Le_g$ , gas phase	3.20
Molecular weight, air [kg/kmol]	28.96
Molecular weight, n-octane [kg/kmol]	114.2
Latent heat at normal boiling point (398.8K), n-octane [kJ/kg]	303.3
Liquid/gas viscosity ratio at time=0, $\mu'_{l,0} / \mu'_{\infty}$	11.44
Liquid/gas conductivity ratio, $\kappa'_l / \kappa'_{\infty}$	1.69
Solid/liquid conductivity ratio, $\kappa'_p / \kappa'_l$	1581
Liquid/gas density ratio, $\rho'_l / \rho'_{\infty}$	252
Solid/liquid density ratio, $\rho'_p / \rho'_l$	3.87
Liquid/gas specific heat ratio at constant pressure, $c'_{p,l} / c'_{p,\infty}$	1.87
Solid/liquid specific heat ratio, $c'_{p,p} / c'_{p,l}$	0.4

where  $\epsilon$  is the eccentricity of the solid particle center with respect to the geometric center of the slurry droplet.

As seen from the above, the pressure above the solid-particle surface and the solid-particle acceleration are related in an intricate integro-differential manner expressed by Eqs. (E.6) and (E.7). These two equations describe the dynamic interaction of the liquid and the solid phase. Numerical integration of Eq. (E.6) is performed to determine the pressure distribution  $p_l(\theta)$  assuming a known value of  $\gamma_p$ . An updated value for  $\gamma_p$  is subsequently obtained from Eq. (E.7) using the pressure distribution  $p_l(\theta)$  calculated from Eq. (E.6).

## E.6 Treatment of Solid-Particle Motion

As mentioned previously, the liquid-phase motion over the solid particle results in a drag force exerted on the particle along the axis of symmetry. As a result of the generally unequal liquid and solid accelerations, a separation of the particle center from the geometric center of the slurry droplet occurs. The geometric center of the slurry droplet also coincides with the origin of the liquid-phase-motion reference frame. The above separation is expressed as the distance between the center of the solid particle from the geometric center of the slurry droplet and is denoted as eccentricity  $\epsilon$ . The displacement of the particle causes the eccentric positioning of the center of mass of the slurry droplet as well. The relative axial motion of all three points of interest, i.e., center of solid particle, center of mass and geometric center of the slurry droplet, is monitored throughout the calculation. The acceleration of the geometric center of the droplet is related to the acceleration of its center of mass and the acceleration of the solid particle through the following equation

$$\gamma_{gc} = \frac{1 + A\rho'_p/\rho'_l}{1 + A}\gamma_{cm} + \frac{A}{1 + A}\left(1 - \frac{\rho'_p}{\rho'_l}\right)\gamma_p \quad (\text{E.8})$$

where  $A = ((a/a_p)^3 - 1)^{-1}$ . The above equation does not consider the effect of the liquid surface regression due to vaporization.

The acceleration of the center of mass of the slurry droplet ( $\gamma_{cm}$ ) is calculated at each instant through the drag force exerted on the droplet as a result of the gas flow around it. The details of the drag force calculation are reported elsewhere in [21]. As mentioned in the previous section, the acceleration of the solid particle ( $\gamma_p$ ) is calculated from the drag force exerted on the particle as a result of the liquid flow around it. The velocities of the three points of interest are updated throughout the simulation using the calculated values of the respective accelerations. The knowledge of the velocities and accelerations of the solid particle and the geometric center of the slurry droplet, results in the timewise determination of the eccentricity of the solid particle with respect to the origin of the reference frame, and thus of the relative position of solid and liquid throughout the simulation.

## E.7 Numerical Solution Procedure

Before attempting a numerical solution, the related equations were transformed to generalized non-orthogonal coordinates  $(\xi, \eta)$ , which allow for any arbitrary shaped body as well as for changes in droplet radius with time due to vaporization. The non-linear, highly coupled equations describing the slurry droplet dynamics were discretized by implicit finite-difference schemes. The conditions employed for the boundaries of the computational domain were identical to those used in Ref. [21] with the exception of the outflow condition for pressure that was substituted by the condition  $\frac{\partial p}{\partial x} = 0$ . The calculations were performed on a rectangular mesh with equal spacings ( $\Delta\xi = \Delta\eta = 1$ ). The iterative solution procedure requires the calculation of the Jacobian and other metrics of the transformation, anytime the grid is adjusted to conform to the motion of the solid particle along the axis and the regressing droplet surface.

The model allows for independent motion of the solid particle within the bulk of the surrounding liquid. The forces exerted by the liquid-flow motion (pressure field and viscous stress contributions) on the solid particle along its axis of symmetry are used sequentially to adjust the position of the solid particle core with respect to the geometric center of the slurry droplet. This feature allows the monitoring of the relative motion of the two components (solid, liquid) of the slurry droplet and provides important data on a problem that has not been addressed yet in relevant investigations. Our simulations showed that the rapid motion of the solid particle with respect to the liquid phase eventually resulted in grid Peclet numbers appreciably higher than unity. For this reason, a hybrid (central difference/upwind) discretization scheme was employed for the convective terms of both energy and vorticity equations in the liquid phase [70]

The developed numerical code employs an iterative solution procedure [21] for the determination of the fields of interest in the solid, liquid and gas phases, and calculates the related drag coefficients and transfer numbers [21]. Two checks were performed on the reliability of the results obtained using the numerical model. The first involved the influence of the computational far-field distance from the center of the slurry droplet. We found that a distance  $r_\infty = 16\alpha_0$  was adequate in order to obtain far-field independent results. The second check examined the grid and time-step dependence of the results. We found that a grid of  $71 \times 41$  nodes and a time step of  $\Delta\tau_{H_2} = 8 \times 10^{-4}$  were needed in order to assure grid and time-step independence. The fine grid in concert with the great disparity of the characteristic time scales involved (thus necessitating a fine time step), required extensive computations that were performed on a CRAY Y-MP and a CONVEX-240 supercomputer.

## E.8 Results and Discussion

The base case calculation was selected to simulate a liquid n-octane droplet of initial radius  $a'_0$  containing a concentric aluminum particle of radius  $a'_0/2$ . The slurry droplet is assumed to be initially at a uniform temperature  $T'_0 = 300K$ . This droplet is suddenly ( $t' = 0$ ) injected in a uniform air stream characterized by a velocity  $U'_{\infty,0}$ , a temperature  $T'_\infty = 1250K$  and a pressure  $p'_\infty = 10atm$ . The initial Reynolds number was selected to be  $Re_g = 2U'_{\infty,0}a'_0\rho'_\infty/\mu'_\infty = 50$  at the beginning of the simulation. The values of physical parameters and non-dimensional groups employed in the base case calculation are given in Table 1. These conditions correspond to an initial solid mass fraction of 36 % that is on the low end of the range observed in realistic slurry droplet applications.

The computational mesh employed in the gas phase consisted of 37 (radial direction)  $\times$  41 (angular direction) nodes, while a mesh of 24 (radial direction)  $\times$  41 (angular direction) was employed for the liquid phase. The liquid-phase grid concentration was higher above the solid surface and below the gas/liquid interface. A mesh of 10  $\times$  41 was used for the solid phase. As mentioned previously, the grid locations have to be adjusted continuously in order to accommodate the motion of the solid particle with respect to the geometric center of the slurry droplet, as well as the droplet surface regression due to vaporization. The base case calculation was carried only to non-dimensional time  $\tau_{Hg} = 1.5$  due to the rise of strong oscillations of the velocity and pressure fields over the solid-particle surface. A discussion relevant to this behavior follows after the presentation of the results during the stable period. At the instant of termination of the simulation only 0.6% of the available liquid mass had vaporized.

The gas-phase contours for the slurry droplet calculation resemble those calculated in the case of an all-liquid droplet [21]. However, the liquid-phase contours are significantly affected by the presence and motion of the solid particle. Figure E.2 displays the liquid-phase streamlines (upper half) and velocity vectors (lower half) at an instant  $\tau_{Hg} = 1$  of the base case simulation. The velocities were calculated from the stream function values and have been expressed with respect to a reference frame moving with the geometric center of the droplet, which is indicated by a circle on the axis of symmetry. The development of a vortex directly above the solid-particle surface is apparent in this figure. The vortex, which is asymmetric with respect to the vertical axis through the center of the slurry droplet, moves clockwise towards the aft of the droplet during the simulation. It is worth noting that the solid-particle surface is not a streamline due to the significant relative motion of the solid with respect to the geometric center of the slurry droplet. This relative motion is clearly demonstrated by the liquid-phase velocity vector field at the same instant. A sequence of figures similar to Fig. E.2 showed that the liquid/gas interface velocities and the relative velocity of the solid particle with respect to the center of the droplet increase

monotonically with time. As also seen on Fig. E.2, the maximum liquid velocities occur on the liquid/gas interface and near the vortex region. The axial motion of the solid particle within the liquid volume enhances the liquid circulation which is initiated on the droplet surface due to shear interaction of the liquid droplet and the gas flow. The increasing relative velocity between the solid and the liquid results in increasingly higher eccentricities  $\epsilon$ .

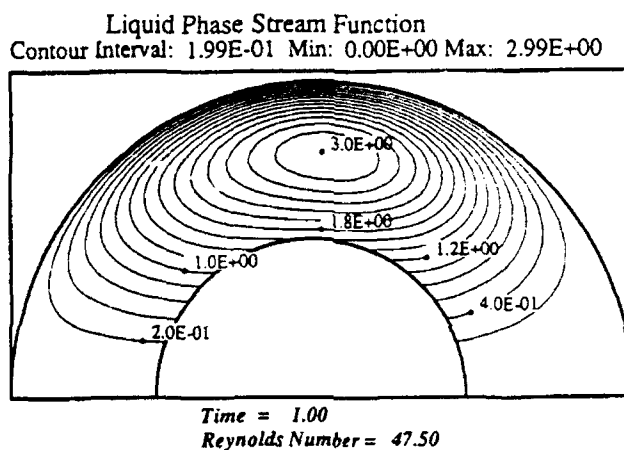


Figure E.2: Liquid-phase streamlines (upper half) and velocity vectors (lower half) at  $\tau_{Hg} = 1$  of the base case slurry simulation. The outer circle represents the gas/liquid interface, while the inner one represents the solid-particle surface. The gas flow is directed from left to right.

Figure E.3 shows the spatial variations of the isothermal contours in the slurry droplet interior at three different times of the base case simulation ( $\tau_{Hg} = 0.5, 1$  and  $1.5$ ). During the very early stages of the simulation (Fig. E.3A), a thermal boundary layer is rapidly formed within the liquid regions adjacent to the droplet surface. The steep temperature gradients associated with this layer result in conductive transfer of energy from the gas/liquid interface to the inner regions of the droplet. Simultaneously, the convective mechanisms, which develop as a result of the exposure of the droplet surface to the gas flow, transfer hot liquid from the gas/liquid interface to the droplet interior. This convective transfer results in the exposure of the solid material to heated liquid which is transported over its surface (Fig. E.3B). Due to the high conductivity of the metal considered herein (aluminum), the temperature within

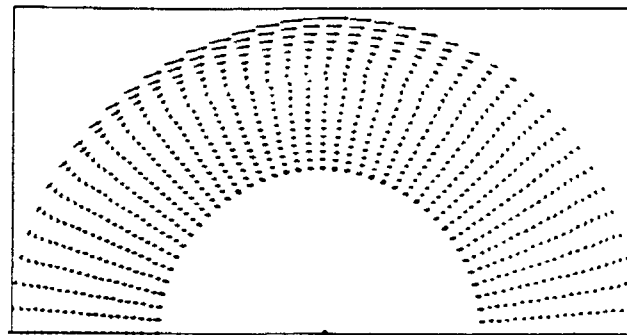
the particle remains spatially uniform even though it is temporally varying. The form of the temperature contours at later times (Fig. E.3C), suggest the importance of the convective mechanisms in the transfer of energy within the liquid phase at this stage of the calculation. As it will be shown in the following, the thermal pattern indicated in Fig. E.3 is reinforced by the significant relative motion of the solid with respect to the liquid-carrier fluid.

The relative motion of the solid particle with respect to the center of mass and the geometric center of the slurry droplet is monitored by the time variations of the corresponding velocities. Figure E.4 shows the time variation of the axial velocities of the three centers of interest with respect to a stationary frame for the base case calculation; namely, the center of the solid particle, the center of mass and the geometric center of the slurry droplet. It is apparent that the geometric center of the droplet moves faster than its center of mass, while the solid particle remains essentially stationary throughout the simulation, thus indicating a monotonically increasing eccentricity  $\epsilon$ .

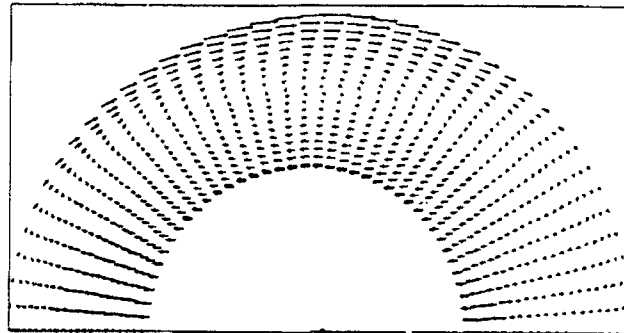
A series of figures, showing the angular variation of several quantities on the solid/liquid and the liquid/gas interface, is used to assess the flow field within and around the slurry droplet as well as the importance of the convective effects. The time variation of the angular distribution of the solid-particle surface temperature was initially investigated. The high conductivities of the solid phase resulted in almost spatially uniform surface temperatures throughout the simulation. Our observations consistently showed that the aluminum phase remains essentially isothermal, even though its temperature is temporally varying during the calculations.

The angular variation of pressure over the solid-particle surface is depicted in Fig. E.5 at three different instants of the base case calculation ( $\tau_{H_0} = 0.4, 0.8$  and  $1$ ). The pressure at  $\theta = 0^\circ$  is used as a reference value. As seen in Fig. E.5, the pressures above the particle surface are consistently higher than the reference pressure, except at regions with  $160^\circ < \theta < 180^\circ$ . The higher pressures around  $\theta \approx 130^\circ$  result in a force pushing the solid particle in the upstream direction with respect to the liquid flow. In essence, the angular variation of  $p_l(\theta)$  at a specific instant, as depicted in Fig. E.5, was obtained by a simple integration of Eq. (E.6). The importance of the terms on the right-hand side of Eq. (E.6) was investigated by examining their relative magnitude. We found that the term containing the particle acceleration  $\gamma_p$  was rather insignificant, especially when compared to the viscous term  $\partial^2 V_\theta / \partial n^2$ . The importance of these terms was investigated by neglecting their respective contributions in Eq. (E.6) and examining the effect on the liquid-phase fields and some global quantities (primarily the corresponding values of  $\epsilon$ ). Even though the angular distribution of pressure over the solid particle, as displayed in Fig. E.5, could be interpreted as a strong pseudo-hydrostatic effect on the rear side of the particle ( $\theta \approx 180^\circ$ ), our analysis showed that the particle acceleration term does not significantly contribute to the calculated values of  $p_l(\theta)$ . This unusual pressure result might be attributed to the non-uniformity of

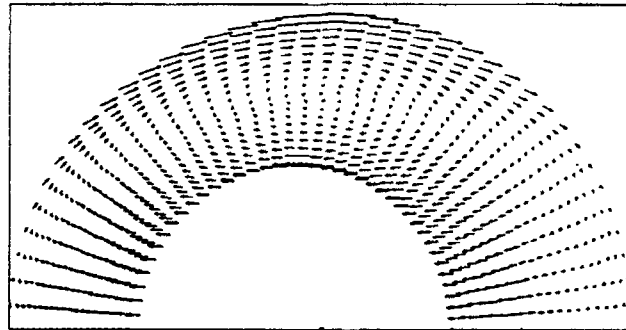
## Liquid Phase Velocity Vectors



*Time = 0.50*  
*Reynolds Number = 48.60*



*Time = 1.00*  
*Reynolds Number = 47.50*



*Time = 1.50*  
*Reynolds Number = 46.52*

Figure E.3: Time variation of the velocities of the three centers of interest in the base case slurry droplet simulation. These velocities are expressed with respect to a stationary reference frame.

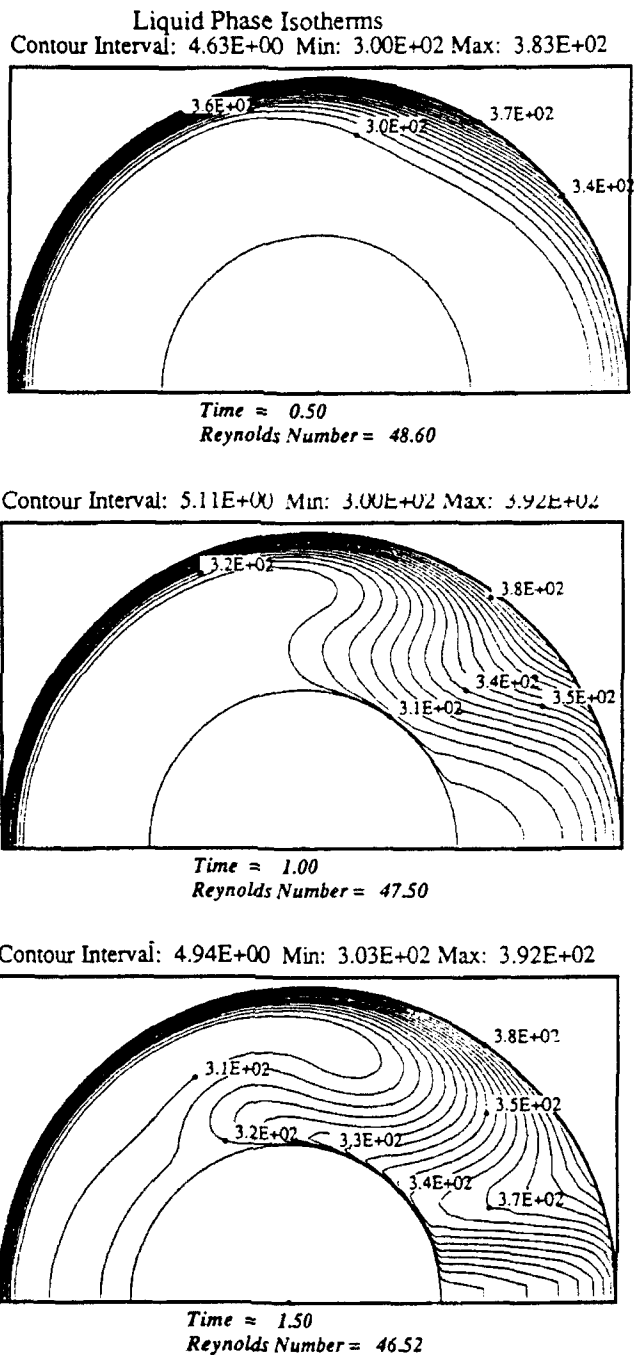


Figure E.4: Liquid-phase isothermal contours at three different times of the base case slurry simulation; (A)  $\tau_{Hg} = 0.5$ , (B)  $\tau_{Hg} = 1$  and (C)  $\tau_{Hg} = 1.5$ . The outer circle represents the gas/liquid interface, while the inner one represents the solid particle surface. The gas flow is directed from left to right.

the liquid flow around the particle, combined with the bounded character of the liquid flow field.

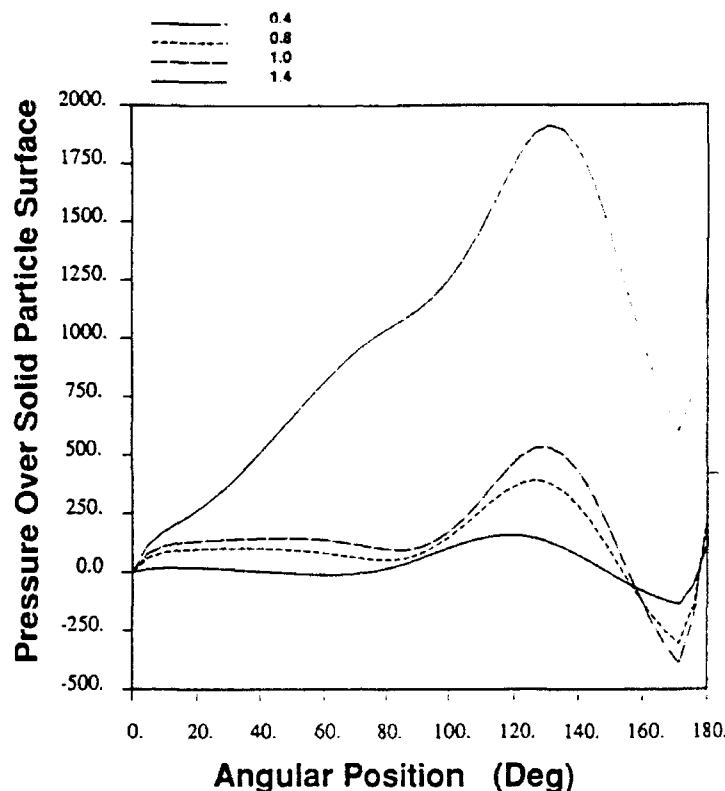


Figure E.5: Angular variation of pressure differential (in  $N/m^2$ ) over the solid-particle surface at three different times of the base case simulation ( $\tau_{Hg} = 0.4, 0.8$  and  $1$ ). The pressure at  $\theta = 0^\circ$  over the solid surface was used as a reference value.

Figure E.6 depicts the angular variation of the tangential velocity  $V_\phi$  at four different times of the base case simulation ( $\tau_{Hg} = 0.4, 0.8, 1$  and  $1.4$ ). As seen, there is a strong tangential acceleration of the liquid surface throughout the simulation. The above values of  $V_\phi$  are very similar to those obtained in the all-liquid droplet calculation by Chiang et al. [21]. This suggests that the presence of the solid particle within the liquid bulk does not significantly alter the gas/liquid interface motion. It will be shown in the following, that even though this result is counter-intuitive, it can be attributed to the lagging motion of the solid particle with respect to the liquid surrounding it.

Figure E.7 shows the angular variation of temperature on the gas/liquid interface at four different times of the base case simulation ( $\tau_{Hg} = 0.4, 0.8, 1$  and  $1.4$ ). The temperature of the liquid surface is clearly spatially non-uniform, with slightly higher values than those calculated by Chiang et al. [21] for the all-liquid droplet. At each instant, both points of maximum and minimum temperature for the slurry-droplet surface correspond to locations adjacent to the recirculating wake in the aft

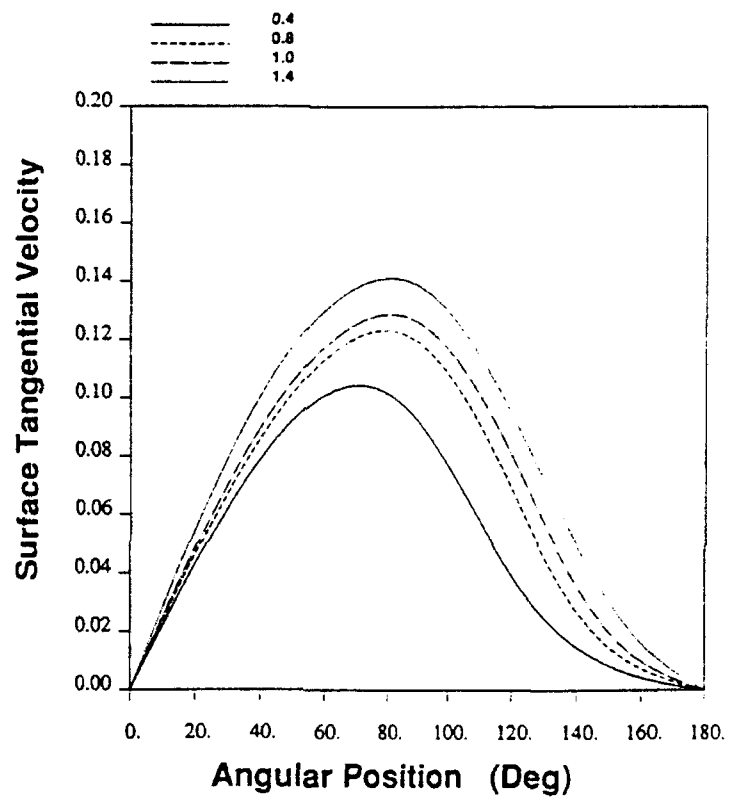


Figure E.6: Angular variation of tangential velocity on the gas/liquid interface at four different times of the base case simulation ( $\tau_{Hg} = 0.4, 0.8, 1$  and  $1.4$ ).

of the droplet. This is a result of the presence of the vortex within the liquid, which enhances the heat-transfer mechanisms in a substantial way. The base case simulation showed that, in contrast to the temperature angular distribution, the maximum value of the local Nusselt number  $Nu = 2a\kappa_g \frac{\partial T_g}{\partial n} / (1 - T)$  corresponds to the front stagnation point of the slurry droplet. In addition, the values of the local  $Nu$  remained almost unchanged throughout the simulation. The angular variation of the local Sherwood number  $Sh = 2a\rho_g D_g \frac{\partial Y_f}{\partial n} / (Y_{f,\infty} - Y_f)$  on the gas/liquid interface also displayed maximum values at the front stagnation point of the flow. The temporal variation of  $Sh$  was very weak at all angles with the exception of the regions near the recirculating wake.

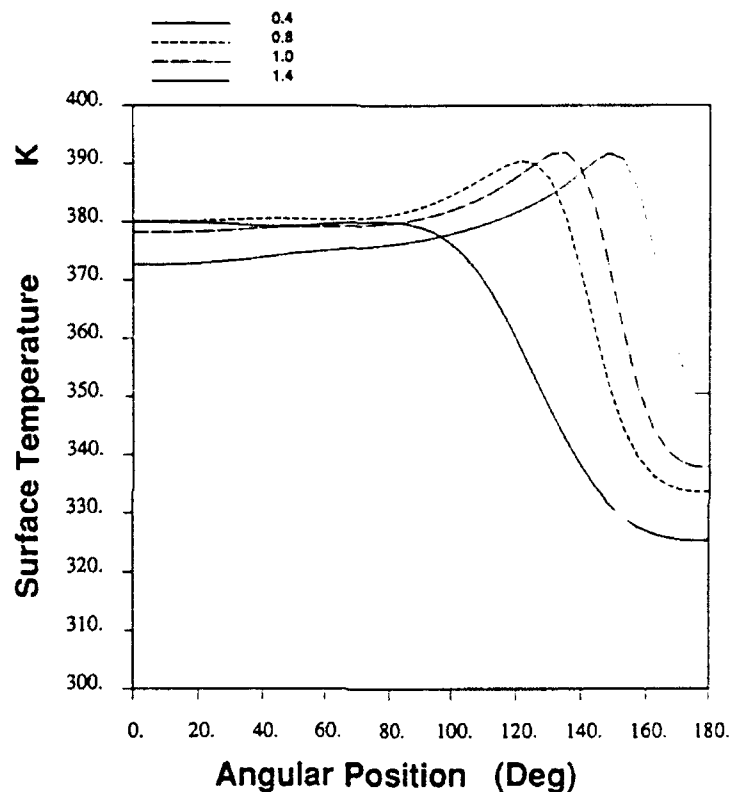


Figure E.7: Angular variation of temperature on the gas/liquid interface of the slurry droplet at four different times of the base case simulation ( $\tau_{Hg} = 0.4, 0.8, 1$  and  $1.4$ ).

Figure E.8 depicts the angular variation of the vaporization mass flux ( $\rho_g V_{g,n}$ ) over the liquid surface at four different times of the base case simulation ( $\tau_{Hg} = 0.4, 0.8, 1$  and  $1.4$ ). Since the liquid-surface temperatures are relatively low, the associated vaporization fluxes are not substantial. This figure, however, clearly demonstrates the non-uniformity of the vaporization flux over the surface of a droplet in a convective environment. The flux peaks at regions close to the front stagnation point of the slurry droplet. It should be also noted that, even though the maximum of the surface temperature occurs at regions closer to the recirculating wake (Fig. E.7),

the vaporization flux does not follow this behavior. This is primarily because the vaporization rate depends strongly on the local convective gas-phase conditions which are very intense near the front stagnation point of the flow ( $\phi \approx 0^\circ$ ). Some slightly negative values of the vaporization flux at the aft of the droplet (Fig. E.8) suggest some condensation of the liquid vapor, mainly due to the relatively low local surface temperatures (Fig. E.7) and the accumulation of fuel vapor in the recirculating wake region.

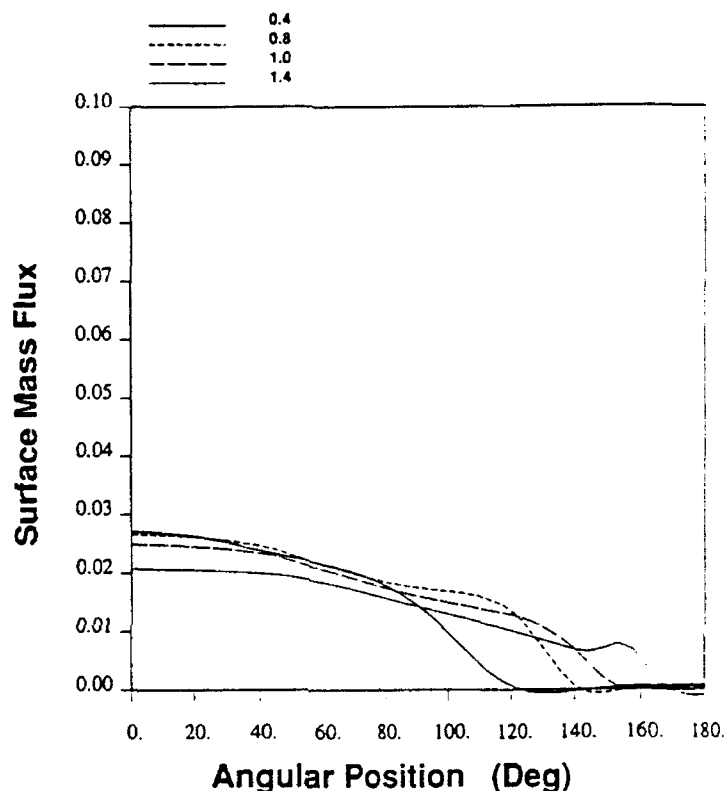


Figure E.8: Angular variation of vaporization mass flux ( $\rho_g V_{g,n}$ ) on the gas/liquid interface at four different times of the base case simulation ( $\tau_{Hg} = 0.4, 0.8, 1$  and  $1.4$ ).

As mentioned previously, the base case calculation was terminated at  $\tau_{Hg} = 1.5$  when strong oscillations of the velocity and pressure fields over the solid-particle surface caused unstable temporal behavior of the particle accelerations. Further investigation of this behavior showed that the instability originates at  $\tau_{Hg} \approx 1.3$  from the term  $\frac{\partial^2 V_g}{\partial n^2}$  of Eq. (E.6) thus rendering the results of the calculations unreliable after  $\tau_{Hg} = 1.5$ . Prior to that time, the calculated quantities of the gas/liquid interface displayed normal behavior. The time of first appearance of the instability was not affected by changes in the solid-particle size and properties. Also, the solution behavior prior to the onset of instability was highly insensitive to the computational grid and the utilized time step. The origin of the instability was investigated by running two additional simulations with different Reynolds numbers ( $Re_g = 100, 20$ ). These simulations revealed a dramatic change for the time of first appearance of

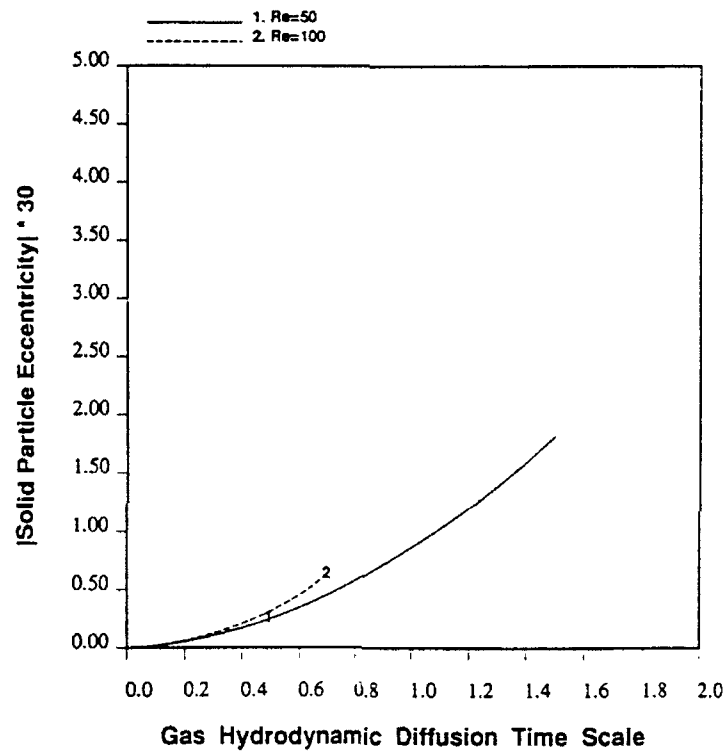


Figure E.9: Time variation of solid particle eccentricities for three slurry droplets with different initial Reynolds numbers ( $Re_g \approx 100, 50, 20$ ). The eccentricity is defined as the distance of the solid particle center from the geometric center of a slurry droplet.

the instability. The case with  $Re_g = 100$  showed unstable behavior appearing after  $\tau_{Hg} \approx 0.7$ , while the  $Re_g = 20$  case showed a delayed appearance ( $\tau_{Hg} \approx 3.7$ ) of the pressure oscillations. By monitoring the temporal variation of the liquid-phase Reynolds number based on solid-particle diameter and relative velocity between solid and liquid, we found that for all cases at the time of initiation of the above instability the liquid-phase Reynolds number was of the order of 100.

Further investigation of the source of unstable behavior over the solid/liquid interface showed the time of first appearance of the instability to be very sensitive to the value of the relaxation factor  $\omega$  employed in the numerical solution of the liquid-phase stream function equation. Certain values of the relaxation factor  $\omega$  (1.2, 1.5 and 1.8) were studied in the sensitivity analysis. We found that the value  $\omega = 1.5$  delayed the onset of instability the most. For the other values of  $\omega$ , unstable behavior was initiated over the particle surface at much earlier stages of the corresponding simulation. Experience indicates that an optimal value of  $\omega$  exists for maximizing the rate of convergence. Our observations strongly suggest that the unstable behavior experienced by the model is numerical. However, the high degree of consistency of the model predictions for  $\omega = 1.5$  during the stable period supports the view that the model provides reliable data during that period.

The above numerical instability appears to be a result of the strong dynamic interaction of the liquid and solid phases. We should emphasize that our axisymmetric calculation would be inadequate to resolve three-dimensional effects. In addition, the assumption of sphericity for the slurry droplet may also be inadequate when the relative velocity between solid and liquid becomes very important. Even though our model cannot adequately represent the slurry droplet dynamic and thermal behavior at later stages, it does provide some important insight for the early stable period.

Figure E.9 shows the absolute values of the solid-particle eccentricities ( $\epsilon$ ) with respect to the geometric center of the slurry droplets for the three different values of initial Reynolds number based on droplet diameter and relative velocity between gas and liquid at the time of injection. The actual values of  $\epsilon$  are always negative due to the choice of the coordinate system. The termination of a curve indicates the end of the stable period. It is apparent from Fig. E.9 that higher values of  $Re_g$  cause the solid particle to separate from the slurry droplet center at a faster rate, thus causing larger values of  $|\epsilon|$ .

The effects of solid-particle size and density during the stable period were investigated with our slurry droplet model. In addition to the base case calculation ( $a_p = 0.5$ ,  $\rho'_p = 2,707 \text{ kg/m}^3$ ,  $\rho'_i = 700 \text{ kg/m}^3$ ), two other cases were studied; one with a solid particle of radius  $a_p = 0.5$  and density  $\rho'_p = 1,760 \text{ kg/m}^3$ , and another with a solid particle of density  $\rho'_p = 2,707 \text{ kg/m}^3$  and radius  $a_p = 0.397$ , corresponding to a solid volume half of that used in the base case calculation. For both additional

simulations, the liquid-phase density employed was  $\rho_l' = 835 \text{ kg/m}^3$  in order to maintain the mass of the slurry droplet identical to that used in the base case calculation. These two additional slurry droplet cases are denoted as "lower solid-density" and "half solid-volume" calculations, respectively. The corresponding solid mass fractions are 23 % and 18 %, respectively. All other parameters used in these calculations were identical to those employed in the base case simulation. Even though the two cases mentioned above describe slurry droplets with the same total mass, the corresponding solid-particle masses are not identical. More specifically, the "lower solid-density" particle is 35 % lighter than the base case solid particle, while the "half solid-volume" particle is 50 % lighter than the base case solid particle. The accelerations of the above slurry droplets with respect to a stationary frame maintained values much higher than the gravity value, therefore, our assumption of negligible gravity effects is justified a posteriori.

Figure E.10 shows the absolute values of the solid-particle eccentricities for the three slurry cases considered with  $Re_g = 50$ . For all three cases, the droplets are characterized by the same mass and are accelerated by identical gas streams. It is apparent from Fig. E.10 that the heavier solid particle within the base case slurry droplet tends to separate from the droplet center faster than the lighter particles in the "lower solid-density" and "half solid-volume" calculations. The above behavior can be physically explained when we compare the forces acting on the solid particle. The drag force, which acts on the solid particle as a result of the liquid-phase motion around it, tends to decrease the values of  $|\epsilon|$  and is proportional to the square of the particle radius ( $\propto a_p^2$ ). On the other hand, the solid-particle inertia tends to increase the values of  $|\epsilon|$  and is proportional to the product of the solid density and the cube of the particle radius ( $\propto \rho_p a_p^3$ ). This reasoning leads to the conclusion that the displacement of the solid particle from the geometric center of the slurry droplet changes according to the product  $\rho_p a_p$ , therefore, the trends depicted in Fig. E.10 are physically expected. As also shown by the same figure, the eccentricity of the solid particle along the axis of symmetry with respect to the geometric center of the slurry droplet becomes very substantial early in the lifetime of the droplet. This displacement is very significant, as clearly demonstrated by the liquid-phase fields displayed in Figs. E.2 and E.3. The increasingly faster rates of solid-particle separation from the geometric center of the slurry droplet strongly suggest a high possibility of secondary atomization at a subsequent stage. Such an event in a practical system would significantly enhance the liquid vaporization and would expose the solid particle to the hot environment of the combustion gases at an early stage.

Figure E.11 compares the time variation of the average liquid-surface and solid temperatures for the three slurry droplets considered herein. The liquid-phase temperatures show that the base case slurry droplet surface heats up faster compared to the other two. It is also apparent that there is a significant lapse between the time that the liquid phase starts heating up and the instant the solid phase starts absorbing a significant amount of heat depicted by a gradual temperature increase.

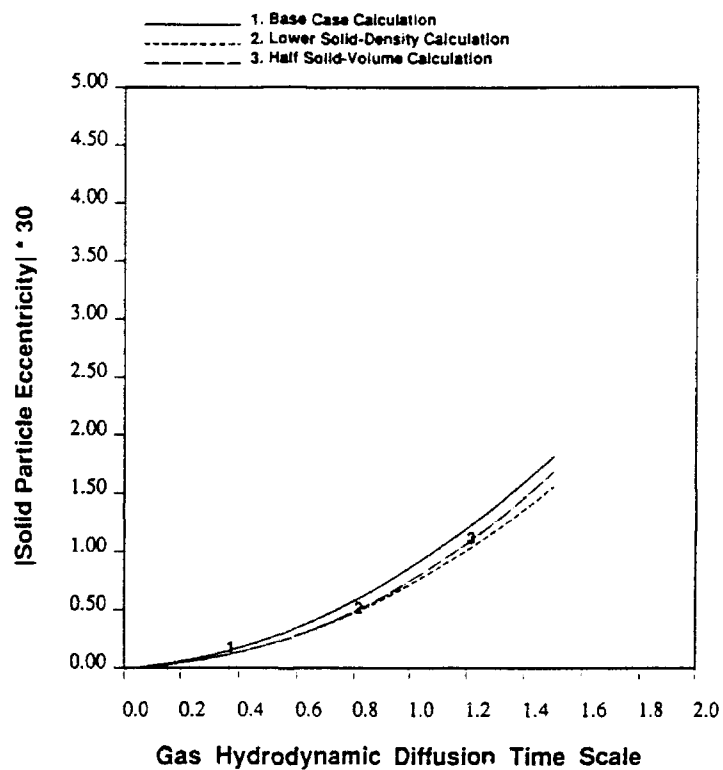


Figure E.10: Time variation of solid particle eccentricities  $|\epsilon|$  for the three slurry droplet cases studied.

Since the simulation was only carried to  $\tau_{Hg} = 1.5$  the solid temperatures remained substantially lower than those on the liquid surface. Finally, the time variation of droplet drag coefficients showed almost identical values for all three cases compared herein.

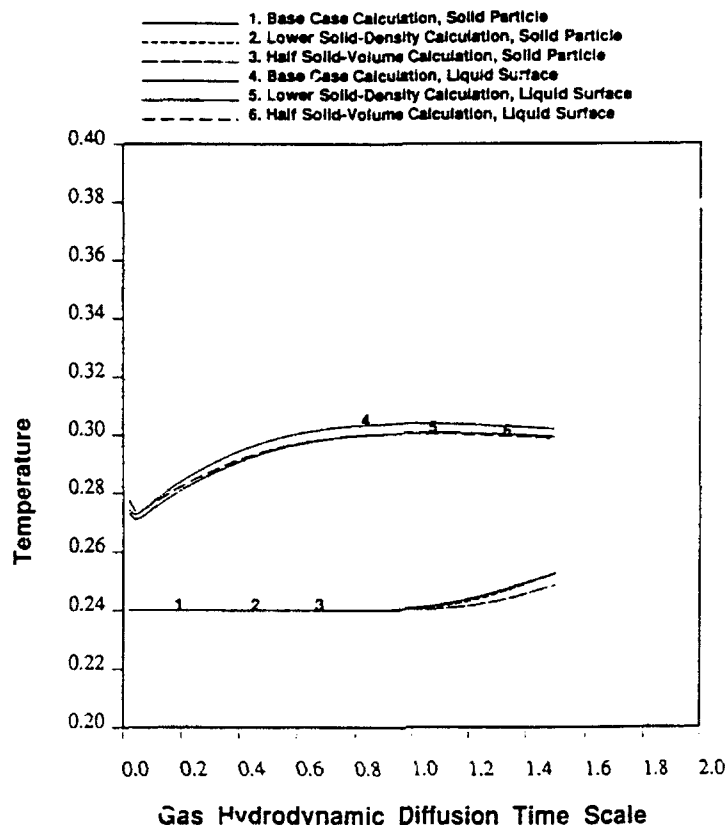


Figure E.11: Time variation of surface-averaged temperature on the gas/liquid interface and solid-particle temperature for the three slurry droplet cases studied.

The results obtained for the slurry simulations during the early stable period were compared to those obtained by Chiang et al.<sup>9</sup> for an all-liquid droplet. The relatively short periods of the slurry droplet lifetime resolved herein do not allow firm conclusions for later stages where the vaporization would be more vigorous.

The comparisons of slurry and all-liquid droplet results at the early stages of the droplet lifetime were performed using two gas/liquid interface quantities. First, the surface-averaged Nusselt number which is given by

$$Nu_{av,s} = \frac{a \int_0^\pi \kappa_g \frac{\partial T_s}{\partial n} \sin \phi d\phi}{1 - T_{av,s}} \quad (E.9)$$

with the surface-averaged temperature  $T_{av,s}$  calculated from

$$T_{av,s} = \frac{1}{2} \int_0^\pi T \sin \phi d\phi$$

Second, the surface-averaged Sherwood number which is given by

$$Sh_{.v,s} = \frac{a \int_0^\pi \rho_g D_g \frac{\partial Y_f}{\partial n} \sin\phi d\phi}{Y_{f,av,\infty} - Y_{f,av,s}} \quad (E.10)$$

where the average gas-phase mass fractions are calculated from

$$Y_{f,av} = \frac{1}{2} \int_0^\pi Y_f \sin\phi d\phi$$

The time variation of  $Nu_{av,s}$ , showed that the values of the heat transfer coefficient remain almost unchanged throughout all three slurry simulations, except during the very early stages when  $Nu_{av,s}$  shows a monotonically decreasing behavior. The corresponding values are nearly the same for all the slurry droplets, staying consistently above the all-liquid droplet values. The time variation of  $Sh_{av,s}$  for the four cases studied showed very similar values at all times, except during the very early stages of the simulation. This suggests that the presence of a large solid particle inside a liquid droplet does not significantly affect the mass transfer coefficients across the gas/liquid interface. We should emphasize, though, that our comparisons of slurry and all-liquid droplets are applicable during the very early stages of a droplet lifetime. Subsequent trends may be substantially different.

## E.9 Conclusions

A numerical investigation of the fundamental processes governing the momentum, energy and mass exchanges between the solid, liquid and gas phases of a slurry droplet suddenly injected in a hot-gas stream is presented. The axisymmetric configuration studied consists of an isolated slurry droplet containing a solid particle in its core and vaporizing in a laminar convective environment. The model allows for independent motion of the solid particle along the axis of symmetry of the flow, and it accounts for variable gas-phase properties as well as variable liquid-phase viscosities and latent heat of vaporization. In addition, the model considers internal liquid circulation with transient droplet heating, droplet surface regression due to vaporization, and droplet deceleration with respect to the free flow due to drag.

The slurry droplet calculation was terminated at an early stage when unstable behavior of the velocity and pressure fields over the solid-particle surface caused strong oscillations of the particle accelerations. The sensitivity of the instant of first appearance of the instability on numerical parameters and Reynolds number suggests that the instability is of numerical nature and is a result of the strong dynamic interaction of the liquid and solid phases. Even though our model cannot

adequately predict the slurry droplet dynamic and thermal behavior at later stages, it does provide some important insight for the early stable period.

The computed liquid-phase fields for the slurry droplet show that the presence of a large solid particle in the bulk of the liquid-carrier fluid is very important throughout the simulation. Continuous monitoring of the relative position of the solid and liquid constituents of the slurry droplet revealed that the solid particle is inertially lagging the motion of the liquid carrier, which is accelerated due to its shear interaction with the gaseous free stream. The axial motion of the particle within the liquid volume was found to be very significant, thus enhancing the internal liquid circulation. The liquid-phase isotherms indicate that convection is the dominant energy transfer mechanism within the slurry droplet. Despite the large spatial gradients of liquid temperature at any specific instant, the temperature within an aluminum particle was found to remain spatially uniform, even though it is temporally varying.

The angular variation of several quantities over the slurry droplet surface showed that the heat and mass transfer coefficients peak at regions close to the front stagnation point of the flow, while the maximum surface temperature occurs at regions closer to the recirculating wake behind the droplet. The results also suggested some condensation of the fuel vapor on the liquid surface near the recirculating wake region.

The effects of solid-particle size and density were also investigated with the slurry droplet model. We found that the displacement of the solid particle from the droplet center is reduced with decreasing particle size and density, when all other conditions remain unchanged. For all slurry droplets considered, a steadily increasing separation of the solid particle from the geometric center of the slurry droplet was found. The rate of increase of the solid-particle eccentricity during the stable period strongly suggests a high possibility of secondary atomization occurring through penetration of the solid particle through the gas/liquid interface at a subsequent stage. Such an event in a practical system would significantly enhance the liquid vaporization and would expose the solid particle to the hot environment of the combustion gases at a very early stage.

Even though our model provides some interesting trends for the early stages of the combustion of a slurry droplet which contains a large particle in its core, future work is needed to resolve the subsequent unstable stages, and consider other significant effects, such as gas/liquid interface non-sphericity.

## Appendix F

# Analysis Of Shell Formation From A Vaporizing Metal Slurry Droplet

### F.1 Introduction

In this section, a detailed two-dimensional numerical study, which takes into consideration an unsteady gas-phase, internal circulation in the liquid-phase, and motion of solid particles due to drag as a result of liquid recirculation is proposed. The formulation incorporates the effects of variable gas-and-liquid-phase properties, the effect of the presence of solid particles on the liquid phase.

### F.2 Analysis

Figure F.1 represents a schematic of the model. A single fuel droplet of n-octane with many fine aluminum particles dispersed in the liquid phase is injected into hot air. The slurry droplet is treated as a spherical droplet of known initial metal mass fraction. We assume that the droplet retains its spherical shape as time progresses. There are three distinct phases of vaporization before the solid shell thickens and becomes a rigid shell. Phase I of this process consists of establishing of a recirculating vortex inside the droplet, with droplet heating and vaporization from the droplet surface. This process is very similar to the case of a pure liquid droplet. During this period, the fine metal particles inside the droplet experience the drag force due to the recirculating liquid field and start moving very closely tracing the streamlines. Gradually these particles start deviating from the liquid streamlines and move towards the surface. Phase II of this process is marked by formation of a

solid agglomerate at the droplet surface while the droplet surface continues to regress. During this phase, the solid shell forms due to the collection of particles at the droplet surface, but the shell does not have sufficient strength to support itself. Hence, the shell moves along with the liquid surface allowing liquid to permeate through the shell. At this time, the circulation inside the droplet is observed to slow down as the presence of a solid shell at the gas-liquid interface inhibits the viscous drag forces from driving the recirculation inside the droplet. Phase III of this process starts after the first layer of shell has completely formed and the flow inside the droplet becomes very slow. This phase consists of very weak convection inside the droplet. Conduction then dominates the droplet heating process and the shell thickens due to droplet surface regression because of evaporation until it gains sufficient strength to become a rigid solid shell. Beyond this point, the droplet surface does not regress any further and a bubble forms inside the droplet as predicted and observed in previous studies. A description of various processes and different modes of slurry-droplet vaporization can be found in figure F.2. The scope of the present study is limited to the stage when the solid shell rigidizes yielding no further regression. The details of these processes have been discussed in the following sections.

#### Phase I: Liquid Droplet Heating

In this case, the proposed model is based on an isolated fuel droplet injected suddenly into a hot stream of air. The same model was used by Chiang and Sirignano [1991] for a pure liquid droplet vaporization case. The gas-phase equations remain the same and they will not be repeated here. However, the liquid-phase equations have been modified to consider the effects of the presence of particles by incorporating proper source terms in the liquid phase. The analysis is based on a primitive variable formulation of the Navier-Stokes and energy equations in two dimensions for both gas and liquid phases along with the species equation and the gas equation of state. The liquid and gas phases are formulated using a Eulerian coordinate system. The particles are dispersed in the liquid phase uniformly at the time of injection. The particles are tracked individually in the flow field using Lagrangian equations of motion. The number of equations for the particles are reduced by solving for a limited number of particles, each representing a number of particles in the immediate vicinity. This greatly reduces the computational effort to a great extent. The effects of variable properties in the gas and liquid phases have been taken into consideration for this formulation. The modified liquid-phase and particle equations are given below.

#### Assumptions

1. The Weber number is small, thereby ensuring the spherical shape of the droplet.
2. Gravitational effects are neglected in this analysis.
3. Phase equilibrium is assumed at the droplet surface.

4. The thermal radiant and Dufour energy flux terms are assumed to be negligible.
5. The air-fuel vapor mixture is assumed to behave like an ideal gas.
6. The flow is assumed to be isentropic.
7. The metal particles are small enough to allow point-mass approximation without causing substantial error.
8. The Mach number of the flow is small so that the dissipation terms are negligible.

### Gas-Phase Equations

#### Continuity Equation

$$\frac{\partial}{\partial \tau_{Hg}}(r\rho_g) + \frac{\partial}{\partial r}(rRe_g\rho_g V_r) + \frac{\partial}{\partial z}(rRe_g\rho_g V_z) = 0 \quad (F.1)$$

#### Momentum Equation in r-direction

$$\begin{aligned} \frac{\partial}{\partial \tau_{Hg}}(r\rho_g V_r) + \frac{\partial}{\partial r}\{rRe_g(\rho_g V_r V_r + p_g)\} + \frac{\partial}{\partial z}(rRe_g\rho_g V_r V_z) &= \frac{2}{3} \frac{\partial}{\partial r}\{r\mu_g(2\frac{\partial V_r}{\partial r} - \frac{V_r}{r} - \frac{\partial V_z}{\partial r})\} + \\ \frac{\partial}{\partial z}\{r\mu_g(\frac{\partial V_r}{\partial z} + \frac{\partial V_z}{\partial r})\} + Re_g p_g - \frac{2\mu_g}{3}(2\frac{V_r}{r} - \frac{\partial V_r}{\partial r} - \frac{\partial V_z}{\partial z}) & \quad (F.2) \end{aligned}$$

#### Momentum Equation in z-direction

$$\begin{aligned} \frac{\partial}{\partial \tau_{Hg}}(r\rho_g V_z) + \frac{\partial}{\partial r}(rRe_g\rho_g V_r V_z) + \frac{\partial}{\partial z}\{rRe_g(\rho_g V_z V_z + p_g)\} &= \frac{\partial}{\partial r}\{rRe_g(\frac{\partial V_r}{\partial z} + \frac{\partial V_z}{\partial r})\} + \\ \frac{2}{3} \frac{\partial}{\partial z}\{r\mu_g(2\frac{\partial V_z}{\partial z} - \frac{V_r}{r} - \frac{\partial V_r}{\partial r})\} & \quad (F.3) \end{aligned}$$

#### Energy Equation

$$\begin{aligned} C_{pg}\{\frac{\partial}{\partial \tau_{Eg}}(r\rho_g T_g) + \frac{\partial}{\partial r}(rPe_g\rho_g V_r T_g) + \frac{\partial}{\partial z}(rPe_g\rho_g V_z T_g)\} + (h_o - h_f)\{\frac{\partial}{\partial \tau_{Eg}}(r\rho_g Y_o) + \frac{\partial}{\partial r}(rPe_g\rho_g Y_o V_r) \\ + \frac{\partial}{\partial z}(rPe_g\rho_g Y_o V_z)\} = \frac{\partial}{\partial r}(r\kappa_g \frac{\partial T_g}{\partial r}) + \frac{\partial}{\partial z}(r\kappa_g \frac{\partial T_g}{\partial z}) - \frac{\partial}{\partial r}(rLe_g(C_{pf} - C_{po})T_g\rho_g L_g \frac{\partial Y_o}{\partial r}) \end{aligned}$$

$$-\frac{\partial}{\partial z}(rLe_g(C_{pf} - C_{po})T_g\rho_g D_g \frac{\partial Y_o}{\partial z}) \quad (F.4)$$

### Species Equation

$$\frac{\partial}{\partial r_S}(r\rho_g Y_i) + \frac{\partial}{\partial r}(r\frac{Pe_g}{Le_g}\rho_g V_r Y_i) + \frac{\partial}{\partial z}(r\frac{Pe_g}{Le_g}\rho_g V_z Y_i) = \frac{\partial}{\partial r}(r\rho_g D_g \frac{\partial Y_i}{\partial r}) + \frac{\partial}{\partial z}(r\rho_g D_g \frac{\partial Y_i}{\partial z}) \quad (F.5)$$

### Equation of State

$$p_g = \frac{R}{M}(\rho_g T_g - M) \quad (F.6)$$

### Liquid-Phase Equations

#### Continuity Equation

$$\frac{\partial}{\partial r_{HL}}(r\rho_l) + \frac{\partial}{\partial r}(rRe_l\rho_l V_r) + \frac{\partial}{\partial z}(rRe_l\rho_l V_z) = 0 \quad (F.7)$$

#### Momentum Equation in r-direction

$$\begin{aligned} \frac{\partial}{\partial r_{HL}}(r\rho_l V_r) + \frac{\partial}{\partial r}\{rRe_l(\rho_l V_r V_r + p_l)\} + \frac{\partial}{\partial z}(rRe_l\rho_l V_r V_z) &= \frac{2}{3}\frac{\partial}{\partial r}\{r\mu_l(2\frac{\partial V_r}{\partial r} - \frac{V_r}{r} - \frac{\partial V_z}{\partial r})\} + \\ \frac{\partial}{\partial z}\{r\mu_l(\frac{\partial V_r}{\partial z} + \frac{\partial V_z}{\partial r})\} + Re_l p_l - \frac{2\mu_l}{3}(2\frac{V_r}{r} - \frac{\partial V_r}{\partial r} - \frac{\partial V_z}{\partial z}) - S_r & \quad (F.8) \end{aligned}$$

#### Momentum Equation in z-direction

$$\begin{aligned} \frac{\partial}{\partial r_{HL}}(r\rho_l V_z) + \frac{\partial}{\partial r}(rRe_l\rho_l V_r V_z) + \frac{\partial}{\partial z}\{rRe_l(\rho_l V_z V_z + p_l)\} &= \frac{\partial}{\partial r}\{rRe_l(\frac{\partial V_r}{\partial z} + \frac{\partial V_z}{\partial r})\} + \\ \frac{2}{3}\frac{\partial}{\partial z}\{r\mu_l(2\frac{\partial V_z}{\partial z} - \frac{V_r}{r} - \frac{\partial V_r}{\partial r})\} - S_z & \quad (F.9) \end{aligned}$$

### Energy Equation

$$C_{p'l} \left\{ \frac{\partial}{\partial \tau_{EL}} (r \rho_l T_l) + \frac{\partial}{\partial r} (r P e_l \rho_l V_r T_l) + \frac{\partial}{\partial z} (r P e_l \rho_l V_z T_l) \right\} = \frac{\partial}{\partial r} (r \kappa_l \frac{\partial T_l}{\partial r}) + \frac{\partial}{\partial z} (r \kappa_l \frac{\partial T_l}{\partial z}) - S_T \quad (F.10)$$

### Pressure-Density-Temperature Relation<sup>1</sup>

$$\frac{1}{\rho'_l} = \frac{1}{\rho'_{l, sat}} \left[ 1 - c \ln \left( \frac{\beta + p'_l}{\beta + p'_{vp}} \right) \right] \quad (F.11)$$

where  $\beta$  is calculated from

$$\beta / p'_{crit} = -1 + a(1 - T_r)^{1/3} + b(1 - T_r)^{2/3} + d(1 - T_r) + e(1 - T_r)^{4/3} \quad (F.12)$$

The values of the constant are available from Reid et al.

### Source Terms

$$S_r = \frac{2}{3} \sum_{j=1}^N \delta(r - r_{pj}) \delta(z - z_{pj}) \frac{N_j}{\Delta z \Delta r} \rho_p R_{pj}^3 \frac{dU_{jr}}{d\tau_{HL}} \quad (F.13)$$

$$S_z = \frac{2}{3} \sum_{j=1}^N \delta(r - r_{pj}) \delta(z - z_{pj}) \frac{N_j}{\Delta z \Delta r} \rho_p R_{pj}^3 \frac{dU_{jz}}{d\tau_{HL}} \quad (F.14)$$

$$S_T = \frac{2}{3} \sum_{j=1}^N \delta(r - r_{pj}) \delta(z - z_{pj}) \frac{N_j}{\Delta z \Delta r} \rho_p C_{pp} R_{pj}^3 \frac{dT_j}{d\tau_{EL}} \quad (F.15)$$

## Particle Dynamics

### Equation of Motion in r-direction

$$\frac{dr_p}{dt} = U_{pr} \quad (F.16)$$

<sup>1</sup>This relation is known as the Hankinson-Brobst-Thomson technique for predicting the compressed liquid density

$$\frac{dU_{r,p}}{dt} = \frac{3}{16} \frac{\nu}{R_p^2} \frac{\rho_l}{(\rho_p + 0.5\rho_l)} C_{r,D} Re_{r,p} (U_r - U_{r,p}) + \frac{\rho_l}{2\rho_p + \rho_l} \frac{dU_r}{dt} \quad (\text{F.17})$$

Equation of Motion in z-direction

$$\frac{dz_p}{dt} = U_{pz} \quad (\text{F.18})$$

$$\frac{dU_{z,p}}{dt} = \frac{3}{16} \frac{\nu}{R_p^2} \frac{\rho_l}{(\rho_p + 0.5\rho_l)} C_{z,D} Re_{z,p} (U_z - U_{z,p}) + \frac{\rho_l}{2\rho_p + \rho_l} \frac{dU_z}{dt} \quad (\text{F.19})$$

$$C_{r,D} = \frac{24}{Re_{r,p}} \left\{ 1 + \frac{Re_{r,p}^{\frac{2}{3}}}{6} \right\}$$

and

$$C_{z,D} = \frac{24}{Re_{z,p}} \left\{ 1 + \frac{Re_{z,p}^{\frac{2}{3}}}{6} \right\}$$

$$Re_{r,p} = \frac{2R_p |U_r - U_{r,p}|}{\nu}$$

and

$$Re_{z,p} = \frac{2R_p |U_z - U_{z,p}|}{\nu}$$

Energy Equation

$$\rho_p C_{pp} \frac{dT_p}{dt} = \frac{3}{R_p} h (T_l - T_p) \quad (\text{F.20})$$

where h can be found from:

$$Nu = \frac{2hR_p}{\kappa_l}$$

$$Pr = \frac{\mu_l C_{pl}}{\kappa_l}$$

$$Nu = 1 + (1 + RePr)^{\frac{1}{3}} Re^{0.077}$$

$$Re_p = \frac{2R_p|U_l - U_p|}{\nu}$$

### Phase II: Shell Spread Around The Droplet

When a recirculation vortex is established inside the liquid droplet, the particles start moving at a faster rate towards the droplet surface. At a later time, they start reaching the surface and thus start forming a solid agglomerate at the surface. In this analysis, we exclude the possibility of diffusion of particles into the droplet interior after they reach surface. This can be supported by the fact that the particles are not small enough to permit significant Brownian motion. Hence, the particles start agglomerating at the droplet surface. After reaching the surface, the particles follow the liquid to the backward stagnation point and start stacking to form the first layer of particles around the droplet. This shell envelope grows with time and gradually covers the droplet with a single layer. During this period, all of the equations mentioned above remain the same except for the boundary condition at the interface. In this analysis, we assume a permeable shell and neglect capillary action due to the presence of the shell at the interface. But the presence of a solid shell at the interface prevents any slip between the shell and the tangential components of gas and liquid-phase velocities along the shell surface become zero. The presence of the shell however does not affect the radial component of velocity and thereby does not affect evaporation. During this stage, the main driving force behind the circulation of the liquid droplet gradually diminishes and, due to viscous dissipation, the flow inside the droplet slows down.

### Phase III: Conductive Heating of Droplet Surface interior

When one layer of shell has formed, the recirculation almost stops due to viscous dissipation. So the effect of convection becomes insignificant compared to conduction and the droplet continues to get heated due to conduction heat transfer. During this period, the basic mode of heat transfer during this period is conduction. At this time, we discontinue solving the momentum equations for the liquid phase as the liquid velocities become insignificant. There, the convective terms in the liquid-phase energy equation are negligible. The droplet, however, continues to regress due to evaporation. During this period, the droplet surface interface sweeps through the particles which become almost stationary in the surrounding stagnant liquid. So, the shell growth is mainly driven by the rate of droplet surface regression. We assume that when the shell thickness reaches three particle diameter thickness, it gains enough strength to rigidize. Beyond this time, the outside droplet diameter becomes fixed but

the liquid continues to evaporate because of heating. This supports the observations made by previous chapters regarding the existence of a core inside the droplet because of presence of a vapor-air bubble inside the interior of the droplet.

### F.3 Solution Procedure

A detailed description of the solution procedure for the gas and liquid phases is given in [21]. The pressure correction equation is solved using successive-over-relaxation scheme. The momentum and energy equations are solved using the alternating-direction-predictor-corrector method. The ODEs for the particles are solved using a fourth order Runge-Kutta method.

### F.4 Results

The results of numerical simulations with different droplet radii, particle loading and Reynolds number are presented in this section. Slower convergence due to the primitive variable formulation and the effect of solid particles on the liquid phase makes complete simulation prior to the formation of the three diameter thick shell prohibitive. Hence, a compromise between computational resources and the physical phenomenon is made. The base case of  $Re = 100$ , particle loading of 25% and particle radius of 0.01 is calculated until the shell is rigidized. The other cases are simulated until the completion of the second shell. The results are presented in two sections, i.e., a detailed analysis of the flow-field and its deviation from the classical pure liquid droplet and a parametric comparison of different cases with different types of particle.

#### Description of the Flow-Field

The following results were obtained using  $Re = 100$ , a particle loading by volume of 25% and particle radius equal to 0.01. Figures F.3-9 describe the flow-field for a droplet at different stages of time. Figures F.10-11 are a similar description for a pure liquid droplet for the sake of comparison. Figures F.3 and 4 are descriptions of the velocities and streamlines inside the droplet before the shell formation. These figures are very similar to those for the pure droplet case. Figure F.5 is the temperature profile inside the droplet. It should be noted that even though the principal mode of heat transfer is convection, it is, however, less prominent in this case than the pure liquid droplet. Figures F.6-8 are the velocity, streamline and temperature profiles inside the droplet after the formation of the first layer of shell. It should be noted

that the stream functions have lower maximum values than those in Figure F.4, implying a reduction in liquid recirculation. Figure F.8 indicates that the basic mode of heat transfer is once again changing back to conduction. Along the shell, the tangential velocity is zero due to the presence of a solid shell. In this present model, the shell starts to form at the backward stagnation point. Hence, the velocity near the backward stagnation point decelerates faster resulting in almost a stagnant situation near the backward stagnation point. This is supported by the change in orientation of streamlines in Figure F.6. The vortex center moves towards the forward stagnation point. Figure F.9 presents the temperature profile inside the droplet after the shell becomes rigid. This profile indicates that conduction is the basic mechanism for heat transfer. The gas phase behaves in a very similar manner like the case of a pure liquid droplet.

Figure F.13 shows the motion of a particle inside the droplet. The particle follows the liquid stream function very closely; however, as time progresses, it starts deviating outward to the droplet surface. This is caused by the drag forces on the particle.

#### Effect of Different Parameters

The table below summarizes the results of the simulations.

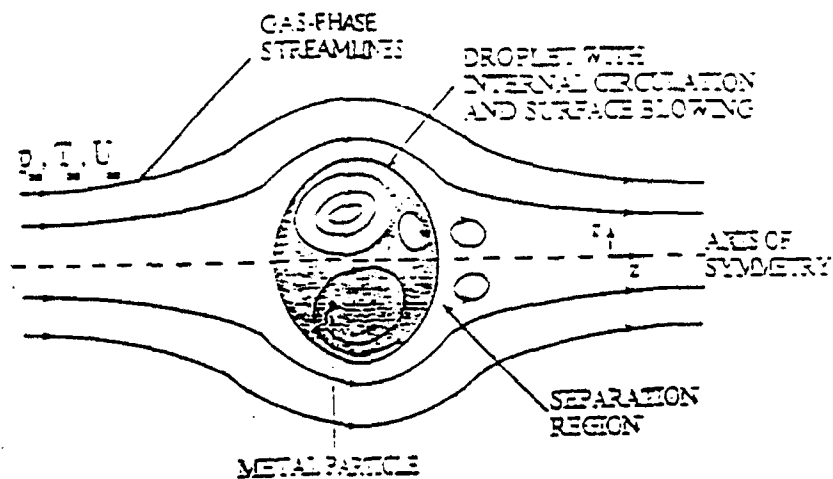
Re	$r_p$	Time (1st shell)	Time (2nd shell)	Time (3rd shell)
100	0.01	0.0848 ms	0.26 ms	0.42 ms
100	0.0075	0.076 ms	0.19 ms	NA
75	0.01	0.0892 ms	NA	NA
100	0.015	0.1010 ms	NA	NA

It is quite obvious from the table that shell formation time is significantly affected by liquid recirculation. The formation of first layer is hastened considerably because of the tendency of the particles to move towards the surface. Gradually, the effect of convection reduces and, hence, the rate at which the particles strike the surface reduces and eventually the process of particle motion almost stops. Then, the growth of shell is governed by the droplet surface regression. The particles strike the droplet surface towards the forward stagnation point and are quickly transported to the backward stagnation point to start forming the shell. This was experimentally observed by Law and Lee. They observed that the shell started in the front and swiftly spread all around the droplet. Decrease in particle size and increase in Reynolds number results in shorter shell formation time. The formation of a shell at the interface affects the liquid-phase circulation significantly. In Figure F.14, liquid-phase

circulation experiences considerable reduction with time. The vaporization rates are unaffected by the radius of the particles, however, it is significantly affected by particle loading. Due to the particle loading, the overall specific heat of the droplet is increased and as a result the average volume temperature is less than that of the pure liquid case (Fig. F.15). However, the amount of heat that convects into the droplet interior is less due to weaker liquid convection and, as a result, the surface temperatures are higher for the droplet with particles resulting a higher evaporation rate. Initially, the droplet radius increases by about 7% due to a drop in density arising from droplet heating, but it gradually starts decreasing due to loss of liquid mass because of evaporation. The drag coefficient experiences some fluctuations, which are numerical in nature and, is a result of sudden change in boundary condition due to shell formation. However, it should be noted that the drag coefficient of the droplet after the formation of a solid shell is higher (Fig. F.17) than for the pure liquid droplet. This is due to a rise in the friction drag because of the presence of the shell. However, a change in particle size affects the shell formation time, while the drag coefficient, liquid circulation, evaporation rate are not considerably affected.

## F.5 Conclusions

The results obtain throw an *interesting insight into the fundamental mechanism* of shell agglomerate formation. The particles move towards the droplet surface due to the drag forces and the time taken to reach the surface is significantly less than the droplet lifetime. However, the growth of shell will slowly decelerate liquid recirculation and eventually convection inside the droplet will become insignificant. The results indicate that estimation of shell formation time without considering the effect of liquid recirculation will tend to overestimate the shell formation time.



FLOW OVER A VAPORIZING DROPLET

Figure F1 Schematic of the problem

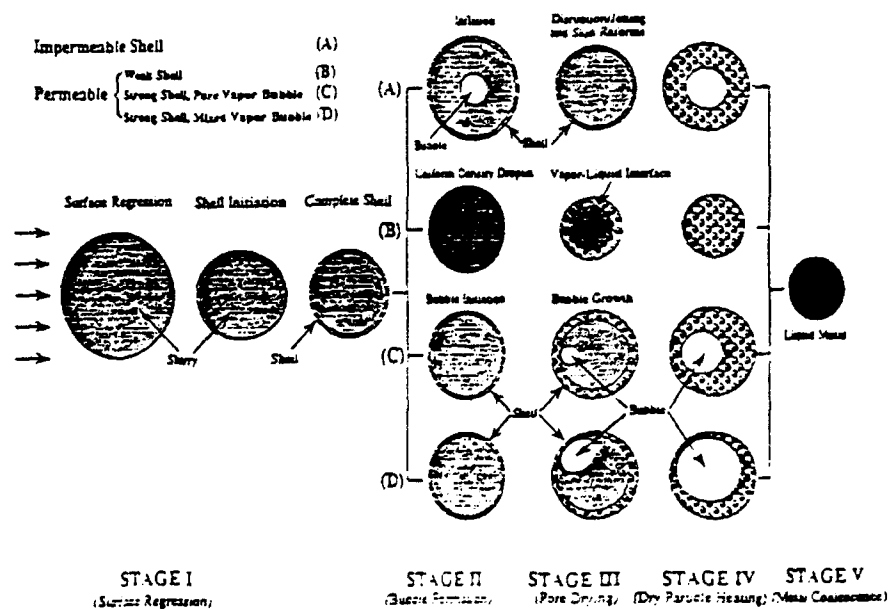
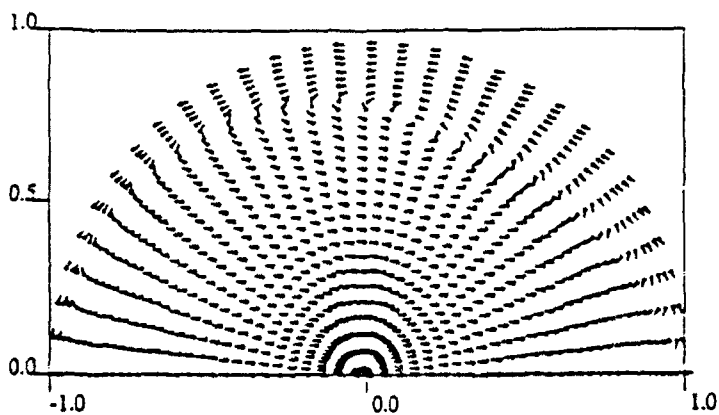


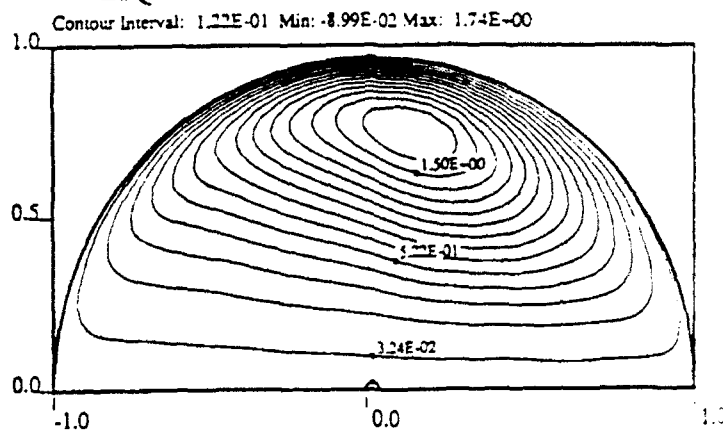
Figure F2 Different processes in slurry droplet vaporization. (taken from Bhatta and Sirignano, 1992, with author's permission)

LIQUID-PHASE VELOCITY VECTORS



Time = 0.68 , Instantaneous Reynolds Number = 97.35  
 Ambient Temperature = 1200 K  
 Initial Droplet Temperature = 300 K  
 Initial Reynolds Number = 100  
 N-Octane Droplet Vaporizing in Nitrogen Environment  
 Ambient Pressure = 10 atm

LIQUID-PHASE STREAM FUNCTION

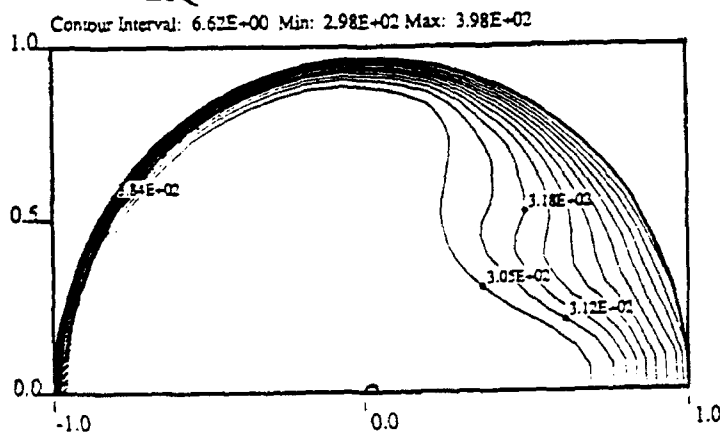


Time = 0.68 , Instantaneous Reynolds Number = 97.35  
 Ambient Temperature = 1200 K  
 Initial Droplet Temperature = 300 K  
 Initial Reynolds Number = 100  
 N-Octane Droplet Vaporizing in Nitrogen Environment  
 Ambient Pressure = 10 atm

Figure F3 Liquid-phase velocity vectors of a slurry droplet with particle loading (by volume) = 25%

Figure F4 Liquid-phase stream functions of a slurry droplet with particle loading (by volume) = 25%

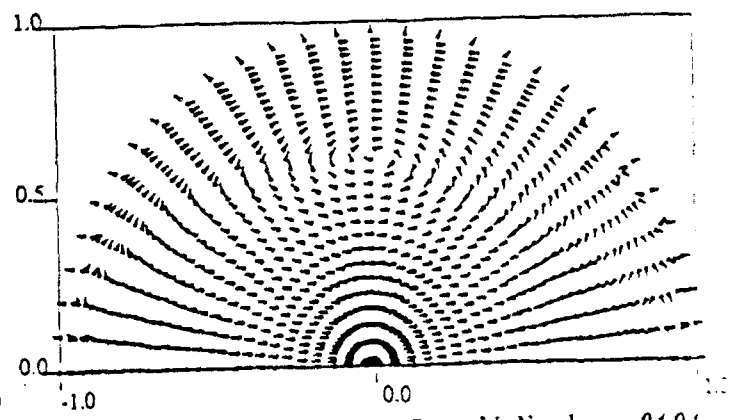
LIQUID-PHASE ISOTHERMS



Time = 0.68 , Instantaneous Reynolds Number = 97.35  
 Ambient Temperature = 1200 K  
 Initial Droplet Temperature = 300 K  
 Initial Reynolds Number = 100  
 N-Octane Droplet Vaporizing in Nitrogen Environment  
 Ambient Pressure = 10 atm

Figure F5 Liquid-phase isotherms of a slurry droplet with particle loading (by volume) = 25%

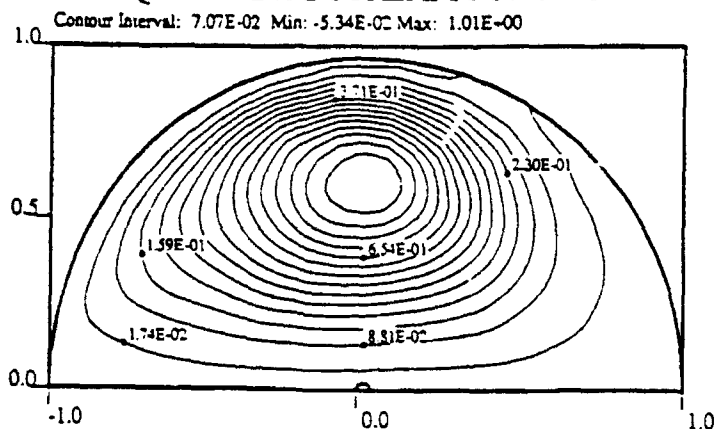
LIQUID-PHASE VELOCITY VECTORS



Time = 1.36 , Instantaneous Reynolds Number = 94.94  
 Ambient Temperature = 1200 K  
 Initial Droplet Temperature = 300 K  
 Initial Reynolds Number = 100  
 N-Octane Droplet Vaporizing in Nitrogen Environment  
 Ambient Pressure = 10 atm

Figure F6 Liquid-phase velocity vectors of a slurry droplet with particle loading (by volume) = 25% after the completion of the first layer of the shell.

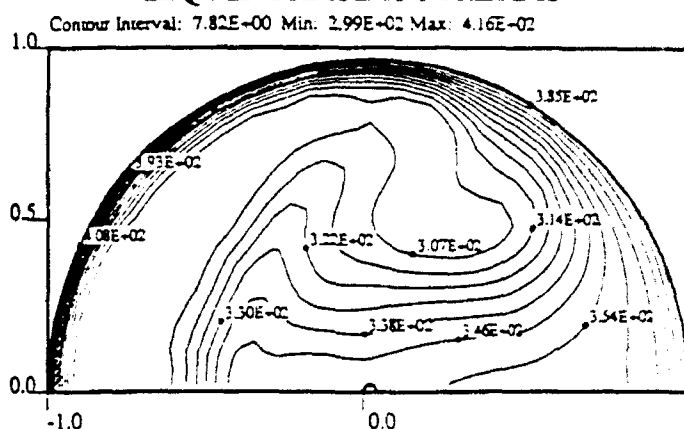
### LIQUID-PHASE STREAM FUNCTION



Time = 1.36 , Instantaneous Reynolds Number = 94.94  
 Ambient Temperature = 1200 K  
 Initial Droplet Temperature = 300 K  
 Initial Reynolds Number = 100  
 N-Octane Droplet: Vaporizing in Nitrogen Environment  
 Ambient Pressure = 10 atm

FigureF.7 Liquid-phase stream functions of a slurry droplet with particle loading (by volume) = 25% after the completion of the first layer of the shell.

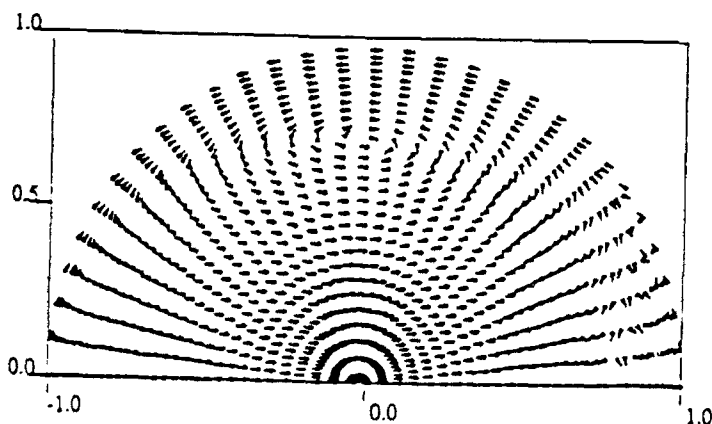
### LIQUID-PHASE ISOTHERMS



Time = 1.36 , Instantaneous Reynolds Number = 94.94  
 Ambient Temperature = 1200 K  
 Initial Droplet Temperature = 300 K  
 Initial Reynolds Number = 100  
 N-Octane Droplet: Vaporizing in Nitrogen Environment  
 Ambient Pressure = 10 atm

FigureF.8 Liquid-phase isotherms of a slurry droplet with particle loading (by volume) = 25% after the completion of the first layer of the shell.

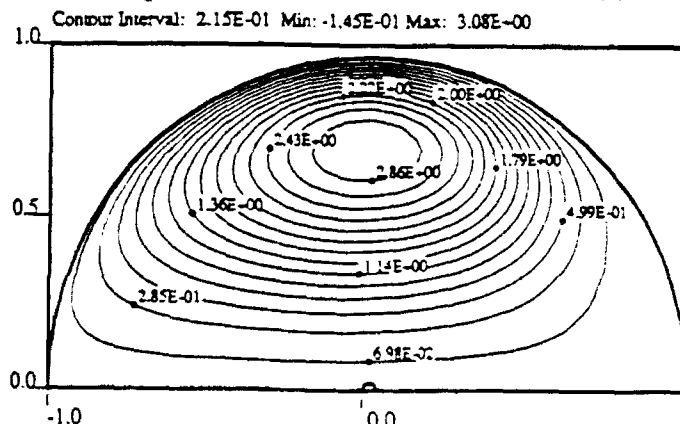
### LIQUID-PHASE VELOCITY VECTORS



Time = 1.40 , Instantaneous Reynolds Number = 91.83  
 Ambient Temperature = 1200 K  
 Initial Droplet Temperature = 300 K  
 Initial Reynolds Number = 100  
 N-Octane Droplet Vaporizing in Nitrogen Environment  
 Ambient Pressure = 10 atm

FigureF.9 Liquid-phase velocity vectors of a pure liquid droplet with particle loading (by volume) = 25%

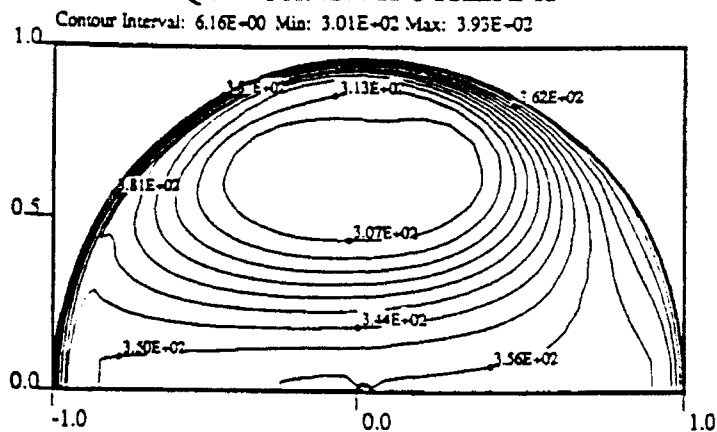
### LIQUID-PHASE STREAM FUNCTION



Time = 1.40 , Instantaneous Reynolds Number = 91.83  
 Ambient Temperature = 1200 K  
 Initial Droplet Temperature = 300 K  
 Initial Reynolds Number = 100  
 N-Octane Droplet: Vaporizing in Nitrogen Environment  
 Ambient Pressure = 10 atm

FigureF.10 Liquid-phase stream functions of a pure liquid droplet.

## LIQUID-PHASE ISOTHERMS



Time = 1.40 , Instantaneous Reynolds Number = 91.83

Ambient Temperature= 1200 K

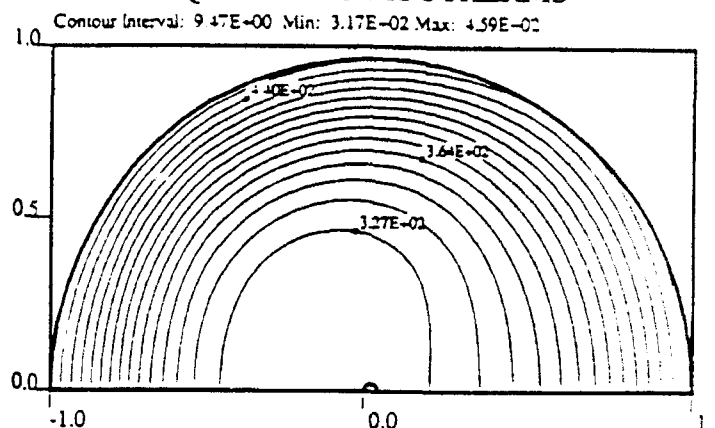
Initial Droplet Temperature= 300 K

Initial Reynolds Number = 100

N-Octane Droplet Vaporizing in Nitrogen Environment

Ambient Pressure = 10 atm

## LIQUID-PHASE ISOTHERMS



Time = 6.78 , Instantaneous Reynolds Number = 76.32

Ambient Temperature= 1200 K

Initial Droplet Temperature= 300 K

Initial Reynolds Number = 100

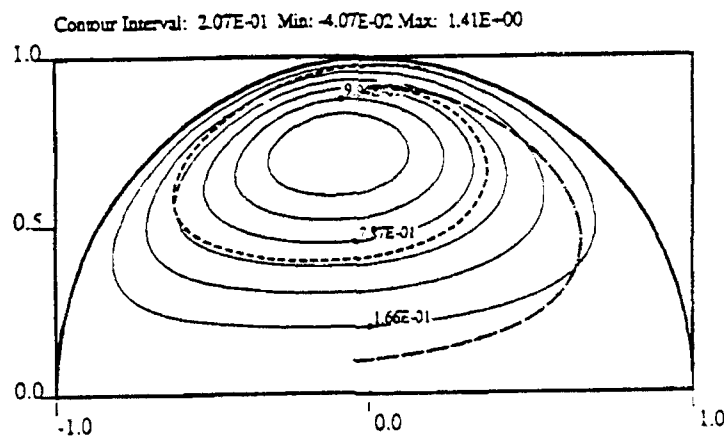
N-Octane Droplet Vaporizing in Nitrogen Environment

Ambient Pressure = 10 atm

Figure F.11 Liquid-phase isotherms of a pure liquid droplet. Figure F.12

Liquid-phase isotherms of slurry droplet with particle loading (by volume) = 25% after the completion of the third layer of shell.

## LIQUID-PHASE STREAM FUNCTION WITH METAL PARTICLES



Time = 2.28 , Instantaneous Reynolds Number = 81.98

Ambient Temperature= 1250 K

Initial Droplet Temperature= 300 K

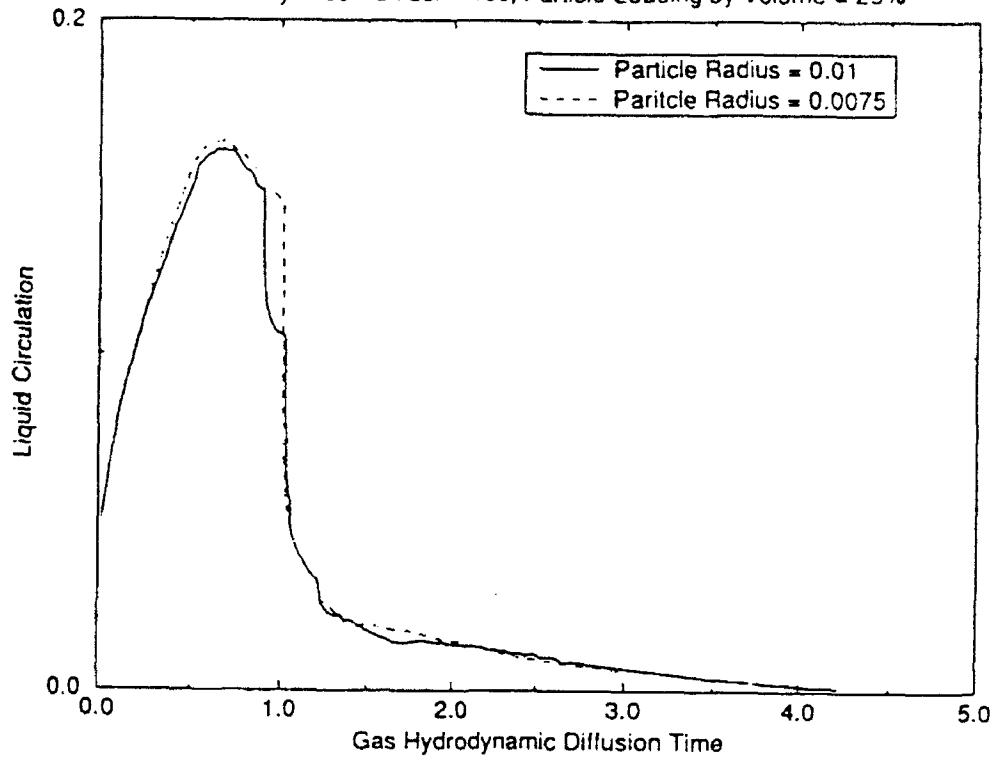
Initial Reynolds Number = 100

Figure F.13 Liquid-phase stream function and the motion of metal particles.

## Liquid Circulation

Initial Reynolds Number = 100, Particle Loading by Volume = 25%

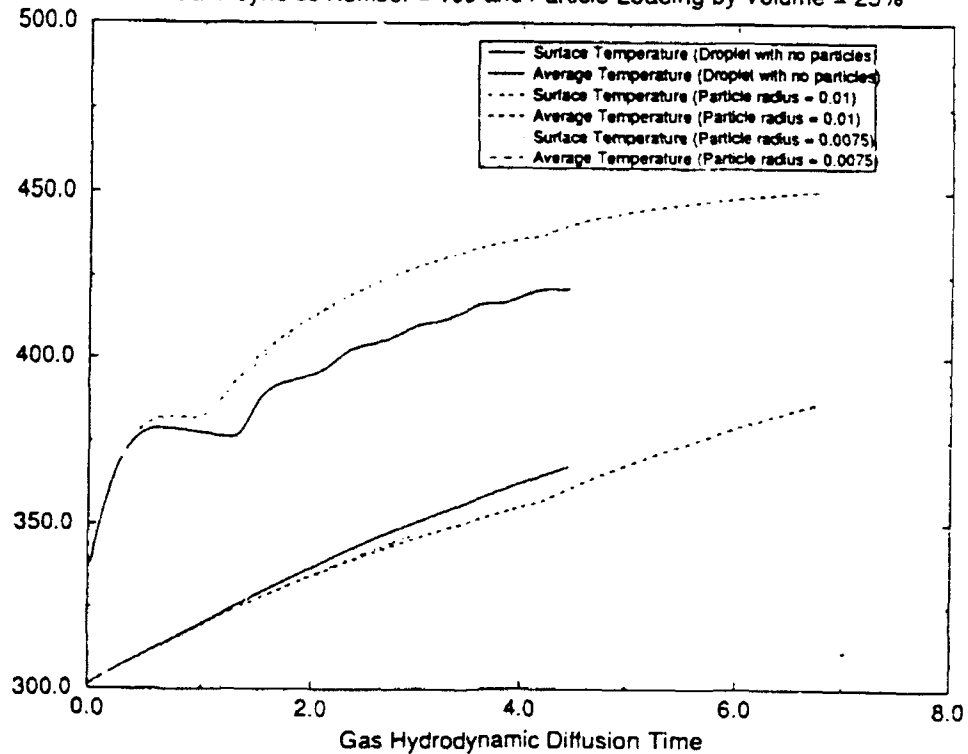
198



FigureF.14 Liquid-phase circulation (non-dimensional) vs. time.

## Temperature

Initial Reynolds Number = 100 and Particle Loading by Volume = 25%



FigureF.15 Average surface and volume temperatures vs. time.

### Liquid Mass and Droplet Radius

Initial Reynolds Number = 100 and Particle Loading (by volume) = 25%

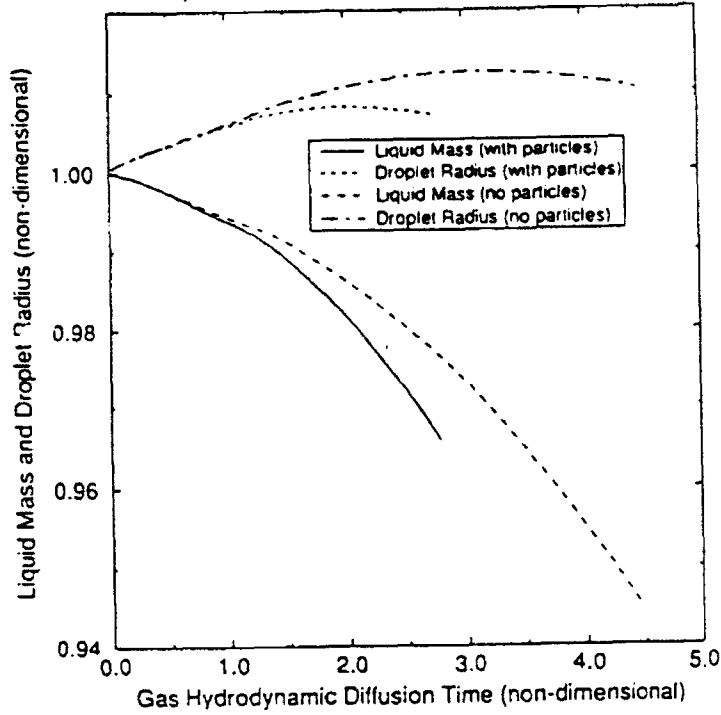


Figure F.16 Droplet radius and liquid mass vs. time.

### Drag Coefficient

Initial Reynolds Number = 100

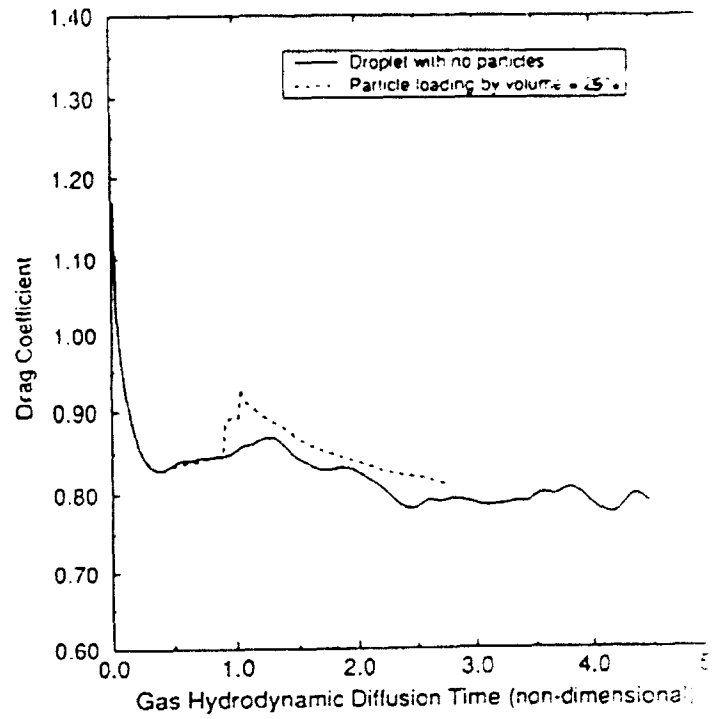


Figure F.18 Drag coefficient vs. time.

### Drag Coefficient

Initial Reynolds Number = 100, Particle Loading by volume = 25%

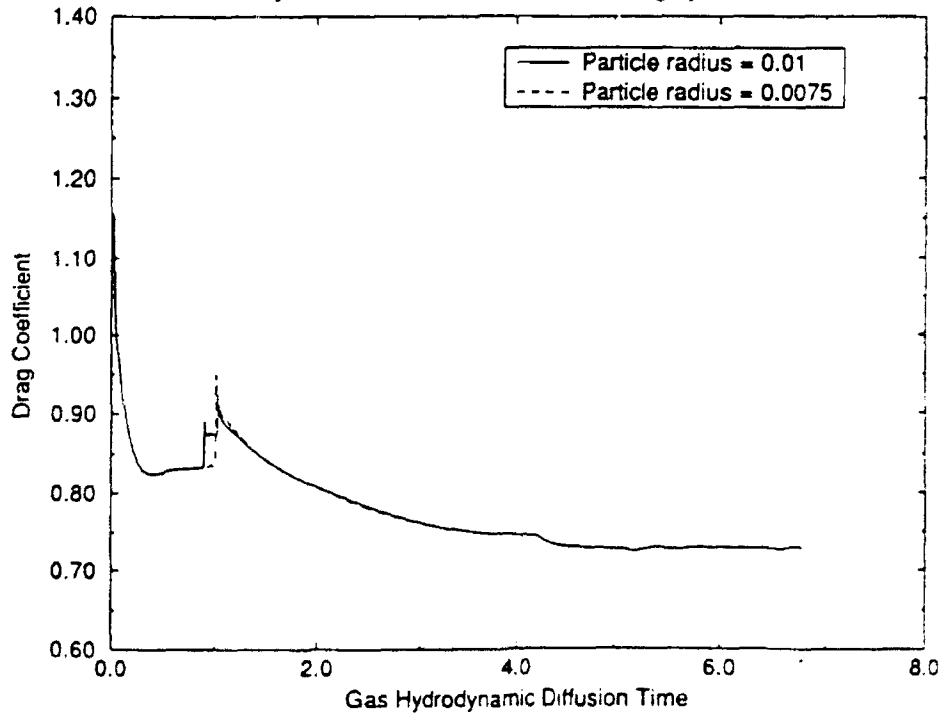


Figure F.17 Drag coefficient vs. time.